







Faculteit Wetenschappen  
Departement Chemie

# Plasma catalysis: Study of packing materials on CO<sub>2</sub> reforming in a DBD reactor

Proefschrift voorgelegd tot het behalen van de graad van  
**doctor in de wetenschappen: chemie**  
aan de Universiteit Antwerpen  
te verdedigen door  
**Inne Michielsen**

Promotoren: Dr. Vera Meynen en Dr. Annemie Bogaerts  
Antwerpen 2019





# INDEX

---

List of Figures .....	V
List of Tables.....	X
Acknowledgements .....	XIII
Preface.....	1
1 Introduction .....	3
1.1 General Introduction.....	4
1.1.1 CO <sub>2</sub> mitigation and global warming .....	4
1.1.2 Biogas as a value-added CO <sub>2</sub> source .....	7
1.1.3 Renewable energy.....	8
1.2 CO <sub>2</sub> conversion approaches.....	12
1.2.1 Thermal CO <sub>2</sub> splitting .....	12
1.2.2 Thermal Dry reforming.....	14
1.2.3 Novel CO <sub>2</sub> conversion approaches.....	16
1.2.4 Catalytic conversion.....	21
1.3 Plasma technology for CO <sub>2</sub> conversion.....	22
1.3.1 General plasma properties.....	22
1.3.2 Plasma catalysis .....	30
1.3.3 State of the art.....	35
1.4 Aim of this research .....	52
2 Materials and methods .....	53

2.1	Plasma.....	54
2.1.1	Experimental setup.....	54
2.1.2	Electrical characterization.....	60
2.2	Catalysis.....	62
2.2.1	Packing materials .....	62
2.2.2	Drip casting .....	63
2.2.3	Characterisation methods.....	65
3	Study of CO <sub>2</sub> splitting: understanding the fundamentals of plasma catalysis .....	67
3.1	State of the art.....	68
3.2	Results and discussion .....	71
3.2.1	Effect of bead material and bead size .....	71
3.2.2	Combined effect of bead size and gap size .....	80
3.2.3	Effect of glass wool or quartz wool packing .....	85
3.2.4	Interaction between dielectric barrier and bead material .....	91
3.3	Conclusion.....	93
4	Study of Dry Reforming: focus on selectivity.....	95
4.1	State of the art.....	96
4.2	Results and discussion .....	97
4.2.1	CO <sub>2</sub> conversion in DRM and comparison with CO <sub>2</sub> splitting .....	97
4.2.2	CH <sub>4</sub> and total conversion .....	100
4.2.3	Comparison studies $\alpha/\gamma$ -Al <sub>2</sub> O <sub>3</sub> .....	105
4.2.4	Carbon, hydrogen and oxygen balances .....	108
4.2.5	Product fractions.....	110

4.2.6	Discussion .....	114
4.3	Conclusion.....	119
5	Study of Dry reforming: the peculiar case of BaTiO <sub>3</sub> packing material.....	121
5.1	State of the art.....	122
5.2	Experimental setup.....	123
5.3	Results and discussion .....	126
5.3.1	Conversion for DRM in comparison with the conversion of the individual components, at equal flow rate.....	126
5.3.2	Product fractions.....	130
5.3.3	Discussion .....	132
5.4	Conclusion.....	135
6	General conclusion .....	137
7	Summary .....	143
8	Samenvatting .....	145
9	Appendix .....	147
9.1	IR data .....	147
9.2	Plasma Stabilisation .....	147
9.3	Material characterisation.....	151
9.3.1	UV-DR.....	152
9.3.2	N <sub>2</sub> -sorption.....	154
9.3.3	Hg-porosimetry.....	157
9.3.4	SEM-EDX.....	161
9.3.5	Material stability against coking.....	173
9.3.6	Profilometry .....	179

9.4	Detailed carbon, hydrogen and oxygen balances.....	181
9.5	Reaction schemes from literature .....	188
9.6	Yields and selectivities for DRM .....	191
10	Bibliography .....	195
11	Curriculum Vitae .....	213
11.1	List of Publications .....	213
11.2	List of conference contributions.....	214
11.2.1	Oral presentations.....	214
11.2.2	Poster presentations.....	215
11.3	Awards .....	215
11.4	Extra-curricular activities .....	215

# LIST OF FIGURES

---

Figure 1: The global average long-term atmospheric concentration of CO <sub>2</sub> , measured in ppm [5].	4
Figure 2: Scheme of the incoming and outgoing radiation, balancing the Earth's energy balance. All values are in W m <sup>-2</sup> and for the period from March 2000 to May 2004 [6].	5
Figure 3: Overview of the renewable energy sources for the different novel technologies for CCU.	9
Figure 4: Key performance indicators of six different CO <sub>2</sub> utilisation technologies: (a) urea production; (b) FT synthesis; (c) hydrogenation to methanol; (d) hydrogenation to formic acid; (e) electrochemical reduction; and (f) thermal DRM. Adapted from ref. [23].	11
Figure 5: Calculated theoretical thermal conversion (left axis) and corresponding energy efficiency (right axis) as a function of temperature for the splitting of CO <sub>2</sub> [9].	13
Figure 6: Calculated theoretical thermal conversion (left axis) and corresponding energy efficiency (right axis) as a function of temperature for DRM [9].	15
Figure 7: Example of an electrochemical cell to convert CO <sub>2</sub> to formate/formic acid [36].	17
Figure 8: Schematic view of the two-step solar thermochemical cycle for CO <sub>2</sub> and H <sub>2</sub> O splitting based on metal oxide redox reactions [9].	18
Figure 9: Photocatalytic reaction mechanism of an unmodified metal oxide semiconductor [40].	19
Figure 10: Utilisation of CO <sub>2</sub> to produce biofuels from microalgae [12].	21
Figure 11: Common methods of CO <sub>2</sub> activation over catalytic surfaces [42].	22
Figure 12: Different types of DC discharges depending on the voltage and current [48].	27
Figure 13: Typical current and voltage-profile (left) and visual image (right) for a filamentary (top) and homogeneous (bottom) Helium DBD [50].	29
Figure 14: Overview of the various effects of the catalyst on the plasma and of the plasma on the catalyst, which may give rise to a synergistic plasma catalytic operation. Adapted from ref. [53].	33
Figure 15: Schematic representation of several factors active in plasma catalysis [53]	34

Figure 16: Setup of the packed bed DBD reactor applied in this study (adapted from ref [93]). The packing is illustrated with beads but can also be filled with glass wool, quartz wool or other material shapes. .... 55

Figure 17: Experimental setup applied in this work. .... 56

Figure 18: Part of a gas chromatogram obtained in this work, zoomed in on the baseline. .... 57

Figure 19: Typical Q-U Lissajous figure for a DBD [72]. .... 61

Figure 20: Typical current profile for a DBD, obtained with an oscilloscope [98]. .... 61

Figure 21: Schematic representation of the drip casting setup. 1) Feed vessel with magnetic stirrer; 2) air pressure controller; 3) Vibration generator with frequency and amplitude control; 4) nozzle; 5) stroboscopic lamp; 6) coagulation bath [113]. .... 64

Figure 22: Conversion (a) and energy efficiency (b) as a function of bead size (diameter) for different bead materials, for an alumina dielectric barrier, 4.5 mm gap, stainless steel outer electrode, 23.5 kHz, at 50 ml/min gas flow rate, and 100 Watt power. The error bars are calculated based on 12 GC measurements. A comparison is also made with the results for a non-packed reactor (i.e. without packing), both at the same flow rate (50 ml/min) and the same residence time as in the packed bed reactor (i.e. 5.52 sec, corresponding to a flow rate of 192 ml/min). .... 73

Figure 23: Relative pore volume for  $\alpha$ -Al<sub>2</sub>O<sub>3</sub> and BaTiO<sub>3</sub> beads. .... 78

Figure 24: Conversion (a) and energy efficiency (b) as a function of bead size and gap size (indicated at the bottom of the columns, in mm), for BaTiO<sub>3</sub> beads, an alumina dielectric barrier, stainless steel outer electrode, 23.5 kHz, at 50 ml/min, for 100 Watt input power. The plasma power (Watt) is indicated by a blue line. .... 82

Figure 25: Conversion (a) and energy efficiency (b) in a non-packed reactor (left), a non-packed reactor with glass wool at the sides (middle) and a reactor completely filled with glass wool (right) at two different flow rates, for 100 Watt power, alumina dielectric barrier, stainless steel electrode, at 23.5 kHz and 4.5 mm gap. .... 86

Figure 26: Effect of a glass wool packing on the CO<sub>2</sub> conversion, for different gap sizes, in comparison with the results by Duan et al. for a quartz wool packing. .... 88

Figure 27: Conversion (a) and energy efficiency (b) for two different dielectric barriers and packing materials, as indicated in the x-axis, at 50 ml/min, for 100 Watt power, 4.5 mm gap, 23.5 kHz and a stainless steel electrode. .... 89

Figure 28: Conversion (a) and energy efficiency (b) for SiO<sub>2</sub> and  $\alpha$ -Al<sub>2</sub>O<sub>3</sub> beads, with quartz and alumina dielectric barriers, at 50 ml/min, for 100 Watt power, 4.5 mm gap, 23.5 kHz and a stainless steel electrode. .... 92

Figure 29: CO <sub>2</sub> conversion for different bead sizes and materials, compared to the results for the non-packed reactor, at the same flow rate (50 ml/min) and at the same residence time (5.52 s; flow rate of 192 ml/min) for both DRM and pure CO <sub>2</sub> splitting. The bars with pattern fill show the results for DRM, whereas the full bars show the results for CO <sub>2</sub> splitting (see Chapter 3). .....	100
Figure 30: CH <sub>4</sub> conversion for different bead sizes and materials, compared to the results for the non-packed reactor, at the same flow rate (50 ml/min) and at the same residence time (5.52 s; flow rate of 192 ml/min). .....	101
Figure 31: Total conversion for different bead sizes and materials, compared to the results for the non-packed reactor, at the same flow rate (50 ml/min) and at the same residence time (5.52 s; flow rate of 192 ml/min). .....	103
Figure 32: Calculated CH <sub>4</sub> and CO <sub>2</sub> conversion as a function of residence time in a non-packed DBD reactor, adopted from modelling. Adopted with permission from ref. [47]. Copyright 2018 American Chemical Society. ....	104
Figure 33: CO <sub>2</sub> , CH <sub>4</sub> and total conversion for different bead sizes and materials, compared to the results for the non-packed reactor, at the same flow rate (50 ml/min) and at the same residence time (5.52 s; flow rate of 192 ml/min). .....	105
Figure 34: Comparison of the CO <sub>2</sub> , CH <sub>4</sub> and total conversion between $\gamma$ -Al <sub>2</sub> O <sub>3</sub> and $\alpha$ -Al <sub>2</sub> O <sub>3</sub> (2.0-2.24 mm beads). .....	106
Figure 35: Carbon, hydrogen and oxygen balance for different bead sizes and materials, as well as the non-packed reactor. ....	108
Figure 36: Product fractions for different bead sizes and materials, as well as for the non-packed reactor. ....	110
Figure 37: CO <sub>2</sub> and CH <sub>4</sub> conversion in DRM in comparison with the pure component conversions, as a function of different bead size ranges and gap sizes, at 50 ml/min and constant SEI (experiment set 1a, 2 and 3). .....	126
Figure 38: CO <sub>2</sub> , CH <sub>4</sub> and total conversion in DRM, as a function of different bead size ranges and gap sizes, at 5.5 seconds residence time and 50 ml/min. ....	128
Figure 39: IR camera image of ZrO <sub>2</sub> beads of 2.0-2.24 mm, in a 4.5 m gap, at 23.5 kHz, CO <sub>2</sub> , 100 Watt input power, 50 ml/min. ....	147
Figure 40: Conversion (a), energy efficiency (b), peak-to-peak voltage (c), plasma power (d) and breakdown voltage (e) as a function of stabilisation time, for an alumina dielectric barrier, at 50 ml/min, for 100 Watt power with 2.0-2.24 mm SiO <sub>2</sub> beads. ....	151
Figure 41: UV-DR spectra of SiO <sub>2</sub> before (blue graph) and after (red graph) plasma exposure (milled beads). ....	153

Figure 42: UV-DR spectra for ZrO <sub>2</sub> before (blue graph) and after (red graph) plasma exposure (milled beads). .....	153
Figure 43: UV-DR spectra for BaTiO <sub>3</sub> before (blue graph) and after (red graph) plasma exposure (milled beads). .....	154
Figure 44: Nitrogen Sorption for SiO <sub>2</sub> .....	155
Figure 45: Nitrogen Sorption for ZrO <sub>2</sub> . .....	155
Figure 46: Nitrogen Sorption for α-Al <sub>2</sub> O <sub>3</sub> . .....	156
Figure 47: Nitrogen Sorption for γ-Al <sub>2</sub> O <sub>3</sub> .....	156
Figure 48: Nitrogen Sorption for BaTiO <sub>3</sub> . .....	157
Figure 49: Hg-porosimetry for SiO <sub>2</sub> .....	158
Figure 50: Hg-porosimetry for ZrO <sub>2</sub> . .....	158
Figure 51: Hg-porosimetry α-Al <sub>2</sub> O <sub>3</sub> . .....	159
Figure 52: Hg-porosimetry γ-Al <sub>2</sub> O <sub>3</sub> .....	159
Figure 53: Hg-porosimetry BaTiO <sub>3</sub> . .....	160
Figure 54: SEM-EDX SiO <sub>2</sub> beads (before plasma).....	163
Figure 55: SEM-EDX SiO <sub>2</sub> beads (after plasma). .....	164
Figure 56: SEM-EDX ZrO <sub>2</sub> beads (before plasma). .....	165
Figure 57: SEM-EDX ZrO <sub>2</sub> beads (after plasma).....	166
Figure 58: SEM-EDX α-Al <sub>2</sub> O <sub>3</sub> beads (before plasma). .....	167
Figure 59: SEM-EDX α-Al <sub>2</sub> O <sub>3</sub> beads (after plasma).....	168
Figure 60: SEM-EDX γ-Al <sub>2</sub> O <sub>3</sub> beads (before plasma).....	169
Figure 61: SEM-EDX γ-Al <sub>2</sub> O <sub>3</sub> beads (after plasma). .....	170
Figure 62: SEM-EDX BaTiO <sub>3</sub> beads (before plasma). .....	171
Figure 63: SEM-EDX BaTiO <sub>3</sub> beads (after plasma).....	172
Figure 64: Raman spectrum for SiO <sub>2</sub> , before and after plasma exposure. ....	174
Figure 65: Raman spectrum for ZrO <sub>2</sub> , before and after plasma exposure.....	174
Figure 66: Raman spectrum for α-Al <sub>2</sub> O <sub>3</sub> , before and after plasma exposure. For both beads (before and after plasma), two spectra are recorded: one with 90 % of the light filtered out, and one with 99 % of the light filtered out. ....	175
Figure 67: Zoomed-in (at coking regions) Raman spectrum for α-Al <sub>2</sub> O <sub>3</sub> , before and after plasma exposure. For both beads (before and after plasma), two spectra are recorded: one with 90 % of the light filtered out, and one with 99 % of the light filtered out. .	175
Figure 68: Raman spectrum for γ-Al <sub>2</sub> O <sub>3</sub> , before and after plasma exposure. ....	176
Figure 69: Zoomed-in (at coking regions) Raman spectrum for γ-Al <sub>2</sub> O <sub>3</sub> , before and after plasma exposure. ....	176
Figure 70: Raman spectrum for BaTiO <sub>3</sub> , before and after plasma exposure.....	177



Figure 71: Zoomed-in (at coking regions) Raman spectrum for BaTiO <sub>3</sub> , before and after plasma exposure. ....	177
Figure 72: Visual image of the beads before and after plasma treatment. ....	179
Figure 73: Profilometry profile for SiO <sub>2</sub> beads of 2.0-2.24 mm. ....	180
Figure 74: Profilometry profile for ZrO <sub>2</sub> beads of 2.0-2.24 mm. ....	180
Figure 75: Profilometry profile for α-Al <sub>2</sub> O <sub>3</sub> beads of 2.0-2.24 mm. ....	180
Figure 76: Profilometry profile for BaTiO <sub>3</sub> beads of 2.0-2.24 mm. ....	181
Figure 77: Profilometry profile for γ-Al <sub>2</sub> O <sub>3</sub> beads of 2.0-2.24 mm. ....	181
Figure 78: Total carbon balance for different bead sizes and materials. ....	182
Figure 79: Detailed carbon balance for different bead sizes and materials, without CO <sub>2</sub> and CH <sub>4</sub> contribution. ....	182
Figure 80: Normalized carbon balance for different bead sizes and materials, without CO <sub>2</sub> and CH <sub>4</sub> contribution. ....	183
Figure 81: Total hydrogen balance for different bead sizes and materials. ....	183
Figure 82: Detailed hydrogen balance for different bead sizes and materials, without CH <sub>4</sub> contribution. ....	184
Figure 83: Normalized hydrogen balance for different bead sizes and materials, without CH <sub>4</sub> contribution. ....	184
Figure 84: Total oxygen balance for different bead sizes and materials. ....	185
Figure 85: Detailed oxygen balance for different bead sizes and materials, without CO <sub>2</sub> contribution. ....	185
Figure 86: Normalized oxygen balance for different bead sizes and materials, without CO <sub>2</sub> contribution. ....	186
Figure 87: Carbon, hydrogen and oxygen balance for the experiments in Figure 37. ....	186
Figure 88: Carbon, hydrogen and oxygen balance for the experiments in Figure 38. ....	187
Figure 89: Reaction scheme to illustrate the main pathways for the conversions of CH <sub>4</sub> and O <sub>2</sub> and their interactions. Adopted with permission from ref. [157]. Copyright 2018 American Chemical Society. ....	188
Figure 90: Reaction scheme to illustrate the main pathways for DRM. Adopted with permission from ref. [157]. Copyright 2018 American Chemical Society. ....	189
Figure 91: Reaction scheme to illustrate the main pathways for the conversions of CO <sub>2</sub> and H <sub>2</sub> O and their interactions. Adopted with permission from ref. [150]. Copyright 2018 Wiley-VCH. ....	190

## LIST OF TABLES

---

Table 1: European Commission TRL definition.....	12
Table 2: Subdivision of plasmas according to the temperature of the different components. $T_0$ is the gas temperature, $T_i$ the ion temperature, $T_r$ the rotational temperature, $T_v$ the vibrational temperature and $T_e$ the electron temperature.....	24
Table 3: Typical plasma processes. ....	25
Table 4: Summary of a selection of literature for CO <sub>2</sub> splitting in a non-packed and a packed DBD reactor.....	38
Table 5: Summary of a selection of literature for DRM in a non-packed and a packed DBD reactor.....	40
Table 6: Physical and chemical characteristics of the packing materials. ....	62
Table 7: Specifics of the equipment for all characterization techniques. ....	65
Table 8: Different parameters studied, as well as their variations. ....	71
Table 9: Electrical characterisation as a function of bead size (diameter) for different bead materials, for an alumina dielectric barrier, 4.5 mm gap, stainless steel outer electrode, 23.5 kHz, at 50 ml/min gas flow rate, and 100 Watt power. A comparison is also made with the results for a non-packed reactor (i.e. without packing), both at the same flow rate (50 ml/min) and the same residence time as in the packed bed reactor (i.e. 5.52 sec, corresponding to a flow rate of 192 ml/min). ....	74
Table 10: Electrical characteristics of the various beads used in this study, determined by analysing the Lissajous figures. ....	75
Table 11: Parameters used for investigating the influence of the gap size and bead size, at equal ratio, equal bead size or equal gap size. ....	80
Table 12: Electrical characterisation as a function of bead size and gap size for BaTiO <sub>3</sub> beads, an alumina dielectric barrier, stainless steel outer electrode, 23.5 kHz, at 50 ml/min, for 100 Watt input power. ....	84
Table 13: Electrical characterisation for Figure 25.....	90
Table 14: Electrical characterisation for Figure 27.....	90
Table 15: Electrical characterisation for SiO <sub>2</sub> and $\alpha$ -Al <sub>2</sub> O <sub>3</sub> beads, with quartz and alumina dielectric barriers, at 50 ml/min, for 100 Watt power, 4.5 mm gap, 23.5 kHz and a stainless steel electrode. ....	91
Table 16: Parameters used in this chapter.....	97

Table 17: Ratio of CH <sub>4</sub> conversion over CO <sub>2</sub> conversion, and of the CO over H <sub>2</sub> product fraction, for the different bead sizes and materials, as well as for the non-packed reactor .....	102
Table 18: Electrical characterisation for Figure 33 and Figure 34.....	107
Table 19: Product fractions for different bead sizes and materials (the highest fractions for each component are highlighted). .....	113
Table 20: Operating conditions and materials used in this work.....	123
Table 21: Summary of the combination of gap size, bead sizes and flow rates used in this work.....	125
Table 22: Electrical characterisation for Figure 37 (DRM, pure CO <sub>2</sub> conversion and pure CH <sub>4</sub> conversion). .....	129
Table 23: Electrical characterisation for Figure 38.....	129
Table 24: Product fractions in DRM, as a function of different bead size ranges and gap sizes. ....	131
Table 25: SEM-EDX measurements for all beads before and after plasma, measured at 3 points per bead. ....	161
Table 26: Identified products, ranked in decreasing order of their yields, for the different packing materials and the non-packed reactor. The components highlighted are present for more than 1 %, the others for more than 100 ppm.....	191
Table 27: Product selectivities (%) for the different packing materials and sizes and for the non-packed reactor. The highest selectivities for each component are highlighted. ....	192

*The scientists of today think deeply instead of clearly. One must be sane to think clearly, but one can think deeply and be quite insane.*

*Nicola Tesla*

*If at first you don't succeed, try doing it the way your mom told you in the beginning.*

*Inne*

## ACKNOWLEDGEMENTS

---

Danku, merci, thank you, Благодаря ви, grazie, ممنون, rahmat, teşekkür ederim, ...

First of all, to my promotors, Vera and Annemie. For the discussions, the insights, the help, the understanding, the confidence, the growth, the long hours, the talks, the freedom, the guidance, ...

I would also like to thank IWT for the funding. En danku Yannick, voor alle hulp in het labo, en om de magie in mijn plasma te steken.

Dan, voor mijn ouders. Voor alles. Echt, te veel om op te noemen. Om mij te steunen, te begrijpen, te knikken als jullie me niet begrepen, vragen te stellen, me los te laten en toch dichtbij te blijven, me te leren om te gaan met alles, er te zijn, me aan te moedigen, enthousiast te zijn en me graag te zien. En die ons geluk altijd boven het hunne hebben geplaatst.

Dan, voor mijn broer. Om me uit te dagen het leven aan te gaan, om met mij aan tafel te studeren, om pauzes te pakken, om me de waarde van powernaps te leren, en om de beste broer te zijn die een zus zich kan wensen. Voor Charlotte, om er te zijn voor mijn broer, en om onze familie te accepteren zoals ze is. Vooral mij dan. En mijn broer. Ok, vooral mijn broer.

Voor ons moeke, die me graag zag. Altijd. Overal. Die zoveel moeite heeft gedaan dit doctoraat altijd mee te volgen en te begrijpen. Die de beste moeke ooit is. Die mij geleerd heeft dat familie heel belangrijk is, zeker als het moeilijk gaat.

Voor ons vokka. Mijn peter. Die me altijd kan laten lachen. Altijd. Die de rots is waarop onze familie gebouwd is.

Voor nonkel Steven, Dien en Lies. Voor alle chips die niet in potjes gedaan werd, keukentafel gesprekken, familiefeesten, opgesloten worden tijdens het babysitten, en omdat ik 21 mag blijven. En voor Cindy, Imke en Bregje.

Voor tante Christel en nonkel Peter, en alle kinderen, schoonkinderen en kleinkinderen: voor alle mini-vakanties met jullie, de heerlijke tajines, de luchtige en de zware gesprekken, en om me niet te vragen mijn doctoraat uit te leggen.

Voor nonkel Mario, Eef, Tessa en Nikki. Bedankt om van elk familiefeest een vrolijke bedoening te maken.

Voor Hilde Claes, Hilde Van den Abeele, Ann Delen, Paula Van Gorp en Lieve Van Herck, die me mysterie en wetenschap leerden en Chris Brouwers, die me altijd carte blanche gaf.

Voor Wendy en Pascal, voor alle gezellige avonden en alle babbels.

Liese en Shana, bedankt om er na al die jaren nog te zijn voor mij. Voor alle films, spelletjes, vol-au-vent en chilli con carne.

Dorien, Liesbeth, Sanne en Sneha: voor alle fijne avonden, etentjes, drankjes, babbels, roddels, gegibber en gelach. Bedankt voor alle vriendschap, en op nog vele jaren!

Ben, Carl, Wim, Tim, Sebastiaan, Jens, Pieter: ik zie jullie hopelijk elke Kerst, bedankt voor de fijne jaren aan de UA!

For Antonin: Merci d'avoir faciliter le travail, pour ton amitié, pour être là quand j'en avais le plus besoin, et de m'avoir hébergée pendant les moments difficiles. Pour les blagues, les mèmes, les tags et les pandas qui s'ennuient. Pour tout.

For Antonin, Georgi, Vincent and Yannick: for coffee, for tea, for lunch, for trips, for Slavic video's, for goose riding, for meeting your families, for drama, for awesome playlists, for BMW driving, for facts that I didn't know and some I didn't want to know. For friendship. May it last long(er than wine with Antonin around).

Voor Jonas, Vincent en Yannick: voor de etentjes, de motivatie voor push-ups, zelfgemaakte spinnensnoepjes, gekookt vlees, asperges, en de kennis om niet met Vincent gezelschapspellen te spelen.

Voor Jonas, Kristof, Stijn, Vincent en Yannick: voor de fake-tattoos, de poolparties, de buzzfeed quizen, de tv-programma's, wikihow's en boeken (die Kristof nog altijd moet schrijven), en alle random info die ik niet moest weten.

Voor Sanne, Annelore, Qi en Jeroen: bedankt om naar mij te luisteren. Voor de leuke sfeer en de toffe pauzes.

Voor Marleen: voor alle kerstmarktjes, Disney-kalenders en veel te veel chocolade.

For Antonin, Marleen, Maryam and Amin: best office ever. Really. Ever.

For Neda, azizam, and Amin: thanks for the Turkish!

For Maryam, Amin, Neda, Parisa: for the Persian and the fun. Ta durudi digar bedrud!

Voor Stijn Huygh, Chris Verlackt, Nick, Tim, Ramses: bedankt om super collega's te zijn!

En voor de kindjes: nog veel succes! Jullie gaan dat goed doen, maak me trots!

For Abraham, Ravi, Siraj, Radu, Stefano, Umid, Maksud, Jamol: thanks for being awesome colleagues!

Voor Ingrid, Nelly, Fabiana, Karen, Luc en Karel: bedankt dat ik altijd bij jullie terecht kon, voor alles.

Voor Elke, Sofie, Nick Slegers, Elise Daems: om het labo leuk te maken en me tegen te houden als studenten het zoveelste foute antwoord gaven.

For my ENMIX colleagues and Elias: thanks for all the fruitful meetings, the discussions and the fun!

For my VITO colleagues: thank you for the collaborations, the knowledge, the spheres and the measurements.

Voor de arbeidspsycholoog, zonder wie dit hele werk ook niet tot stand had gekomen. Ook aan Shana, Georgi en Antonin een geweldige danku, voor het nalezen van mijn thesis! En bedankt aan Marlies, voor de cover art!

Voor Shana, die de definitie van een goede vriendin belichaamt. Ik zou niet zijn waar ik vandaag ben, zonder jou. Jij bent mijn steun en toeverlaat, en ik kan altijd bij je terecht. Ik zie je graag.

And lastly. For you. For us. For ever.

- She does not fear what is in front of her, because of who stands behind her.





# PREFACE

---

Converting carbon dioxide, and other greenhouse gases, into value-added chemicals or fuels is necessary, but also quite challenging. In this work, we will present a plethora of reasons why the mitigation and valorisation of CO<sub>2</sub> is necessary, what the challenges are and how this can be achieved in an efficient way.

One of the key challenges in CO<sub>2</sub> conversion is that it is often situated in geographically widespread locations. An example is biogas, containing both CO<sub>2</sub> and CH<sub>4</sub> as waste stream, which is widespread over different locations and in varying volumes. Another essential and geographically widespread component in CO<sub>2</sub> conversion is renewable energy, which is moreover highly intermittent. An apt solution is thus to convert waste gas, present in e.g. biogas, which consists of two greenhouse gases, with renewable energy, to value-added chemicals through flexible technology, able to handle both widespread locations and volumes as well as an intermittent supply. This work will focus most on dry reforming, the simultaneous conversion of CO<sub>2</sub> and CH<sub>4</sub>.

This conversion is not straightforward, and when done thermally, requires a high temperature and a catalyst that is often prone to coking. Bypassing these severe conditions and meeting the requirements for flexible production driven by renewable energy supply, can be achieved by combining plasma technology with catalysis. The plasma can work at mild conditions, i.e. room temperature and ambient pressure, but is a very reactive mixture, which is highly unselective. Therefore, a catalytic material is added to the plasma. This material can be a packing consisting of a support material with or without additional activation with catalytic elements, and can enhance the plasma performance both chemically and/or physically. Although the general principles of plasma catalysis are described, it is a new field of research with many aspects yet to be discovered.

This work aims at revealing some of these aspects by studying the impact of packing materials on the conversion and selectivity of dry reforming of methane in a packed-bed dielectric barrier discharge (DBD) plasma reactor. Moreover, a comparison will be made to the conversion for CO<sub>2</sub> and CH<sub>4</sub> as individual components, to unravel insights about the mutual effect of both gases on each other, influencing the performance of dry reforming in a packed-bed DBD.

This way, we hope to gain insights to further improve the synergy between the plasma and the packing material, and thus to aid with the transition towards a sustainable future.

# 1 INTRODUCTION

---

## 1.1 GENERAL INTRODUCTION

### 1.1.1 CO<sub>2</sub> mitigation and global warming

Today's worldwide energy demands (domestic, industrial and transportation) are mainly fulfilled by combusting natural gas and fossil fuels, leading to a considerable emission of CO<sub>2</sub> [1,2]. Since the industrial revolution, which was accompanied by an increasing use of fossil fuels, the CO<sub>2</sub> concentration in the atmosphere has increased from around 280 ppm to more than 400 ppm, and has reached levels that are much higher than the level of natural fluctuations (see Figure 1) [3,4].

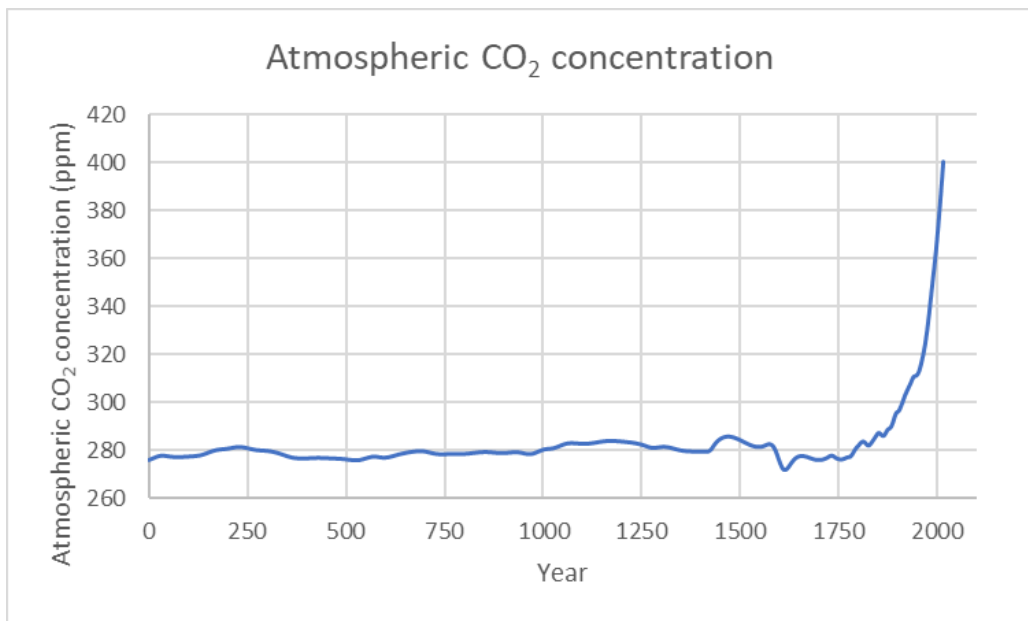


Figure 1: The global average long-term atmospheric concentration of CO<sub>2</sub>, measured in ppm [5].

Greenhouse gases are naturally present in the atmosphere, and the energy coming from radiation is balanced through the mechanisms depicted in Figure 2, keeping our atmosphere at relatively constant temperature ranges. Here, it is shown that greenhouse gases play a crucial role in maintaining this balance, by absorbing and reflecting radiation. However, additional anthropogenic emissions of CO<sub>2</sub>, CH<sub>4</sub>, N<sub>2</sub>O, SF<sub>6</sub>, chlorofluorocarbons (CFCs) and hydrochlorofluorocarbons (HCFCs) enhance this

greenhouse effect and disturb this balance in favour of the absorption. This increases the Earth's temperature, which causes climate change, altering the local weather, decreasing the pH of the oceans and increasing their level [5].

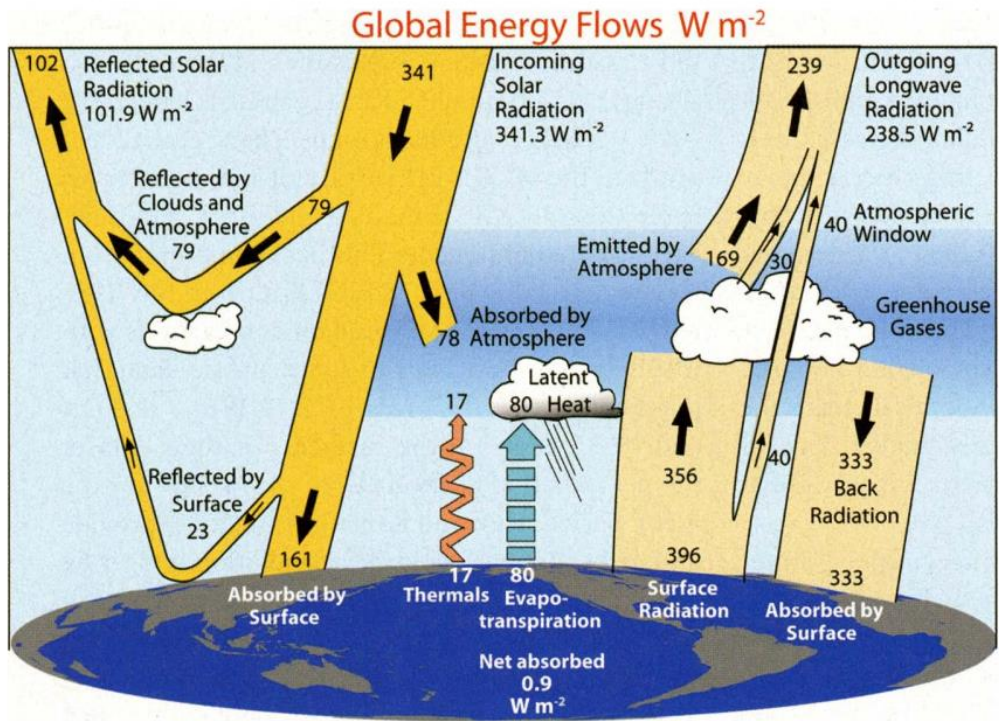


Figure 2: Scheme of the incoming and outgoing radiation, balancing the Earth's energy balance. All values are in  $W m^{-2}$  and for the period from March 2000 to May 2004 [6].

The contribution of gases to the enhanced greenhouse gas effect is calculated based on their concentration, their residence time and on how strongly they absorb energy. The latter two are combined into a factor known as the GWP (Global Warming Potential). While  $CO_2$  (GWP = 1) is more abundant in the Earth's atmosphere, other gases, like  $CH_4$  and  $NO_x$ , have a higher GWP. Indeed,  $CH_4$  has a GWP between 28 and 36, and for  $NO_x$  the GWP even lies between 265 and 310. The high concentration of  $CO_2$  in combination with its high stability and thus lifetime in the atmosphere and its contribution to the enhanced greenhouse gas effect, necessitates its mitigation and valorisation [7]. With its valorisation comes another advantage, namely diminishing our dependence on fossil fuels, which are not only used as an energy source, but to some

extent also as a raw material for many products and materials used in our society. These two goals have given the incentive to researchers in several fields to convert CO<sub>2</sub> to value-added chemicals and fuels, known as carbon capture and utilisation (CCU) [8]. The research fields mentioned include traditional thermal CO<sub>2</sub> conversion (see sections 1.2.1 and 1.2.2), but also (photo- or bio-) electrochemical, solar thermochemical, photochemical and biochemical pathways (see section 1.2.3) [9]. Since all these pathways for CO<sub>2</sub> conversion have a substantial energy demand, catalysis can play a crucial role in all of them, lowering the energy barrier. Last but not least, plasma technology also contributes to the progress made towards converting CO<sub>2</sub> and other greenhouse gases (see section 1.3), and forms the focus of this research.

Plasma conversion technology is a broad field of research, including different conversion processes and reactor types. For CO<sub>2</sub> conversion, the most applied plasma types are dielectric barrier discharges (DBDs), microwave (MW) plasmas and gliding arc (GA) discharges. Other, less studied discharges for CO<sub>2</sub> conversion include corona, glow, spark, radiofrequency and nanosecond pulsed discharges [9]. All these discharge types have different opportunities and challenges, which are described in a recent comprehensive review [9].

Most research on CO<sub>2</sub> utilization focusses on improving the conversion and the energy efficiency when studying CO<sub>2</sub> splitting towards CO and O<sub>2</sub> (see section 1.2.1). However, when adding a hydrogen source, the selectivity towards value-added chemicals, e.g. methanol, formaldehyde or formic acid, is considered for improvement as well. The hydrogen sources used are mostly CH<sub>4</sub> (Dry Reforming of Methane (DRM), see section 1.2.2), H<sub>2</sub> (hydrogenation of CO<sub>2</sub>) or H<sub>2</sub>O (artificial photosynthesis).

As mentioned, all of the above mentioned technologies are part of a larger concept, called Carbon Capture and Utilisation (CCU). The purpose of CCU is to convert CO<sub>2</sub> into value-added products, ideally via a process with both a high demand and high economic value [10–12].

### 1.1.2 Biogas as a value-added CO<sub>2</sub> source

Similar to CO<sub>2</sub>, CH<sub>4</sub> is formed as a byproduct/waste product in some processes. As also CH<sub>4</sub> has a very high GWP, making it even more problematic when released into the atmosphere, thus also necessitating its conversion to value-added chemicals. Of course, pure CH<sub>4</sub> can be used as a chemical and as a fuel, but often CH<sub>4</sub> streams are impure and need purification, which is cost- and energy-intensive.

A very common, renewable source of both CO<sub>2</sub> and CH<sub>4</sub> is biogas. Biogas is formed by the anaerobic decay of organic matter/waste, where almost all organic matter can be used as a biogas feedstock [13–15]. Most used waste sources are livestock manure, wastewater sludge and gasification of biomass.

However, the use of waste products is particularly advantageous as it can prevent the unnecessary waste of useful energy sources and offers increased financial profits to plant operators. Industries that generate biogas from waste products could use it directly on-site as a fuel and/or for electricity generation that could be resold to the national grid [16].

Water vapour, H<sub>2</sub> and trace compounds, such as sulphides, siloxanes, aromatics and halogenated compounds, may also be present, depending on the biogas feedstock [17]. The effect of these impurities, and whether or not pre-separation is necessary for the conversion of the biogas, will depend on the concentration and the type of impurities. Sulphur content for example is known to be poisonous for some catalysts. Other impurities, like nitrogen, might even be beneficial for the conversion [18].

While combustion of renewable CH<sub>4</sub> sources does emit CO<sub>2</sub>, it is more favourable than fossil fuel combustion. The carbon in biogas was originally absorbed from the atmosphere by plants during photosynthesis. Eventually, the same amount of carbon is returned to the atmosphere during combustion of the plant-derived fuel; therefore no additional carbon is introduced into the Earth's carbon cycle. Provided that the plant source is regenerated, the fuel can be considered carbon-neutral. Although this process is rather slow, as it takes time for plants to grow, it is still in contrast to combustion of fossil fuels where carbon that has been removed from the carbon cycle for millions of

years is reintroduced without an efficient removal mechanism. Therefore, plasma based conversion of biogas is seen as a potential valuable option to convert biogas in value-added chemicals or liquid fuels, increasing its economic potential while enhancing its environmental benefits [15].

### 1.1.3 Renewable energy

As stated in the previous section, alternative technologies for converting CO<sub>2</sub> include plasma chemical, (photo-/bio-) electrochemical, solar thermochemical, photochemical and biochemical conversion. Converting CO<sub>2</sub>, no matter whether this takes place in the presence or absence of a hydrogen source or catalyst, requires energy. When the supplied energy is accompanied by the emission of CO<sub>2</sub>, there might not be a net loss in CO<sub>2</sub> concentration in the atmosphere. Therefore, it is important to meet the need for energy depicted in Figure 3 with alternative technologies [19].

Biochemical, photo(electro)chemical and solar thermochemical conversion of CO<sub>2</sub> rely on the light and/or heat from the sun, with an average solar flux of 175 W/m<sup>2</sup> [9]. This means that  $8.9 \times 10^{13}$  kWh is at our disposal each hour, while only  $1.4 \times 10^{14}$  kWh is consumed worldwide per year (2008) [20]. While (bio)electrochemical and plasma chemical conversion need electricity, the latter has the advantage that it can be derived from solar energy but is not limited to it, allowing a larger renewable energy mix as energy source.

The global share of renewable energy is enhancing in the total energy consumption – from 15 % in 2005 to 20.5 % at the end of 2016. It is therefore becoming more abundant as a source of electricity, with a global share of 26.5 % at the end of 2017 [21]. The main disadvantage of renewable energy is the difficulty in transportation and storage of the produced electricity. Since renewable energy production often arises at times when and in places where it is not necessary (e.g. during the day in the Sahara, while needed during the night in a city), there is a requirement for efficient storage and transportation.



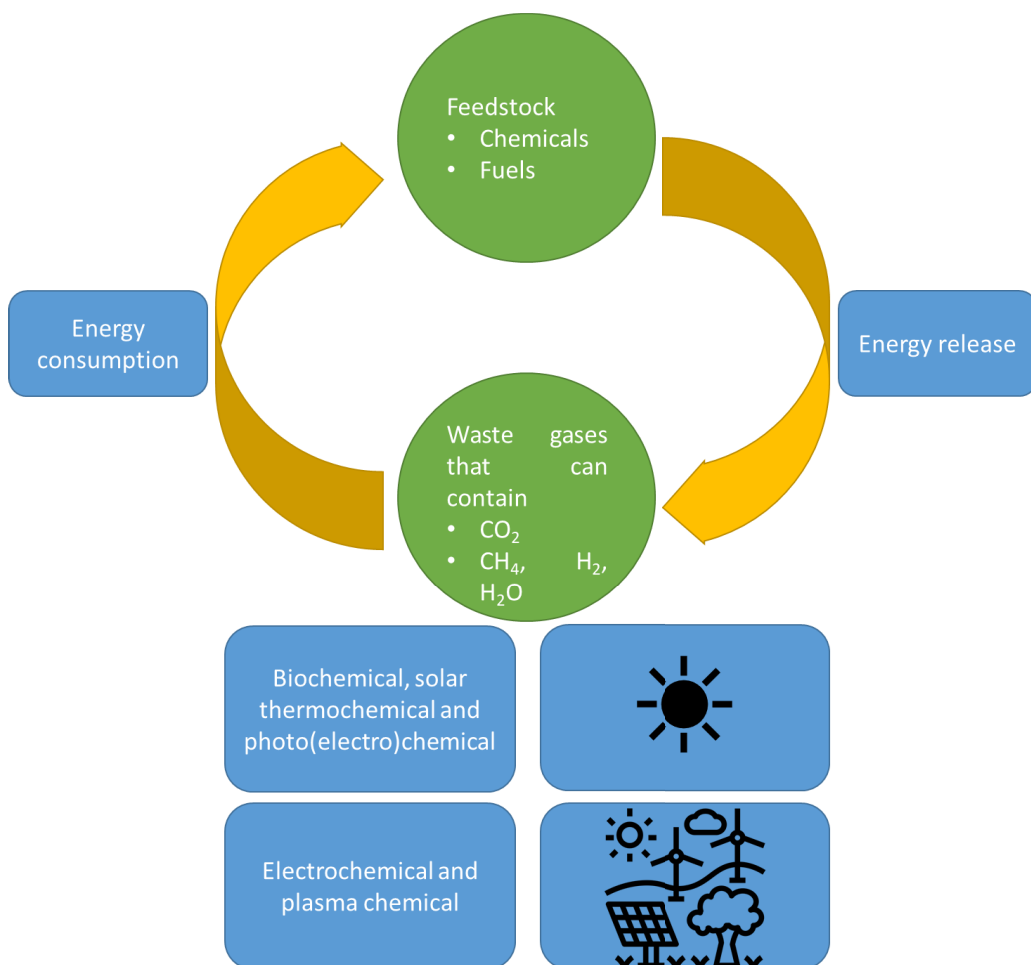
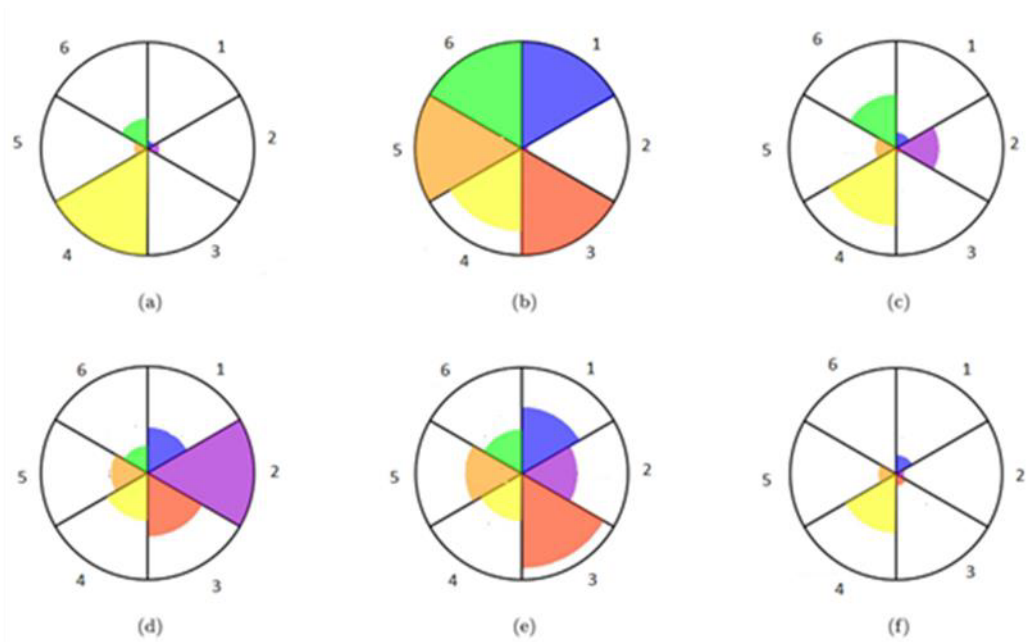


Figure 3: Overview of the renewable energy sources for the different novel technologies for CCU.

The most energy dense medium to store energy (denser than typical batteries) is in (liquid) fuels, and thus via chemical storage [22]. Chemical storage means that the available electricity is stored by using it to convert waste chemicals to higher value-added chemicals/fuels (power-to-liquids). An example (and focus of this work) is the conversion of  $\text{CO}_2$ , i.e. a waste molecule, together with  $\text{CH}_4$  as a hydrogen source, into value-added chemicals and fuels, such as formic acid, formaldehyde and methanol. The latter molecule is regarded as a very interesting one, since it is both a building block in the chemical industry and a fuel. Moreover, it is a liquid and fits in our current infrastructure. The key advantages of converting  $\text{CO}_2$  and  $\text{CH}_4$  to methanol with renewable energy are the adaptability with current fuel infrastructure, the ease of

production (since it is the simplest liquid chemical containing only one carbon), the lack of fossil fuels needed in such an economy and the diminishing of the greenhouse effect. A recent economic study by Jarvis and Samsatli has proven that DRM is indeed one of the best pathways for CO<sub>2</sub> utilisation. Figure 4 shows the key performance indicators (KPIs) for six processes: urea production, FT (Fischer-Tropsch) synthesis, hydrogenation to methanol, hydrogenation to formic acid, electrochemical reduction and thermal DRM. The six KPIs are the Capital Expenditure (CAPEX), Operational Expenditure (OPEX), Electricity Usage, Technology Readiness Level (TRL, see also Table 1), Product Price and CO<sub>2</sub> conversion. The first three should be as low as possible, while the latter three should be as high as possible. Figure 4 shows that for dry reforming the three KPI's in the right part are very low, making it the most promising pathway. However, the three KPIs in the left part are also still low, i.e. lower than for some other pathways, indicating that there is still room for improvement. For thermal DRM, the CAPEX is 23.85 £/t, which is higher than for urea production and hydrogenation to methanol, but lower than for FT synthesis, hydrogenation to formic acid and electrochemical reduction. The OPEX is the second lowest, with 100.55 £/t, and only FT synthesis has a lower OPEX. For hydrogenation to formic acid, this cost is even 1300.90 £/t. The electricity usage is described in the study of Jarvis and Samsatli, but as their work is based on (at least partially) thermal conversion processes, it is not comparable with the electricity use in a plasma based process where the plasma also provides the energy for the reaction. The three other KPIs discussed (TRL, product price and CO<sub>2</sub> utilisation) need to be as high as possible, and there we see that there is still room for improvement. The TRL of thermal DRM is 5, which is higher than the TRL of hydrogenation to formic acid (4) and electrochemical reduction (4), but lower than the TRL of urea production (9), FT synthesis (7) and hydrogenation to methanol (6.5). The product price is also rather low, and only lower for urea production. However, the study considers DRM to convert CO<sub>2</sub> and CH<sub>4</sub> to syngas, whereas this PhD will focus on the conversion towards higher hydrocarbons and other products with a higher product price. The CO<sub>2</sub> utilisation is lower for DRM compared to FT and the hydrogenation technologies described in the

study of Jarvis and Samsatli, but compared to steam reforming which is CO<sub>2</sub> emitting, it still utilises a small amount of CO<sub>2</sub> (0.02–0.72 t CO<sub>2</sub>/t). However, as in this PhD a waste gas mixture is used in a circular way, avoiding emission together with the aim to produce higher (oxygenated) hydrocarbons C<sub>1</sub>-C<sub>5</sub>, the CO<sub>2</sub> utilisation might be more beneficial, although it is difficult to compare the plasma based DRM directly with the thermal conversion. Thus an LCA study will need to be done to confirm if our very rough and simplified reasoning is valid for plasma catalytic conversion.



1. CAPEX (£/t)
2. OPEX (£/t)
3. Electricity usage (MWh/t)
4. Average TRL
5. Product price (£/t)
6. CO<sub>2</sub> conversion (t<sub>CO2</sub>/t)

Figure 4: Key performance indicators of six different CO<sub>2</sub> utilisation technologies: (a) urea production; (b) FT synthesis; (c) hydrogenation to methanol; (d) hydrogenation to formic acid; (e) electrochemical reduction; and (f) thermal DRM. Adapted from ref. [23].

Table 1: European Commission TRL definition.

TRL	Definition
1	Basic principles observed
2	Technology concept formulated
3	Experimental proof of concept
4	Technology validated in lab
5	Technology validated in relevant environment (industrially relevant environment in the case of key enabling technologies)
6	Technology demonstrated in relevant environment (industrially relevant environment in the case of key enabling technologies)
7	System prototype demonstration in operational environment
8	System complete and qualified
9	Actual system proven in operational environment (competitive manufacturing in the case of key enabling technologies; or in space)

All technologies investigated for the conversion of CO<sub>2</sub> will help pave the way for the transition from fossil fuels to renewable energy for the chemical industry. They can thus be valorised in more technologies than CO<sub>2</sub> conversion, e.g. the production of ammonia, hydrogen, olefins, benzene-, toluene-, and xylene-isomers, methanol, ... [24].

## 1.2 CO<sub>2</sub> CONVERSION APPROACHES

### 1.2.1 Thermal CO<sub>2</sub> splitting

CO<sub>2</sub> splitting refers to the following reaction:



This reaction not only has a high enthalpy, indicating that it a high temperature is needed to obtain a negative Gibbs free energy, and thus a spontaneous reaction. Moreover, CO<sub>2</sub> is a thermodynamically stable molecule, since it has more electrons in bonding orbitals, than electrons in anti-bonding orbitals. Therefore, the splitting of CO<sub>2</sub>

requires i) a high energy input, ii) optimal reaction conditions, iii) the removal of one of the products and/or iv) a catalyst. As an indicator, the thermal conversion of  $\text{CO}_2$ , in the absence of a catalyst, via  $\text{CO}_2$  splitting has a calculated equilibrium production (Figure 5) of  $\text{CO}$  and  $\text{O}_2$  varying from less than 1 % at temperatures below 2000 K up to 45–80 % at 3000–3500 K. It can reach 100 % at 5000 K, but this is accompanied by a drastic drop in energy efficiency towards 35 %. The maximum energy efficiency lies at 47 %, with a conversion of 80 % (at 3250 K). However, in most research, a temperature of 1500 K is used, in combination with a catalyst. Another option is to remove one or both products, for instance by using a membrane. Examples of membranes used for this purpose include a calcium-stabilized zirconia membrane with  $\text{CO}$  as a sweep gas, an oxygen permeable yttria-stabilized zirconia membrane with argon as a sweep gas and a  $\text{SrCo}_{0.5}\text{FeO}_3$  membrane with  $\text{CH}_4$  as a sweep gas [25–27]. To date, the maximum conversion reached lies between 0.5 and 2 %, with the only advantage that lower temperatures can be used.

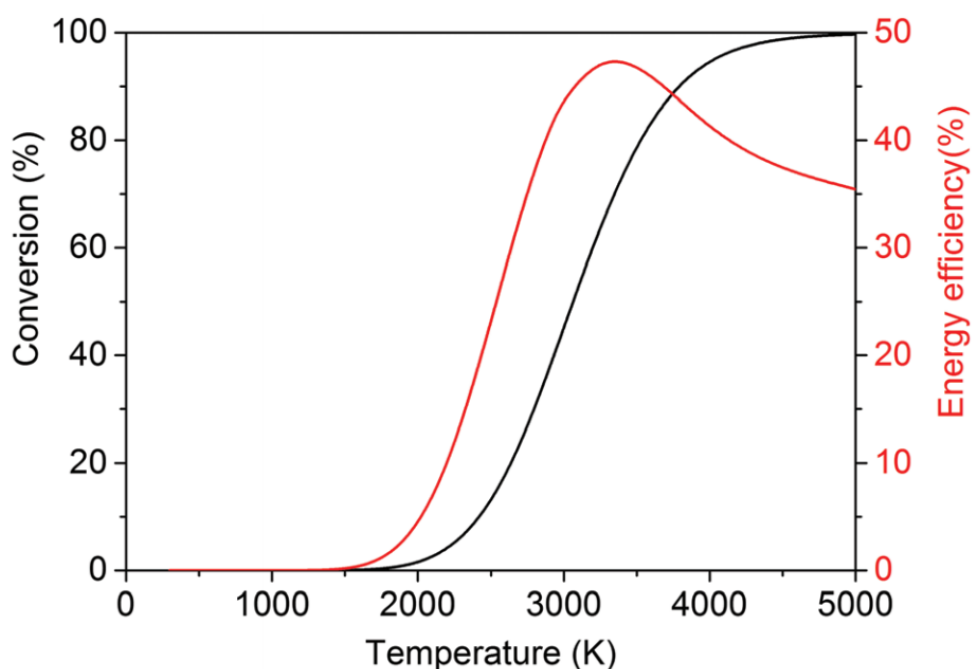
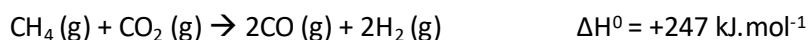


Figure 5: Calculated theoretical thermal conversion (left axis) and corresponding energy efficiency (right axis) as a function of temperature for the splitting of  $\text{CO}_2$  [9].

### 1.2.2 Thermal Dry reforming

Thermodynamically, it is more favorable to convert CO<sub>2</sub> ( $\Delta G^0 = - 394.4 \text{ kJ.mol}^{-1}$ ) in the presence of a co-reactant with a higher Gibbs free energy [28], like CH<sub>4</sub> ( $\Delta G^0 = - 50.70 \text{ kJ.mol}^{-1}$ ). This molecule can then provide its intrinsic chemical energy to assist in the CO<sub>2</sub> conversion. The reaction between CO<sub>2</sub> and CH<sub>4</sub>, forming syngas, is called Dry Reforming of Methane (DRM):



Although less endothermic than CO<sub>2</sub> splitting, DRM still requires temperatures of more than 640 °C, and is often combined with catalysis. The theoretical thermal (non-catalysed) conversion and energy efficiency are plotted in Figure 6, showing that 100 % conversion can be reached above 1500 K, accompanied by an energy efficiency of 60 %. The highest achievable energy efficiency is 70 %, which is reached at 1000 K and accompanied by a conversion of 83 %.

Two major problems related to high temperatures are coking and sintering of the catalyst, causing a loss in activity. Regarding the first problem, the carbon deposition, the temperature of this reaction is in practice always higher than 750 °C, since carbon formation is favoured between 560 and 700 °C [29]. Since coking is an unwanted side-reaction of DRM, it is important to prevent it using coking management, which means the selection of the right reaction conditions, reactor design, promoters, metals, the structure of the catalyst, ... [30].

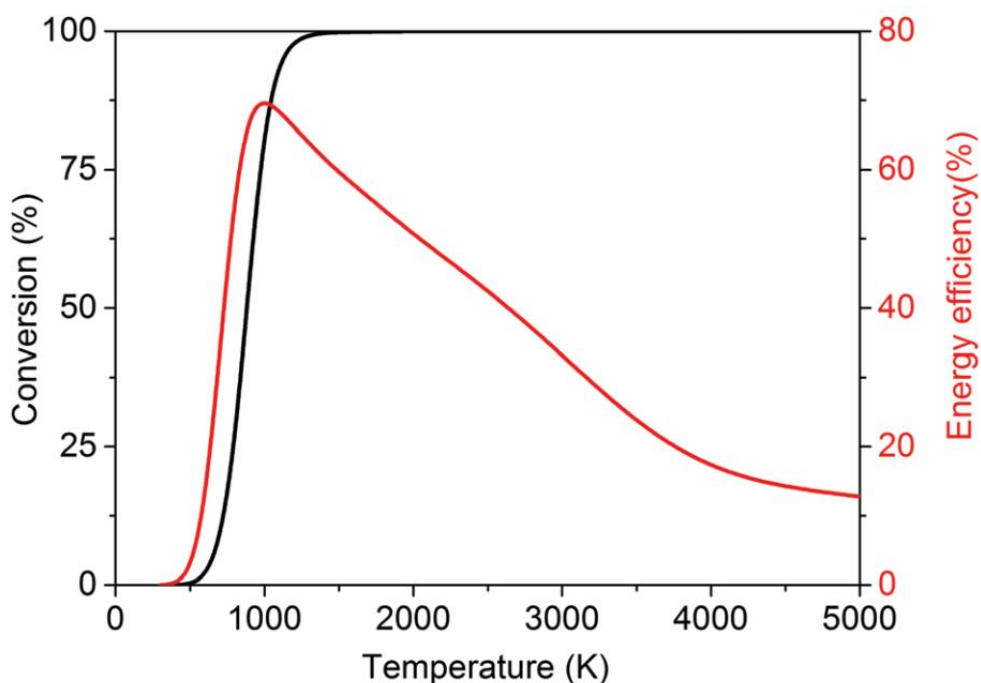


Figure 6: Calculated theoretical thermal conversion (left axis) and corresponding energy efficiency (right axis) as a function of temperature for DRM [9].

To influence the DRM reaction, a catalyst is often added, with transition metals (Fe, Co, Ni and Cu) and noble metals (Ru, Rh, Pd, Ir and Pt) being the most popular ones [31]. Since noble metals are more active, but also more expensive, or part of the critical raw materials list, research focusses on the use of supported bimetallic catalysts or the use of metal promoters. Frequently used supports are  $\text{SiO}_2$ ,  $\text{Al}_2\text{O}_3$ ,  $\text{MgO}$ ,  $\text{CaO}$ ,  $\text{CeO}_2$ ,  $\text{ZrO}_2$  or  $\text{La}_2\text{O}_3$  with the purpose of increasing the surface area, providing a high dispersion of the active metal and being stable at high temperatures. Their purpose is thus not to be catalytically active itself, but some catalytic activity or other effects of the support cannot be excluded. An example is the acidity/basicity of the support, with carbon deposition being favoured on acidic supports such as  $\text{SiO}_2$ , whilst base supports have been reported to reduce carbon deposition [32]. Furthermore, Lewis bases (e.g.  $\text{MgO}$ ) have a high affinity for the chemisorption of  $\text{CO}_2$ , therefore they are also able to shift the equilibrium of DRM to the right [33].

Other techniques to circumvent coke deposition are the Calcor process and the SPARG (sulphur-passivated reforming) process. The Calcor process produces very pure CO and consists of DRM in excess CO<sub>2</sub> at low pressure and high temperature to reduce the H<sub>2</sub> content in the final gas composition [34]. In the SPARG process, H<sub>2</sub>S is added to the feed, which blocks the active sites of the catalyst that would otherwise promote carbon nucleation [35].

### 1.2.3 Novel CO<sub>2</sub> conversion approaches

Both CO<sub>2</sub> splitting and DRM can decrease the greenhouse gas concentration in the atmosphere and transform waste molecules into value-added chemicals, evolving in the transition towards a circular economy. In addition, both processes can be executed by using renewable energy, enabling technological development for the transition towards the enhanced use of renewable energy in chemical industry, making the investigation of these processes worthwhile. Indeed, the thermal processes for both reactions have severe drawbacks: low conversions at lower temperatures, and thus the need of excessive heat when aiming for higher conversions and energy efficiency, the need for a catalyst that is not prone to coking or sintering processes, and so on. Therefore, the focus of current research often lies on other techniques than thermal conversion, utilising renewable energy. Indeed, electrochemistry, solar thermochemistry, photochemistry, biochemistry and plasma technology are often studied, as well as their combination and integration. To reduce energy barriers, a catalyst is often added.

Electrochemical conversion of CO<sub>2</sub> into various types of fuels is achieved by applying a potential difference between two electrodes. A schematic representation of an electrochemical cell for the conversion of CO<sub>2</sub> to formate/formic acid is shown in Figure 7. This process is influenced by multiple parameters: the applied potential difference, the temperature and pressure, the material of the catalyst and the electrodes, the interelectrode medium (i.e. electrolyte, solvent, membranes, etc.), its pH, and the CO<sub>2</sub> concentration. The main advantages of electrochemical conversion is that water can be used as a hydrogen source, and the reaction can take place at room temperature, since



the driving force is the electric potential. The main disadvantage is the low solvability of  $\text{CO}_2$  in water [36].

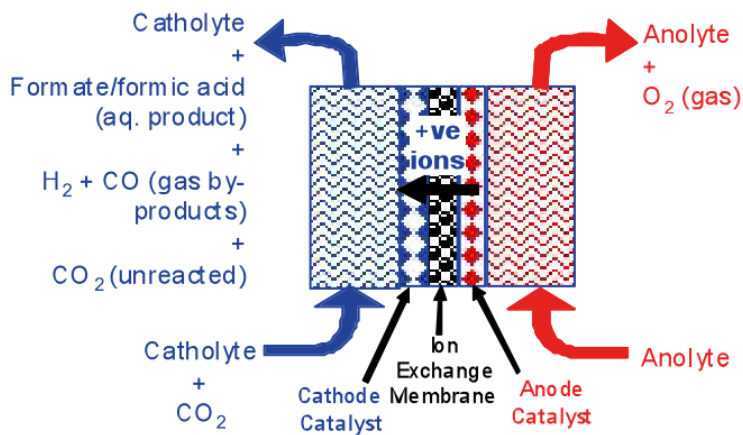


Figure 7: Example of an electrochemical cell to convert  $\text{CO}_2$  to formate/formic acid [36].

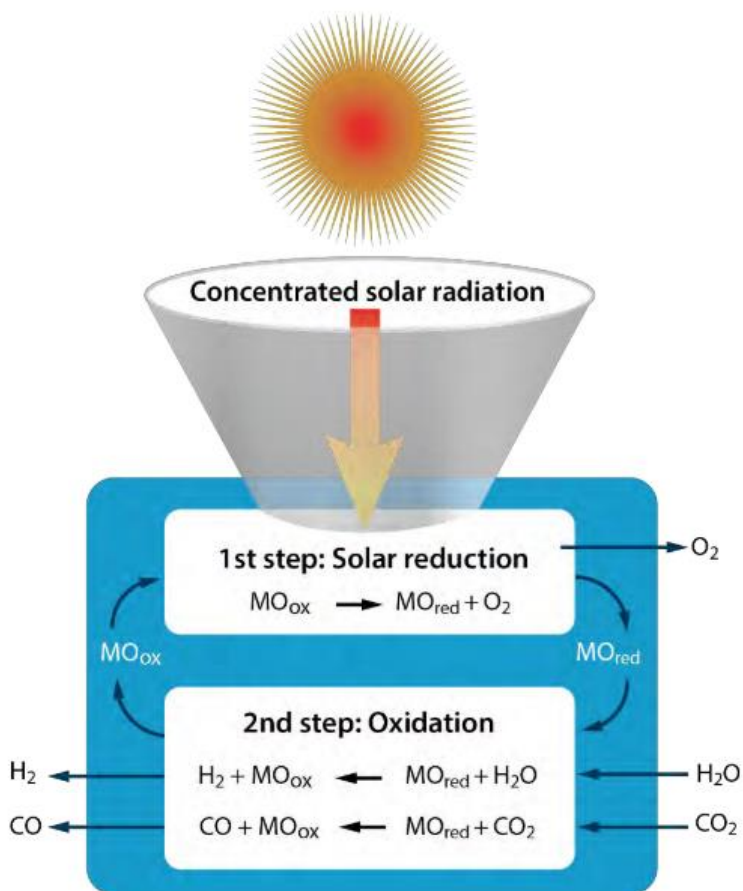


Figure 8: Schematic view of the two-step solar thermochemical cycle for  $CO_2$  and  $H_2O$  splitting based on metal oxide redox reactions [9].

Two other techniques, making direct use of sunlight, are solar thermochemical conversion and photochemical conversion. Solar thermochemical conversion uses a concentrated form of radiated sunlight to increase the reaction temperature, and therefore mitigates the need for external heating, as used in conventional thermal conversion. Interesting about this technique is that in its basic form, it only requires  $CO_2$ , and  $H_2O$  as feedstock, when aiming for hydrocarbons. The aim lies in  $CO_2$  splitting and converting  $H_2O$  into  $H_2$ , so the  $CO$  and  $H_2$  can be combined to form syngas. The  $H_2$  can be generated with renewable energy. Later the produced syngas can be converted to value-added chemicals, preferably with renewable energy. The main drawbacks,

limiting the economic viability, are the material characteristics and their resistance to the high operating temperature [37]. A schematic view is shown in Figure 8.

In photochemical conversion, it is no longer the (concentrated) heat and thus thermal capacity of the solar radiation that is used, but the energy of the photons themselves. Indeed, in photochemical reduction of  $\text{CO}_2$ , a photon hits the surface of a catalyst, exciting an electron from the valence band to the conduction band, as illustrated in Figure 9. Water (as a hydrogen source in this example) will react with the emerged hole in the valence band, and split into a proton and oxygen, and at the same time,  $\text{CO}_2$  reacts with one or more protons, while being reduced by the electron in the conduction band, to form value-added chemicals.

The catalyst is most often a transition-metal complex, since these complexes can absorb a significant part of the solar spectrum, have long-lived excited states, and can promote the activation of small molecules. The production of formic acid, formaldehyde, methanol, glyoxylic acid, acetic acid, methane, ethane and ethylene have been reported already [38]. The major drawback is the low overall efficiency, ranging between 0.01 and 10.9 %, with the maximum obtainable energy efficiency being limited to 17 % [38,39].

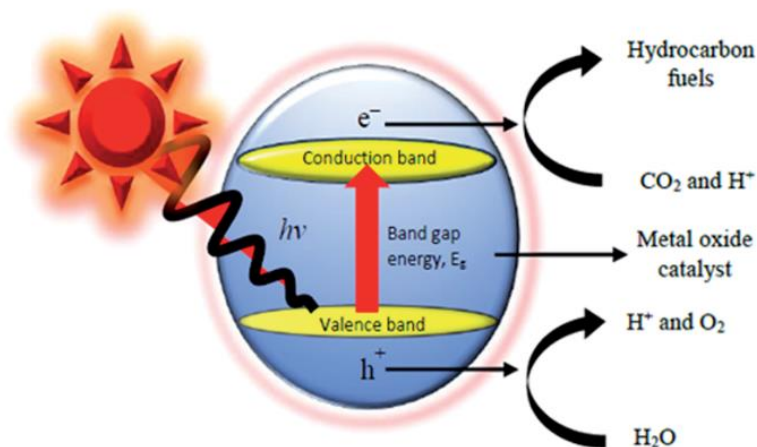


Figure 9: Photocatalytic reaction mechanism of an unmodified metal oxide semiconductor [40].

Photosynthesis is a natural way of accomplishing this conversion. Care has to be taken when choosing the route for this conversion, since the technique needs plants and thus competes for area with agriculture. To avoid this competition, algae could be used [41], since they don't occupy the same area as land for food production. Algae can be used to produce value-added chemicals, and are often used as fish food, since they contain valuable chemicals like proteins, fats, oil, dyes, antioxidants, ... . As with fossil fuel, algae fuel releases CO<sub>2</sub> when burnt, but the latter does not increase the overall CO<sub>2</sub> content in the atmosphere since similar amounts of CO<sub>2</sub> are removed from the atmosphere to perform the photosynthesis. Other advantages are that algae can grow with a minimal impact on freshwater resources, they can be produced using saline and wastewater, have a high flash point, and are biodegradable and relatively harmless to the environment if spilled. On the other hand, algae have a high CAPEX and OPEX, and thus have a high cost per unit mass [23]. Algae can produce a lot of value-added chemicals, including fish food, ethanol, acetone, butanol, methane, hydrogen, fuel gas, charcoal, and biodiesel [41]. The basic principle to convert CO<sub>2</sub> to biofuels via algae is shown in Figure 10.

The current disadvantage that is limiting the breakthrough of this technique is the stability of biodiesel itself. Indeed, since it contains more polyunsaturated fats, it is more prone to lose its fluidity at low temperature, therefore hindering its stability. Besides the drawback of stability, and the complexity for tackling this, as well as the high CAPEX and OPEX, the algae are also very sensitive to the cultivation temperature, mixing, fluid dynamics and hydrodynamic stress, gas bubble size and distribution, gas exchange, mass transfer, light cycle and intensity, water quality, pH, salinity, mineral and carbon regulation/bioavailability, cell fragility, cell density and growth inhibition.

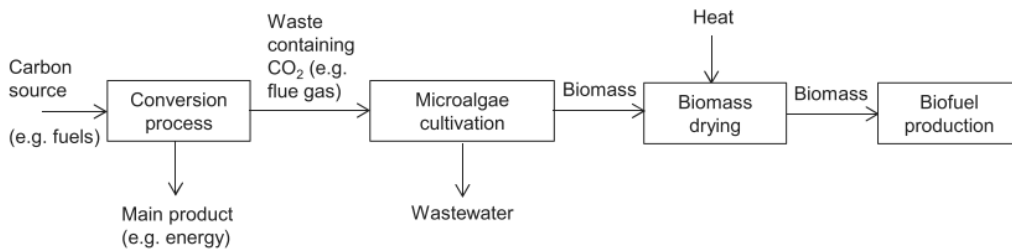


Figure 10: Utilisation of CO<sub>2</sub> to produce biofuels from microalgae [12].

#### 1.2.4 Catalytic conversion

The main principle of catalysis is that it reduces the activation energy, and thus the energy barrier that has to be crossed, to reach the product. Therefore, the catalysed reaction will proceed faster and the equilibrium between feed and products will be obtained sooner. The problems with the application of current existing catalysts, adapted from thermal CO<sub>2</sub> conversion, in the above mentioned novel emerging techniques for CO<sub>2</sub> conversion, is that they are either made of rare-earth metals and therefore don't fit in a sustainable economy, or that they are not adapted to the particular working principle of the non-thermal technology. Five important steps can be identified in a catalytic process, being (i) diffusion of the reagents towards the catalytic surface; (ii) adsorption; (iii) chemical reaction; (iv) desorption of the reaction products; and (v) diffusion away from the surface. For every different technology, all of these steps will be influenced differently, and therefore a catalyst can be very suitable for one technology, while being unfitting for another. Moreover, this is even more complicated for plasma technology, since then the mix of species interacting with the catalyst is more complex and elaborate than for a gas mixture. Therefore, catalytic development has a high priority when combining it with alternative technologies, and care has to be taken that the catalyst is suited for the chosen technology. Possible combinations of catalysis with other technologies for CO<sub>2</sub> conversion are demonstrated in Figure 11.

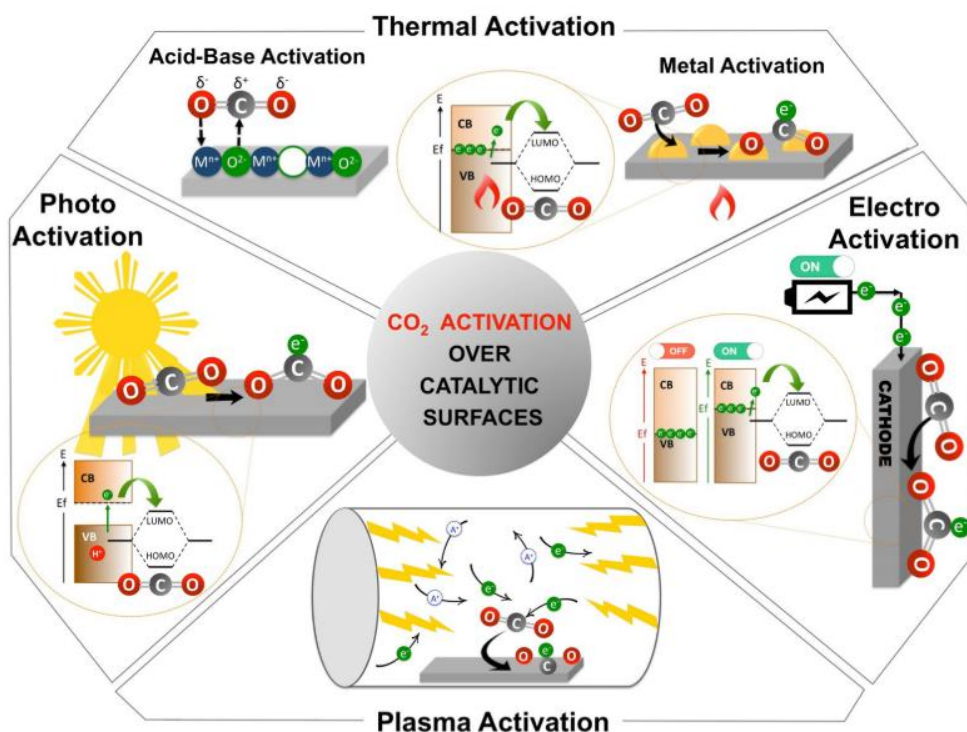


Figure 11: Common methods of CO<sub>2</sub> activation over catalytic surfaces [42].

### 1.3 PLASMA TECHNOLOGY FOR CO<sub>2</sub> CONVERSION

Another technique that has emerged in the field of CO<sub>2</sub> conversion (for CO<sub>2</sub> splitting, DRM and CO<sub>2</sub> conversion in combination with other hydrogen sources like H<sub>2</sub> or H<sub>2</sub>O) is plasma technology. Just like the other described techniques, plasma also has advantages and drawbacks. They will be described in the following paragraphs, together with the main characteristics of plasma technology and its suitability towards CO<sub>2</sub> splitting and DRM.

#### 1.3.1 General plasma properties

Plasma is produced by applying energy to a gas or fluid medium, leading to full or partial ionization. This energy can be acquired from heating, by applying an electric field, an energetic beam or by compressing the gas adiabatically. This will dissociate or ionise at least part of the molecules and create a very reactive mixture, consisting of neutral

species, excited species, ions, electrons, photons and radicals. The fact that there are many charged species makes the plasma, in contradiction to a neutral gas, electrically conductive. Although both negatively and positively charged species are present, the entire plasma will be quasi-neutral, with both positive and negative charges being equally present (except in the plasma sheath, a region adjacent to an electrode or dielectric material, which is characterized by a strong electric field and has a net positive space charge [43]).

The plasma types discussed in this thesis are artificially generated, but in addition, plasma also occurs naturally. Indeed, more than 99 % of the visible universe is in plasma state, with the interstellar medium being weakly ionized, and stars being essentially thermal plasma giants. On Earth, natural plasmas also occur, like lightning, Aurora Borealis, Aurora Australis and the solar wind.

Artificial plasmas find their origin in the early 1800's, when electrical arcs were first studied, and Siemens developed a plasma device to synthesize ozone from oxygen gas, with the ozone being used for water purification [44]. The name 'plasma' first occurred in 1920, and was given by Langmuir [45].

Although plasmas are used in several applications (see below), a complete understanding of their working principles and how they interact with other components (e.g., materials, catalysts, living matter,...) is still missing in many cases.

Some examples of applications are given below:

- Plasma TV's;
- CO<sub>2</sub> laser discharges for cutting and welding;
- Plasma hardening, etching and other surface treatments;
- Thin film deposition;
- Destruction of pollutants such as VOCs and odorous molecules;
- Lighting (e.g. neon lamps);
- Plasma medicine: tissue engineering, blood coagulation, deactivation of micro-organisms, sterilisation of instruments and surfaces, cancer treatment;
- Chemical synthesis (such as the ozone generation mentioned before).

Plasmas can occur as high- and low-temperature plasmas, depending on their temperature. Furthermore, the presence or absence of a thermal equilibrium between all components specifies whether the plasma is thermal (and thus all components are in thermal equilibrium, qualifying them as LTE - local thermal equilibrium) or non-thermal (non-LTE, where different components can be characterised by a different temperature). The latter type is often characterised by a very high electronic temperature ( $10^4 - 10^5$  K), while the other species in the plasma can stay near room temperature. The typical temperature ranges are shown in Table 2.

Table 2: Subdivision of plasmas according to the temperature of the different components.  $T_0$  is the gas temperature,  $T_i$  the ion temperature,  $T_r$  the rotational temperature,  $T_v$  the vibrational temperature and  $T_e$  the electron temperature.

Low-temperature plasma		High-temperature plasma
Non-thermal plasma	Thermal Plasma	
$T_0 \approx T_i \approx T_r < T_v \ll T_e \leq 10^5 \text{ K}$	$T_0 \approx T_i \approx T_r \approx T_v \approx T_e \leq 2 \times 10^4 \text{ K}$	$T_0 \approx T_i \approx T_r \approx T_v \approx T_e \geq 10^7 \text{ K}$

A non-thermal plasma is often generated by applying an electric field to a gas between two or more electrodes. A gas always has some free electrons (due, for example, to cosmic radiation), which will be accelerated when applying a voltage. When a certain threshold voltage (called the breakdown voltage,  $U_b$ ) is reached, the plasma will ignite. The breakdown voltage depends on the gas pressure and the distance between the two electrodes, which is a rule known as Paschen's law. The ignition occurs in the following stages: First, the accelerated electrons in the gap between the electrodes will cause a sharp increase in the current flow. They will collide with the gas molecules and cause them to excite, dissociate, ... The main and typical processes that occur in a plasma, starting from the ignition, are shown in Table 3.



Table 3: Typical plasma processes.

Electron/Molecular reactions	
Excitation	$e^- + A_2 \rightarrow A_2^* + e^-$
Dissociation	$e^- + A_2 \rightarrow 2A + e^-$
Attachment	$e^- + A + B \rightarrow AB^-$
Dissociative attachment	$e^- + A_2 \rightarrow A + A^-$
Ionisation	$e^- + A_2 \rightarrow A_2^+ + 2e^-$
Dissociative ionisation	$e^- + A_2 \rightarrow A^+ + A + 2e^-$
Dissociative recombination	$e^- + A_2^+ \rightarrow A + A$
Detachment	$e^- + A_2^- \rightarrow A_2 + 2e^-$
Atomic/Molecular reactions	
Penning dissociation	$M^* + A_2 \rightarrow M + 2A$
Penning ionisation	$M^* + A_2 \rightarrow M + A_2^+ + e^-$
Charge transfer	$A^* + B \rightarrow A + B^*$
Ion recombination	$A^- + B^+ \rightarrow AB$
Neutral recombination	$A + B + M \rightarrow AB + M$

Besides the species shown in this table, photons are also present in the plasma. The photons are generated by de-excitation of excited molecules or atoms. Indeed, in case of electronically excited species, an electron is excited and can thus be found in a high energy orbital, further away from the nucleus, leaving a hole in the lower orbital. Since this state is metastable, the molecule or atom can spontaneously return to the ground state, releasing the excess energy as a photon. Since many excited species exist in the plasma, many photons can be formed, therefore giving plasmas a visible glow, depending on the wavelength of the photons.

As can be seen from Table 3, various types of ions can be present in the plasma. Their number density is defined by the degree of ionisation, which indicates the ratio of the density of charged particles to the density of neutral species. For most gas processing

applications, this ionisation degree is rather low, and lies typically between  $10^{-6}$  –  $10^{-4}$  [46].

Radical densities in a DBD plasma range for DRM between  $10^{14}$  and  $10^{15}$   $\text{cm}^{-3}$  [47].

Not only ions and photons have their typical role in the plasma, other species also contribute in their own way. Electrons pass their initial energy on to the rest of the gas, creating reactive species through collisions. Gas heating takes place via vibrational excitation and subsequent vibrational-translational relaxation. The enhanced gas temperature will also contribute to accelerating chemical reactions. Synthesis of components often proceeds via ions and radicals, and they can react at temperatures lower than required for thermal processes. Hence, a plasma is a very reactive, complex mixture, which makes controlled and selective conversion very challenging and dependent on many different parameters. Depending on the intended outcome and application, different types of plasma can be applied, which differ based on the type of applied electric field, discharge type and the design of the reactor and will thus lead to different temperature profiles and a different distribution of species. The electric field can be created both by applying a direct current (DC) or an alternating current (AC), either continuous or pulsed. Moreover, the frequency can range from radio frequency to microwave frequency, thus ranging between kHz and GHz.

### *1.3.1.1 Direct current (DC) discharges*

When using DC, the characteristics of the discharge will depend on the voltage and the current, as shown in Figure 12. First, when the current is low, breakdown takes place and the plasma is categorised as a Townsend discharge. More and more collisions will lead to an increase in charged species density and thus an increase in current, converting the Townsend discharge to a corona, and subsequently to subnormal glow discharge and a normal glow discharge. This decreases the voltage, and a normal glow discharge has a constant current density, only partially covering the cathode surface. When the current increases further, the discharge will completely cover the cathode surface and become an abnormal glow discharge. This transition increases the voltage

until it peaks and decreases again, while the current still increases, creating an arc discharge. In this stage, thermionic emission from the high-voltage electrode is the main source of electrons.

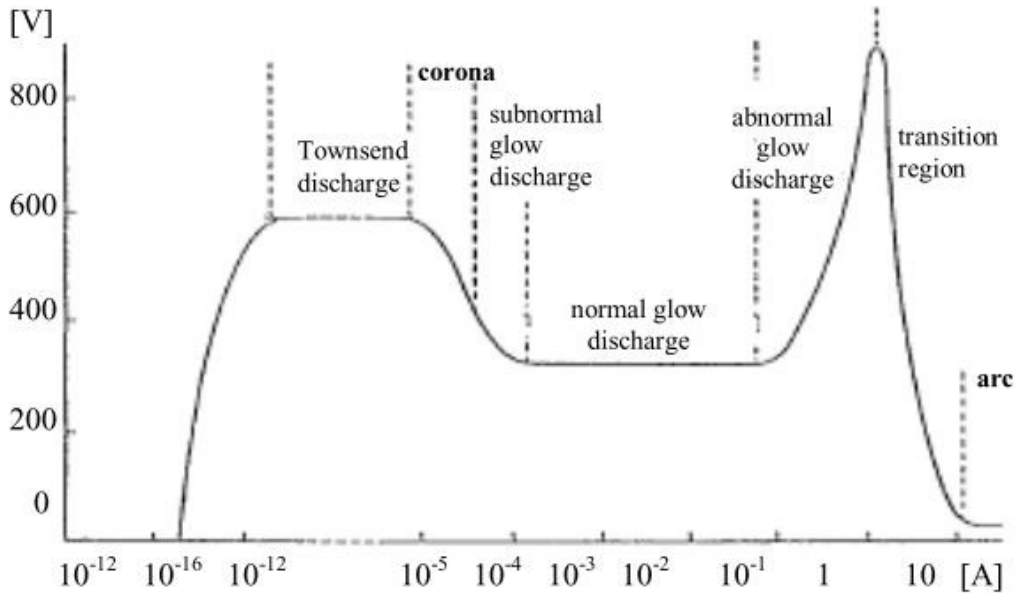


Figure 12: Different types of DC discharges depending on the voltage and current [48].

A glow discharge can easily be generated at low pressures, but it is difficult to generate at atmospheric pressure. According to Paschen's Law, it is possible to increase the pressure, as long as  $pd$  (pressure times discharge gap) remains constant, thus reducing the gap. When the gap remains constant and the pressure increases, too many charged species would arise, increasing the electrical current. This would heat up both the gas and the electrodes, resulting in arc formation. To prevent the build-up of too many charged species, a dielectric barrier can be used to cover one or two electrodes (giving rise to a dielectric barrier discharge; see below). Arc formation needs to be avoided, since this will lead to a plasma in thermal equilibrium, which is less beneficial for the output parameters of  $\text{CO}_2$  conversion.

### 1.3.1.2 *Alternating current (AC) discharges: DBD*

Igniting a plasma in a reactor with a dielectric barrier, while applying DC, will prevent arc formation by limiting the current, but the plasma will extinguish quite rapidly since there will be a charge build-up in the dielectric barrier. To preserve the discharge, it is necessary to apply an alternating current (AC) to alternate the polarity of the electrodes, which will dissipate the induced charge on the barrier. A discharge at atmospheric pressure, with a dielectric barrier to prevent arc formation, and applying alternating current, is called a dielectric barrier discharge (DBD).

The operating frequency is typically between 50 Hz and 500 kHz, and even while the plasma is at atmospheric pressure, it is far from thermal equilibrium [49]. It is used in various industrial applications, with a cylindrical or planar setup. In a cylindrical setup, it consists of an inner electrode and an outer electrode, comprising a discharge gap ranging from 0.1 mm to several cm wide. The two electrodes are separated by one or two dielectric barriers, covering one or both electrodes. The dielectric barrier consists of a material with a (high) relative permittivity (or dielectric constant), which is a measure for the material's ability to store electrical charge, compared to that of vacuum. The reason this material is needed for a dielectric barrier discharge is to limit the transition to an arc regime by limiting the electric current, as mentioned above. Indeed, when a microdischarge hits the surface of the dielectric barrier, it will extinguish, charging the dielectric surface locally. The formation of a new microdischarge upon switching the polarity of the electrodes very likely takes place where a previous microdischarge extinguished, since there is a lot of residual charge. DBDs are often not homogeneous and consist of several tiny microdischarges (filaments). These microdischarges take place on the entire dielectric surface and reach the opposite electrode. The difference between a homogeneous and a filamentary discharge is shown in Figure 13.

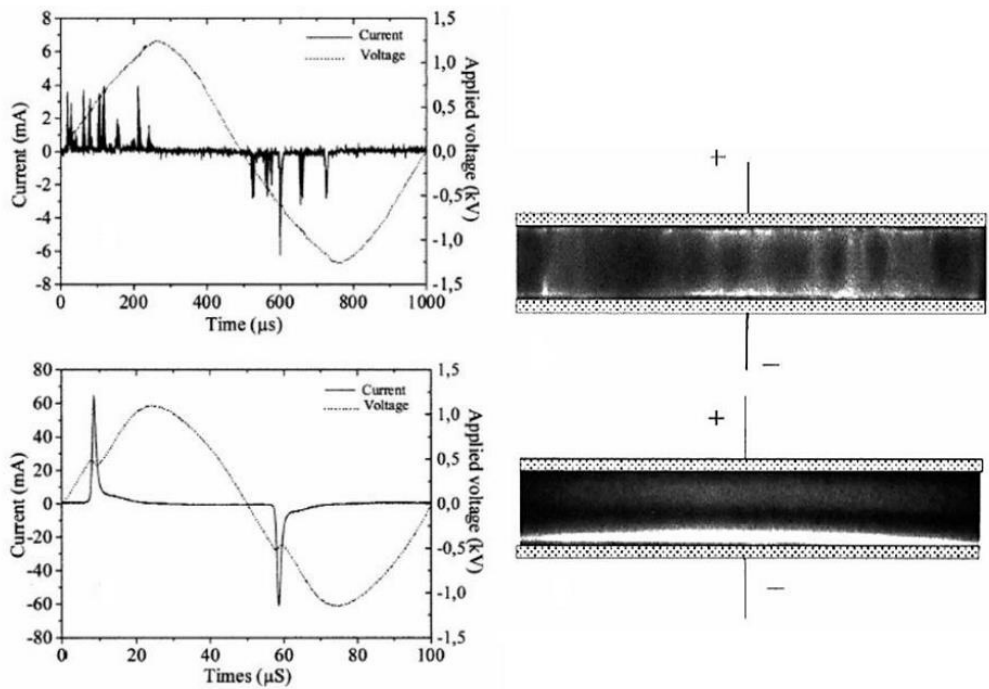


Figure 13: Typical current and voltage-profile (left) and visual image (right) for a filamentary (top) and homogeneous (bottom) Helium DBD [50].

In a non-packed DBD, the gas, the electrode/dielectric material, the pressure and the gap define whether the discharge will be homogeneous or filamentary. A homogeneous discharge is only achieved in e.g. argon or nitrogen, and with specific requirements regarding the reactor design (gap, pressure, ...). The filamentary regime is more common in DBDs and consists of several discharge filaments. These filaments are cylindrical, about 100 μm in radius, and have a lifetime of several nanoseconds and they initiate when the applied voltage exceeds the breakdown voltage.

Since adding a dielectric material to cover one or two electrodes has a significant impact on the plasma behaviour, it can also be used to alter the plasma characteristics in the discharge gap itself. This is where the packed-bed DBD reactor finds its origin, where dielectric pellets, beads, or other shapes can be inserted in the gap. This might change the discharge type from a volume discharge to a surface discharge [51].

Indeed, the packing material can concentrate electrostatic lines of flux, which leads to an enhanced electric field, both at the contact points between the beads, as well as at

the contact points between the beads and the dielectric barrier. Since there are many contact points in a packed bed DBD, the average electric field may increase by a factor 10 to 250, increasing the electron energy and thus altering the conversion and energy efficiency of the process [52]. This electric field enhancement factor depends on the dielectric constant of the material, the curvature and the contact angle [52]. Moreover, apart from an impact on the mass and heat transfer, and the discharge properties of the plasma, catalytic elements can be coated on the packing material, adding an extra dimension to their role in plasma-assisted conversion reactions. This leads us to the next section about plasma catalysis.

### 1.3.2 Plasma catalysis

As mentioned above, both CO<sub>2</sub> splitting and DRM have been studied with several plasma types: corona, gliding arc, microwave, atmospheric pressure glow discharge (APGD) and DBD. Although promising results have been obtained already, there is still room for improvement, in terms of conversion, energy efficiency and selectivity, as well as a clear need to gain better understanding of the processes occurring in the plasma. Of the aforementioned goals, improving the selectivity of the conversion process is the hardest, since a plasma has the advantage of creating very reactive species in an efficient way, but through a complex mixture, in which a lot of different species exist. Indeed, for dry reforming, the major product obtained is syngas, but it would be more preferred to selectively form higher hydrocarbons (C<sub>2</sub> – C<sub>5</sub>) and oxygenates. To achieve this, the plasma can be combined with heterogeneous catalysis. This can indeed be advantageous, since plasma provides a low-temperature process that can be used intermittently, and combining it with catalyst can bring an increased conversion and selectivity by enhancing the electric field, changing the discharge type, altering the densities of the plasma species, ... [53]. Indeed, when the catalyst enhances the formation of certain plasma species, interacts with certain plasma species and/or the adsorption/desorption is stronger towards specific species, the reactions of these species will be altered. Since the type of species present in a plasma differ from the

ones present in thermal catalysis, a lot of knowledge on these material-plasma interactions are still unknown and requires more research.

The use of plasma catalysis is, up to now, mostly used for pollutant destruction ( $\text{NO}_x$ , CFCs and VOCs) and for the production of syngas. For the destruction of pollutants, the typical gas flow contains waste gas, with a pollutant concentration below 1000 ppm, while for syngas production, the gas mostly consists of  $\text{CO}_2$ , with additional  $\text{CH}_4$ ,  $\text{H}_2\text{O}$  or  $\text{H}_2$ . Additional impurities can be present, like  $\text{N}_2$ , which in case of plasma have a beneficial effect up to about 50% [18].

The combination of plasma and catalysis can be realized in two different configurations, namely single-stage or two-stage. For the latter, the catalyst is placed before or after the plasma discharge, making the catalyst either function as pre-treatment of the gas, before it enters the plasma, or interacting with the long-lived species and/or end-products of the plasma, respectively. Since the vibrationally and electronically excited species have an estimated lifetime between 1 and 100 ns [54,55], the time-frame for the interaction between these species and the catalyst surface is very narrow. The lifetime of ions in the afterglow is 100  $\mu\text{s}$  [47], and the negative ions typically have a shorter lifetime in the afterglow than the positive ions [47]. The density of radicals also drops after the plasma, but there still is radical density of  $10^{11} \text{ cm}^{-3}$  after 1 second [47]. These species can still interact with the catalyst, but to maximise the interaction between catalyst and reactive plasma species, a single-stage configuration will be applied in this work, where the catalyst is placed directly into the plasma discharge. Interactions are now possible between the catalyst and the short-lived active species, such as excited atoms and molecules, radicals, electrons and photons. Moreover, the packing can in this case also play an important role in physically altering the plasma properties and thus species densities.

Although this combination of plasma and catalysis has the potential to increase the conversion, selectivity and energy efficiency, it makes the matrix of interactions bigger and thus more complex to understand. This matrix is shown in Figure 14, and shows that both the physical and chemical properties of the catalyst can be influenced by the

plasma, and vice versa. This means that the catalyst, packing materials and/or supports on which the catalyst can be coated, can increase the conversion, selectivity and energy efficiency, under the preconditions that the catalyst and plasma are adjusted to each other.

Several underlying principles can be identified that have an influence, but it is important to mention that there is still a lot unknown about the plasma, the catalyst/packing and their possible interactions [56]. The catalyst/packing material, on the one hand, can enhance the electric field in the plasma, resulting in an enhanced efficiency for the chemical reactions, and can also change the discharge type. For example, the dielectric constant of the packing material will affect the electric field strength and electron temperature, which will in turn alter the reaction rates [57].

The surface of the catalyst can adsorb plasma species, therefore affecting the concentration of the species. It is even possible to use a plasma to overcome thermal limitations in catalysis, e.g. plasma-induced vibrational excitations of  $N_2$  decrease dissociation barriers without influencing subsequent reaction steps [58].

When the packing/catalyst has pores larger than several 100 nm, a microdischarge can be formed inside these pores [59]. Void spaces in between the beads, and channels of voids between multiple beads, also affect the electric field strength and electron temperature, and thus the chemistry [57].



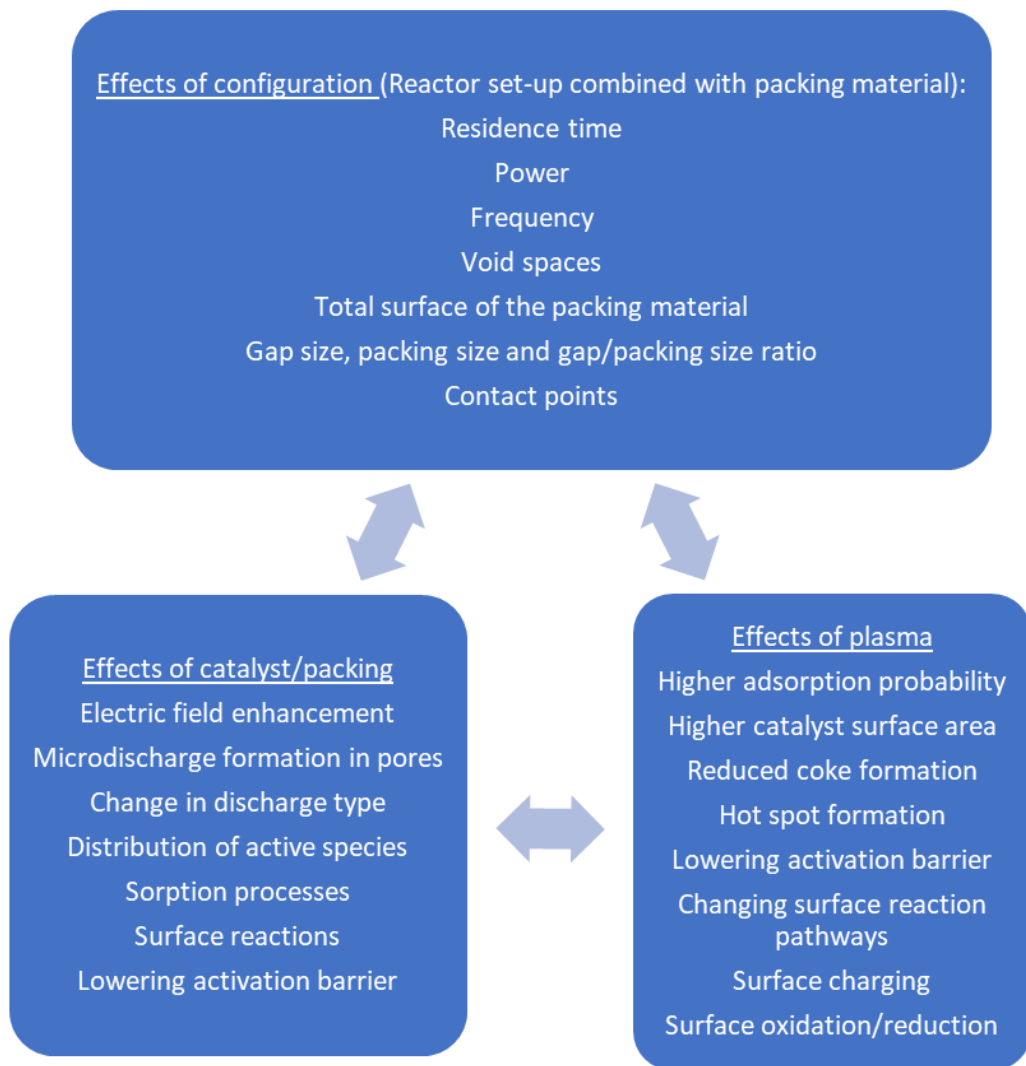


Figure 14: Overview of the various effects of the catalyst on the plasma and of the plasma on the catalyst, which may give rise to a synergistic plasma catalytic operation. Adapted from ref. [53].

The plasma, on the other hand, can alter the catalyst surface and increase its surface area, reduce metal oxides to metals, change the oxidation state or the work function, reduce coke formation on the surface and increase the adsorption probability of the plasma species on the catalytic surface, which can increase the retention time of these species. Moreover, hot spots can be formed, which increase the local temperature, the activation barrier can be lowered (both by the plasma and the catalyst) and the reaction

pathways can be changed as well. Furthermore, photon irradiation of the plasma might activate the catalyst, although it is reported that the photon intensity in the plasma is actually too low for this process to happen [60], but other plasma species, like electrons, can induce similar effects. Some of these effects are illustrated in Figure 15, and all of these effects can have a positive or a negative influence.

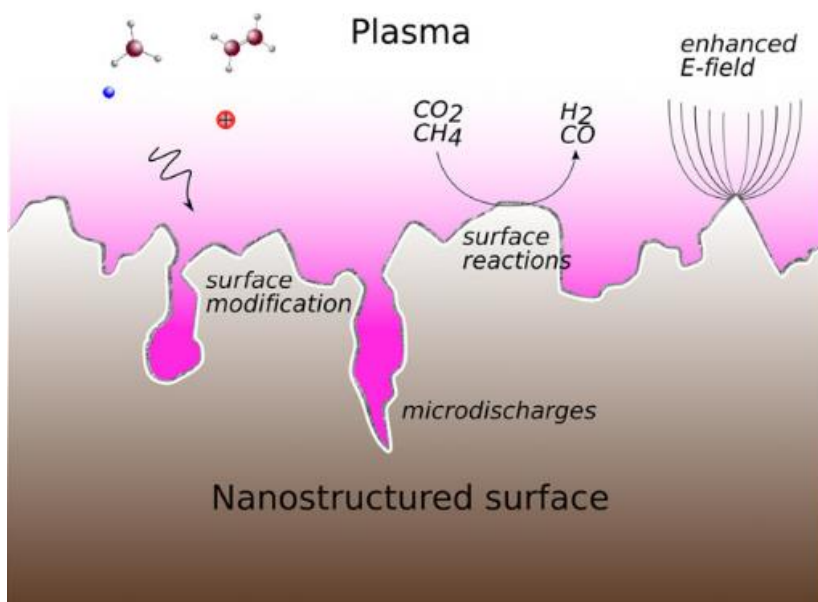


Figure 15: Schematic representation of several factors active in plasma catalysis [53]

Depending on the combination of all these influences, certain processes can be favoured over others, thus creating chemicals more selectively and/or efficiently. The main advantage over thermal catalysis is that the gas stream in plasma catalysis contains many different reactive species, such as radicals and excited species, that can adsorb on the catalyst surface. Indeed, the internal energy of the ions, radicals and electronically excited species is higher than the activation energy required for thermal catalysis. Moreover, the excited species can have a lower adsorption energy than the ground state species, favouring plasma catalysis over thermal catalysis.

When all given parameters (physical and chemical) are indeed adjusted, a synergy can arise between plasma and catalyst, meaning that the combination of the two methods yields a better result than the sum of both methods separately.

In this PhD thesis, we will therefore study the influence of the basic design of a catalyst/packing material on the plasma-catalytic splitting of CO<sub>2</sub> and dry reforming of methane, by comparing a packed bed DBD with a non-packed reactor, giving more insight into the above-mentioned processes.

### 1.3.3 State of the art

Plasma and plasma catalysis for CO<sub>2</sub> splitting and DRM have been studied extensively in DBD reactors, both with and without (catalytic) packing materials, as summarised Table 4 and Table 5, respectively. Even though the state of the art is quite extensive, the current literature indicates that still a substantial amount of work lies ahead to unravel all aspects of CO<sub>2</sub> splitting DRM in a packed bed DBD. Indeed, some important observations can be made when comparing literature, that underline the need for further research. For example, some papers contradict each other with respect to the influence of frequency on CO<sub>2</sub> splitting in a non-packed reactor, reporting either a rise or a drop or no influence of frequency on the results (see details in Table 4)[61–63]. Similar discrepancies have been observed for DRM in packed bed DBD plasma reactors. For instance, adding a packing has been reported to increase the conversion [64–71], while several other papers report a decrease in conversion of both CO<sub>2</sub> and CH<sub>4</sub> [71–73], and still other papers show only an effect on one of the two reacting gases [70,74–76] (see Table 5). Moreover, also vast differences in selectivity are being described, even for similar packing materials, as detailed in Table 5. Moreover, it is clear that even for the non-packed reactor, both the process conditions and the reactor design already affect the selectivity tremendously [64,74,77].

Furthermore, very often catalytically activated packing materials are being introduced and discussed, without evaluating the impact of the non-activated packing on the DRM process [64–67,70–72,78,79], even though the latter can be expected to have an

influence on the conversion and selectivity as well [53,74,80]. Indeed, in those papers where the packing materials are being studied with and without catalytic activation, an influence of the packing material itself can be observed [64,68,73–75,77,78]. For instance, Wang et al. reported the formation of liquid products and a significant influence on the selectivity, when comparing different catalytic activations with non-activated packing. Unfortunately, they only compared to one type of packing material [74]. Krawczyk et al. [68] and Sentek et al. [73] indicated only minor alterations in selectivity and conversion when adding a catalytic element on a certain packing, whereas different packing materials with the same active elements yielded major changes, suggesting that the packing itself could be responsible for the selectivity and conversion, and not the catalytic element per se. Other research [70,77] shows a larger influence of the catalytic element on the conversion and selectivity. Unfortunately, these studies are limited to specific packing materials and do not allow to compare the impact of different non-activated packing materials, which would be necessary to elucidate a synergic combination of packing material and catalytic active site. However, a large influence on (and possible control over) the conversion and selectivity is in principle possible, depending on the packing, the catalytic element, the reactor and the operating conditions. The packing material on itself is not necessarily catalytically active (although it can have some catalytic activity or promoting effect as well), but it is typically used as support and/or influences the plasma characteristics in a physical way (e.g. through changes in electric field, discharge, sorption processes). Most used catalytic elements for catalytic activation of the packing in plasma-assisted DRM are Ni, Co, Fe, Mn, Cu, Ag and Pd [9]. These are used since they are transition metals, where their interaction with adsorbates is determined by the position of the metal in the periodic table. Less noble metals interact stronger with the atoms than with undissociated molecules, which leads to molecular dissociation. More noble metals, on the other hand, show the opposite trend, which preserves the molecules intact. This determines their place on the volcano plot, where the material on top (having a strong affinity for the reagents and a poor affinity for the products) should be chosen.

Unfortunately, these interactions and thus the resulting volcano plot, are only calculated and measured for thermal DRM, and not for plasma catalytic DRM. Therefore, most catalytic elements are chosen based on their performance in thermal DRM, and not for specific suitability in plasma catalytic DRM [60].

Also for other plasma-assisted processes, such as the abatement of diluted VOC's, numerous studies have shown that physical size and material properties of the packing materials in a DBD reactor play a role to convert chemicals [81–88]. Even more, VOC decomposition is mainly influenced by the adsorption process, rather than by the discharge characteristics [53,89].

Table 4: Summary of a selection of literature for CO<sub>2</sub> splitting in a non-packed and a packed DBD reactor.

Study	Reactor		Operating conditions				Implementing packing and/or catalysts			Conclusion	Highest conversion	Ref.
	Gap (mm)	Power (Watt)	Flow (ml/min)	Reactor volume (cm <sup>3</sup> )	Frequency	SEI (kJ/L)	Packing/Catalyst	Shape	Packing size			
CO <sub>2</sub> splitting/ non-packed	1.5	70	150	21.9	5-65 kHz	28				No influence of frequency Conversion <input checked="" type="checkbox"/> when flow rate <input checked="" type="checkbox"/> , T <sub>gas</sub> <input checked="" type="checkbox"/> , P <input checked="" type="checkbox"/> . Best frequency depends on power	10%	[90]
	2	100-200	50-500	13.56	10-90 kHz	12-240				Conversion <input checked="" type="checkbox"/> when flow rate <input checked="" type="checkbox"/> , barrier thickness <input checked="" type="checkbox"/> , frequency <input checked="" type="checkbox"/> and power <input checked="" type="checkbox"/>	30%	[62]
	2	10-97	50-2000	15.1	16.2-28.6 kHz	0.3-116				Conversion <input checked="" type="checkbox"/> when power <input checked="" type="checkbox"/> and discharge length <input checked="" type="checkbox"/> Cokes: small on inner electrode	35%	[63]
	4	21.6-35.3	40	30.17	13 kHz	32.4-53				Conversion <input checked="" type="checkbox"/> when power <input checked="" type="checkbox"/> and discharge length <input checked="" type="checkbox"/> Cokes: small on inner electrode	13%	[91]
	4.5, 3.5, 2.5 or 2	60	50	17.67	26.5 kHz	72				Conversion <input checked="" type="checkbox"/> when flow rate <input checked="" type="checkbox"/>	12%	[80]
	4	21.6-35.3	40	30.17	13 kHz	32.4-53	Silica gel	Beads	20-40 mesh		14%	[91]

CO <sub>2</sub> splitting/ packed	3	20-50	50	10.1	9 kHz	24-60	Quartz	Pellets with rigid edges	20-40 mesh	silica gel < $\alpha$ -Al <sub>2</sub> O <sub>3</sub> < quartz $\approx \gamma$ -Al <sub>2</sub> O <sub>3</sub> < CaTiO <sub>3</sub> Cokes: limited on inner electrode	16%		
							$\gamma$ -Al <sub>2</sub> O <sub>3</sub>	Beads	20-40 mesh		16%		
							$\alpha$ -Al <sub>2</sub> O <sub>3</sub>	Beads	20-40 mesh		15%		
							CaTiO <sub>3</sub>	Beads	20-40 mesh		20.5%		
	Glass	1 mm	1 mm	Beads	1 mm	Glass < BaTiO <sub>3</sub>	22% (16% without packing)	[92]					
							BaTiO <sub>3</sub>	Beads	1 mm	28% (16% without packing)			
	4.5, 3.5, 2.5 or 2	60	50	17.67	26.5 kHz	72	Glass wool	Beads	1.25-2.24 mm	Conversion $\square$ when # contact points $\square$ , void space volumes $\square$ and bead/gap size ratio $\square$ . Impact of the packing material (chemistry and physical), also influenced by setup	10%	[80]	
							Quartz wool	Beads	1.25-2.24 mm		10%		
							SiO <sub>2</sub>	Beads	1.25-2.24 mm			16%	

																		19%
																		17%
																		26%

*Table 5: Summary of a selection of literature for DRM in a non-packed and a packed DBD reactor*

Study	Reactor Gap (mm)	Operating conditions					Implementing packing and/or catalysts					Selectivity	Conclusion	Highest conversion	Ref.		
		Power (W att)	Flow (ml/min)	Reactor volume (cm <sup>3</sup> )	Frequency	Ratio CO <sub>2</sub> /CH <sub>4</sub>	T	SEI (kJ/L)	Packing/ Catalyst	Shape	Packing size						
DRM/ non-packed	3	30-60	25-100	11.4	30-40 kHz	1	/	18-144						Highest achieved selectivity per component	Conversion when flow rate and P <input checked="" type="checkbox"/>	50.4% CH <sub>4</sub> , 30.5% CO <sub>2</sub>	[78]
														45% CO, 29% H <sub>2</sub> , 5% C <sub>2</sub> H <sub>2</sub> /C <sub>2</sub> H <sub>4</sub> , 22% C <sub>2</sub> H <sub>6</sub> , 2% C <sub>3</sub> H <sub>6</sub> , 12% C <sub>3</sub> H <sub>8</sub> (estimation)	Conversion when flow rate and P <input checked="" type="checkbox"/>		



1	25-75	30-75	4.4	30 kHz	0.66 - 3	/	20-150	76% CO, 57% H <sub>2</sub>	Conversion <input checked="" type="checkbox"/> when flow rate <input type="checkbox"/> , P <input checked="" type="checkbox"/> . CH <sub>4</sub> conversion <input type="checkbox"/> , CO <sub>2</sub> conversion ≈ when ratio <input type="checkbox"/>	59.7% CH <sub>4</sub> , 36.9% CO <sub>2</sub>	[64]
1	80-130	10-40	4.7	20 kHz	0.25-1	/	120-780	73.8% CO, 65.9% H <sub>2</sub> , 18.0% C <sub>2</sub> , 10.2% C <sub>3</sub> , 6.2% C <sub>4</sub>	Conversion <input checked="" type="checkbox"/> when flow rate <input type="checkbox"/> , P <input checked="" type="checkbox"/> . CH <sub>4</sub> conversion <input type="checkbox"/> , CO <sub>2</sub> conversion ≈ when ratio <input type="checkbox"/>	64% CH <sub>4</sub> , 34% CO <sub>2</sub>	[77]
3	10	40	2.12	12 kHz	4	/	15	20% CO, 34% H <sub>2</sub> , <1% C <sub>2</sub> H <sub>2</sub> , <1% C <sub>2</sub> H <sub>4</sub> , 12% C <sub>2</sub> H <sub>6</sub> , 1% C <sub>3</sub> H <sub>8</sub> , <1% C <sub>4</sub> H <sub>10</sub> , 11.9% methanol, 11.9% ethanol, 33.7% acetic acid, 1.6% acetone, 0% HCHO	Impact depends on catalyst, both <input checked="" type="checkbox"/> and <input type="checkbox"/> conversion and differs from pure packing	18% CH <sub>4</sub> , 15% CO <sub>2</sub>	[74]

DRM/ packed	3	30-60	25-100	11.4	30-40 kHz	1	/	18- 144	10 wt% Ni@ $\gamma$ -Al <sub>2</sub> O <sub>3</sub>	Pellets	0.5-1.7 mm	55% CO, 33% H <sub>2</sub> , 10% C <sub>2</sub> H <sub>2</sub> /C <sub>2</sub> H <sub>4</sub> , 47% C <sub>2</sub> H <sub>6</sub> , 2% C <sub>3</sub> H <sub>6</sub> , 25% C <sub>3</sub> H <sub>8</sub> (estimation)	Conversion <input checked="" type="checkbox"/> when pellet size <input checked="" type="checkbox"/> , quartz wool is best, impact packing on selectivity	40.2% CH <sub>4</sub> , 30.5% CO <sub>2</sub>	[78]					
																12% Ni/ $\gamma$ - Al <sub>2</sub> O <sub>3</sub>	? ?	? ?	43% CO, 53% H <sub>2</sub>	30% CH <sub>4</sub> , 24% CO <sub>2</sub>
																12% Cu/ $\gamma$ - Al <sub>2</sub> O <sub>3</sub>	? ?	? ?	50% CO, 31% H <sub>2</sub>	7% CH <sub>4</sub> , 5% CO <sub>2</sub>
																1%Cu-12% Ni/ $\gamma$ -Al <sub>2</sub> O <sub>3</sub>	? ?	? ?	45% CO, 51% H <sub>2</sub>	33% CH <sub>4</sub> , 25% CO <sub>2</sub>
																5%Cu-12% Ni/ $\gamma$ -Al <sub>2</sub> O <sub>3</sub>	? ?	? ?	47% CO, 54% H <sub>2</sub>	37% CH <sub>4</sub> , 24% CO <sub>2</sub>
																12%Cu-12% Ni/ $\gamma$ -Al <sub>2</sub> O <sub>3</sub>	? ?	? ?	75% CO, 56% H <sub>2</sub>	69% CH <sub>4</sub> , 75% CO <sub>2</sub>
																16%Cu-12% Ni/ $\gamma$ -Al <sub>2</sub> O <sub>3</sub>	? ?	? ?	64% CO, 57% H <sub>2</sub>	43% CH <sub>4</sub> , 47% CO <sub>2</sub>
																5% Ni- 12%Cu/ $\gamma$ - Al <sub>2</sub> O <sub>3</sub>	? ?	? ?	75% CO, 56% H <sub>2</sub>	43% CH <sub>4</sub> , 45% CO <sub>2</sub>
																16% Ni- 12%Cu/ $\gamma$ - Al <sub>2</sub> O <sub>3</sub>	? ?	? ?	71% CO, 58% H <sub>2</sub>	57% CH <sub>4</sub> , 57% CO <sub>2</sub>
																DRM/ packed	1	25-75	30-75	4.4
12% Cu/ $\gamma$ - Al <sub>2</sub> O <sub>3</sub>	? ?	? ?	43% CO, 53% H <sub>2</sub>	30% CH <sub>4</sub> , 24% CO <sub>2</sub>																
12% Cu/ $\gamma$ - Al <sub>2</sub> O <sub>3</sub>	? ?	? ?	50% CO, 31% H <sub>2</sub>	7% CH <sub>4</sub> , 5% CO <sub>2</sub>																
1%Cu-12% Ni/ $\gamma$ -Al <sub>2</sub> O <sub>3</sub>	? ?	? ?	45% CO, 51% H <sub>2</sub>	33% CH <sub>4</sub> , 25% CO <sub>2</sub>																
5%Cu-12% Ni/ $\gamma$ -Al <sub>2</sub> O <sub>3</sub>	? ?	? ?	47% CO, 54% H <sub>2</sub>	37% CH <sub>4</sub> , 24% CO <sub>2</sub>																
12%Cu-12% Ni/ $\gamma$ -Al <sub>2</sub> O <sub>3</sub>	? ?	? ?	75% CO, 56% H <sub>2</sub>	69% CH <sub>4</sub> , 75% CO <sub>2</sub>																
16%Cu-12% Ni/ $\gamma$ -Al <sub>2</sub> O <sub>3</sub>	? ?	? ?	64% CO, 57% H <sub>2</sub>	43% CH <sub>4</sub> , 47% CO <sub>2</sub>																
5% Ni- 12%Cu/ $\gamma$ - Al <sub>2</sub> O <sub>3</sub>	? ?	? ?	75% CO, 56% H <sub>2</sub>	43% CH <sub>4</sub> , 45% CO <sub>2</sub>																
16% Ni- 12%Cu/ $\gamma$ - Al <sub>2</sub> O <sub>3</sub>	? ?	? ?	71% CO, 58% H <sub>2</sub>	57% CH <sub>4</sub> , 57% CO <sub>2</sub>																

										20% Ni-12%Cu/ $\gamma$ -Al <sub>2</sub> O <sub>3</sub>	?	?	62% CO, 58% H <sub>2</sub>		35% CH <sub>4</sub> , 32% CO <sub>2</sub>	[77]
										$\gamma$ -Al <sub>2</sub> O <sub>3</sub>	Crushed flakes	10-20 mesh	49.2% CO, 51% H <sub>2</sub> , 9.7% C <sub>2</sub> , 5.5% C <sub>3</sub> , 3% C <sub>4</sub>	Packing CO <sub>2</sub> conversion <input checked="" type="checkbox"/> CH <sub>4</sub> conversion <input checked="" type="checkbox"/> After activation: conversion <input checked="" type="checkbox"/> selectivity <input checked="" type="checkbox"/> for H <sub>2</sub> and C <sub>2</sub>	57.6% CH <sub>4</sub> , 30.9% CO <sub>2</sub>	
										2 wt% Ni @ $\gamma$ -Al <sub>2</sub> O <sub>3</sub>	Crushed flakes	10-20 mesh	60.6% CO, 52.3% H <sub>2</sub> , 9.8% C <sub>2</sub> , 5.9% C <sub>3</sub> , 3.2% C <sub>4</sub>		55.4% CH <sub>4</sub> , 32.7% CO <sub>2</sub>	
										5 wt% Ni @ $\gamma$ -Al <sub>2</sub> O <sub>3</sub>	Crushed flakes	10-20 mesh	60.9% CO, 51.9% H <sub>2</sub> , 10.1% C <sub>2</sub> , 5.9% C <sub>3</sub> , 3.2% C <sub>4</sub>		55.7% CH <sub>4</sub> , 33.5% CO <sub>2</sub>	
										7 wt% Ni @ $\gamma$ -Al <sub>2</sub> O <sub>3</sub>	Crushed flakes	10-20 mesh	63.9% CO, 53.5% H <sub>2</sub> , 10.6% C <sub>2</sub> , 6.1% C <sub>3</sub> , 3.6% C <sub>4</sub>		55.5% CH <sub>4</sub> , 32.6% CO <sub>2</sub>	
										10 wt% Ni @ $\gamma$ -Al <sub>2</sub> O <sub>3</sub>	Crushed flakes	10-20 mesh	61.4% CO, 53% H <sub>2</sub> , 10.6% C <sub>2</sub>		55.2% CH <sub>4</sub> , 32.7% CO <sub>2</sub>	
1	130	30	4.7	20 kHz	1	/	260									

											6.2% C <sub>3</sub> , 3.4% C <sub>4</sub>						15% CH <sub>4</sub> , 12.5% CO <sub>2</sub>			[74]		
											23% CO, 55% H <sub>2</sub> , <1% C <sub>2</sub> H <sub>4</sub> , <1% C <sub>2</sub> H <sub>6</sub> , 20% C <sub>3</sub> H <sub>8</sub> , <1% C <sub>4</sub> H <sub>10</sub> , 13% methanol, 9% ethanol, 20% acetic acid, 2% acetone, 0% HCHO	?	?					Impact depends on catalyst, both <input checked="" type="checkbox"/> and <input type="checkbox"/> conversion and differs from pure packing				
											14% CO, 35% H <sub>2</sub> , <1% C <sub>2</sub> H <sub>4</sub> , <1% C <sub>2</sub> H <sub>6</sub> , 15% C <sub>3</sub> H <sub>8</sub> , 2% C <sub>4</sub> H <sub>10</sub> , 11% methanol, 11% ethanol, 42% acetic acid, 2%	?	?									
DRM/ packed	3	10	40	2.12	9 kHz	1	/	15														



5.9	40	80	?	300 Hz	0.07-1	RT- 600 °C	30	Glass	Beads	2 mm	acetone, 11% HCHO	CH <sub>4</sub> concentration $\square$ = C <sub>2</sub> $\square$ . Influence catalyst only > 200 °C, for CO <sub>2</sub> . Effect glass = Al <sub>2</sub> O <sub>3</sub>	25% CH <sub>4</sub> , 56.1% CO <sub>2</sub>	[75]
											70% CO, 19.5% H <sub>2</sub> , 42.9% C <sub>2</sub> , 15% C <sub>3</sub> , 8.7% C <sub>4</sub>		25% CH <sub>4</sub> , 56.1% CO <sub>2</sub>	
											70% CO, 19.5% H <sub>2</sub> , 42.9% C <sub>2</sub> , 15% C <sub>3</sub> , 8.7% C <sub>4</sub>		25% CH <sub>4</sub> , 56.1% CO <sub>2</sub>	
2	40-240	40	?	5-20 kHz	1	/	60- 360	Ni/γ-Al <sub>2</sub> O <sub>3</sub>	Nano- particles	100 nm	86% CO, 73% H <sub>2</sub>	NiFe <sub>2</sub> O <sub>4</sub> /SiO <sub>2</sub> : conversion and selectivity $\square$ , carbon deposit $\square$	64.6% CH <sub>4</sub> , 58% CO <sub>2</sub>	[65]
								Ni-Fe/γ- Al <sub>2</sub> O <sub>3</sub>	Nano- particles	100 nm	87% CO, 74% H <sub>2</sub>		68.7% CH <sub>4</sub> , 60.5% CO <sub>2</sub>	
								Ni-Fe/SiO <sub>2</sub>	Nano- particles	100 nm	88% CO, 75% H <sub>2</sub>		73.5% CH <sub>4</sub> , 62.7% CO <sub>2</sub>	

2	150	40	?	5-100 kHz	1	/	225	NiFe <sub>2</sub> O <sub>4</sub>	Nano-particles	100 nm	89% CO, 77% H <sub>2</sub>	Packing: conversion <input checked="" type="checkbox"/> selectivity <input checked="" type="checkbox"/>	77.4% CH <sub>4</sub> , 67.1% CO <sub>2</sub> 80% CH <sub>4</sub> , 70.3% CO <sub>2</sub> 65% CH <sub>4</sub> , 52% CO <sub>2</sub> 82% CH <sub>4</sub> , 69% CO <sub>2</sub> 84% CH <sub>4</sub> , 72% CO <sub>2</sub> 88% CH <sub>4</sub> , 78% CO <sub>2</sub>
								NiFe <sub>2</sub> O <sub>4</sub> #SiO <sub>2</sub>	Nano-particles	100 nm	90% CO, 81% H <sub>2</sub>		
								Ni/SiO <sub>2</sub>	?	?	87% CO, 73% H <sub>2</sub>		
								LaNiO <sub>3</sub> /SiO <sub>2</sub>	?	?	89% CO, 79% H <sub>2</sub>		
4.5	50	50	?	30-40 kHz	1	/	60	LaNiO <sub>3</sub>	?	?	90% CO, 81% H <sub>2</sub>	non-packed: filamentary discharge, packed: combination of surface discharges, microdischarges, breakdown voltage and conversion <input checked="" type="checkbox"/>	18% CH <sub>4</sub> , 13% CO <sub>2</sub>
								LaNiO <sub>3</sub> @SiO <sub>2</sub>	?	?	92% CO, 84% H <sub>2</sub>		
								Ni/Al <sub>2</sub> O <sub>3</sub>	Pellets	0.85-5 mm	25% CO, 45% H <sub>2</sub> , 10% C <sub>2</sub> , 5% C <sub>3</sub>		
								Ni/Al <sub>2</sub> O <sub>3</sub>	Pellets	1 mm	35% CO, 56% H <sub>2</sub>		
3.5	1.4-4.8	40	27.2	50 Hz	0.5-2	/	2-7.2	Ni/Al <sub>2</sub> O <sub>3</sub>	Pellets	1 mm	52% CH <sub>4</sub> , 43% CO <sub>2</sub> (38% CH <sub>4</sub> , 23% CO <sub>2</sub> non-packed)		
											Conversion <input checked="" type="checkbox"/> with packing Conversion <input checked="" type="checkbox"/> when ratio <input checked="" type="checkbox"/>		

3	19	16.7-33.3	?	6 kHz	1	130-340 °C	34-68	Al <sub>2</sub> O <sub>3</sub>	?	1-2 mm	19% CO, 24% H <sub>2</sub> , 0.6% C <sub>2</sub> H <sub>2</sub> /C <sub>2</sub> H <sub>4</sub> , 10% C <sub>2</sub> H <sub>6</sub> , 0.3% C <sub>3</sub> H <sub>6</sub> , 6% C <sub>3</sub> H <sub>8</sub> , 1.3% CH <sub>3</sub> OH	Conversion <input checked="" type="checkbox"/> with packing	52% CH <sub>4</sub> , 31% CO <sub>2</sub>
								Fe/Al <sub>2</sub> O <sub>3</sub>	?	1-2 mm	14% CO, 21% H <sub>2</sub> , 1.3% C <sub>2</sub> H <sub>2</sub> /C <sub>2</sub> H <sub>4</sub> , 9% C <sub>2</sub> H <sub>6</sub> , 0.3% C <sub>3</sub> H <sub>6</sub> , 5% C <sub>3</sub> H <sub>8</sub> , 1% CH <sub>3</sub> OH	No effect of T or flow rate, Conversion <input checked="" type="checkbox"/> with packing	46% CH <sub>4</sub> , 20% CO <sub>2</sub>
								zeolite Na Y	?	?	10% CO, 21% H <sub>2</sub> , 1% C <sub>2</sub> H <sub>2</sub> /C <sub>2</sub> H <sub>4</sub> , 6% C <sub>2</sub> H <sub>6</sub> , 0.2% C <sub>3</sub> H <sub>6</sub> , 3% C <sub>3</sub> H <sub>8</sub> , 0% CH <sub>3</sub> OH		49% CH <sub>4</sub> , 19% CO <sub>2</sub>
								zeolite Na ZSM-5	?	?	5% CO, 21% H <sub>2</sub> , 0.1% C <sub>2</sub> H <sub>2</sub> /C <sub>2</sub> H <sub>4</sub> ,	Conversion <input checked="" type="checkbox"/> with packing	65% CH <sub>4</sub> , 40% CO <sub>2</sub>



4	15-60	5-50	?	1-100 kHz	1	325-525 °C	18-720	Ni/ $\gamma$ -Al <sub>2</sub> O <sub>3</sub>	Grains	70-100 mesh	9% C <sub>2</sub> H <sub>6</sub> , 0% C <sub>3</sub> H <sub>6</sub> , 5% C <sub>4</sub> H <sub>6</sub> , 0% CH <sub>3</sub> OH	Conversion <input checked="" type="checkbox"/> with packing (fluidized bed)	48% CH <sub>4</sub> , 40% CO <sub>2</sub>	[69]
3	19	16.7-33.3	?	5.7-6 kHz	1-2	120-290 °C	34-68	Al <sub>2</sub> O <sub>3</sub>	?	1-2 mm	38% CO, 28% H <sub>2</sub> , 11% C <sub>2</sub> , 6% C <sub>3</sub> , 4% C <sub>4</sub> , 2% CH <sub>3</sub> OH	Conversion <input type="checkbox"/> with packing	55% CH <sub>4</sub> , 31% CO <sub>2</sub>	[73]
								Pd/Al <sub>2</sub> O <sub>3</sub>	?	1-2 mm	40% CO, 29% H <sub>2</sub> , 15% C <sub>2</sub> , 5% C <sub>3</sub> , 3% C <sub>4</sub> , 1% CH <sub>3</sub> OH		51% CH <sub>4</sub> , 28% CO <sub>2</sub>	
								Ag/Al <sub>2</sub> O <sub>3</sub>	?	1-2 mm	38% CO, 29% H <sub>2</sub> , 10% C <sub>2</sub> , 5% C <sub>3</sub> , 4% C <sub>4</sub> , 2% CH <sub>3</sub> OH		52% CH <sub>4</sub> , 30% CO <sub>2</sub>	
4.5	10-40	50	16.5	30-40 kHz	1	/	12-48	Quartz wool	?	28% CO, 22% H <sub>2</sub> , 1% C <sub>2</sub> H <sub>2</sub> /C <sub>2</sub> H <sub>4</sub> , 7% C <sub>2</sub> H <sub>6</sub> , 0.5% C <sub>3</sub> H <sub>6</sub>	CH <sub>4</sub> conversion: quartz wool > no packing > Al <sub>2</sub> O <sub>3</sub> > zeolite 3A	30% CH <sub>4</sub> , 12% CO <sub>2</sub>	[76]	

DRM/ packed	2.5	7.5-15	25-200	11.6	50 Hz	0.11-9	/	2 - 36	$\gamma$ -Al <sub>2</sub> O <sub>3</sub>	pellets	500-850 $\mu$ m	4% C <sub>3</sub> H <sub>8</sub> (estimation) 32% CO, 18% H <sub>2</sub> , 2% C <sub>2</sub> H <sub>2</sub> /C <sub>2</sub> H <sub>4</sub> , 8% C <sub>2</sub> H <sub>6</sub> , 0.5% C <sub>3</sub> H <sub>6</sub> , 4% C <sub>3</sub> H <sub>8</sub> (estimation)		23% CH <sub>4</sub> , 8% CO <sub>2</sub>
									zeolite 3A	beads	2 mm	22% CO, 30% H <sub>2</sub> , 19% C <sub>2</sub> H <sub>2</sub> /C <sub>2</sub> H <sub>4</sub> , 8% C <sub>3</sub> H <sub>6</sub> , 1% C <sub>3</sub> H <sub>8</sub> , 6% C <sub>3</sub> H <sub>8</sub> (estimation)		7% CH <sub>4</sub> , 3% CO <sub>2</sub>
									Ni/ $\gamma$ -Al <sub>2</sub> O <sub>3</sub>	?	?	37% CO, 33% H <sub>2</sub> , 22% C <sub>2</sub> H <sub>6</sub>	Ni/ $\gamma$ -Al <sub>2</sub> O <sub>3</sub> and Mn/ $\gamma$ -Al <sub>2</sub> O <sub>3</sub> : CH <sub>4</sub> conversion <input checked="" type="checkbox"/> , yields CO and H <sub>2</sub> <input checked="" type="checkbox"/>	19% CH <sub>4</sub> , 9% CO <sub>2</sub>
								Co/ $\gamma$ -Al <sub>2</sub> O <sub>3</sub>	?	?	42% CO, 43% H <sub>2</sub> , 30% C <sub>2</sub> H <sub>6</sub>		15% CH <sub>4</sub> , 8% CO <sub>2</sub>	
								Cu/ $\gamma$ -Al <sub>2</sub> O <sub>3</sub>	?	?	43% CO, 44% H <sub>2</sub> , 30% C <sub>2</sub> H <sub>6</sub>		14% CH <sub>4</sub> , 8% CO <sub>2</sub>	

									Mn/ $\gamma$ -Al <sub>2</sub> O <sub>6</sub>	?	?	35% CO, 34% H <sub>2</sub> , 24% C <sub>2</sub> H <sub>6</sub>		18% CH <sub>4</sub> , 10% CO <sub>2</sub>	
								BaTiO <sub>3</sub>	Be ads	3 mm	50% CO, 56% H <sub>2</sub>	BaTiO <sub>3</sub> size conversions ▾ =		33% CH <sub>4</sub> , 20% CO <sub>2</sub>	
7.5	46-106	25-100	100	25 kHz	1	110 °C	28- 254	Ni/SiO <sub>2</sub>	Pellets	2-3 mm	56% CO, 54% H <sub>2</sub>	Packing conversions ▾ =		20% CH <sub>4</sub> , 12% CO <sub>2</sub>	[71]
								NiFe/SiO <sub>2</sub>	Pellets	2-3 mm	54% CO, 56% H <sub>2</sub>			28% CH <sub>4</sub> , 15% CO <sub>2</sub>	

## 1.4 AIM OF THIS RESEARCH

In this thesis, we study both CO<sub>2</sub> splitting and DRM. Both reactions will be carried out in a non-packed and a packed bed DBD. As discussed in section 1.3.3, there is still a lack of insight in the combination of a packing and a plasma reactor for these two processes. The aim of this PhD work is to gain more insight in the physical and chemical aspects of the interactions between plasma and packing, studied for both CO<sub>2</sub> splitting and DRM. The approach used in this work, as well as the techniques, materials and methods applied, will be discussed in Chapter 2.

Chapter 3 will go into more depth on the CO<sub>2</sub> splitting reaction, and the influence of different materials and sizes on this process. This chapter will serve as the basis for Chapter 4, where DRM will be discussed, and thus the complexity, but also insight in the underlying mechanisms, is enhanced by adding selectivity. In Chapter 5, the influence of the gap size, the ratio between gap size and bead size, and the residence time will be discussed for DRM for the specific and peculiar case of BaTiO<sub>3</sub> packing material. It will be compared to CO<sub>2</sub> splitting and CH<sub>4</sub> reforming. Finally, a general conclusion for this work will be given, together with a future outlook.

## 2 MATERIALS AND METHODS

---

## 2.1 PLASMA

### 2.1.1 Experimental setup

To study the influence of a dielectric packing in a packed bed DBD reactor, we apply the setup illustrated in Figure 16 and shown in Figure 17. Various packing materials can be inserted in the gas gap. To economize on packing material, only the plasma zone (length of the outer electrode, 10 cm) is filled, and glass wool is placed at both sides just outside of the plasma zone to prevent the packing from moving. A stainless steel rod is used as the inner electrode, with an outer diameter of 8, 10, 12 or 13 mm. A dielectric barrier (tubular reactor) is placed around the inner electrode, consisting of either alumina or quartz. Its inner diameter is 17 mm in both cases, resulting in a gas gap of 4.5, 3.5, 2.5 or 2 mm, respectively. Its outer diameter is 21.8 mm, corresponding to a barrier thickness of 2.4 mm. A stainless steel outer electrode is wrapped around the dielectric barrier.

The inner electrode is grounded, while the outer electrode is powered by a high voltage, supplied by a generator and transformer (AFS GmbH, Germany). The applied voltage is measured with a high voltage probe (Trek P6015A), while a Rogowski coil (Pearson 4100) is used to measure the total current. Moreover, the voltage is measured on an external capacitor (10nF) to obtain the generated charges (Q) in the plasma. Finally, all electrical signals are recorded by an oscilloscope (PicoScope 6402 A).

The temperature inside the reactor cannot be measured in our setup, as it would affect the plasma performance, but IR measurements of the dielectric barrier and the outer electrode were taken. An example is added in the appendix (section 9.1) and is representative for all sizes and materials tested for CO<sub>2</sub> splitting in this work (Chapter 3). The temperature obtained from these measurements is in the order of 419 K, but of course it only provides information for the outer electrode and dielectric barrier. We did not observe a correlation between the results obtained and the temperatures measured.

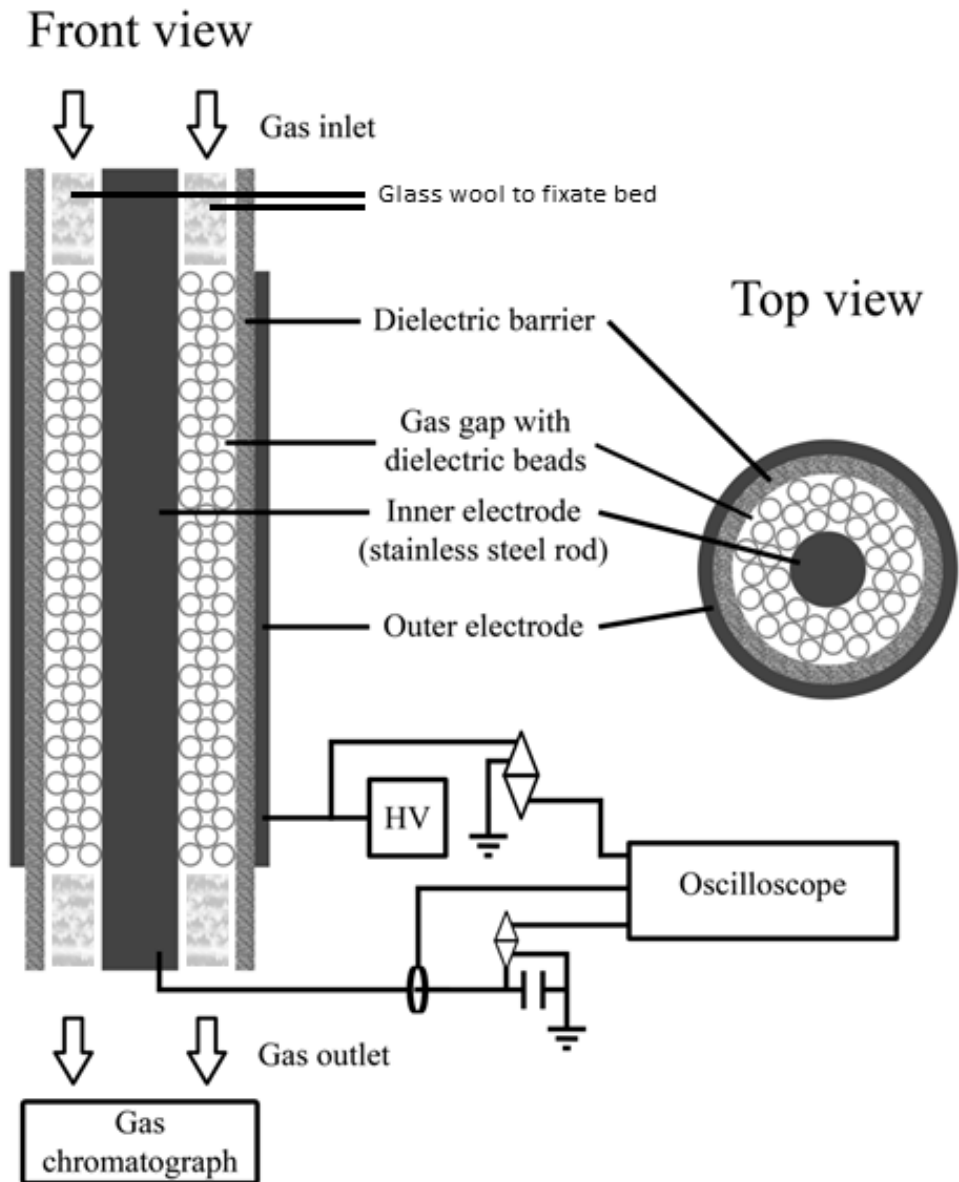
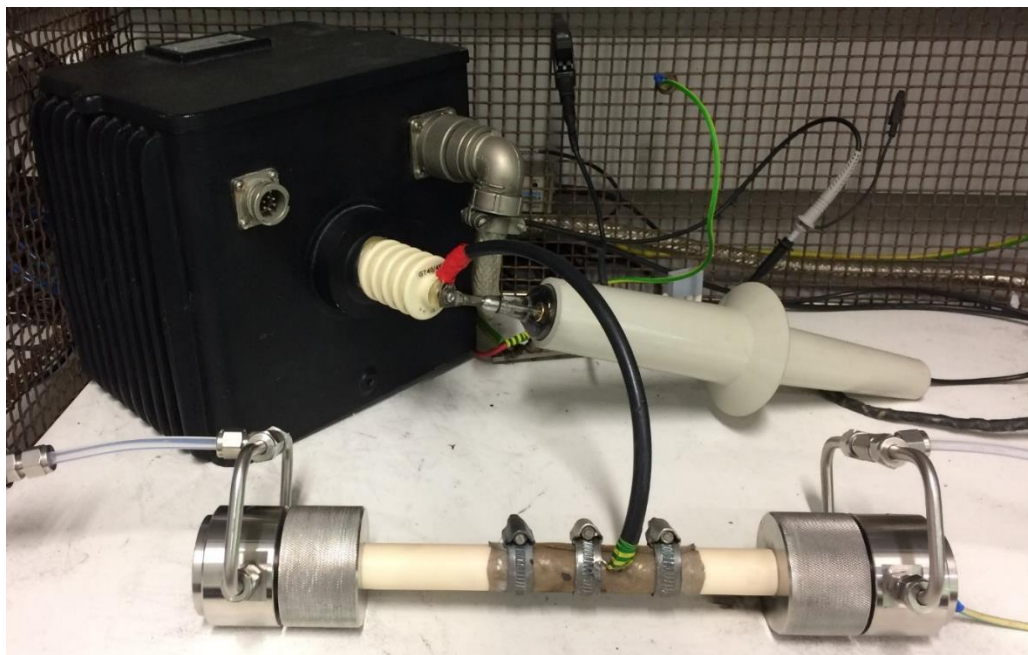


Figure 16: Setup of the packed bed DBD reactor applied in this study (adapted from ref [93]). The packing is illustrated with beads but can also be filled with glass wool, quartz wool or other material shapes.



*Figure 17: Experimental setup applied in this work.*

The input gas flows of CO<sub>2</sub> and CH<sub>4</sub> are controlled by thermal mass flow controllers (Bronkhorst) and the gas at the outlet is analysed by an online gas chromatograph (Trace GC 1310, Interscience). The GC is equipped with a thermal conductivity detector, a flame ionisation detector and four columns: a Molsieve 5A, two RT-Q bonds and a RTX-f column. Figure 18 shows an example of a chromatogram obtained from an experiment with the non-packed reactor at 50 ml/min. It is shown to aid with the estimation of the abundance of the components that were not identified/calibrated in the GC and thus could be the cause for the missing percentages in the carbon, hydrogen (for DRM) and oxygen balance reported in this work.



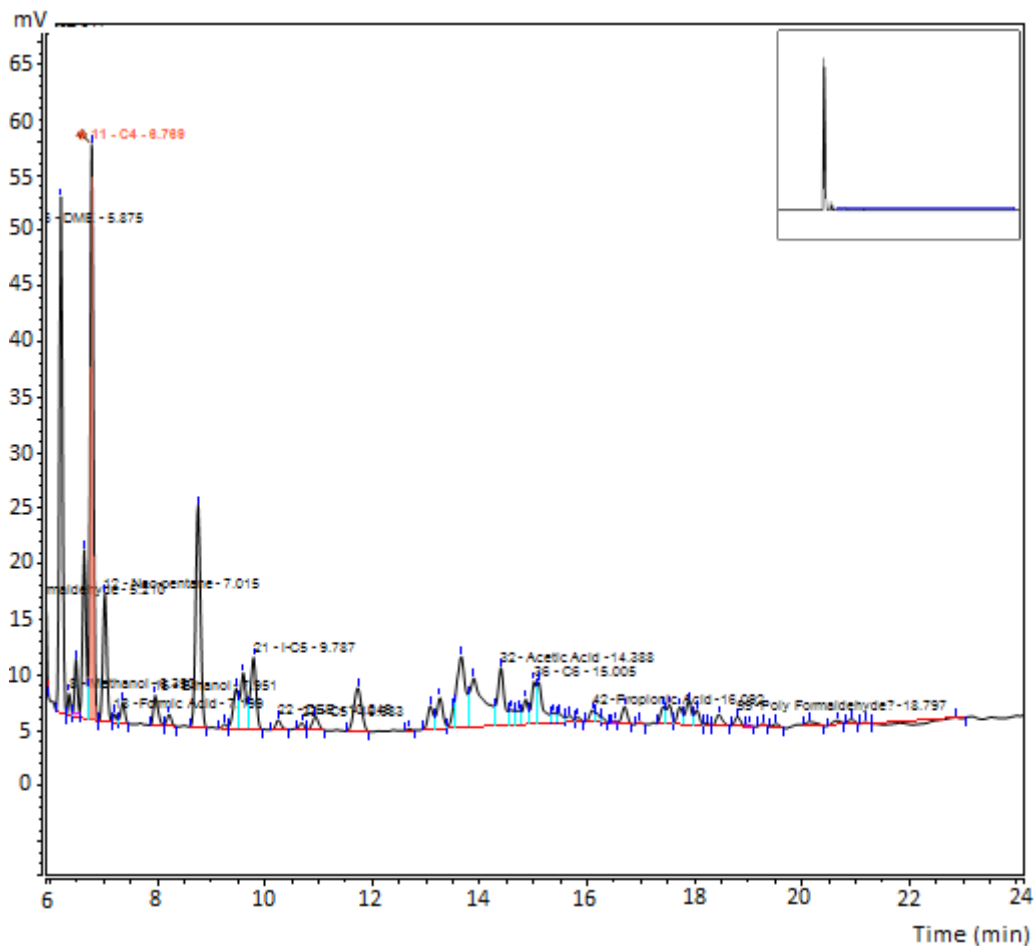


Figure 18: Part of a gas chromatogram obtained in this work, zoomed in on the baseline.

All measurements for the same conditions are repeated three times (to account for the influence of repacking the reactor), and every measurement includes four GC and power measurements to obtain a standard deviation based on 12 measurements of the same condition. Care was taken to pack the reactor reproducibly, with an extra vibrating step, to ensure a dense packing. As can be seen in some figures further in this work, certain results will display large error bars. When this was the case, a Dixon Q test was performed, and no outliers could be rejected. The larger error bars were not material nor parameter dependent, which is why this large uncertainty cannot be explained nor prevented yet.

First, blank measurements of the inlet gas(es) are taken, i.e. without plasma. The amount of CO<sub>2</sub> measured here is defined as CO<sub>2,in</sub>. When CH<sub>4</sub> is (also) present in the inlet gas mixture, the amount after a blank measurement is defined as CH<sub>4,in</sub>. Subsequently, a power of 100 W is applied with a frequency of 23.5 kHz, and after 40 minutes, i.e. when the measured peak-to-peak voltage is more or less constant, GC measurements of CO<sub>2,out</sub> or/and CH<sub>4,out</sub> are taken. Hence, the CO<sub>2</sub> conversion is calculated as follows, based on the moles of CO<sub>2</sub> converted/moles of CO<sub>2</sub> introduced:

$$X_{CO_2} = \frac{CO_{2,in} - CO_{2,out}}{CO_{2,in}} * 100 \% \quad (1)$$

The conversion of CH<sub>4</sub> is calculated as follows:

$$X_{CH_4} = \frac{CH_{4,in} - CH_{4,out}}{CH_{4,in}} * 100 \% \quad (2)$$

The total conversion, in the case of DRM, is calculated by multiplying both conversions with their respective fractions in the inlet gas flow. These formulas (equation 1 and 2) only take the densities of the molecules into consideration, while it is important to also account for the differing velocities of the species at the inlet and the outlet of the reactor (see equation 17 in ref. [94]).

For CO<sub>2</sub> splitting, CO<sub>2</sub> is split into CO and ½ O<sub>2</sub> in this work, without the formation of a substantial amount of other molecules (such as O<sub>3</sub>), and thus every converted CO<sub>2</sub> molecule will give rise to an expansion of the volume by a factor 1.5. As we have a fixed volume sample loop and the GC depressurizes to 1 atm. for each measurement, the actual outlet flow measured is lower than the inlet flow. Hence, the conversion measured by the GC will be lower than the actual conversion. To correct for this, we adapted the equation of ref. [94], based on the mass flow conservation and taking into account a constant reactor tube cross section, to the following formula:

$$X_{GC} = \frac{2X_{CO_2}}{3 - X_{CO_2}} \quad (3)$$

More details about the meaning and use of this correction factor and formula can be found in the work of Pinhão et al. [95]. Based on this real conversion (corrected X<sub>CO<sub>2</sub></sub> = X<sub>GC</sub>), the energy efficiency of the process can be calculated. The following formula is used for this purpose:

$$\eta (\%) = \frac{\Delta H_r \left(\frac{kJ}{mol}\right) * X_{CO_2} (\%)}{SEI \left(\frac{kJ}{L}\right) * 22.4 \left(\frac{L}{mol}\right)} \quad (4)$$

$\Delta H_R$  is the reaction enthalpy of CO<sub>2</sub> splitting (i.e. 283 kJ/mol);  $X_{CO_2}$  is the amount of CO<sub>2</sub> converted, determined from equations (1) and (3); and SEI is the specific energy input in the plasma, defined as:

$$SEI \left(\frac{kJ}{L}\right) = \frac{Plasma\ Power\ (kW)}{Flow\ Rate\ \left(\frac{L}{min}\right)} * 60 \left(\frac{s}{min}\right) \quad (5)$$

This can be converted to a Specific Energy Input (SEI) in eV/molecule via equation 6:

$$SEI \left(\frac{eV}{molecule}\right) = \frac{Power\ (Watt) * 60 \left(\frac{s}{min}\right) * 1000 \left(\frac{mL}{L}\right) * 22.4 \left(\frac{L}{mol}\right) * 6.24 * 10^{18} \left(\frac{eV}{J}\right)}{Flow\ \left(\frac{mL}{min}\right) * 6.22 * 10^{23} \left(\frac{molecule}{mol}\right)} \quad (6)$$

The power in the above formula is the power supplied to the plasma, i.e. the so-called plasma power, as is most common in literature [61,70,96–98]. The applied power is kept fixed at 100 W, as mentioned above, but the actual plasma power can be slightly different for each gas composition, and is obtained by means of the Lissajous figures (see 2.1.2).

For DRM, the number of molecules that is lost depends on the conversion, but also on components that are formed and the product distribution, making it difficult (if not impossible) to take this gas expansion factor into account. Yet it is still important to know that this process plays a role and will thus influence the conversion and selectivities.

For DRM, not only the conversion will be shown in Chapters 4 and 5, but also the carbon (CB), oxygen (OB) and hydrogen (HB) balance. These will be calculated as follows:

$$CB (\%) = \frac{CO_{2,out} + CH_{4,out} + CO + 2 * C_2H_6 + 2 * C_2H_4 + 2 * C_2H_2 + 2 * C_2H_5OH + 2 * C_2H_6O + 3 * C_3H_8 + CH_2O + CH_4O}{CO_{2,in} + CH_{4,in}} \quad (7)$$

$$HB (\%) = \frac{2 * H_2 + 4 * CH_{4,out} + 6 * C_2H_6 + 4 * C_2H_4 + 2 * C_2H_2 + 6 * C_2H_5OH + 6 * C_2H_6O + 8 * C_3H_8 + 2 * CH_2O + 4 * CH_4O}{4 * CH_{4,in}} \quad (8)$$

$$OB (\%) = \frac{2 * CO_{2,out} + CO + C_2H_5OH + C_2H_6O + CH_2O + CH_4O}{2 * CO_{2,in}} \quad (9)$$

The total gas flow rate is in all experiments either 50 ml/min or 192 ml/min. More specifically, for the experiments with packing, the total flow rate is always kept fixed at 50 ml/min, but in the non-packed reactor, experiments are performed both at 50

ml/min (same flow rate) and at 192 ml/min (same residence time as in the packed bed reactor). The reasoning behind this is that inserting a packing in the reactor reduces the reactor volume and thus the residence time at constant flow rate. For different bead sizes, the reduction in reactor volume is constant [99]. When different gap sizes are investigated, the reactor volume is no longer constant and therefore, the residence time changes.

For DRM, the total gas flow rate is the sum of the flow rates for CO<sub>2</sub> and CH<sub>4</sub>, with a 1:1 ratio between the two components.

### 2.1.2 Electrical characterization

Plotting the charge (Q) as a function of the applied voltage (U) gives us a Q-U Lissajous plot (see Figure 19). Combining this with a current profile (see Figure 20), characterises the electrical properties in the plasma. Analysing the Lissajous figures and current profiles is a common method for the investigation of the electrical characteristics in a DBD [76,100–102]. These data are processed and used to calculate the actual plasma power, the average number of discharges, the charge per filament, the minimal voltage, the peak-to-peak voltage and the average current. The average charge per filament is calculated by dividing the dissipated charge in the discharge phase (line DA of the Lissajous figure) by the number of pulses in the discharge phase. The calculation of the number of discharges is done after smoothing the current profile, and calculating the values above a certain threshold, with a certain resolution. Since this is an approximative calculation, the values are prone to error and should be compared with caution.

To ensure a steady state of the plasma, the plasma is first stabilised for 40 minutes, before measuring Lissajous figures and performing GC measurements. The reasoning behind this is explained in section 9.2 ('Plasma Stabilisation') of the Appendix.

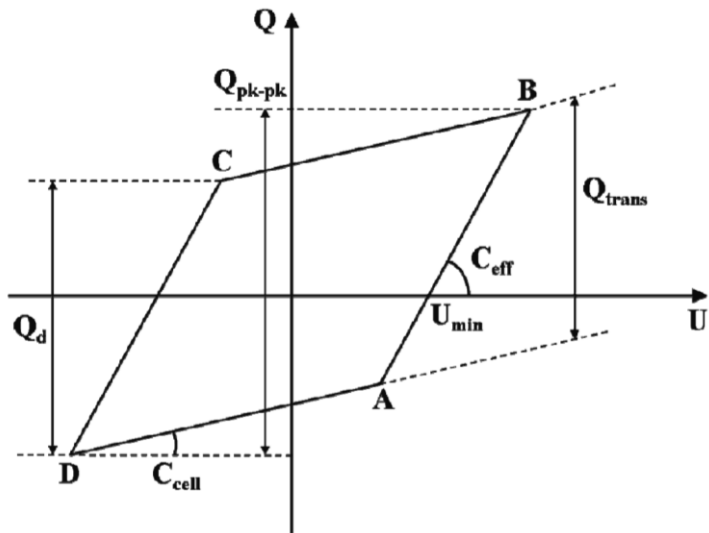


Figure 19: Typical Q-U Lissajous figure for a DBD [72].

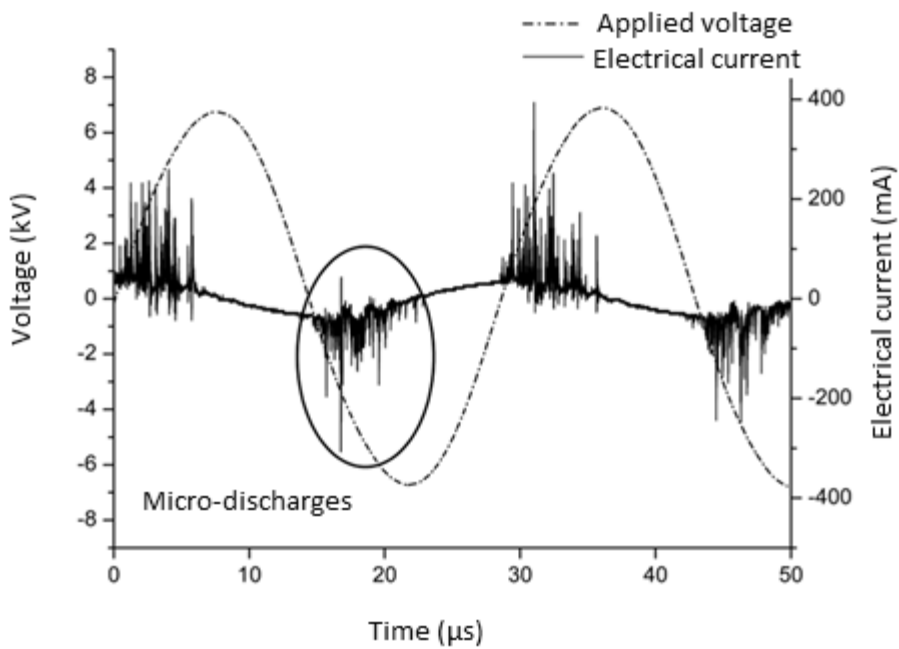


Figure 20: Typical current profile for a DBD, obtained with an oscilloscope [98].

## 2.2 CATALYSIS

### 2.2.1 Packing materials

The packing inserted in the plasma reactor is either glass wool (VWR, Belgium), quartz wool (Quantachrome, Germany) or spherical beads.

Table 6: Physical and chemical characteristics of the packing materials.

	BaTiO <sub>3</sub>	ZrO <sub>2</sub>	SiO <sub>2</sub>	α-Al <sub>2</sub> O <sub>3</sub>	γ-Al <sub>2</sub> O <sub>3</sub>
<b>Molar mass (g/mol)</b>	233.20	123.22	60.08	101.96	101.96
<b>Density (g/cm<sup>3</sup>)</b>	6.02	5.70	2.20	3.89	3.65
<b>Thermal conductivity (W/m.K)<sup>a</sup></b>	2.85	1.70	1.38	28.0 - 35.0	28.0 - 35.0
<b>Thermal expansion coefficient (10<sup>-6</sup>/°C)<sup>a</sup></b>	11.4	12.2	0.550	5.8-8	5.8-8
<b>Specific heat capacity (J/(g.K))<sup>b</sup></b>	0.406	0.456	0.99	0.798	0.850
<b>Band gap (eV)<sup>c</sup></b>	3.2	4.2	8.9	7.0	8.7
<b>Dielectric strength (10<sup>6</sup> V/m)<sup>a</sup></b>	>30.0	5	32.5	8	8
<b>Dielectric constant<sup>a</sup></b>	4000	23.0	3.9	9.00	9.00
<b>Molar heat (J/(mol.K))<sup>a</sup></b>	94.68	56.23	59.64	81.38	108.7
<b>BET specific surface (m<sup>2</sup>/g)<sup>d</sup></b>	0.8	0	0.5	0.08	336
<b>Total open pore volume (mm<sup>3</sup>/g)<sup>e</sup></b>	158.0	≈0	≈0	8.47	500
<b>Pore size (μm)<sup>e</sup></b>	0.87	≈0	≈0	0.080	0.54
<b>Surface roughness (nm)<sup>f</sup></b>	590±15	84±1	82±3	150±4	3600 ± 460

a: Taken from [103–112].

b: Calculated from the molar heat and the molar mass.

c: Obtained from UV-vis DR spectra, for milled beads (Figure 41, Figure 42, Figure 43).

d: Obtained from nitrogen sorption (Figure 44, Figure 45, Figure 46, Figure 47, Figure 48).

e: Obtained from Hg-porosimetry, for 1.6-1.8 mm beads (Figure 49, Figure 50, Figure 51, Figure 52, Figure 53).

f: Obtained from profilometry, for 2.0-2.24 mm beads in collaboration with ULB (Figure 73-Figure 77) [80].

The SiO<sub>2</sub> (soda lime glass) and ZrO<sub>2</sub> (Y stabilised) beads are purchased at SiLiBeads (Germany). The BaTiO<sub>3</sub> beads are supplied by Catal (UK) and the γ-Al<sub>2</sub>O<sub>3</sub> beads by Caldic, BASF. The α-Al<sub>2</sub>O<sub>3</sub> beads are made in-house at VITO, according to the method described in 2.2.2. For the five different spherical materials, some of their typical physical and chemical characteristics are mentioned in Table 6 (glass wool and quartz wool have the same characteristics as SiO<sub>2</sub>, aside from surface roughness, BET and porosity).

### 2.2.2 Drip casting

To warrant high sphericity of the α-Al<sub>2</sub>O<sub>3</sub> beads in combination with a narrow and controlled size distribution in the ranges applied in this work, α-Al<sub>2</sub>O<sub>3</sub> beads were produced via a controlled shaping process. The shaping process was done via vibrational droplet coagulation with a Spheronisator M from Brace GmbH (Germany). A schematic overview of the setup is shown in Figure 21.

The synthesis procedure is based on a recently developed method using alginate based droplet coagulation to shape ceramic α-Al<sub>2</sub>O<sub>3</sub> particles [113].

The ceramic suspension is made of sodium alginate (0.53 %), water (49.38 %), Darvan C (a dispersant, 0.23 %) and Al<sub>2</sub>O<sub>3</sub> powder (49.86 %, α-Al<sub>2</sub>O<sub>3</sub> A16 SG purchased from Almatix with a d<sub>50</sub> of 0.5 μm and specific surface area of 9 m<sup>2</sup>/g.). The coagulation bath contains a 4 wt. % CaCl<sub>2</sub> aqueous solution and isopropanol is, if needed, added to lower the surface tension. After formation, thermal treatment is performed: drying at 100 °C for 4h followed by calcination and sintering. All organic additives are thus removed. Sinter procedure: room temperature to 600 °C at a rate of 120 °C/h, holding at 600 °C for 1h, with subsequent heating to 1490 °C at a rate of 180 °C/h and additional heating to 1540 °C at a rate of 60 °C/h, holding it again at 1540 °C for 1h and finally cooling down at a rate of 120 °C/h.

The final characteristics of the α-Al<sub>2</sub>O<sub>3</sub> beads (and 9.2 % CaO.6Al<sub>2</sub>O<sub>3</sub>) are a diameter of 1.4, 1.7 and 2.1 mm, obtained by using a nozzle of 0.9 mm, 0.7 mm or 1.2 mm, respectively.

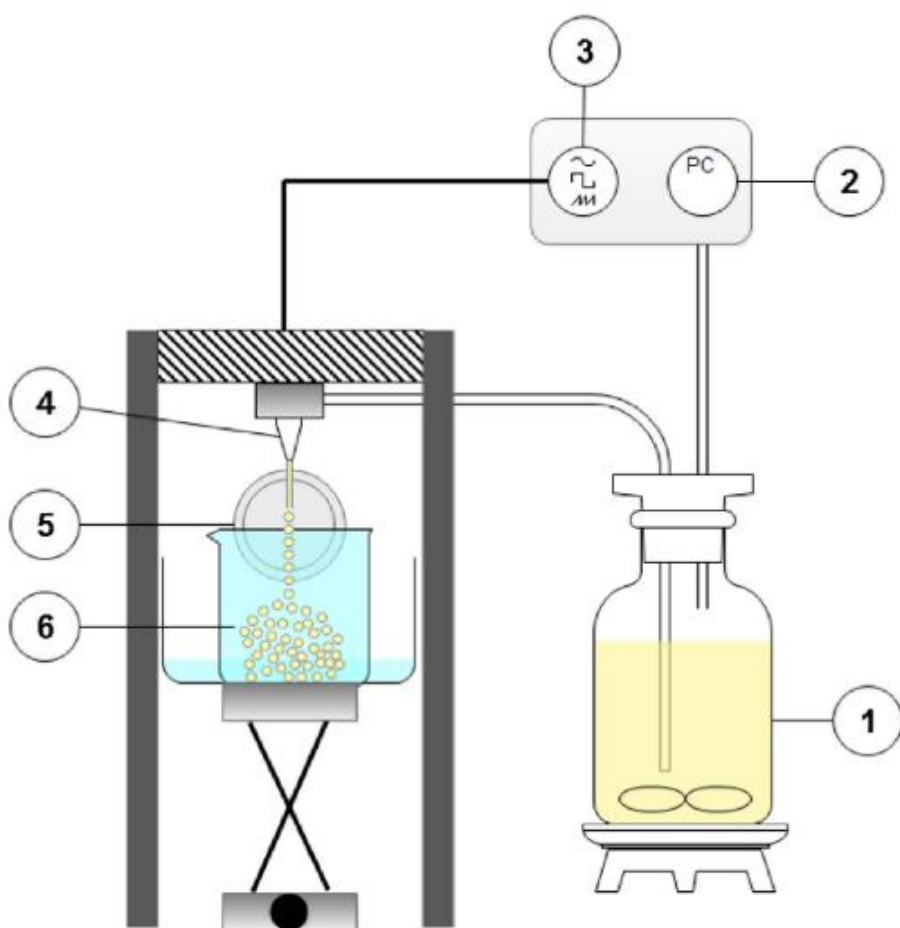


Figure 21: Schematic representation of the drip casting setup. 1) Feed vessel with magnetic stirrer; 2) air pressure controller; 3) Vibration generator with frequency and amplitude control; 4) nozzle; 5) stroboscopic lamp; 6) coagulation bath [113].

The open porosity of the beads was measured by Mercury Intrusion Porosimetry (Pascal 140, ThermoScientific, USA), which measures the pore size distribution and the pore volume [114]. The surface area was determined with  $N_2$ -sorption (Quantachrome QUADRASORB SI, USA), after degassing the samples at 150 °C for 16 h under high vacuum. The surface roughness was determined with profilometry, for the 2.0-2.24 mm beads, and a Brücker Dektak XT stylus profiler was used for the 3D mappings. It was equipped with a 2  $\mu$ m radius stylus and was controlled and analyzed with the Vision 64



software. The scans were performed on a 300 x 300  $\mu\text{m}$  square with a stylus strength of 0.5 mg.

### 2.2.3 Characterisation methods

The material characteristics of the different packing materials can influence the different aspects of the results obtained in this work, i.e. conversion, energy-efficiency and selectivity. Moreover, the study of these characteristics can provide insight on how the plasma interacts with the catalyst and how the plasma can alter the catalyst surface. All packing materials are studied with UV-DR, nitrogen sorption, Hg-porosimetry, SEM-EDX, Raman, TGA and profilometry. The specifics of the equipment are listed in Table 7 and the results are shown in the appendix.

*Table 7: Specifics of the equipment for all characterization techniques.*

UV-DR	Thermo-electron evolution 500 UV-VIS spectrometer, using a Thermo-electron RSA UC40 Diffuse Reflectance cell
N <sub>2</sub> -sorption	Quantachrome Autosorb Degasser and Quantachrome Quadrasorb SI
Hg-porosimetry	Mercury Intrusion Porosimetry (Pascal 140, Thermo Scientific, USA)
SEM-EDX	Quanta 250 FEG ESEM (high-vacuum)
Raman	Horiba Xplora Plus micro-Raman, 10x enlarged, 532 nm wavelength laser
TGA	Mettler Toledo TGA/SDTA851
Profilometry	Brücker Dektak XT stylus profiler

When aiming for an improved understanding of plasma catalysis, in-situ techniques could be used as well, e.g. in-situ Raman and IR spectroscopy (for the in-situ study of the material surface under working conditions) [115], molecular beam mass spectrometry (to measure the concentration profiles of radical as well as stable species) [111], optical emission spectroscopy (to determine the elements in the sample quantitatively, although this is difficult for product mixtures with many components as

is the case in this work [115]) and DRIFTS-MS (to measure changes in the relative height of vibrational lines of CO<sub>2</sub> and CO on the surfaces of potential catalysts [115]).

### 3 STUDY OF CO<sub>2</sub> SPLITTING: UNDERSTANDING THE FUNDAMENTALS OF PLASMA CATALYSIS

---

This Chapter is published as:

I. Michielsen, Y. Uytendhouwen, J. Pype, B. Michielsen, J. Mertens, F. Reniers, V. Meynen, A. Bogaerts, CO<sub>2</sub> dissociation in a packed bed DBD reactor: First steps towards a better understanding of plasma catalysis, Chem. Eng. J. 326 (2017) 477–488.  
Doi:10.1016/j.cej.2017.05.177

### 3.1 STATE OF THE ART

Great efforts in research towards an energy efficient conversion of CO<sub>2</sub> in a non-packed DBD reactor, were already made, as can be seen in Table 4. The highest value obtained so far for CO<sub>2</sub> splitting in CO and O<sub>2</sub> is 50 % conversion, with 2.6 % energy efficiency. By altering the conditions (lower SEI), the energy efficiency can reach 11.1 %, but this corresponds to a drop in the conversion to only 7.5 % [116].

To improve the energy efficiency, product selectivity and/or yield, a catalytic material can be added to the plasma reactor [54,89,117,118]. For instance, it was demonstrated for pure CO<sub>2</sub> splitting that the introduction of a dielectric packing into a DBD plasma reactor can enhance both the CO<sub>2</sub> conversion and energy efficiency up to a factor 1.9 and 2.2, respectively, compared to a non-packed DBD reactor [70,93,119]. Another study suggests that the conversion and energy efficiency double for DRM when adding a Ni/Al<sub>2</sub>O<sub>3</sub> catalyst. Indeed, introducing a packing into a DBD can have multiple effects on the conversion and energy efficiency, by enhancing the electric field, changing the discharge type, altering the reactant concentration, etc. [53].

Other studies on CO<sub>2</sub> splitting were performed in packed bed DBD reactors with Ni, Ag or Pd catalysts, coated on an Al<sub>2</sub>O<sub>3</sub> support [72,73,77,120], quartz wool, or zeolite 3A [76]. Comparison between the various experiments, in order to draw conclusions, is not straightforward, because of the difference in physical appearance between quartz wool, Al<sub>2</sub>O<sub>3</sub> pellets of 500-850 μm and zeolite 3A beads of 2 mm, and thus, the effect is most likely not only correlated to one parameter (or one reactor configuration). In other papers [121,122], only one type of support was studied, therefore only investigating the enhancement of adding a catalytic element and neglecting the effect of the support. According to previous work, quartz wool also improves the conversion of plasma-based DRM in a DBD with two quartz dielectric barriers [76], and enhances the conversion of CH<sub>4</sub> and the yield of H<sub>2</sub> due to the physical properties of the discharge. A higher intensity of microdischarge filaments [76] and a change in discharge type from

microdischarges to surface discharges on the quartz wool have been reported as reasons for these improved conversions [78].

Another important characteristic, as demonstrated by Van Laer and Bogaerts (both through modelling and experiments for a  $ZrO_2$  packing), is the catalyst/packing size. Packing beads should have a diameter of at least  $1/3$  of the gap size to enhance the conversion and energy efficiency of  $CO_2$  splitting [93], with even a possible negative effect of very small beads, since the packing lowers the residence time. When the latter effect is larger than the positive effect due to electric field enhancement, it will eventually reduce the conversion [119].

Previous work also reported that adding a packing inside the gap reduces the available discharge volume, which limits the possible trajectory of the filamentary microdischarges. Therefore, only weak filaments can be generated in the voids between beads and between beads and a dielectric barrier, which has a negative effect on the conversion and energy efficiency, as was demonstrated for a  $Ni/Al_2O_3$  packing material. The determining factor for the generation of these filaments is stated to be the distance between the beads or the beads and the dielectric barrier [72].

Next to the material of the catalyst/packing and the bead size, also the material properties of the dielectric barrier affect the interaction between the beads and the dielectric. The influence of the dielectric barrier material itself [123], being the reactor tube, was demonstrated for  $Ca_{0.7}Sr_{0.3}TiO_3$  with 0.5 wt.%  $Li_2Si_2O_5$ ,  $Al_2O_3$  and silica glass ( $SiO_2$ ), where the  $CO_2$  conversion was reported to decrease in this order. However, this research was performed for a non-packed DBD, so no interaction with a packing could be studied here [124,125].

Moreover, various reports indicate that the conversion and energy efficiency also depend on the morphology, dielectric properties and chemical activity (e.g. acid-base properties) of the packing material, which was seen by Yu et al [91] and Duan et al [126] in their studies of  $CO_2$  decomposition on materials such as quartz, alumina, CaO and MgO. Other materials have been studied as well, like  $BaTiO_3$  and  $ZrO_2$ , which have been found to improve the conversion and energy efficiency in a packed bed DBD reactor for

CO<sub>2</sub> splitting. However, these experiments were performed for only one dielectric barrier material [91,126]. Therefore, they cannot be simply combined in a general conclusion towards the effect of dielectric packing and dielectric barrier material for the splitting of CO<sub>2</sub>.

Although several experimental studies have been performed to better understand and optimise plasma catalysis, as outlined above, the interactions between the plasma and the catalyst/packing are still poorly understood [72,73,76,77,120–122,127–130]. The most important element that is limiting this understanding and further progress is the fact that no distinction can be made between the chemical and physical effects that may cause the synergy between plasma and catalyst. Most works combine a plasma with a commercial catalyst, which is a catalytic active element deposited on a support and sometimes also containing binders and promoters [72,73,76,77,118,120–122,129,131–138].

In the present study, we thus investigate the influence of specific packing material (without catalytic activation, although we cannot exclude intrinsic catalytic activity of the support material itself) and reactor properties, as well as reactor/bead configuration, on the conversion and energy efficiency of CO<sub>2</sub> splitting in a packed bed DBD reactor. More specifically, we focus our study on the interaction between (different types of) dielectric barriers (for different materials) and the physicochemical packing properties (size and chemical composition of the packing beads).

The packing materials consists of glass wool, quartz wool and spherical beads of SiO<sub>2</sub>, ZrO<sub>2</sub>,  $\alpha$ -Al<sub>2</sub>O<sub>3</sub> and BaTiO<sub>3</sub> with different controlled sizes. The dielectric barrier material consists of quartz and alumina. Although we cannot study all material combinations, a selection has been made based on diverging material properties with an initial focus on dielectric constant, and valuable insights in these combined effects are revealed.

A summary of the experimental parameters used in this chapter is shown in Table 8.

Table 8: Different parameters studied, as well as their variations.

Parameters studied	Variations			
Packing morphology	Glass wool	Quartz wool	Dielectric beads	
Gap size (mm)	2	2.5	3.5	4.5
Bead size for fixed bead/gap size ratio ( $\pm 0.6$ ) experiments (mm) (only BaTiO <sub>3</sub> beads)	1.18-1.25	1.4-1.6	2.0-2.24	
Dielectric barrier material	Quartz	Alumina		
Dielectric bead material	SiO <sub>2</sub>	ZrO <sub>2</sub>	$\alpha$ -Al <sub>2</sub> O <sub>3</sub>	BaTiO <sub>3</sub>
Bead size (mm) for the different materials, at fixed gap size of 4.5 mm	1.25-1.4	1.6-1.8	2.0-2.24	

## 3.2 RESULTS AND DISCUSSION

### 3.2.1 Effect of bead material and bead size

#### 3.2.1.1 General results

The influences of bead material (SiO<sub>2</sub>, ZrO<sub>2</sub>,  $\alpha$ -Al<sub>2</sub>O<sub>3</sub> and BaTiO<sub>3</sub>) and bead size (ranges of 1.25-1.4, 1.6-1.8 and 2.0-2.24 mm diameter) are investigated by comparing with the conversion and energy efficiency in the non-packed reactor (Figure 22).

The first observation to be made is that BaTiO<sub>3</sub>, for the three different bead sizes, yields a higher conversion than the non-packed reactor for the same flow rate. The second is that the largest beads of  $\alpha$ -Al<sub>2</sub>O<sub>3</sub> yield a higher conversion than the non-packed reactor. Thus, in these cases, the positive contribution of the packing [51] compensates for the lower residence time. For SiO<sub>2</sub> and ZrO<sub>2</sub>, as well as for the smaller beads of  $\alpha$ -Al<sub>2</sub>O<sub>3</sub>, the CO<sub>2</sub> conversion is lower than in the non-packed reactor, illustrating that the packing effect does not compensate here for the lower residence time. When comparing this at the same residence time (i.e. 5.5 s corresponding to 192 ml/min for the non-packed reactor),  $\alpha$ -Al<sub>2</sub>O<sub>3</sub> also systematically yields higher conversions, and in some cases, the

conversion with  $\text{ZrO}_2$  and  $\text{SiO}_2$  beads is slightly higher as well. The highest values obtained are close to 20 % conversion for the  $\alpha\text{-Al}_2\text{O}_3$  and  $\text{BaTiO}_3$  beads with the largest size.

For the energy efficiency (Figure 22 (b)), the same results are obtained as for the conversion when comparing at equal flow rate. Only a higher energy efficiency is obtained for  $\text{BaTiO}_3$ , for the three different bead sizes, as well as for the largest beads of  $\alpha\text{-Al}_2\text{O}_3$ . This is logical since the flow rate is part of the formula for calculating the energy efficiency out of the conversion. When comparing with the non-packed reactor at the higher flow rate of 192 ml/min (and thus the same residence time of 5.52 s), none of the packed bed results surmounts the energy efficiency of the non-packed reactor, as the higher flow rate yields a lower SEI, compensating for the lower conversion in the non-packed reactor, overall resulting in a higher energy efficiency. Nevertheless, for the largest bead sizes, both  $\alpha\text{-Al}_2\text{O}_3$  and  $\text{BaTiO}_3$  have a similar and even slightly higher energy efficiency (3.5 %) than the non-packed reactor at equal residence time (and thus higher flow rate), but, at the same time, they have a four times higher conversion, as is obvious from Figure 22(a). This conversion and energy efficiency is roughly a factor two higher than in the non-packed reactor with the same flow rate. This coincides well with values reported in literature and is even slightly better. Indeed, in previous work from our group, the  $\text{CO}_2$  conversion and energy efficiency were simultaneously enhanced by up to a factor 1.9 and 2.2, respectively, for  $\text{ZrO}_2$  beads, compared to the values in a non-packed DBD reactor at the same flow rate [93,119]. Likewise, the conversion and energy efficiency for DRM were reported to double when adding a  $\text{Ni/Al}_2\text{O}_3$  catalyst [79] (ratio gap/packing size is 10), while we observe that adding  $\alpha\text{-Al}_2\text{O}_3$  alone can already almost double the  $\text{CO}_2$  conversion and energy efficiency. This means that the combination of plasma and these packing materials, with or without further catalytic activation, is very promising for improving the  $\text{CO}_2$  conversion. Moreover, it emphasizes the importance of studying the properties-activity correlation of the packing materials itself (both chemical and structural properties), prior to further catalytic activation, in terms of improved



conversion and energy efficiency, to identify the real impact of the catalytic element itself.

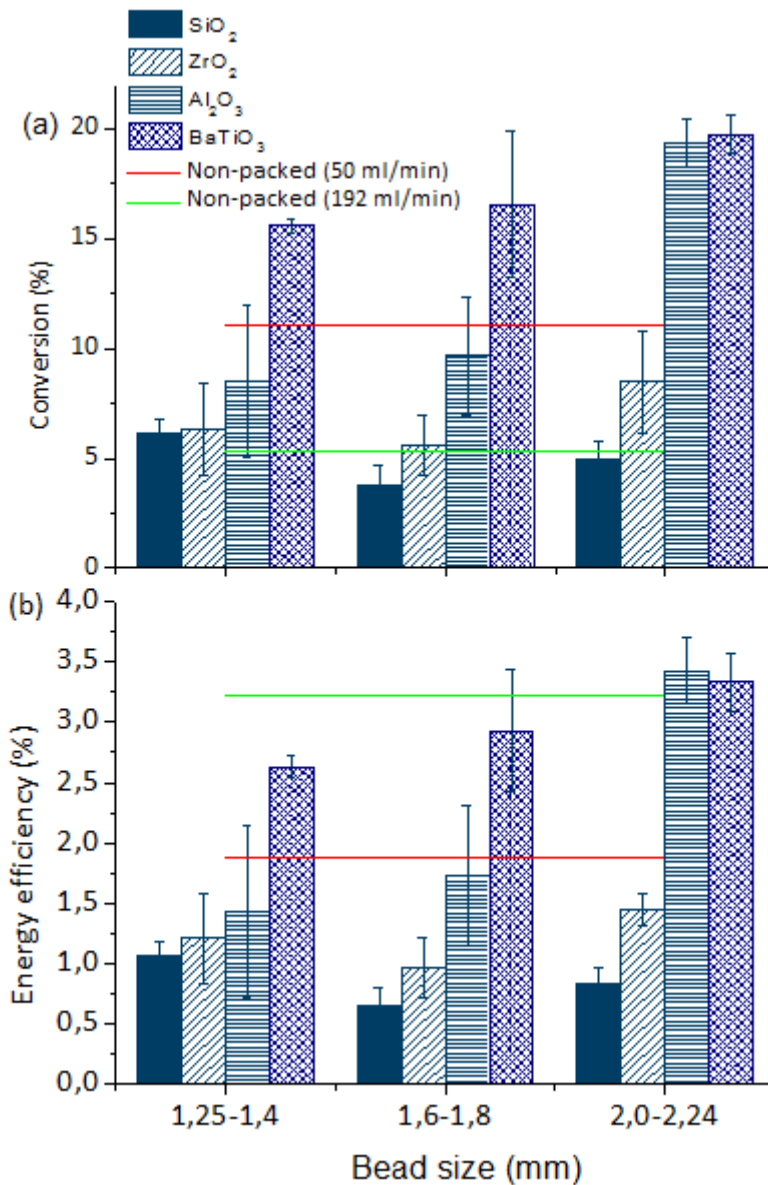


Figure 22: Conversion (a) and energy efficiency (b) as a function of bead size (diameter) for different bead materials, for an alumina dielectric barrier, 4,5 mm gap, stainless steel outer electrode, 23.5 kHz, at 50 ml/min gas flow rate, and 100 Watt power. The error bars are calculated based on 12 GC measurements. A comparison is also made with the results for a non-packed reactor (i.e. without packing), both at the same flow rate (50 ml/min) and the same residence time as in the packed bed reactor (i.e. 5.52 sec, corresponding to a flow rate of 192 ml/min).

Table 9: Electrical characterisation as a function of bead size (diameter) for different bead materials, for an alumina dielectric barrier, 4.5 mm gap, stainless steel outer electrode, 23.5 kHz, at 50 ml/min gas flow rate, and 100 Watt power. A comparison is also made with the results for a non-packed reactor (i.e. without packing), both at the same flow rate (50 ml/min) and the same residence time as in the packed bed reactor (i.e. 5.52 sec, corresponding to a flow rate of 192 ml/min).

Conditions		Plasma Power (W)	$U_{bur}$ (kV)	$U_{pp}$ (kV)	Average charge per filament (nC)	Number of discharges	$I_{RMS}$ (mA)
Non-packed reactor	50 ml/min	61.25	3.68	15.36	210.59	2.58	27.51
	192 ml/min	66.27	4.15	15.32	43641.74	8.85	27.89
SiO <sub>2</sub>	1.25 - 1.4 mm	59.69	2.85	12.87	5.24	85.28	34.49
	1.6 - 1.8 mm	60.64	2.69	12.40	5.01	84.53	36.19
	2.0 - 2.24 mm	61.67	2.50	15.04	4.10	108.40	34.67
ZrO <sub>2</sub>	1.25 - 1.4 mm	54.25	1.92	14.17	4.48	115.60	44.54
	1.6 - 1.8 mm	60.00	2.09	11.81	4.88	98.11	45.50
	2.0 - 2.24 mm	61.19	2.40	11.67	4.58	113.10	42.12
$\alpha$ -Al <sub>2</sub> O <sub>3</sub>	1.25 - 1.4 mm	62.66	2.96	15.65	2131.74	141.61	35.45
	1.6 - 1.8 mm	59.06	2.78	16.51	3719.08	132.75	37.11
	2.0 - 2.24 mm	58.99	2.75	16.57	3511.43	138.98	38.14
BaTiO <sub>3</sub>	1.25 - 1.4 mm	61.85	1.98	13.87	4.78	149.89	53.76
	1.6 - 1.8 mm	58.65	1.99	12.86	5.01	143.42	53.05
	2.0 - 2.24 mm	61.85	2.08	13.14	4.41	148.00	51.42

The electrical characteristics for the experimental results shown in Figure 22 are given in Table 9, but they do not reveal clear trends that can explain the observed differences in conversion and/or energy efficiency.

### 3.2.1.2 Effect of the material characteristics

To better understand the differences induced by the various materials, we looked at different material characteristics that might be correlated to their performance (Table 10). A first important observation is that none of the packing materials introduced in the reactor showed coking during the plasma experiments, which was confirmed with TGA measurements. The power introduced in the plasma reactor for the different packing materials, at a constant applied power of 100 W, is also mentioned in the table, as it is used to calculate the energy efficiency. If the plasma power for a certain packing

material would be much higher for the same applied power, it could lead to a higher CO<sub>2</sub> conversion. However, as is clear from Table 10, the plasma power is very similar for the four different packing materials. The differences in plasma power with varying bead size are represented by the error bars.

Table 10 also shows the breakdown voltage as a function of the bead material. A higher dielectric constant should give rise to a higher electric field and thus a lower breakdown voltage. However, there is a plateau in increasing electric field with an increasing dielectric constant [139], and therefore also in decreasing breakdown voltage. Since there is also an experimental error on the breakdown voltages measured, this can explain why e.g. the breakdown voltage of ZrO<sub>2</sub> is lower than the one of BaTiO<sub>3</sub>.

The results of Figure 22 show a general trend (although some error bars overlap), with SiO<sub>2</sub> consistently yielding the lowest conversion and energy efficiency, followed by ZrO<sub>2</sub>, α-Al<sub>2</sub>O<sub>3</sub> and then BaTiO<sub>3</sub>, inducing the highest conversion and energy efficiency. Therefore, the materials are listed in this order in the table. Important to note is that the relationship of size and its impact on conversion is not linear for any of the materials, nor is the correlation similar for the different materials, indicating that divergent and/or multiple interplaying mechanisms/properties are at the origin of these changes.

*Table 10: Electrical characteristics of the various beads used in this study, determined by analysing the Lissajous figures.*

	SiO <sub>2</sub>	ZrO <sub>2</sub>	α-Al <sub>2</sub> O <sub>3</sub>	BaTiO <sub>3</sub>
Dielectric constant [57,111]	3.9	25	9.1	4000
Plasma power (Watt)	61±1	57±5	60±4	61±3
Breakdown voltage (kV)	1.47	0.82	1.84	0.97

As mentioned in section 3.1, the effect of the packing is usually correlated to the enhanced electric field at the contact points, due to polarization of the beads [93]. Hence, based on this, one would expect to see an increasing conversion and energy efficiency upon rising dielectric constant of the beads, as the latter typically gives rise to more pronounced electric field enhancements and higher electron temperatures

[57]. As can be seen from Table 10, this correlation is only partially true for our results. Indeed, the conversion rises from  $\text{SiO}_2$  ( $\epsilon \sim 3.9$ ) to  $\text{BaTiO}_3$  ( $\epsilon \sim 4000$ ), but the results for  $\text{ZrO}_2$  and  $\alpha\text{-Al}_2\text{O}_3$  do not follow this trend. Moreover, their size dependence is not the same. Even at the largest size,  $\alpha\text{-Al}_2\text{O}_3$  has the same conversion as  $\text{BaTiO}_3$  even though the dielectric constant is much lower.

Van Laer et al. investigated both the influence of the bead size and the dielectric constant by modelling a helium discharge in a packed bed DBD reactor [139]. The modelling results illustrate that the dielectric constant of the beads influences the plasma density in the gap, the electric current profile, the electric field strength and the electron temperature, irrespective of the bead size.

Most importantly, upon increasing the dielectric constant, the time-averaged electric field strength is enhanced, which leads to a higher electron temperature, but a lower electron density, because the electrons get lost more easily at the walls. This will lead to a shift from full gap discharge to localized discharges upon rising dielectric constant of the beads. Moreover, at larger bead sizes, the shift from full gap discharge to localized discharges will occur at a higher dielectric constant, which can be explained through the larger voids in between the larger beads.

In this work, the highest conversion and energy efficiency were obtained with the largest  $\text{BaTiO}_3$  beads. In accordance with the modelling results obtained by Van Laer et al., the electric field is enhanced upon increasing the dielectric constant, but will not be enhanced further upon increasing bead size of  $\text{BaTiO}_3$ . On the other hand, larger beads will result in a higher electron density in the plasma. Therefore, the combination of a high dielectric constant and a large bead size will lead to a stronger electric field and the highest electron density, thus increasing the conversion and energy efficiency [139]. This electric field enhancement is also correlated to the surface roughness, also mentioned in Table 6. Although the increase in surface roughness appears in the same order as the increase in conversion and energy efficiency, there is no linear trend visible. Therefore, there must be other material characteristics that can influence the

conversion and energy efficiency, like surface acidity, surface area, specific and molar heat capacity, total open pore volume and pore size, or others (Table 6) [56].

There is no correlation between the increase in conversion and energy efficiency with the molar or specific heat capacity. Since we add the same volume of beads to each experiment, and thus the weight and number of moles differ, this explains the fact that there is no correlation.

Another characteristic that might play a role are the structural properties of the beads. There are three different characteristics that define the beads: pores, edges through porosity and surface roughness. In general, the electric field may be enhanced by some form of roughness or geometric distortion in the reactor, and this enhancement of the electric field strength can cause a higher conversion and energy efficiency [53].

The first two characteristics both correlate to the porosity of the beads. The porosity of  $\alpha\text{-Al}_2\text{O}_3$  is created in the manufacturing process, since all beads here are sintered at 1540 °C, creating minor porosities in the  $\alpha\text{-Al}_2\text{O}_3$  beads. As the other beads are purchased, we cannot conclude on the manufacturing of the beads and thus Hg porosimetry was conducted.  $\text{SiO}_2$  and  $\text{ZrO}_2$  have a very low porosity, whereas  $\alpha\text{-Al}_2\text{O}_3$  and  $\text{BaTiO}_3$  have a higher porosity (Table 6). The pore size distributions for  $\alpha\text{-Al}_2\text{O}_3$  and  $\text{BaTiO}_3$  are illustrated in Figure 23. The results indicate that the  $\alpha\text{-Al}_2\text{O}_3$  beads have a pore size distribution with an average pore diameter of 0.08  $\mu\text{m}$ , whereas the  $\text{BaTiO}_3$  beads mainly have pores with a diameter of 0.87  $\mu\text{m}$ , which is more than tenfold the value of the  $\alpha\text{-Al}_2\text{O}_3$  beads. According to model calculations (for a helium plasma) carried out in our group, a pore diameter of 0.87  $\mu\text{m}$  is too small for plasma generation inside the pores [140], although streamers might still be able to penetrate [141], and especially the edges induced by the porosity can still enhance the electric field and thus influence the results for conversion and energy efficiency. For air (and probably also  $\text{CO}_2$ , plasma generation is possible when the pore diameter is larger than 0.60  $\mu\text{m}$  [59]. Although multiple parameters will be different and could be the underlying reason, these differences might contribute to the rise in  $\text{CO}_2$  conversion and energy efficiency for both  $\alpha\text{-Al}_2\text{O}_3$  as well as  $\text{BaTiO}_3$ .

It is clear from the above results that the conversion and energy efficiency are not only correlated to the dielectric constant of the packing beads, but also to other material properties. However, in order to draw final conclusions on the exact influence of the material properties, further thorough research needs to be conducted in a systematic way, based on materials with very controlled material properties, which can only be obtained by careful manufacturing of the beads instead of using commercial beads. This controlled manufacturing process is also not straightforward [113], and requires more investigation.

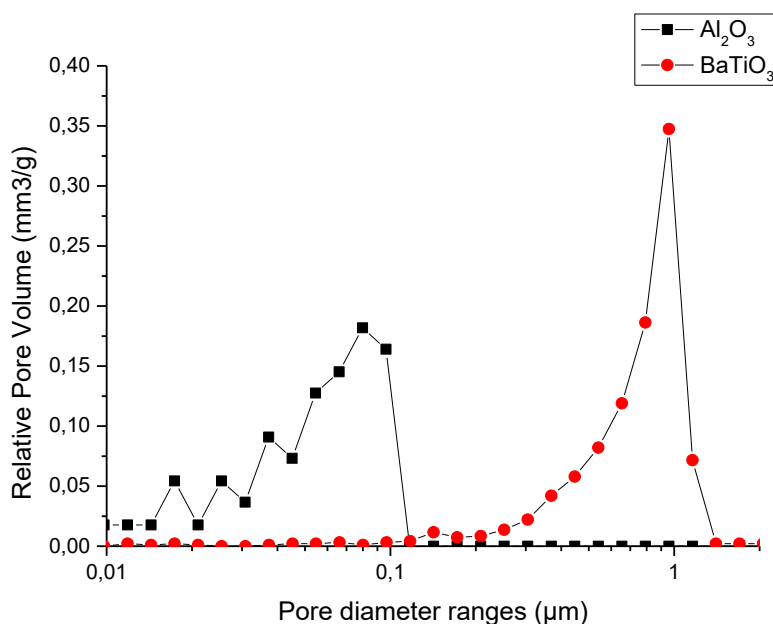


Figure 23: Relative pore volume for  $\alpha$ -Al<sub>2</sub>O<sub>3</sub> and BaTiO<sub>3</sub> beads.

### 3.2.1.3 Effect of the bead size

Figure 22 shows a clear influence of the bead size affecting the conversion and energy efficiency. Moreover, the results differ depending on the packing material inserted in the DBD. On the one hand, SiO<sub>2</sub> and ZrO<sub>2</sub> show no clear (linear) trend of bead size. For SiO<sub>2</sub>, the conversion and energy efficiency increase in the following order: 1.6-1.8 mm < 2.0-2.24 mm < 1.25-1.4 mm, while for ZrO<sub>2</sub> the results rise in the following order: 1.6-

1.8 mm < 1.25-1.4 mm < 2.0-2.24 mm. On the other hand, for  $\alpha$ -Al<sub>2</sub>O<sub>3</sub> and BaTiO<sub>3</sub>, the results increase upon increasing bead size (1.25-1.4 mm < 1.6-1.8 mm < 2.0-2.24 mm). Note, however, that the exact trends have to be considered with caution, as some of the error bars overlap.

There are multiple possible explanations as to why the effect of bead size is different for the different bead materials.

Firstly, the electric field enhancement in the reactor due to the packing is expected to give rise to a higher conversion and energy efficiency. This electric field enhancement is attributed to polarization effects and the accumulation of charges on the surface of the (dielectric) beads. It is governed by the contact angle, the curvature and the dielectric constant of the beads. Moreover, there are more contact points between the smaller beads (and also between the beads and the dielectric barrier), and the electric field enhancement takes place at these contact points [51,93]. Hence, one could expect that smaller beads would give rise to a higher conversion and energy efficiency, but due to its dependence on the dielectric constant, differences might be present. Modelling results show a higher electric field for smaller beads and a higher overall enhancement for packing beads with a higher dielectric constant, indicating that trends can indeed be different, based on both the size and dielectric constant of the beads [139].

Secondly, since the discharges take place in the voids between the beads and larger bead sizes have larger void spaces, the electrons are not so easily absorbed at the surfaces of the beads, so there are more electrons available for electron impact dissociation of CO<sub>2</sub>, which can lead to a higher conversion and energy efficiency. This would mean that larger beads can give rise to a higher conversion and energy efficiency. Not only the electrons can get adsorbed at the surface of the beads, other species can interact with the surface as well. Indeed, the surface may enhance O recombination to form O<sub>2</sub> as well as the backwards reaction of O with CO to form CO<sub>2</sub>. The surface can also delay the same reactions, by quenching CO and/or O.

Depending on which effect is dominant, the final result in conversion or energy efficiency will be higher for either the smaller or the larger beads. The latter appears to

be material-dependent, which is not unexpected, because the electric field enhancement is determined by the dielectric constant of the materials. Nevertheless, to be able to exclude other effects, further research through modelling and studies with more controlled material properties are required to confirm the extent of these effects.

### 3.2.2 Combined effect of bead size and gap size

The experiments for the combined influence of gap size and bead size are conducted with the BaTiO<sub>3</sub> beads, for which the best results are obtained at 50 ml/min. Results are shown for: (1) a constant ratio between average bead size and gap size but with varying dimensions; (2) a constant bead size but a varying gap; and (3) vice versa (already shown in Figure 22). Table 11 summarises the combinations of gap size and bead size investigated.

*Table 11: Parameters used for investigating the influence of the gap size and bead size, at equal ratio, equal bead size or equal gap size.*

Bead size range	Gap size	Ratio
1.18-1.25	2	<u>0.6075</u>
1.4-1.6	2.5	<u>0.6000</u>
<u>2.0-2.24</u>	3.5	<u>0.6057</u>
<u>2.0-2.24</u>	<u>4.5</u>	0.4711
1.6-1.8	<u>4.5</u>	0.3777
1.25-1.4	<u>4.5</u>	0.2944

As is clear from Figure 24, the conversion and energy efficiency rise upon increasing gap size and bead size, as long as the ratio between both is constant (cf. the first three data points). The values increase from 18 % to 26 % conversion and from 3 % to 4 % energy efficiency. When comparing column 3 and 4 in Figure 24, using the same bead size but a larger gap size and thus a lower ratio bead/gap size (hence allowing slightly



more beads in the same gap), we can observe that the conversion and energy efficiency decrease again. In addition, at a fixed gap (4.5 mm), increasing the bead size from 1.25-1.4 to 2.0-2.24 mm resulted in an increase of conversion and energy efficiency, as observed in Figure 22. The maximum conversion (20 %) and energy efficiency (~3.7 %) obtained in this case, however, are lower than the conversion and energy efficiency in the smaller gap size of 3.5 mm. Hence, it is clear that in order to optimize the conversion and energy efficiency, the bead size and gap size have to be adjusted to each other.

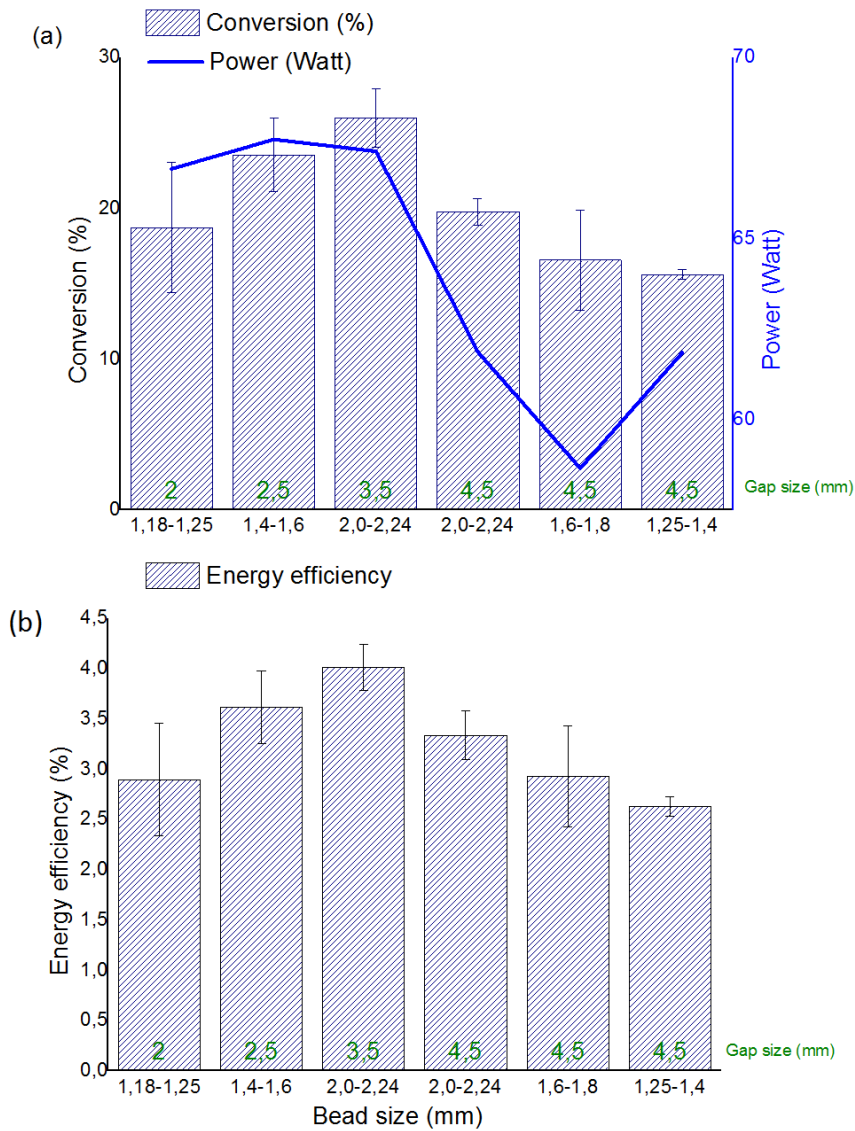


Figure 24: Conversion (a) and energy efficiency (b) as a function of bead size and gap size (indicated at the bottom of the columns, in mm), for BaTiO<sub>3</sub> beads, an alumina dielectric barrier, stainless steel outer electrode, 23.5 kHz, at 50 ml/min, for 100 Watt input power. The plasma power (Watt) is indicated by a blue line.

The same is seen in a paper by Van Laer and Bogaerts [93], who found that the ideal ratio between ZrO<sub>2</sub> beads and the gap size is higher than 1/3. Since our results are only obtained for BaTiO<sub>3</sub> and for few data points, no general conclusions can be drawn.

Nevertheless, it is important to state that all the above aspects are important to take into account: the gap size, the void spaces in between the beads, the surface to volume ratio, the number of contact points between the beads, and between the beads and the dielectric barrier, as they all influence the conversion and energy efficiency. For instance, the relative rise in conversion and energy efficiency upon increasing bead size (from 1.18-1.25 mm to 2-2.24 mm) is 40 % and 33 % (i.e. from 18 to 26 % conversion and from 3 to 4 % energy efficiency) in the case of constant bead size/gap size ratio, while it is 27 % (i.e. from 16 to 20 % conversion and from 2.6 to 3.3 % energy efficiency) in case of constant gap size, for the same rise in bead size.

The stronger rise upon increasing bead size at a constant bead/gap size ratio might be caused by the constant number of beads and thus contact points, while in the case of constant gap size, the number of contact points will drop upon increasing bead size.

Lastly, the alteration in gap size and bead size and their ratio will affect the surface to volume ratio and how many beads fit in the gap, and thus the possible surface interactions and the packing profile of these beads. Therefore, this will also alter the path the gas will take and how it comes into contact with the surface of the packing material. Depending on which species are adsorbed on the surface and how much different species come in contact with said surface, this will alter the residence time distribution and thus the conversion and energy efficiency.

Ideally, taking the previous observations into account, a packing material should thus have large voids present between the particles, allowing less electron losses, in balance with a large number of contact points and an adjusted gap size to have a maximum enhancement of the electric field. Following this conclusion, it could be interesting to investigate even larger bead sizes, along with larger gap sizes, although this might not be beneficial in terms of plasma catalysis, as it will yield a lower catalyst surface area. Hence, there will be an optimum combination, keeping in mind both physical and chemical (surface) effects.

The power indicated on Figure 24 only varies between 58.6 and 67.7 Watt and does not follow the same trend as the conversion or energy efficiency. Therefore, the results obtained here cannot be explained through a variation of the actual plasma power.

The change in the power itself can be explained through the losses caused by transferring the power from the power supply to the reactor. Since this is a very unstable process, the power changes a little over the different conditions.

For completeness, we also present the electrical characteristics for the different bead sizes and gap sizes. However, they do not reveal clear trends that can explain the observed differences in conversion and/or energy efficiency. It is important to note that (for all electrical characterisation), differences in the average charge per filament can be induced by the reactor configuration; the fact that a low charge and many pulses gives the same result as a high charge and few pulses; the fact that a non-packed reactor often gives few strong pulses while a packed reactor gives many weak pulses. Moreover, it is impossible to determine the difference between a streamer between the electrode and the dielectric barrier, between the electrode and a bead, between 2 beads, between a bead and the dielectric barrier, in the current profile. Therefore, it is also impossible to determine the difference between surface discharges versus local filamentary discharges.

*Table 12: Electrical characterisation as a function of bead size and gap size for BaTiO<sub>3</sub> beads, an alumina dielectric barrier, stainless steel outer electrode, 23.5 kHz, at 50 ml/min, for 100 Watt input power.*

Gap size	Bead size	Plasma Power (W)	U <sub>bur</sub> (kV)	U <sub>pp</sub> (kV)	Average charge per filament (nC)	Number of discharges	I <sub>RMS</sub> (mA)
2 mm	1.18 - 1.25 mm	66.92	1.20	12.94	7.22	155.69	70.52
2.5 mm	1.4 - 1.6 mm	67.73	1.62	13.20	9.32	153.17	58.47
3.5 mm	2.0 - 2.24 mm	67.40	2.12	13.19	5140.98	159.13	56.56
4.5 mm	2.0 - 2.24 mm	61.85	2.08	13.14	4.41	148.00	51.42
4.5 mm	1.6 - 1.8 mm	58.65	1.99	12.86	5.01	143.42	53.05
4.5 mm	1.25 - 1.4 mm	61.85	1.98	13.87	4.78	149.89	53.76

### 3.2.3 Effect of glass wool or quartz wool packing

Duan et al. performed experiments with a quartz wool packed DBD reactor [126] and reported that the insertion of quartz wool yields better results, in terms of conversion, than inserting beads of different materials and sizes. As we always use glass wool to fix the packing material in our reactor, we measured the influence of both glass and quartz wool packing in the reactor.

A first set of experiments compares a completely non-packed reactor, a reactor with glass wool, but only outside of the discharge zone, and a reactor completely filled with glass wool. The experiments are carried out at two different flow rates, i.e. 50 and 192 ml/min. The results for conversion and energy efficiency are plotted in Figure 25. The plasma power for these experiments is  $(67 \pm 2)$  Watt.

We can see that, when taking the error bars into account, there is no significant effect of inserting glass wool in the reactor. The effect is negligible for both energy efficiency and conversion. The conversion is around 10-11 % at a flow rate of 50 ml/min, and around 5-6 % at a flow rate of 192 ml/min, while the energy efficiency is about 1.7-1.9 % and 3-4 % for the gas flow rates of 50 and 192 ml/min, respectively. In section 3.2.1 above, we already observed that SiO<sub>2</sub> beads have a negative effect on the conversion and energy efficiency, compared to a non-packed reactor, since the enhancement of the electric field is too limited, probably due to the low dielectric constant. Hence, it seems that the improvement, which might be expected from the enhanced electric field at the contact points and edges of the glass wool packing, is entirely compensated by the reduction in residence time of the packed reactor, which of course limits the conversion and thus the energy efficiency.

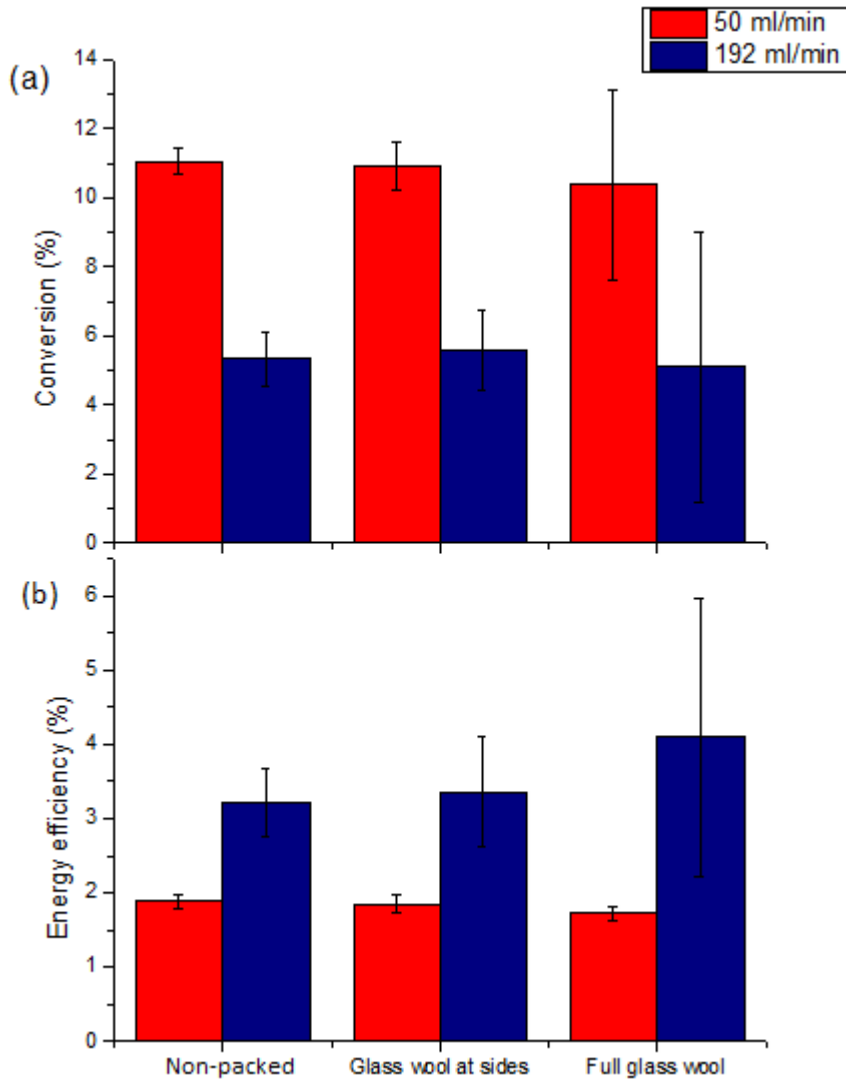


Figure 25: Conversion (a) and energy efficiency (b) in a non-packed reactor (left), a non-packed reactor with glass wool at the sides (middle) and a reactor completely filled with glass wool (right) at two different flow rates, for 100 Watt power, alumina dielectric barrier, stainless steel electrode, at 23.5 kHz and 4.5 mm gap.

Our results are thus different from the ones obtained by Duan et al., where an improved conversion was reported in case of a quartz wool packing [126]. Note, however, that our setup differs from the one of Duan et al. in several aspects. Indeed,

they used an aluminium foil as outer electrode, a much smaller gap size of 0.6 mm, a different frequency (18 kHz) and a different flow rate (19.8 ml/min).

The major difference between our reactor setup and their reactor setup is the different gap size (i.e. 4.5 mm vs 0.6 mm), so it might be possible that the effects reported by Duan et al. only occur in a microgap. Therefore, we also performed additional experiments in a microgap reactor. The reactor setup is the same as used before, but different inner electrodes are used, with varying outer diameter and thus influencing the gap. The gap sizes obtained are 268  $\mu\text{m}$ , 455  $\mu\text{m}$ , 705  $\mu\text{m}$  and 1230  $\mu\text{m}$ . The results are summarised in Figure 26. Note that the results in the 268 – 1230  $\mu\text{m}$  gaps were obtained with different flow rates to yield the same residence time of about 7.5 seconds (in case of the packing), whereas the residence time in the 4.5 mm gap reactor was 5.5 seconds and it was 1 second in the experiments of Duan et al.

It can be clearly seen from Figure 26 that the conversion for a non-packed reactor is higher than for a reactor filled with glass wool, in the case of a 268  $\mu\text{m}$  gap and a 455  $\mu\text{m}$  gap. However, for the 705 and 1230  $\mu\text{m}$  gaps, the reactor filled with glass wool yields a significantly higher conversion than the non-packed reactor, in agreement with the results of Duan et al. for the quartz wool packing. This means that the influence of glass wool (or quartz wool) on the conversion is indeed gap size dependent, and this can explain the difference in results compared to Duan et al. Furthermore, it is obvious from Figure 26 that the  $\text{CO}_2$  conversion in the smaller gaps is larger. This can partially be explained by the enhanced electric field and electron temperature in the smaller gaps, as predicted by model calculations [57]. The effect of micrometre gap sizes in correlation to packing properties was further investigated in our group, but is outside the scope of this thesis [142].

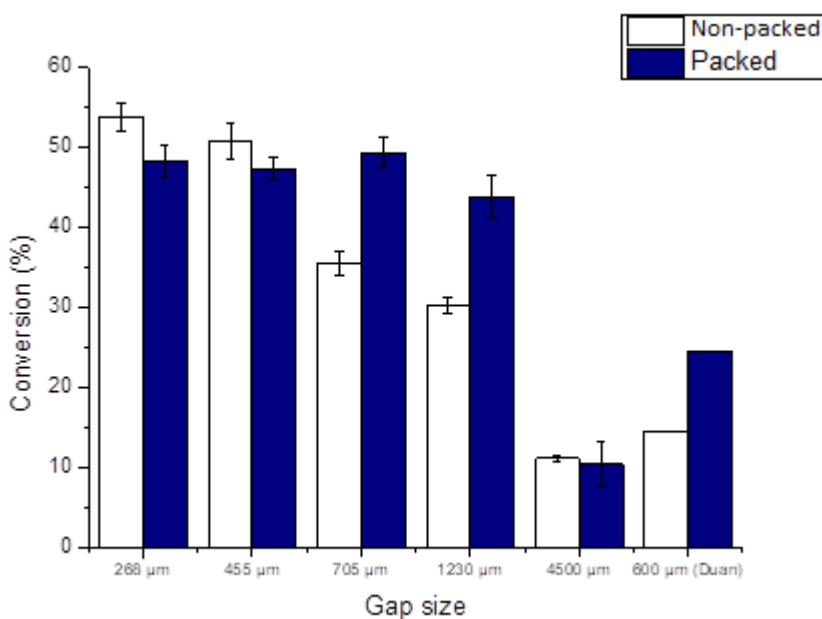


Figure 26: Effect of a glass wool packing on the CO<sub>2</sub> conversion, for different gap sizes, in comparison with the results by Duan et al. for a quartz wool packing.

To exclude that the difference with the results of Duan et al. is attributed to the different packing material (i.e. glass wool vs quartz wool, as used by Duan et al.) or reactor material, we also performed a second set of experiments, comparing glass wool and quartz wool packing, as well as an alumina and quartz dielectric tube, to investigate the impact of the chemical nature of the dielectric tube as well, as in the experiments of Duan et al. quartz wool was applied in combination with a quartz dielectric barrier. The results for the conversion and energy efficiency are shown in Figure 27.

Again, no significant difference in conversion or energy efficiency compared to the non-packed reactor or among each other is observed, keeping in mind the error bars in the results. Therefore, these experiments show us that there is no influence of using quartz wool or glass wool as a packing material in the 4.5 mm gap reactor. Furthermore, it also indicates that, at least in our 4.5 mm gap reactor, we can use glass wool (or quartz wool) to fixate the spherical beads (as done in the other parts of this thesis), without affecting the conversion or energy efficiency.



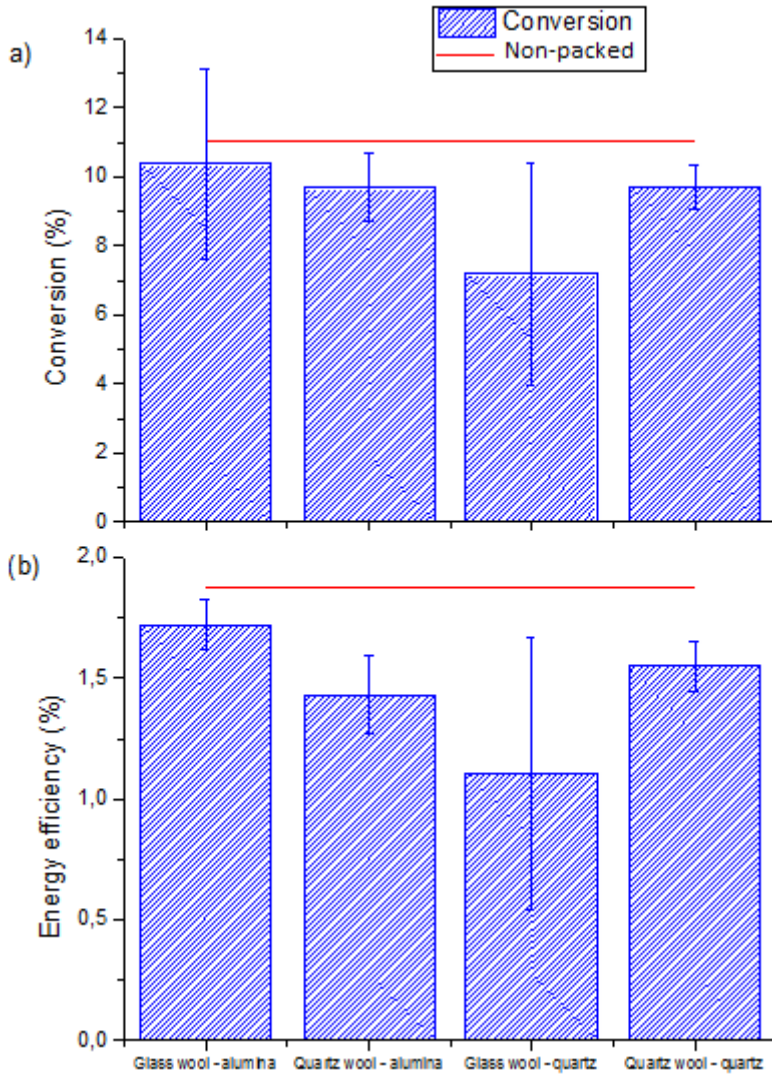


Figure 27: Conversion (a) and energy efficiency (b) for two different dielectric barriers and packing materials, as indicated in the x-axis, at 50 ml/min, for 100 Watt power, 4.5 mm gap, 23.5 kHz and a stainless steel electrode.

Our results are in correlation with literature results for DRM, where it was reported that the conversion of  $\text{CH}_4$  was slightly improved by the addition of quartz wool to the discharge gap, from 23 to 27 % at a discharge power of 30W in comparison to a non-packed reactor, while the  $\text{CO}_2$  conversion did not increase [76].

Again, the electrical characteristics are shown for Figure 25 and Figure 27 in Table 13 and Table 14, respectively, but it is not possible to explain all obtained results based on these values. It is again important to note that differences in the average charge per filament can be induced by the reactor configuration; the fact that a low charge and many pulses gives the same result as a high charge and few pulses; the fact that a non-packed reactor often gives few strong pulses while a packed reactor gives many weak pulses. Moreover, it is impossible to determine the difference between a streamer between the electrode and the dielectric barrier, between the electrode and a bead, between 2 beads, between a bead and the dielectric barrier, in the current profile. Therefore, it is also impossible to determine the difference between surface discharges versus local filamentary discharges.

*Table 13: Electrical characterisation for Figure 25.*

Conditions	Plasma Power (W)	$U_{bur}$ (kV)	$U_{pp}$ (kV)	Average charge per filament (nF)	Number of discharges	$I_{RMS}$ (mA)
Non-packed	61.25	3.68	15.36	210.59	2.58	27.51
Glass wool at sides	61.58	3.77	15.25	83.92	3.61	27.51
Full glass wool	62.85	3.44	12.97	7.98	55.35	28.64

*Table 14: Electrical characterisation for Figure 27.*

Dielectric barrier	Packing	Plasma Power (W)	$U_{bur}$ (kV)	$U_{pp}$ (kV)	Average charge per filament (nF)	Number of discharges	$I_{RMS}$ (mA)
Alumina	Glass wool	70.06	3.78	13.62	6671.54	69.72	28.38
Alumina	Quartz wool	69.73	3.78	15.57	3.73	119.11	33.35
Glass	Quartz wool	65.31	3.88	19.59	2.61	155.59	30.94
Glass	Glass wool	72.00	4.01	17.65	7.09	55.18	26.78

### 3.2.4 Interaction between dielectric barrier and bead material

Finally, the influence of the interaction between dielectric barrier material and bead material is studied by comparing the results for SiO<sub>2</sub> beads and α-Al<sub>2</sub>O<sub>3</sub> beads of 1.6-1.8 mm diameter, both with a quartz and an alumina dielectric barrier. In this way we can compare all possible interactions between the SiO<sub>2</sub> and α-Al<sub>2</sub>O<sub>3</sub> packing versus the dielectric reactor tube. Figure 28 illustrates that there is no significant effect of altering the dielectric barrier material for both conversion and energy efficiency, while there is a significant effect when using SiO<sub>2</sub> or α-Al<sub>2</sub>O<sub>3</sub> beads, as elaborated in section 3.1 above. Thus, like for the glass wool and quartz wool packing (see previous section), the dielectric barrier seems to play only a minor role in the conversion and energy efficiency. The electrical characteristics are shown in Table 15, but cannot explain the obtained conversions and/or energy efficiencies. It is again important to note that differences in the average charge per filament can be induced by the reactor configuration; the fact that a low charge and many pulses gives the same result as a high charge and few pulses; the fact that a non-packed reactor often gives few strong pulses while a packed reactor gives many weak pulses. Moreover, it is impossible to determine the difference between a streamer between the electrode and the dielectric barrier, between the electrode and a bead, between 2 beads, between a bead and the dielectric barrier, in the current profile. Therefore, it is also impossible to determine the difference between surface discharges versus local filamentary discharges.

*Table 15: Electrical characterisation for SiO<sub>2</sub> and α-Al<sub>2</sub>O<sub>3</sub> beads, with quartz and alumina dielectric barriers, at 50 ml/min, for 100 Watt power, 4.5 mm gap, 23.5 kHz and a stainless steel electrode.*

Dielectric barrier	Packing	Plasma Power (W)	U <sub>bur</sub> (kV)	U <sub>pp</sub> (kV)	Average charge per filament (nC)	Number of discharges	I <sub>RMS</sub> (mA)
Glass	SiO <sub>2</sub>	65.99	2.68	18.20	6.26	75.54	37.49
Glass	α-Al <sub>2</sub> O <sub>3</sub>	43.28	2.06	23.17	3.77	89.83	33.92
Alumina	SiO <sub>2</sub>	60.64	2.69	12.40	5.01	84.53	36.19
Alumina	α-Al <sub>2</sub> O <sub>3</sub>	59.06	2.78	16.51	3719.08	132.75	37.11

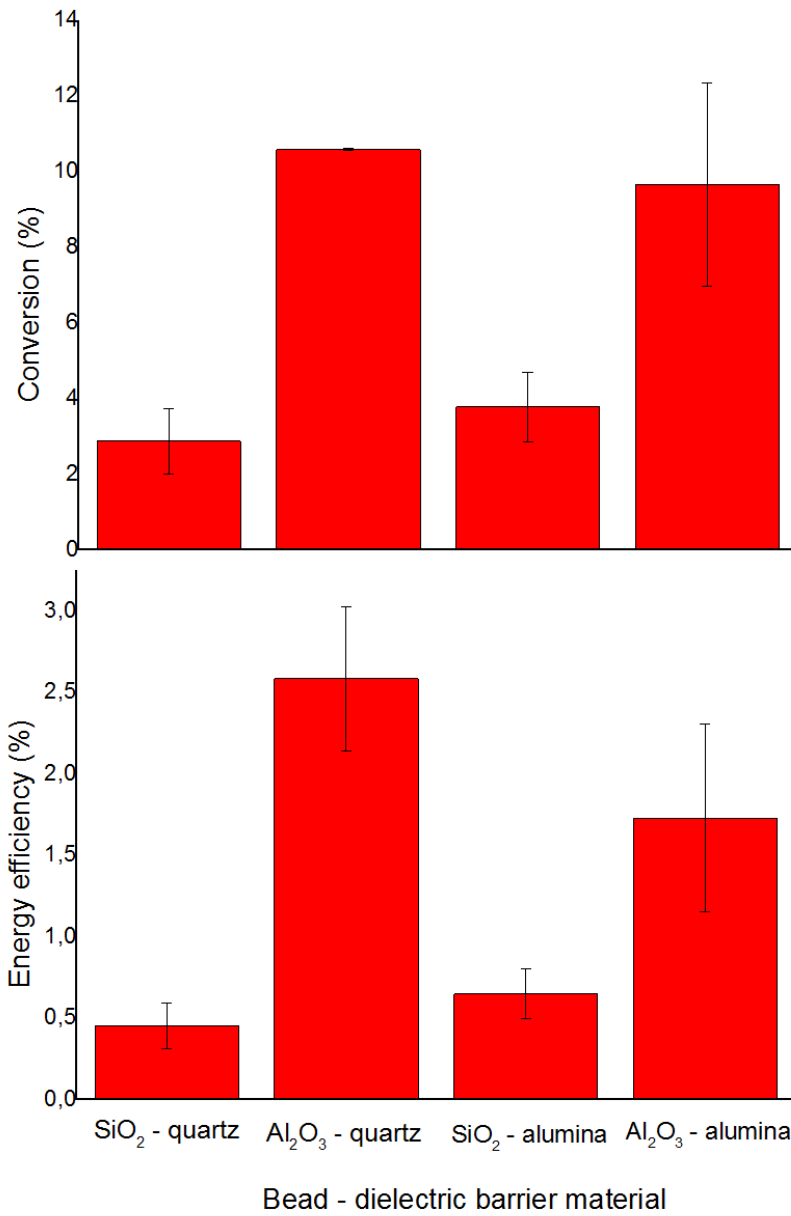


Figure 28: Conversion (a) and energy efficiency (b) for SiO<sub>2</sub> and  $\alpha$ -Al<sub>2</sub>O<sub>3</sub> beads, with quartz and alumina dielectric barriers, at 50 ml/min, for 100 Watt power, 4.5 mm gap, 23.5 kHz and a stainless steel electrode.

### 3.3 CONCLUSION

We showed a clear influence of specific material and reactor properties on the conversion and energy efficiency of CO<sub>2</sub> splitting in a packed bed DBD reactor. This indicates that correlating results from literature obtained in different setups is not straightforward and should be considered with care.

The highest obtained conversion in this work was 25 %, with a corresponding energy efficiency of 4.5 %. When comparing the results for different materials and bead sizes in the reactor gap of 4.5 mm, the highest conversion was roughly a factor two higher than in the non-packed reactor with the same flow rate, and a factor four higher than in the non-packed reactor with the same residence time. The energy efficiency was the same when compared at the higher flow rate, but again almost twice as high when compared at the same flow rate.

It is clear that three effects play a role: (1) the positive contribution of the packing, due to electric field enhancement at the contact points; (2) a negative contribution due to the lower residence time in the presence of a packing; and (3) the influence of the voids between particles, with a positive or negative effect depending on the material inserted. Depending on the bead size and material, one or the other effect will dominate, explaining their different behaviour in conversion and energy efficiency. The changes in conversion can only partially be related to the dielectric constant of the beads, indicating that also other material parameters must play a role. In general, our results indicate that material performances should be compared with similar reactor setups as the latter have a vast impact on the materials influence. Further improvement in conversion and energy efficiency can be expected when a large number of contact points can be generated, while maintaining large void space volumes and a large ratio of bead size/gap size.

Finally, when searching for the most optimal catalyst, the impact of the packing material (chemistry and physical properties) itself, apart from the catalytic activation, cannot be neglected, since it can by itself already significantly improve the conversion and energy efficiency. This shows the large area of further improvement that relies in

packed bed plasma reactors for CO<sub>2</sub> conversion and for other chemical conversion reactions.

## 4 STUDY OF DRY REFORMING: FOCUS ON SELECTIVITY

---

This Chapter is published as:

I. Michielsen, Y. Uytdenhouwen, A. Bogaerts, V. Meynen, Altering Conversion and Product Selectivity of Dry Reforming of Methane in a Dielectric Barrier Discharge by Changing the Dielectric Packing Material. *Catalysts* 9, 51 (2019).  
Doi:10.3390/catal9010051

## 4.1 STATE OF THE ART

The current state of the art in DRM mostly indicates that depending on the exact conditions, the resulting conversion and selectivity can differ significantly. Indeed, as can be seen in Table 4 and Table 5, the conversion was reported to increase [64–71] and decrease [71–73] for both CO<sub>2</sub> and CH<sub>4</sub> upon adding a packing material, and in other cases, there was only an effect on one of the two components [70,74–76]. Not only the conversion was altered, also the effect on the selectivity was substantial. When comparing different catalytic activations with non-activated packing, there can be a vast influence on the formation of liquid products and the selectivity [68,70,73,74,77]. Chapter 3 suggested a large effect of the reactor setup and reactor/bead size combination on the impact of the packing material on conversion of pure CO<sub>2</sub>. Thus, comparing results obtained in different reactor setups should be done with care. Therefore, the results obtained in different literature reports cannot be easily compared to one another, and no general conclusion towards the impact of the packing material itself on DRM can be drawn. This points towards an important gap in the knowledge required to achieve a maximal synergy between the packing, the active catalytic element and the plasma, ultimately yielding higher conversions and a better selectivity towards the desired components in plasma-based DRM.

The aim of this chapter is thus to provide better insights in the influence of four different (dense, spherical) packing materials, with different chemistry and size, on the conversion and product fractions of DRM in a DBD reactor. Additionally,  $\gamma$ -Al<sub>2</sub>O<sub>3</sub> is evaluated as porous packing material. Although it is not possible to distinguish between catalytic effects of the packing material itself and physical effects caused by inserting the packing, it is important to note that there is no explicit catalytic activation of the packing materials in the present study, i.e. we have not introduced an active element, such as applied in many literature reports (e.g. Cu, Fe, Ni, Co, Pd, Ag, etc. See Table 5 in the Introduction and [9]) on or in the packing materials. Furthermore, the impact of



these packing materials in DRM is being compared to the insights gained for pure CO<sub>2</sub> splitting, providing surprising and valuable information on the influence of adding CH<sub>4</sub>. To our knowledge, such a detailed comparison has not yet been carried out before in literature. A summary of the experimental parameters used in this chapter is shown in Table 16.

*Table 16: Parameters used in this chapter.*

Parameter	Specification
Gap (mm)	4.5
Frequency (kHz)	23.5
Power (Watt)	100
Gas flow (ml/min)	50 of 192
Material type	Non-packed reactor versus SiO <sub>2</sub> , α-Al <sub>2</sub> O <sub>3</sub> , γ-Al <sub>2</sub> O <sub>3</sub> , ZrO <sub>2</sub> and BaTiO <sub>3</sub>
Diameter beads (mm) <sup>a</sup>	1.25 – 1.4; 1.6 – 1.8; 2.0 – 2.24
Gas composition	CO <sub>2</sub> /CH <sub>4</sub> = 1

**a: The γ-Al<sub>2</sub>O<sub>3</sub> beads were only tested for a diameter of 2.0-2.24 mm.**

## 4.2 RESULTS AND DISCUSSION

### 4.2.1 CO<sub>2</sub> conversion in DRM and comparison with CO<sub>2</sub> splitting

The influence of four different packing materials (SiO<sub>2</sub>, ZrO<sub>2</sub>, α-Al<sub>2</sub>O<sub>3</sub> and BaTiO<sub>3</sub>) and three different bead sizes (1.25-1.4, 1.6-1.8 and 2.0-2.24 mm diameter) on the CO<sub>2</sub>, CH<sub>4</sub> and total conversion is displayed in Figure 29, Figure 30 and Figure 31, respectively and summarised in Figure 33. Figure 29 shows the CO<sub>2</sub> conversion in DRM, compared to the conversion that we obtained before for pure CO<sub>2</sub> splitting (see Chapter 3), evidencing a clear impact of the presence of CH<sub>4</sub>. Figure 33 shows all data on conversion (CO<sub>2</sub>-, CH<sub>4</sub>-, and total conversion) combined in one graph, for comparison.

The CO<sub>2</sub> conversion in DRM shows that, when comparing the packed bed reactor to the non-packed reactor, only the largest α-Al<sub>2</sub>O<sub>3</sub> beads achieve a higher CO<sub>2</sub> conversion

than the non-packed reactor at the same flow rate. This indicates that only in this case, the positive influence of the packing compensates for the volume loss (and thus lower residence time) caused by introducing the packing.  $\text{SiO}_2$ ,  $\text{ZrO}_2$ ,  $\alpha\text{-Al}_2\text{O}_3$  (with the smaller bead sizes) and  $\gamma\text{-Al}_2\text{O}_3$  (see Figure 34 below) do not reach this  $\text{CO}_2$  conversion, but still surmount the  $\text{CO}_2$  conversion for the non-packed reactor at the same residence time. In the case of  $\text{BaTiO}_3$ , a negative effect of the packing is observed, even at the same residence time. Furthermore, a clear impact of the size of the packing materials can be observed, although the effect itself depends on the type of material. The order in which the materials perform is  $\text{BaTiO}_3 < \text{ZrO}_2 < \text{SiO}_2 < \alpha\text{-Al}_2\text{O}_3$ , although  $\text{SiO}_2$  only performs better than  $\text{ZrO}_2$  for the largest bead size. When looking at the effect of bead size, only  $\text{SiO}_2$  and  $\alpha\text{-Al}_2\text{O}_3$  show a significantly increased conversion for the largest bead size in comparison to the other bead sizes. In case of  $\text{BaTiO}_3$  and  $\text{ZrO}_2$ , no significant impact of the bead size can be seen.

Interesting differences can be observed when comparing the  $\text{CO}_2$  conversion in DRM with pure  $\text{CO}_2$  splitting obtained in our previous experiments (see Chapter 3). It is important to clarify that the total flow rate (and thus the residence time) is kept constant for  $\text{CO}_2$  splitting and DRM, but with DRM, the concentration of  $\text{CO}_2$  is halved, as it has been 'diluted' with 50 %  $\text{CH}_4$ . Diluting with another gas can influence the conversion, even when the diluting gas does not actively participate in the reactions [98]. Indeed, we have previously shown that the absolute conversion increases (from 5 % to 41 %) with a decreasing percentage (from 100 to 5 % in argon) of  $\text{CO}_2$  [98]. In a 50/50  $\text{CO}_2/\text{Ar}$  mixture, the rise in conversion of  $\text{CO}_2$  is around a factor 1.6, compared to pure  $\text{CO}_2$  splitting. Note, however, that the effective  $\text{CO}_2$  conversion drops upon dilution with argon, because there is less  $\text{CO}_2$  in the mixture. Our experiments clearly reveal that the absolute  $\text{CO}_2$  conversion is also higher for DRM than for  $\text{CO}_2$  splitting, with the exception of  $\text{BaTiO}_3$  and 2.0-2.24 mm  $\text{ZrO}_2$  packing. Indeed, in the non-packed reactor at 50 ml/min and 192 ml/min (straight lines in Figure 29) the conversion is (on average) a factor 1.8 and 1.5 higher in case of DRM, indicating that  $\text{CH}_4$  aids the conversion of  $\text{CO}_2$ . This is confirmed by computer simulations for DRM in a non-packed

DBD reactor, where the  $\text{CO}_2$  conversion was largely determined by collision with  $\text{CH}_2$  radicals [47], originating from  $\text{CH}_4$  dissociation.

For DRM in the packed reactor, the  $\text{CO}_2$  conversion is always higher when using  $\text{SiO}_2$  and  $\alpha\text{-Al}_2\text{O}_3$  packing materials than for pure  $\text{CO}_2$  splitting. However, the enhancement of the  $\text{CO}_2$  conversion due to  $\text{CH}_4$  depends on the size of the spherical packing material and is more significant for  $\alpha\text{-Al}_2\text{O}_3$  than for  $\text{SiO}_2$ , except for the bead size of 1.6-1.8mm. For  $\text{ZrO}_2$ , a complex and striking behaviour depending on the bead size is observed: the conversion drops for DRM for the 2.0-2.4 mm bead size, while it is enhanced (even by a factor 3.3) for the 1.6-1.8 mm beads and to a lesser extent also for the 1.25-1.4 mm beads. Finally,  $\text{CH}_4$  has a clearly negative effect in case of the 2.0-2.24 mm beads of  $\text{BaTiO}_3$ , while the conversion is (more or less) equal for  $\text{CO}_2$  splitting and DRM for the other  $\text{BaTiO}_3$  bead sizes. Last but not least, although  $\text{BaTiO}_3$  in general performs best for  $\text{CO}_2$  splitting, compared to the other packing materials, it yields the worst results for DRM.

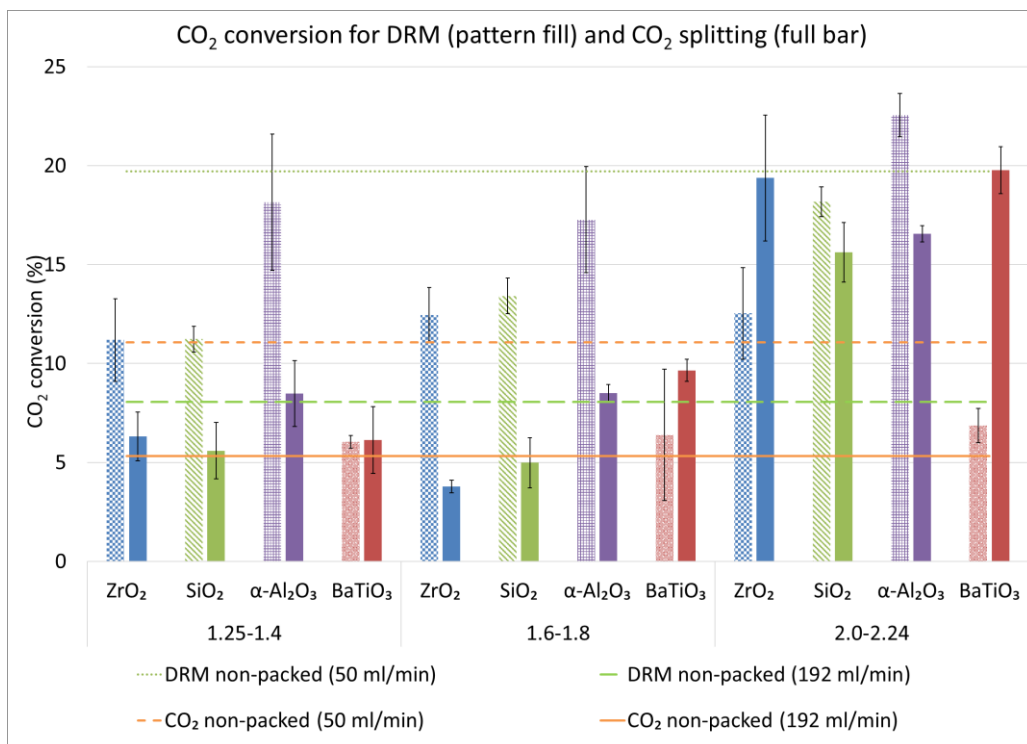


Figure 29: CO<sub>2</sub> conversion for different bead sizes and materials, compared to the results for the non-packed reactor, at the same flow rate (50 ml/min) and at the same residence time (5.52 s; flow rate of 192 ml/min) for both DRM and pure CO<sub>2</sub> splitting. The bars with pattern fill show the results for DRM, whereas the full bars show the results for CO<sub>2</sub> splitting (see Chapter 3).

#### 4.2.2 CH<sub>4</sub> and total conversion

The first observation to be made from Figure 30 is that the CH<sub>4</sub> conversion is always higher than the CO<sub>2</sub> conversion, which is logical, since the dissociation energy of a C-H bond in CH<sub>4</sub> is 412 kJ/mol, while it is 743 kJ/mol for a C=O bond in CO<sub>2</sub> [143].

In comparison to the non-packed reactor again, it can be seen that in contrast to the CO<sub>2</sub> conversion, none of the packing materials allow a better conversion at the same flow rate. However, with the exception of BaTiO<sub>3</sub>, all materials do perform better than the non-packed reactor at the same residence time. BaTiO<sub>3</sub> again performs worse than the non-packed reactor, even at the same residence time. The same trend is seen for the total conversion (Figure 31).

When comparing the results for the different bead sizes and materials, we can make the following observations: similar to the CO<sub>2</sub> conversion, BaTiO<sub>3</sub> performs worst, and

$\alpha$ -Al<sub>2</sub>O<sub>3</sub> performs best, for the four materials tested. Although the bead size had little impact on CO<sub>2</sub> conversion in case of ZrO<sub>2</sub>, increasing the ZrO<sub>2</sub> bead size has a positive effect on the CH<sub>4</sub> conversion. On the other hand, the upward trend in conversion of CO<sub>2</sub> with increasing bead size of SiO<sub>2</sub> is much less pronounced for CH<sub>4</sub> conversion, showing even a slight drop for the largest SiO<sub>2</sub> bead size. Finally, for  $\alpha$ -Al<sub>2</sub>O<sub>3</sub> as well the dependence of bead size is somewhat different for CH<sub>4</sub> and CO<sub>2</sub> conversion. In Table 17, we list the CH<sub>4</sub>/CO<sub>2</sub> conversion ratios for all packing materials and sizes.

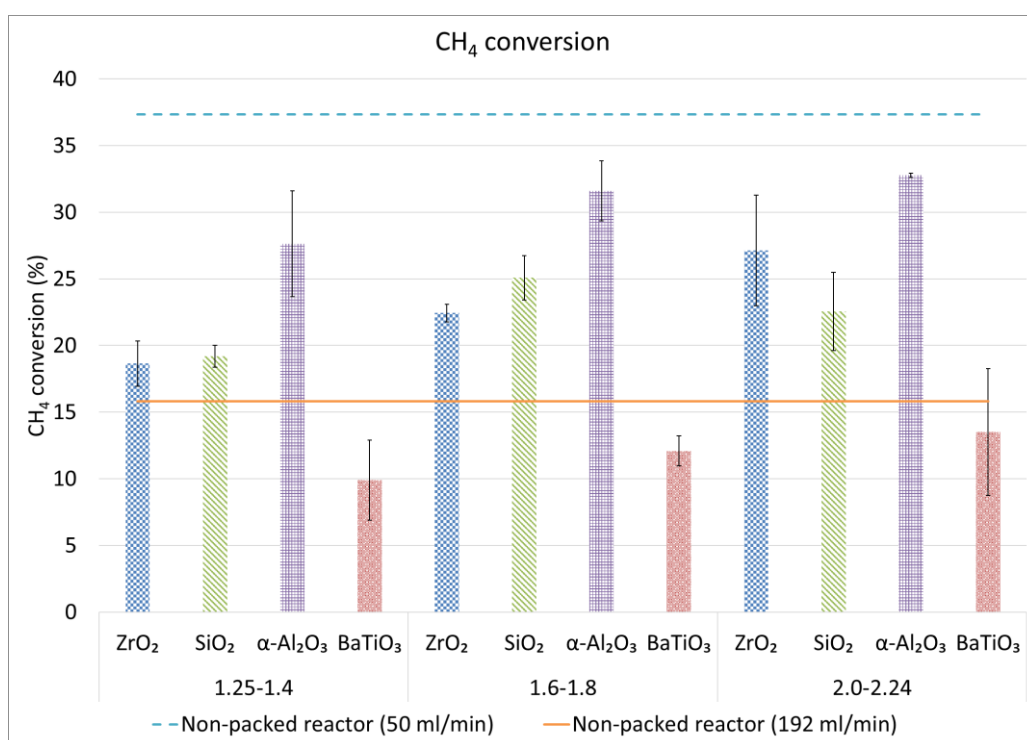


Figure 30: CH<sub>4</sub> conversion for different bead sizes and materials, compared to the results for the non-packed reactor, at the same flow rate (50 ml/min) and at the same residence time (5.52 s; flow rate of 192 ml/min)

To interpret the above results, we compare to modelling results obtained by Snoeckx et al. [47], keeping in mind the differences between their work and this work (70 W and 35 kHz in a non-packed reactor versus 62 W and 23.5 kHz in both non-packed and packed bed reactors, respectively). The conversion of both CO<sub>2</sub> and CH<sub>4</sub> as a function of residence time, as predicted by the model, is plotted in Figure 32. In our work, the residence time is kept constant at 5.52 s, for which the model predicts a CO<sub>2</sub> and CH<sub>4</sub>

conversion of 4.6 and 9.2 %, respectively. We obtained 8.1 % and 15.8 % conversion for CO<sub>2</sub> and CH<sub>4</sub>, respectively, in the non-packed reactor, while the packed bed reactor (with 2.0-2.24 mm α-Al<sub>2</sub>O<sub>3</sub>) can reach 22.5 % (CO<sub>2</sub>) and 32.8 % (CH<sub>4</sub>) conversion.

Table 17: Ratio of CH<sub>4</sub> conversion over CO<sub>2</sub> conversion, and of the CO over H<sub>2</sub> product fraction, for the different bead sizes and materials, as well as for the non-packed reactor .

		CH <sub>4</sub> conversion/CO <sub>2</sub> conversion	CO/H <sub>2</sub>
1.25-1.4 mm	ZrO <sub>2</sub>	1.7	5.5
	SiO <sub>2</sub>	1.7	4.8
	α-Al <sub>2</sub> O <sub>3</sub>	1.5	9.5
	BaTiO <sub>3</sub>	1.6	6.0
1.6-1.8 mm	ZrO <sub>2</sub>	1.8	5.9
	SiO <sub>2</sub>	1.9	4.7
	α-Al <sub>2</sub> O <sub>3</sub>	1.8	8.8
	BaTiO <sub>3</sub>	1.9	6.3
2.0-2.24 mm	ZrO <sub>2</sub>	2.2	6.4
	SiO <sub>2</sub>	1.2	5.3
	α-Al <sub>2</sub> O <sub>3</sub>	1.5	9.0
	BaTiO <sub>3</sub>	2.0	6.9
	γ-Al <sub>2</sub> O <sub>3</sub>	2.3	8.3
Non-packed reactor	50 ml/min	1.9	7.9
	192 ml/min	2.0	7.2

Note that our obtained values in the non-packed reactor are almost a factor two higher than the calculated values, but it is not possible to make an exact comparison, due to the different conditions (cf. above) and geometry. Moreover, the exact calculated values are subject to uncertainties, due to uncertainties in the reaction rate coefficients [144,145]. Hence, they should be interpreted merely based on trends. It is clear,

however, that the packed bed reactor can improve the conversion of both CO<sub>2</sub> and CH<sub>4</sub> with more than a factor two at the same residence time.

Moreover, the data clearly exhibits that the CH<sub>4</sub> conversion is always higher than the CO<sub>2</sub> conversion, both in the model and in the experiments (both for non-packed and packed reactor). In addition, the model predicts that the CH<sub>4</sub> conversion is typically twice as high as the CO<sub>2</sub> conversion, in good agreement with our results for the non-packed reactor, while the packed bed reactors reveal a ratio of CH<sub>4</sub>/CO<sub>2</sub> conversion varying between 1.5 and 2.2, with the exception of the largest SiO<sub>2</sub> beads, where the ratio is only 1.2 (see Table 17), indicating a vast impact of the packing materials on the conversion process.

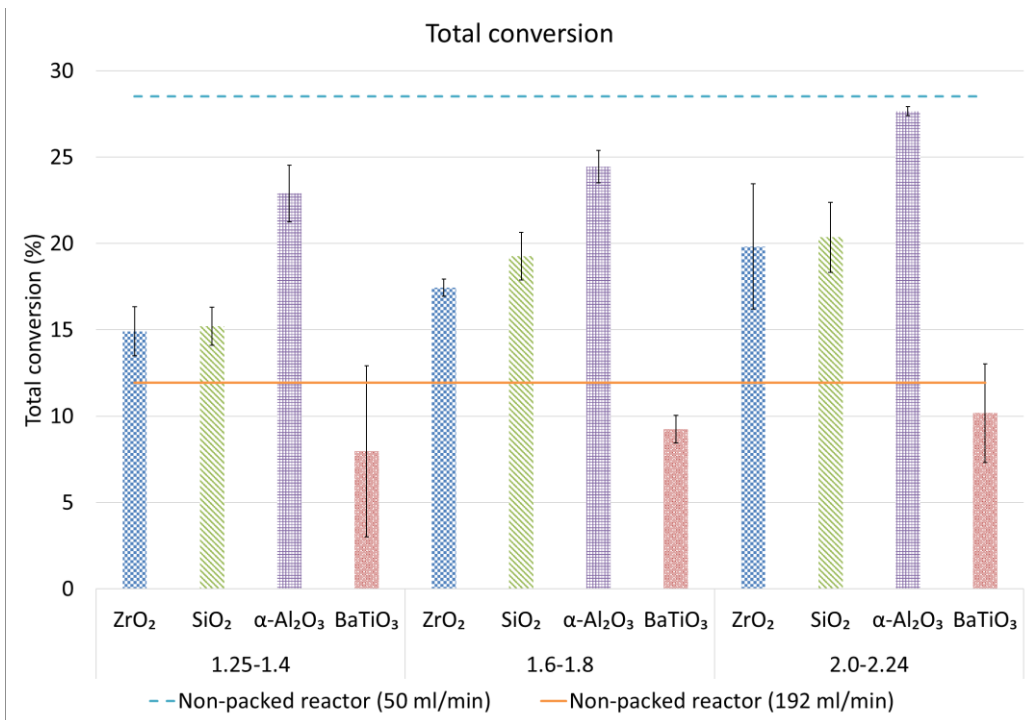


Figure 31: Total conversion for different bead sizes and materials, compared to the results for the non-packed reactor, at the same flow rate (50 ml/min) and at the same residence time (5.52 s; flow rate of 192 ml/min).

The underlying reasons for these differences in conversion are difficult to link to specific material properties, as the materials diverge in many properties, and there is no direct (linear) correlation in the trends in properties that coincide with the trends in

conversions (see material characteristics in the appendix, section 9.3). Hence, more research will be needed, using materials that are modified, in a controlled way, in specific material properties that are expected to play a key role.

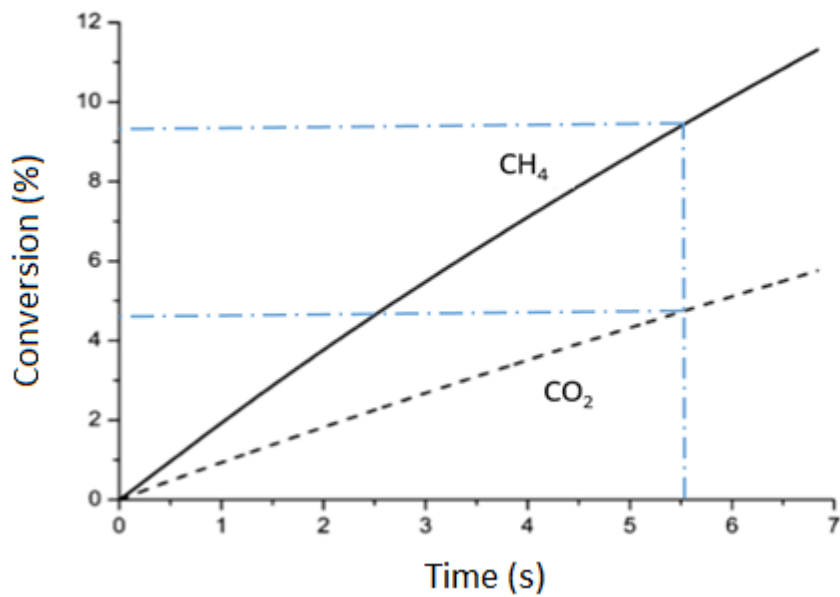


Figure 32: Calculated CH<sub>4</sub> and CO<sub>2</sub> conversion as a function of residence time in a non-packed DBD reactor, adopted from modelling. Adopted with permission from ref. [47]. Copyright 2018 American Chemical Society.



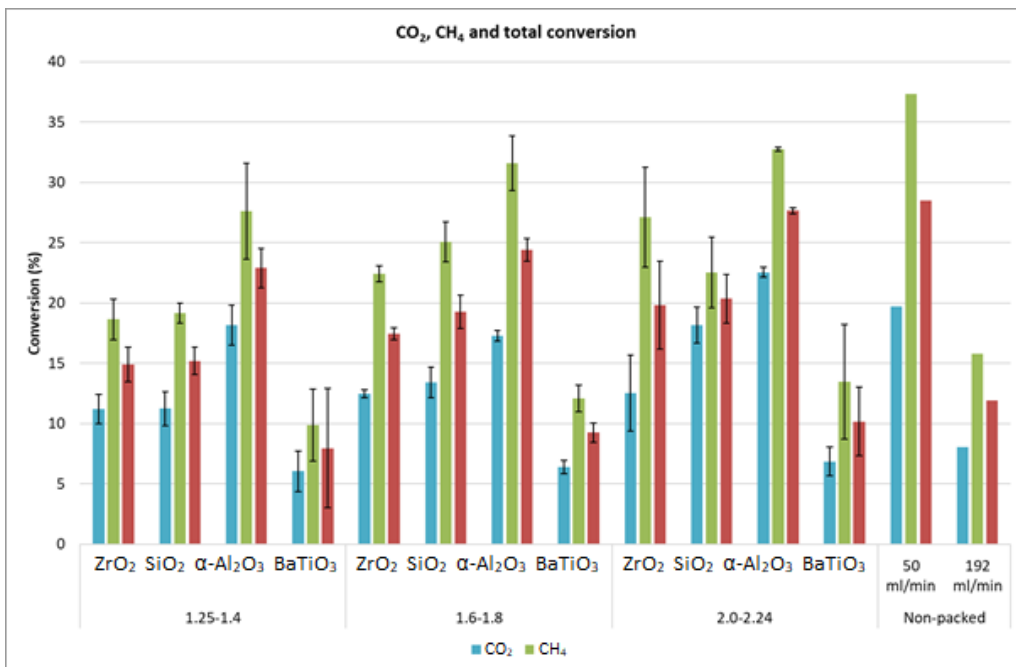


Figure 33: CO<sub>2</sub>, CH<sub>4</sub> and total conversion for different bead sizes and materials, compared to the results for the non-packed reactor, at the same flow rate (50 ml/min) and at the same residence time (5.52 s; flow rate of 192 ml/min).

#### 4.2.3 Comparison studies $\alpha/\gamma$ -Al<sub>2</sub>O<sub>3</sub>

To obtain more insight in the effect of material parameters, we made a comparison between  $\alpha$ -Al<sub>2</sub>O<sub>3</sub> and  $\gamma$ -Al<sub>2</sub>O<sub>3</sub> beads of 2.0-2.24 mm. The CO<sub>2</sub>, CH<sub>4</sub> and total conversion are depicted in Figure 34.

The CO<sub>2</sub> conversion appears a factor 1.7 higher for the  $\alpha$ -Al<sub>2</sub>O<sub>3</sub> beads than for the  $\gamma$ -Al<sub>2</sub>O<sub>3</sub> beads (i.e. 22.5 % vs 13.4 %), while the CH<sub>4</sub> conversion is only a factor 1.05 higher (i.e. 32.8 % vs 31.2 %). The total conversion is a factor 1.24 higher for  $\alpha$ -Al<sub>2</sub>O<sub>3</sub> (i.e. 27.7 % vs 22.3 %). These results show a clear impact of the bead material properties and/or surface area on conversion, possibly due to a higher BET-surface, a difference in crystallinity, acidity, higher porosity and/or total open pore volume of the  $\gamma$ -Al<sub>2</sub>O<sub>3</sub>, as shown in Table 6.

Possibly, the larger surface area, higher porosity and larger pore sizes of  $\gamma$ -Al<sub>2</sub>O<sub>3</sub> result in a higher adsorption of molecules on the surface, causing differences in conversion

due to quenching of specific species from the plasma, changing residence times, etc. that can influence forward and back reactions in different ways. Moreover, differences in surface characteristics, such as the surface acidity, can also influence the conversion [146]. However, to understand which of these, or even other, material aspects are the underlying reasons for this effect, more systematic materials studies (e.g. differing in specific properties within one metal oxide material) and detailed (operando) surface experiments would be needed, which are outside the scope of this thesis.

In conclusion, these differences show the importance of indicating as much as possible, the material properties of the applied packing materials, something that is not systematically done in the majority of the plasma catalysis papers.

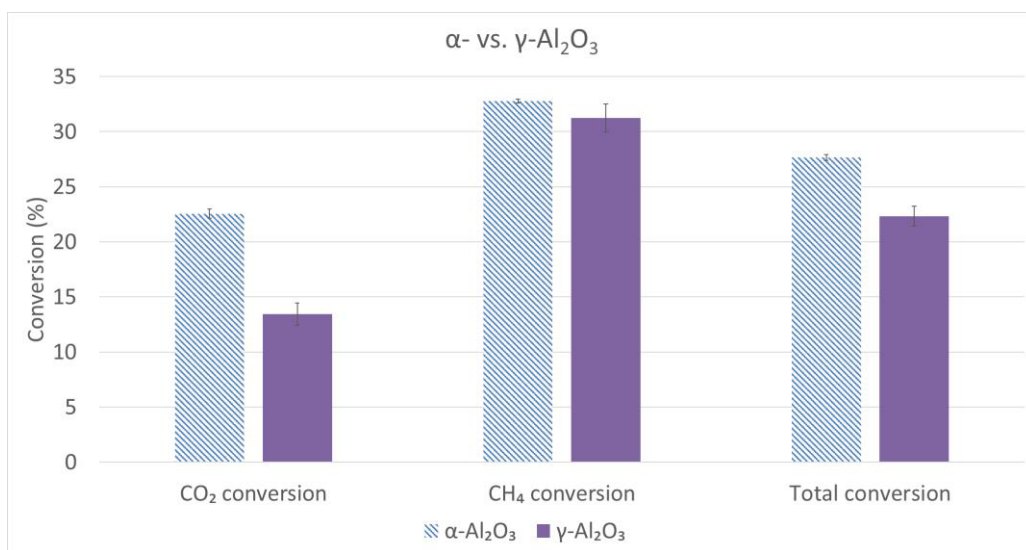


Figure 34: Comparison of the CO<sub>2</sub>, CH<sub>4</sub> and total conversion between γ-Al<sub>2</sub>O<sub>3</sub> and α-Al<sub>2</sub>O<sub>3</sub> (2.0-2.24 mm beads).

The electrical characterisation is shown in Table 18, but do not reveal underlying trends that explain the differences in obtained conversions and/or product fractions. It is again important to note that differences in the average charge per filament can be induced by the reactor configuration; the fact that a low charge and many pulses gives the same result as a high charge and few pulses; the fact that a non-packed reactor often gives

few strong pulses while a packed reactor gives many weak pulses. Moreover, it is impossible to determine the difference between a streamer between the electrode and the dielectric barrier, between the electrode and a bead, between 2 beads, between a bead and the dielectric barrier, in the current profile. Therefore, it is also impossible to determine the difference between surface discharges versus local filamentary discharges.

Table 18: Electrical characterisation for Figure 33 and Figure 34.

Conditions		Plasma Power (W)	$U_{bur}$ (kV)	$U_{pp}$ (kV)	Average charge per filament (nC)	Number of discharges	$I_{RMS}$ (mA)
Non-packed reactor	50 ml/min	62.86	3.861	15.09	16834	20.05	28.11
	192 ml/min	62.33	4.168	15.08	14243	24.93	27.68
SiO <sub>2</sub>	1.25 - 1.4 mm	61.87	2.690	13.19	21534	85.97	36.03
	1.6 - 1.8 mm	62.38	2.797	12.56	5020	92.10	36.26
	2.0 - 2.24 mm	65.16	2.945	12.46	4331	114.67	36.14
ZrO <sub>2</sub>	1.25 - 1.4 mm	61.87	2.690	13.19	5397	85.97	36.03
	1.6 - 1.8 mm	63.53	2.344	12.64	4618	128.65	45.18
	2.0 - 2.24 mm	62.95	2.498	12.04	3610	155.46	43.05
$\alpha$ -Al <sub>2</sub> O <sub>3</sub>	1.25 - 1.4 mm	55.22	2.787	17.16	3214	131.31	35.28
	1.6 - 1.8 mm	59.87	2.772	16.81	4182	112.25	37.15
	2.0 - 2.24 mm	59.18	3.076	16.75	2918	131.27	34.16
$\gamma$ -Al <sub>2</sub> O <sub>3</sub>	-						
	-						
	2.0 - 2.24 mm	59.99	2.861	14.35	3469	146.58	36.98
BaTiO <sub>3</sub>	1.25 - 1.4 mm	63.96	2.077	11.54	5365	132.67	50.77
	1.6 - 1.8 mm	65.28	2.187	11.58	5300	135.91	49.95
	2.0 - 2.24 mm	66.94	2.240	11.27	5240	131.00	49.98

#### 4.2.4 Carbon, hydrogen and oxygen balances

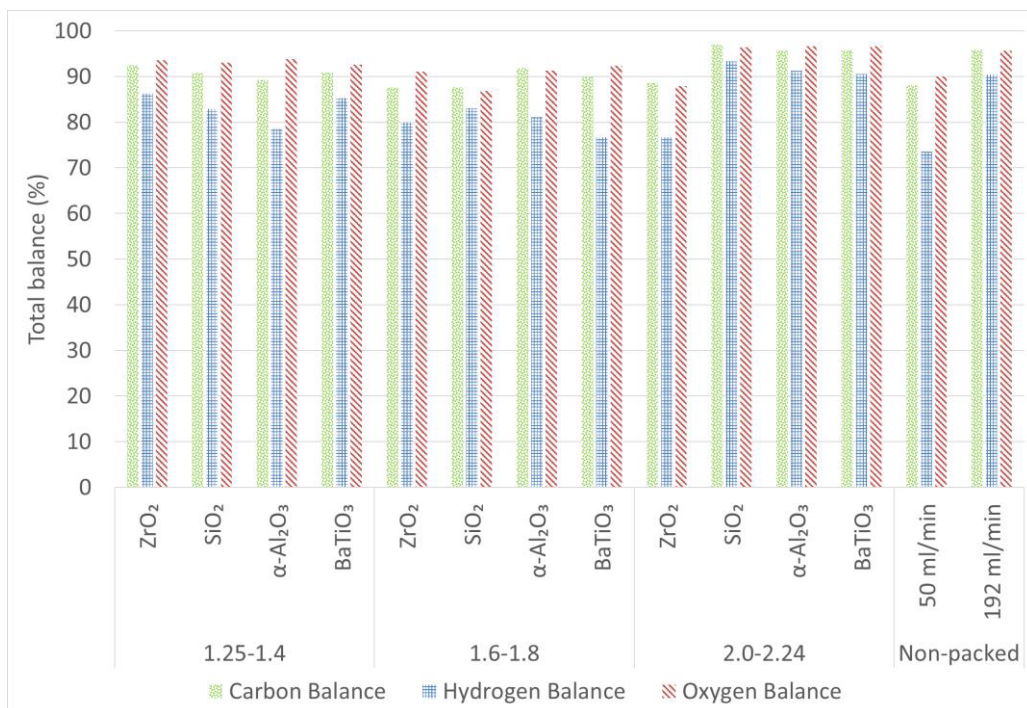


Figure 35: Carbon, hydrogen and oxygen balance for different bead sizes and materials, as well as the non-packed reactor.

To determine whether all products have been identified by the GC, we present the mass balances for carbon, hydrogen and oxygen in Figure 35 (more detailed data can be found in the appendix: Figure 78-Figure 86). Important to note here is that part of the deficit is possibly caused by the gas expansion, as explained above (see Chapter 2: Materials and Methods). As can be seen, the carbon, hydrogen and oxygen balances seldom reach 100 %. The largest deficit (between 20 and 30 % loss of product) is in the hydrogen balance of the non-packed reactor at 50 ml/min, as well as for the BaTiO<sub>3</sub> beads of 1.6-1.8 mm, the α-Al<sub>2</sub>O<sub>3</sub> beads of 1.2-1.4 mm and the ZrO<sub>2</sub> beads of 2.0-2.4 mm. In all other cases, less than 20 % of product remains unaccounted for. Moreover, the oxygen and carbon balances reach much higher values: close to 90 % (and even up to 95 %) and thus less than a 10 % loss. This therefore suggests that mainly products with more than one hydrogen atom are not taken into account in the converted

products. We presume that mostly the formation of H<sub>2</sub>O and the sum of less abundant (oxygenated) hydrocarbons, that were not calibrated on the GC, lie at the basis of these incomplete balances. Indeed, the deficit in the hydrogen balance is for the majority of the experiments double the deficit in the oxygen balance, suggesting the formation of H<sub>2</sub>O. An example of a chromatogram, showing the number (and type) of products that have not been calibrated and accounted for in the mass balances, was shown in Figure 18 in Chapter 2. In addition, also coke deposition could be at the basis of carbon losses. When looking at the Raman measurements (see Appendix: Figure 64 - Figure 71), it is clear that SiO<sub>2</sub> and to a limited extent also α-Al<sub>2</sub>O<sub>3</sub> and ZrO<sub>2</sub> suffer from coking at the bead's surface, unlike the γ-Al<sub>2</sub>O<sub>3</sub> and BaTiO<sub>3</sub> beads. To visually show the amount of cokes deposited on the beads, photos are added in Figure 72 in the Appendix. More detailed carbon, hydrogen and oxygen balances (with the contribution of the different components identified and calibrated by the GC) are shown in section 9.4 of the Appendix. They allow a clear view on all identified products in the treated gas stream, as well as their relative contribution to the total converted products. From these balances, clear differences in product fractions also become apparent when comparing different packing materials. These are discussed in more detail in the following part.

## 4.2.5 Product fractions

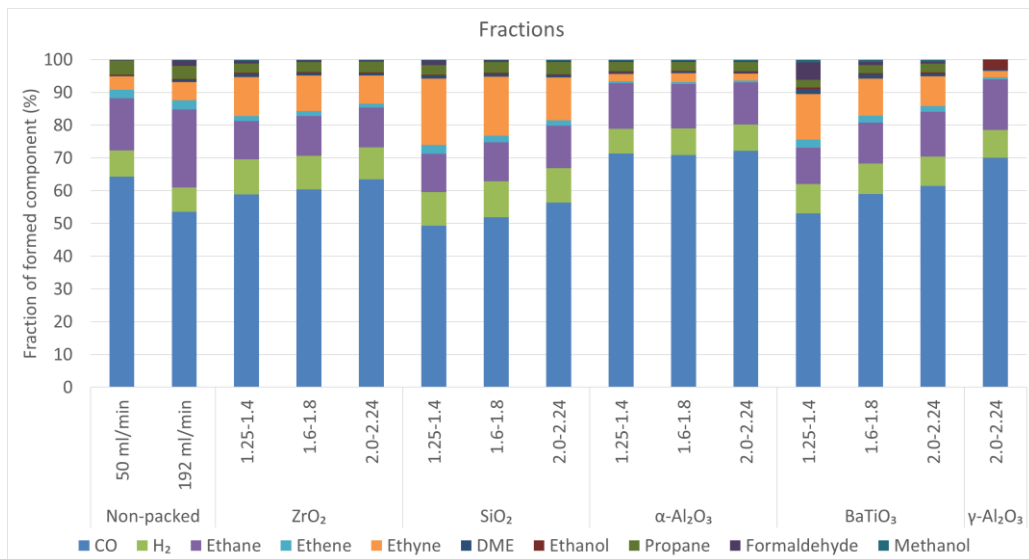


Figure 36: Product fractions for different bead sizes and materials, as well as for the non-packed reactor.

As explained in Chapter 2 (Materials and Methods), the calculation of selectivities and balances induces an uncertainty, caused by the gas expansion. Therefore, we calculated the product fractions in this work (see equation 4), as these values only show the relative contribution of each product in the total identified product mixture, which is not subject to the gas expansion. The product fractions are plotted in Figure 36, to provide a general overview, and are also listed in Table 19, to better compare the trends, based on quantitative data.

Before going into more detail concerning differences for the different packing materials, we can make a general observation for the non-packed reactor. Indeed, it seems that the product fraction is to some extent determined by the flow rate, although the ratio of CH<sub>4</sub> over CO<sub>2</sub> conversion is very similar (see Table 17). Mainly the formation of CO, ethane, ethyne, DME and formaldehyde seem to be affected by this. This can be attributed to different formation rates of different products, as explained in the Discussion section below, because the different flow rate yields a different residence time.

Table 19 and Figure 36 clearly show that CO is always the largest fraction, for all packing materials and for the non-packed reactors. Moreover, by altering the flow rate (non-packed reactor) or packing materials, the relative amount of CO versus higher hydrocarbons or oxygenates can be altered. Indeed, the CO product fraction can vary from about 53 % up to 72 %. Therefore, we list in Table 17 also the obtained CO/H<sub>2</sub> ratio for the different bead sizes and materials. This value ranges from 4.7 to above 9, which is quite striking, because the ratio of CH<sub>4</sub> over CO<sub>2</sub> conversion is always between roughly 1 and 2. It indicates that the majority of C (especially of CO<sub>2</sub>) is converted into CO, while the H (originating from CH<sub>4</sub>) preferentially takes part in the formation of many products, not only for H<sub>2</sub>, but also for higher hydrocarbons.

Furthermore, it is clear from Table 19 and Figure 36 that the type of packing material has a vast impact on the product fractions. Moreover, in case of BaTiO<sub>3</sub> and SiO<sub>2</sub>, also the bead size seems to have a clear impact, while this is much less visible for ZrO<sub>2</sub> and  $\alpha$ -Al<sub>2</sub>O<sub>3</sub>. For example, when high fractions of ethyne are envisioned, the smallest size of the SiO<sub>2</sub> beads seems to be the best choice. The  $\alpha$ - or  $\gamma$ -Al<sub>2</sub>O<sub>3</sub> packing seems to produce the highest CO/H<sub>2</sub> ratios (see also Table 17), while at the same time producing substantially less dehydrogenated hydrocarbons (ethene and ethyne).

When comparing the different types of Al<sub>2</sub>O<sub>3</sub> supports (non-porous  $\alpha$ - and porous  $\gamma$ -Al<sub>2</sub>O<sub>3</sub>), we do not only see differences in conversion (cf. Figure 34 and Table 17), causing a large discrepancy in CH<sub>4</sub>/CO<sub>2</sub> conversion ratio (i.e. 1.5 vs 2.3, respectively), but also interesting changes in the product fractions. Indeed, although the CO fraction is similar, a larger fraction of ethane and ethanol is obtained for the  $\gamma$ -Al<sub>2</sub>O<sub>3</sub> packing, while the fractions of ethyne and propane are lower, and formaldehyde, DME and methanol do not even reach the detection limits.

Furthermore, the BaTiO<sub>3</sub> packing with smallest bead size is the only material able to produce a substantial fraction of formaldehyde and produces overall relatively more oxygenated products, including higher amounts of DME, compared to the other materials.

When looking more closely at the results, four different trends can be observed when taking into account the four largest component fractions (excluding CO, which is always the largest fraction):

- For the non-packed reactor at 50 ml/min and all  $\alpha$ -Al<sub>2</sub>O<sub>3</sub> beads, the order is: ethane > H<sub>2</sub> > propane > ethyne;
- For the non-packed reactor at 192 ml/min, the order is: ethane > H<sub>2</sub> > ethyne > propane > ethene;
- For the smallest ZrO<sub>2</sub> and BaTiO<sub>3</sub> beads and all SiO<sub>2</sub> beads, the order is: ethyne  $\cong$  ethane > H<sub>2</sub> > propane (formaldehyde in case of BaTiO<sub>3</sub>);
- For the two largest BaTiO<sub>3</sub> beads and the intermediate ZrO<sub>2</sub> beads, the order is: ethane > ethyne  $\cong$  H<sub>2</sub> > propane > ethene.

The oxygenated fractions as well, which are much smaller, show clear differences depending on the packing material and size, as detailed in Table 19.



Table 19: Product fractions for different bead sizes and materials (the highest fractions for each component are highlighted).

		CO	H <sub>2</sub>	C <sub>2</sub> H <sub>6</sub>		C <sub>2</sub> H <sub>4</sub>		C <sub>2</sub> H <sub>2</sub>		C <sub>3</sub> H <sub>8</sub>		C <sub>2</sub> H <sub>6</sub> O		C <sub>2</sub> H <sub>5</sub> OH		CH <sub>2</sub> O		CH <sub>3</sub> OH		CO/H <sub>2</sub> ratio
				Ethane	Ethene	Ethene	Ethyne	Propane	DME	Ethanol	Formaldehyde	Methanol								
	Non-packed (50 ml/min)	64.2	8.1	15.9	2.7	4.1	4.3	0.2	0.22	0.14	0.15	7.9								
	Non-packed (192 ml/min)	53.5	7.4	23.8	2.8	5.6	4.0	0.7	0.27	1.63	0.28	7.2								
ZrO <sub>2</sub>	1.25-1.4	58.8	10.8	11.6	1.6	11.9	2.9	0.9	0.33	0.87	0.36	5.5								
	1.6-1.8	60.4	10.2	12.2	1.5	10.9	3.1	0.7	0.33	0.42	0.31	5.9								
	2.0-2.24	63.4	9.8	12.0	1.2	8.6	3.3	0.5	0.34	0.32	0.32	6.4								
SiO <sub>2</sub>	1.25-1.4	49.3	10.3	11.7	2.7	20.3	2.9	0.9	0.24	1.44	0.26	4.8								
	1.6-1.8	51.9	11.0	11.8	2.0	18.0	3.3	0.8	0.28	0.51	0.26	4.7								
	2.0-2.24	56.3	10.6	13.0		13.1	3.7	0.6	0.31	0.41	0.33	5.3								
$\alpha$ -Al <sub>2</sub> O <sub>3</sub>	1.25-1.4	71.3	7.5	14.0	0.5	2.2	2.9	0.5	0.28	0.29	0.43	9.5								
	1.6-1.8	70.9	8.0	13.6	0.6	2.7	2.7	0.4	0.25	0.36	0.41	8.8								
	2.0-2.24	72.2	8.0	12.9	0.5	2.2	2.9	0.4	0.29	0.29	0.46	9								
BaTiO <sub>3</sub>	1.25-1.4	53.1	8.9	11.1	2.5	13.8	2.4	1.6	0.40	5.28	0.86	6								
	1.6-1.8	59.0	9.3	12.4	2.1	11.4	2.5	1.3	0.37	0.96	0.69	6.3								
	2.0-2.24	61.4	8.9	13.7	1.8	9.0	2.8	0.8	0.33	0.59	0.57	6.9								
Y-Al <sub>2</sub> O <sub>3</sub>	2.0-2.24	70.1	8.5	15.4	0.6	2.0	0.4	0.0	3.0	0.0	0.0	8.3								

#### 4.2.6 Discussion

The results of the non-packed reactor show an interesting way of tuning product fractions. By reducing the residence time (higher flow rate), the ratio of  $\text{CO}_2/\text{CH}_4$  conversion is similar, but the fraction of the products can be altered. Indeed, shorter residence times seem to produce less CO and more oxygenates, hinting towards a kinetic effect that will determine the product fractions. Indeed, model calculations predict that the rates of formation of different products are different [147]: some products rise quickly, while others rise more slowly as a function of time, or go over a maximum, because they are converted into another product. Hence, depending on the residence time (and thus flow rate), the product fractions can be altered.

Not only the residence time in the plasma/reactor has an influence on the conversion and product fractions, but also the residence time of species in contact with the surface of the packing materials. Indeed, according to the Sabatier principle, the residence time and binding energy between the adsorbing molecule and the surface should be long/strong enough for conversion to take place, while the residence time and binding energy between the products and the surface should be short/weak, so that the product can easily desorb. However, in case of plasma-assisted conversion, also many other underlying mechanisms, both physical and chemical, that take place simultaneously, can influence the reactions (both partial chemical equilibrium and kinetics) and thus conversion and product distribution.

Indeed, based on the results, packing materials as well clearly influence the plasma chemistry, as can be deduced from the different  $\text{CO}_2/\text{CH}_4$  conversion ratios and product fractions. The difference in the  $\text{CO}_2/\text{CH}_4$  conversion ratio can be caused by many factors, such as differences in discharge type, the number and transferred energy of the streamers, the streamer propagation, electric field enhancement, electron temperature difference, surface adsorption effects, etc. No clear correlation can be made to the material properties (Appendix: section 9.1 and Table 6). Indeed, all these

differences influence the CO<sub>2</sub> and CH<sub>4</sub> conversion, and thus the resulting products formed, due to differences in gain and loss reactions. In the previous chapter on pure CO<sub>2</sub> splitting, we could correlate the impact of bead size and material to differences in number of contact points, size of void spaces and to some extent the dielectric constant of the material, but it could not explain all data, so other underlying mechanisms must be present as well. Even though we expect differences induced by changes in the discharge mode and discharge properties, due to the differences in e.g. dielectric constants of the packing materials, the data extracted from the electrical characterisation display no straightforward correlation to the observed differences in CO<sub>2</sub>/CH<sub>4</sub> conversion. Nevertheless, not all differences in discharge behaviour can be measured. For example, modelling has revealed important differences in streamer propagation and/or streamer versus surface discharge behaviour, positive restrikes and local discharges for packed bed reactors, depending on the dielectric constant of the packing material [148]. Moreover, the same modelling study showed that the impact of the discharge mode will be different for different chemical species, and thus its impact on CO<sub>2</sub> and CH<sub>4</sub> conversion, as well as on the intermediate species and products, might vary, resulting in the observed differences in CO<sub>2</sub>/CH<sub>4</sub> conversion and product distribution. This complex interplay induced by the packing is too complex to postulate the underlying mechanisms for the observed differences in the data [148] and requires much more extended research, focused on materials with systematically altered properties, as well as extensive modelling.

Furthermore, some packing materials, such as Al<sub>2</sub>O<sub>3</sub>, behave superior to the others, both in case of CO<sub>2</sub> and CH<sub>4</sub> conversion, indicating that the observed results are not only related to the dielectric constant and its effects on the electrical properties of the plasma. Indeed, otherwise BaTiO<sub>3</sub> (which has the highest dielectric constant) would provide the best results, which is clearly not the case. Moreover, if the results would only be correlated to the dielectric constant of the material, α- and γ-Al<sub>2</sub>O<sub>3</sub>, both having the same dielectric constant, would yield the same conversion. This indicates that other

effects, such as the surface area and/or the surface acidity, may lie at the base of this difference. Nevertheless, the fact that BaTiO<sub>3</sub> performs worse than the other materials can also be correlated to some extent to the electrical properties, because Wang et al. predicted by modelling that materials with higher dielectric constant constrain the discharge to the contact points of the packing materials. They suggested that this can limit surface activation due to a lower surface area in contact with the discharge [148]. On the other hand, materials with a higher dielectric constant result in a higher electric field enhancement, which will also be beneficial for CO<sub>2</sub> and CH<sub>4</sub> conversion [57,139]. Hence, these are opposite effects, and this could explain why Al<sub>2</sub>O<sub>3</sub> is a superior material, having an “intermediate” dielectric constant of 9, while BaTiO<sub>3</sub> (with a dielectric constant of ~4000 [111]) is performing worse. It should be noted that BaTiO<sub>3</sub> gave the best results in pure CO<sub>2</sub> splitting, indicating that the effect of electric field enhancement was in that case more important than the effect of the surface discharges. The role of surface discharge behaviour on CH<sub>4</sub> conversion (and vice versa) thus seems important, although this is only a hypothesis.

Other literature reports also support this careful hypothesis, suggesting a difference in behaviour of CH<sub>4</sub> and CO<sub>2</sub> conversion. Indeed, Snoeckx et al. predicted by modelling that CO<sub>2</sub> is not only converted during the microdischarge filaments in a DBD reactor, but is also able to react further in the afterglow (both in between filaments as well as post-plasma), whereas CH<sub>4</sub> is mainly converted during the filaments and is being formed again (by recombination of reaction products) in the afterglow [47]. Nevertheless, the effect of different packing materials and sizes on the CH<sub>4</sub>/CO<sub>2</sub> conversion ratios might be more complicated, as a result of several other mechanisms as well, so it is not possible to explain all differences in detail. Thus, due to the complex and intertwined nature of the chemistry and physical effects at play, extensive modelling would be needed to confirm or reject this first hypothesis as part of the possible underlying mechanisms.

In addition to the above possible mechanisms, also other interesting hypotheses can be made, based on the surprising result of the difference in performance of BaTiO<sub>3</sub> in DRM versus pure CO<sub>2</sub> splitting.

Based on the results of pure CO<sub>2</sub> splitting, it is possible that BaTiO<sub>3</sub> strongly promotes the equilibrium of CO<sub>2</sub> splitting towards CO and O. In combination with a high CH<sub>4</sub> conversion (CH<sub>4</sub>/CO<sub>2</sub> conversion ratio of 2), which results in a high fraction of H atoms, the O atoms might recombine with H atoms into OH. The latter can further react towards oxygenated components (explaining the higher fractions of oxygenates in the presence of BaTiO<sub>3</sub>), as well as towards H<sub>2</sub>O (and possibly HO<sub>2</sub> and H<sub>2</sub>O<sub>2</sub>). The trapping of O atoms into OH radicals and H<sub>2</sub>O, when small amounts of CH<sub>4</sub> are added to CO<sub>2</sub> streams, has been predicted by modelling [149]. In the latter paper, it was described as a positive effect, because it allowed easier separation of the produced gas mixture, but the study was only applied for a few % of CH<sub>4</sub> addition to CO<sub>2</sub>. Due to the high performance of BaTiO<sub>3</sub> towards CO<sub>2</sub> splitting, as demonstrated in our previous work (see Chapter 3), a much higher concentration of OH radicals might be present here, engaging in other (more negative) reactions, lowering the conversion. Indeed, recent modelling studies of CH<sub>4</sub>/O<sub>2</sub> mixtures have indicated a preferential formation of H<sub>2</sub>O from OH radicals [147]. These H<sub>2</sub>O molecules will promote the back reaction of CO into CO<sub>2</sub>, as suggested based on CO<sub>2</sub>/H<sub>2</sub>O models [150]. This can explain the lower CO<sub>2</sub> conversion in DRM for a BaTiO<sub>3</sub> packing, compared to pure CO<sub>2</sub> splitting. We cannot measure H<sub>2</sub>O with our GC, but the deficits in the oxygen and hydrogen balance (see Figure 35) suggest that indeed a large amount of H<sub>2</sub>O might be formed. However, more research is needed to verify the above hypotheses. Note that the high amounts of OH radicals can not only cause back reactions of CO into CO<sub>2</sub>, but can also explain the higher oxygenate content in case of the BaTiO<sub>3</sub> packing compared to the other materials. It is thus advised, when aiming for a suitable catalyst for plasma-based DRM, to search for a material that benefits the reaction of OH towards CHO (limiting water formation) or further towards CH<sub>3</sub>O<sub>2</sub> instead of towards H<sub>2</sub>O, therefore quenching the OH radicals in

preferred products rather than in water. Alternatively, a packing material that promotes water splitting could be beneficial. Finally, to limit the formation of H<sub>2</sub>O, a packing material that can function as an oxygen-scavenger at the mild temperatures of a DBD might be useful, although this would require a cyclic process of oxidation and reduction. The different reaction pathways mentioned in this reasoning, and adopted from modelling, are shown in the Appendix, section 9.5 (Figure 89-Figure 91).

Nevertheless, the above reasoning is only a first hypothesis, as other materials exhibiting a lower CO<sub>2</sub> conversion in case of DRM versus pure CO<sub>2</sub> splitting (i.e. ZrO<sub>2</sub> with bead size of 2.0-2.24 mm) do not result in a higher fraction of oxygenated products. This might be due to a difference in kinetics between the back reaction of H<sub>2</sub>O with CO<sub>2</sub> versus oxygenate formation. However, much more experimental and modelling work is needed to substantiate this hypothesis.

Finally, the CH<sub>4</sub> conversion is always higher than the CO<sub>2</sub> conversion, due to the lower C-H bond dissociation energy compared to C=O bond dissociation energy, for all packing materials and bead sizes. However, the CH<sub>4</sub>/CO<sub>2</sub> conversion ratio varies from 1.2 to 2.3 (see Table 17), so the difference is more pronounced for some materials than for others. This suggests that for those packing materials with a lower CH<sub>4</sub>/CO<sub>2</sub> conversion ratio (e.g. 1.25-1.4 mm α-Al<sub>2</sub>O<sub>3</sub> and BaTiO<sub>3</sub>, and 2.0-2.24 mm SiO<sub>2</sub> and α-Al<sub>2</sub>O<sub>3</sub>; see Table 17), the situation is more complicated, e.g. a back reaction or an impact on the kinetics of CH<sub>4</sub> conversion or CO<sub>2</sub> conversion is taking place.

### 4.3 CONCLUSION

The aim of this chapter was to study the influence of different packing materials on the conversion and product fractions formed in DRM in a packed bed DBD reactor, and to compare this to our previous work on CO<sub>2</sub> splitting (cf. the previous chapter).

For this purpose, five different packing materials in three different sizes, that were not explicitly activated with catalytically active elements but could be catalytic in nature, were compared. The following conclusions can be drawn:

The highest CO<sub>2</sub>, CH<sub>4</sub> and total conversion obtained in the packed bed reactor was 22.5 %, 32.8 % and 27.7 %, respectively, for  $\alpha$ -Al<sub>2</sub>O<sub>3</sub> beads with a diameter of 2.0-2.24 mm. In the non-packed reactor at equal flow rate, the CH<sub>4</sub> and total conversion yielded even higher values of 37.3 and 28.5 %, respectively, due to the longer residence time. Analysis of the packing materials before and after plasma confirmed that most of the packing materials have a high resistance to coking, although SiO<sub>2</sub> showed clear D and G bands.

It was clearly evidenced that the type and size of packing materials cannot only influence the overall conversion, but also the CH<sub>4</sub>/CO<sub>2</sub> conversion ratio and the product fractions, even without being activated with catalytic elements. This emphasises the importance of studying all essential aspects of a catalyst in case of plasma catalysis, including the non-catalytically activated support material.

Depending on the packing material applied, very high CO/H<sub>2</sub> ratios can be obtained, hinting to mechanisms where the H atoms (originating from CH<sub>4</sub>) are mainly involved in the formation of hydrocarbons or oxygenated products, rather than into H<sub>2</sub>.

By studying two types of Al<sub>2</sub>O<sub>3</sub> ( $\alpha$  and  $\gamma$ ), with the same dielectric constant, we can conclude that apart from differences in electrical characteristics and discharge behaviour, other materials' chemistry or structural (e.g. porosity) related features have a vast impact on product formation, leading to a very different product distribution, in case of  $\alpha$ -Al<sub>2</sub>O<sub>3</sub> versus  $\gamma$ -Al<sub>2</sub>O<sub>3</sub>. It has to be noted that  $\gamma$ -Al<sub>2</sub>O<sub>3</sub> results in the highest

product selectivity (higher than  $\alpha$ -Al<sub>2</sub>O<sub>3</sub>), with no detectable fractions of oxygenated products, except for a 10-fold higher ethanol formation (fraction of 3 %), in combination with a high CO content (~70 %), the latter being similar to  $\alpha$ -Al<sub>2</sub>O<sub>3</sub>.

Another interesting observation was the discrepancy between the high CO<sub>2</sub> conversion of BaTiO<sub>3</sub> for CO<sub>2</sub> splitting, in contrast to the low CO<sub>2</sub> conversion in case of DRM. A possible explanation for this was put forward, based on models that hint towards the recombination of O and H atoms into OH, and possibly enhanced back reactions. However, further studies, including both extensive modelling and plasma catalysis with materials with systematically altered properties, are required to confirm the complicated interplay of the different mechanisms.

In general, we can conclude that, even without a catalytic activation, the packing material already has a vast effect on the conversions and product fractions. This indicates the importance of studying all materials aspects in case of plasma catalysis, including the non-activated packing materials. Furthermore, it shows that more research is needed, which has to combine extensive modelling with material research, to unravel the mechanisms at play. Finally, it exemplifies the tremendous future opportunities to create catalysts with true synergy in packing material and active element that can significantly impact both conversion and selective production of chemicals, allowing to steer DRM to different types of products, ranging from oxygenates to higher hydrocarbons in a one-step process, making plasma-catalytic DRM competitive with thermal DRM in the future.



## 5 STUDY OF DRY REFORMING: THE PECULIAR CASE OF BaTiO<sub>3</sub> PACKING MATERIAL

---

## 5.1 STATE OF THE ART

In the previous chapters, we gave a detailed overview of recent developments [151], indicating that still a number of aspects of DRM in a packed bed DBD need to be uncovered. For example, when implementing a packing material in the plasma, even without further catalytic activation, there is already a vast impact on the conversion and selectivity [53,74,80]. Nevertheless, researchers do not always compare with non-activated packing materials when implementing a catalytically activated packing material in a DBD reactor, missing some important insights [64–67,70–72,78,79]. Hence, we believe there is a clear need for more detailed studies of the effect of the packing material itself in a DBD, prior to further activation.

In addition, literature on plasma-based DRM reports either an increase in conversion [64–71], a decrease in conversion [71–73], or an effect on only one of the two reacting gases [70,74–76] when adding a packing material to the DBD reactor.

A possible reason for the discrepancy in literature results was hinted in our previous work [80,142], where we observed a large effect of the reactor setup and reactor/bead size combination on the conversion of pure CO<sub>2</sub>. This showed that comparing conclusions made with different setups, is extremely difficult. Nevertheless, it does not explain the exceptional behaviour of BaTiO<sub>3</sub> in the CO<sub>2</sub> splitting reaction versus the DRM reaction, which was performed in the same set-up (reported in Chapter 4). Indeed, BaTiO<sub>3</sub> was the best performing packing material in the splitting of CO<sub>2</sub> into CO and O<sub>2</sub>, while its performance was unexpectedly lowest among the evaluated packing materials when a 50/50 ratio CO<sub>2</sub>/CH<sub>4</sub> was used [151]. Therefore, to better understand the impact of the plasma and the BaTiO<sub>3</sub> packing material on the conversion of both CO<sub>2</sub> and CH<sub>4</sub>, we compare here DRM with experiments carried out for the feed gases (CO<sub>2</sub> and CH<sub>4</sub>), for different reactor/bead size combinations, for the specific case of BaTiO<sub>3</sub>.

These different reactor gap sizes affect the reactor volume, and therefore the residence time at constant flow rate. As both flow rate and residence time affect the conversion,

we will carry out all experiments (for the different bead sizes) both at equal flow rate and at equal residence time.

This way, we hope to reveal important insights, necessary to improve the synergy in plasma catalysis, by a better understanding of the mutual effect between a BaTiO<sub>3</sub> packing and plasma.

## 5.2 EXPERIMENTAL SETUP

Table 20: Operating conditions and materials used in this work.

Parameter	Specification
Gap (mm)	4.5; 3.5; 2.5; 2
Frequency (kHz)	23.5
Applied power on the power supply (Watt)	100
Type of material	BaTiO <sub>3</sub>
Diameter beads (range; mm)	1.18 – 1.25; 1.25 – 1.4; 1.4 – 1.6; 1.6 – 1.8; 2.0 – 2.24
CO <sub>2</sub> /CH <sub>4</sub> ratio	1/1
Temperature	Ambient (no external heating)
Pressure	1 atm. for blanc measurements ± 1.2 atm. for plasma measurements

We used BaTiO<sub>3</sub> as the spherical packing material, because it gave strikingly different results in our previous work for DRM vs CO<sub>2</sub> splitting. Indeed, out of four different packing materials, it performed best in CO<sub>2</sub> splitting (see Chapter 3), while it performed worst for DRM at the same conditions (see Chapter 4). The reactor setup is the same as described in Chapter 2 and the reaction conditions tested in this Chapter are listed in Table 20. All calculations done are also described in Chapter 2.

The resulting electrical data are shown in Table 22 and Table 23. Next to the influence of the four different gap sizes (4.5, 3.5, 2.5 or 2 mm) and five bead size ranges (Table 20), also the influence of the flow rate (residence time) of the gases on the conversion and product fractions for DRM and for the individual components has been evaluated.

Since the residence time changes for different gap and bead sizes at constant flow rate, and it influences the conversion (a longer residence time results in a higher conversion), experiments were performed at a constant residence time (5.5 seconds), hence varying the flow rate. However, for industrial purposes, the flow rate is important, and therefore, we also study the performance at a constant flow rate of 50 ml/min, hence resulting in different residence times.

A summary of the performed experiments is shown in Table 21. When varying the gap size, we also vary the bead size, so that the ratio of bead size/gap size remains constant (first three and last three rows in the table; set 1a and 1b). When keeping the ratio between the bead and gap size constant, the number of contact points between the beads stays constant. Since these contact points have a large effect on the electric field [53], experiments where this factor is kept constant while others are varied, can provide valuable insights.

In addition, we also vary the bead size at constant gap size (middle three rows in Table 21; set 3). In this case, the residence time, and thus also the specific energy input, is the same at constant flow rate. Lastly, we varied the gap size at constant bead size (set 2). Upon altering the bead size and gap size, differences are induced in the void space between 2 beads, the total number of beads in the reactor and the total surface area of the packing. These variations are summarised in the last 3 columns of Table 21.

Table 2.1: Summary of the combination of gap size, bead sizes and flow rates used in this work.

Set	Gap size (mm)	Bead size (mm)	Ratio bead size/gap size	Residence time (s)	Flow (ml/min)	SEI (eV/molecule)	a	b	c
1a	2.0	1.18-1.25	1.7	2.9	50	17	1.2	1255	23342
	2.5	1.4-1.6	1.7	3.6	50	17	1.5	808	22857
	3.5	2.0-2.24	1.7	4.6	50	17	2.1	372	21020
3	4.5	2.0-2.24	2.1	5.5	50	17	2.1	443	25023
	4.5	1.6-1.8	2.7	5.5	50	17	1.7	858	31140
	4.5	1.25-1.4	3.4	5.5	50	17	1.3	1794	39828
1b	2.0	1.18-1.25	1.7	5.4	27	31	1.2	1255	23342
	2.5	1.4-1.6	1.7	5.5	32	26	1.5	808	22857
	3.5	2.0-2.24	1.7	5.5	42	20	1.7	372	21020

a) Average length of a void space between 2 beads (mm) (based on the average bead diameter)

b) Number of beads in the reactor =  $\frac{\text{Volume per bead}}{\text{Total reactor volume}}$

c) Total bead surface area (mm<sup>2</sup>) = Number of beads in the reactor x surface area per bead

## 5.3 RESULTS AND DISCUSSION

### 5.3.1 Conversion for DRM in comparison with the conversion of the individual components, at equal flow rate

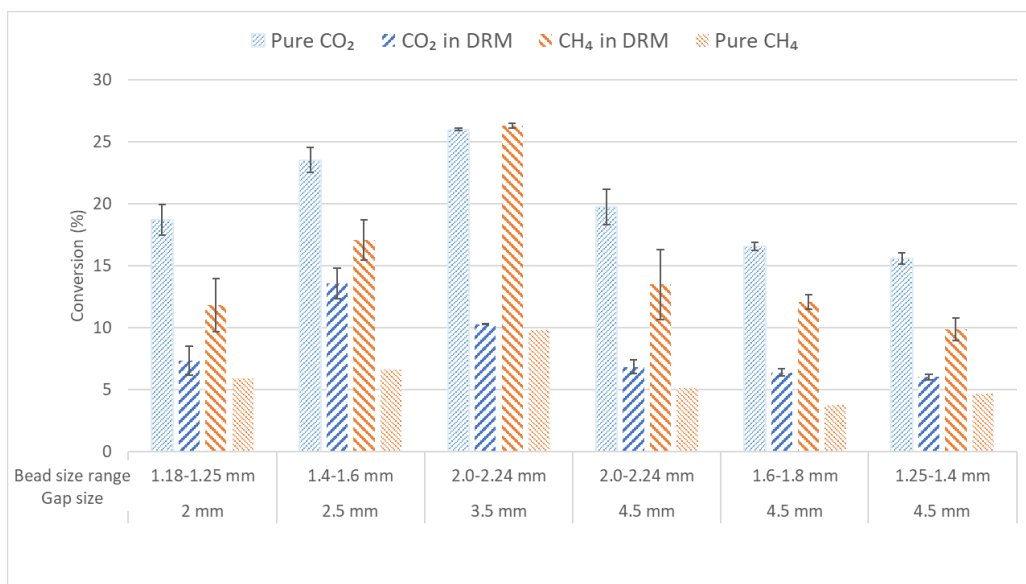


Figure 37: CO<sub>2</sub> and CH<sub>4</sub> conversion in DRM in comparison with the pure component conversions, as a function of different bead size ranges and gap sizes, at 50 ml/min and constant SEI (experiment set 1a, 2 and 3).

In Figure 37, we plot the CO<sub>2</sub> and CH<sub>4</sub> conversions in DRM, for different bead size ranges and gap sizes (two middle bars in each case). Furthermore, also the conversion of pure CO<sub>2</sub> and CH<sub>4</sub> are plotted (right and left of the DRM results). For completeness, the carbon-, hydrogen- and oxygen balance are added in the Appendix (section 9.4, Figure 87). These balances show a strong dependence of the reactor configuration and residence time.

For all DRM experiments the CO<sub>2</sub> conversion is lower than the CH<sub>4</sub> conversion. However, when comparing with the pure gas conversions, an unexpected higher CO<sub>2</sub> (factor of 3 or more) conversion than CH<sub>4</sub> conversion is observed in each of the gap/bed

conditions, even though a lower energy is required to split a C-H bond. Moreover, an interesting observation is that the ratio of CO<sub>2</sub>/CH<sub>4</sub> conversion is not the same for all conditions, even though the CO<sub>2</sub>/CH<sub>4</sub> ratio in the feed is constant. This means that the energy transfer to both gases (or between the gases and species present) is not the same for all applied bead and gap size ranges and combinations. This can be caused by (a combination of) many underlying differences: e.g. residence time, surface area, electric field changes, void space sizes, number of contact points between the beads, differences in discharge behaviour, etc.. Moreover, when comparing the conversion in different gap sizes with the results of the constant gap size (4.5 mm) in the case of DRM, it seems that the residence time has an important impact on the DRM, as it is almost constant at 4.5 mm gap, while it differs (with a maximum at 3.5 mm) at varying gap size. Nevertheless, a direct linear correlation with residence time is not present, as a maximum is observed at 3.5 mm, which is not the highest residence time (see Table 21). Note that again results are very different for pure CO<sub>2</sub> and CH<sub>4</sub> conversion, as they do alter at constant gap size (residence time) in a response to the change in bead size. Hence, it is clear that both CO<sub>2</sub> and CH<sub>4</sub> are affected by multiple differences in the packing and reactor configuration and that a complex behaviour can be expected due to the different response of CO<sub>2</sub> and pure CH<sub>4</sub> (e.g. due to different discharge modes) and their mutual interaction. This was also seen in modelling, although for a non-packed reactor and for different conditions [47].

To elucidate the role of residence time further, the same reactor configuration (data set 1a) was applied but with a constant residence time (data set 1b). The results are compared in Figure 38. Although a more stable total conversion is observed, differences as a function of bead size and gap size ranges remain visible, indicating a more complex underlying mechanism. Furthermore, it is clear from Figure 38, that CO<sub>2</sub> and CH<sub>4</sub> have a different response to bead/gap size configurations as a function of residence time. For completeness, the carbon, hydrogen and oxygen balance are added in the Appendix (section 9.4, Figure 88). As can be seen, these balances strongly depend on the flow rate and the reactor configuration.

Going back to Figure 37, when comparing with the pure gas conversions, the CO<sub>2</sub> conversion always drops upon adding CH<sub>4</sub> to the feed, while the CH<sub>4</sub> conversion always increases upon adding CO<sub>2</sub> to the feed.

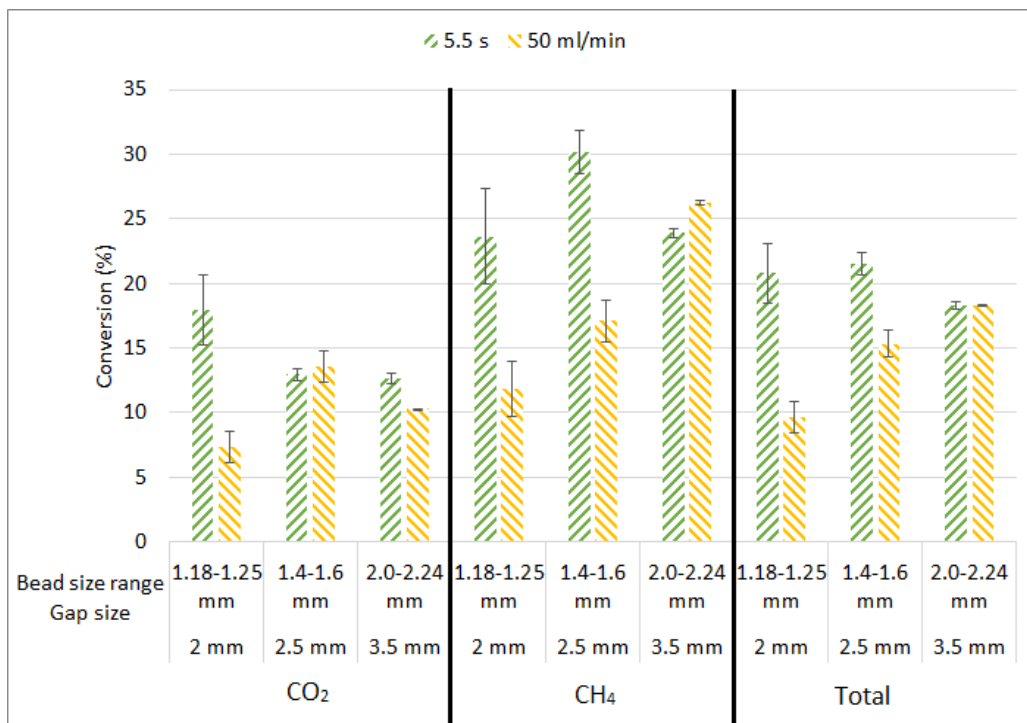


Figure 38: CO<sub>2</sub>, CH<sub>4</sub> and total conversion in DRM, as a function of different bead size ranges and gap sizes, at 5.5 seconds residence time and 50 ml/min.

The electrical data for the experiments discussed in Figure 37 and Figure 38 are shown in Table 22 and Table 23. Again, they do not show a clear correlation between the conversion obtained and the electrical characteristics. It is again important to note that differences in the average charge per filament can be induced by the reactor configuration; the fact that a low charge and many pulses gives the same result as a high charge and few pulses; the fact that a non-packed reactor often gives few strong pulses while a packed reactor gives many weak pulses. Moreover, it is impossible to determine the difference between a streamer between the electrode and the dielectric barrier, between the electrode and a bead, between 2 beads, between a bead and the



dielectric barrier, in the current profile. Therefore, it is also impossible to determine the difference between surface discharges versus local filamentary discharges.

Table 22: Electrical characterisation for Figure 37 (DRM, pure CO<sub>2</sub> conversion and pure CH<sub>4</sub> conversion).

Gap size	Bead size	Plasma Power (W)	U <sub>bur</sub> (kV)	U <sub>pp</sub> (kV)	Average charge per filament (nC)	Number of discharges	I <sub>RMS</sub> (mA)
2 mm	1.18 - 1.25 mm	58.89	2.75	16.57	3511	139	38
2.5 mm	1.4 - 1.6 mm	65.65	3.66	15.41	12892	35	38
3.5 mm	2.0 - 2.24 mm	63.82	3.49	15.75	19897	22	35
4.5 mm	2.0 - 2.24 mm	66.94	2.24	11.27	5240	131	50
4.5 mm	1.6 - 1.8 mm	65.28	2.19	11.58	5300	136	50
4.5 mm	1.25 - 1.4 mm	63.96	2.08	11.54	5365	133	51
2 mm	1.18 - 1.25 mm	66.92	1.20	12.94	7.22	156	71
2.5 mm	1.4 - 1.6 mm	67.73	1.62	13.20	9.32	153	58
3.5 mm	2.0 - 2.24 mm	67.40	2.12	13.19	5140	159	57
4.5 mm	2.0 - 2.24 mm	61.85	2.08	13.14	4.41	148	51
4.5 mm	1.6 - 1.8 mm	58.65	1.99	12.86	5.01	143	53
4.5 mm	1.25 - 1.4 mm	61.85	1.98	13.87	4.78	150	54
2 mm	1.18 - 1.25 mm	50.28	1.70	10.99	4810	135	51
2.5 mm	1.4 - 1.6 mm	56.62	1.84	10.92	4858	150	51
3.5 mm	2.0 - 2.24 mm	70.05	2.32	11.70	5348	138	49
4.5 mm	2.0 - 2.24 mm	69.52	2.15	12.24	4726	150	52
4.5 mm	1.6 - 1.8 mm	69.62	2.24	11.09	5082	130	50
4.5 mm	1.25 - 1.4 mm	66.34	2.32	11.51	7495	102	51

Table 23: Electrical characterisation for Figure 38.

Gap size	Bead size	Plasma Power (W)	U <sub>bur</sub> (kV)	U <sub>pp</sub> (kV)	Average charge per filament (nC)	Number of discharges	I <sub>RMS</sub> (mA)
2 mm	1.18 - 1.25 mm	50.28	1.70	10.99	4810	135	51
2.5 mm	1.4 - 1.6 mm	56.62	1.84	10.92	4858	150	51
3.5 mm	2.0 - 2.24 mm	70.05	2.32	11.70	5348	138	49

### 5.3.2 Product fractions

Table 24 shows the product fractions for the different experiments at equal flow rate and equal residence time for all data sets.

There are clear difference in specific product fractions (formaldehyde, ethyne, CO and DME), and less distinct differences for the other product fractions.

When looking at the fraction of DME, it is clearly visible that, when keeping the ratio between bead size and gap size constant, the fraction remains 0%, no matter at which residence time (data set 1a and 1b). The difference in fractions of DME at larger gap sizes seems to be caused by another characteristic than those mentioned in Table 21. For formaldehyde on the other hand, the residence time/flow rate has a clear influence on the product fractions, since dataset 1a and 1b only differ in residence time and have a very different fraction of formaldehyde. Nevertheless, the correlation between the fraction of formaldehyde and residence time is not linear, nor the only influencing condition, indicating that other parameters play a role as well. This is also confirmed by the differences in dataset 3, which shows a clear difference in formaldehyde content although the residence time/flow rate is constant.

Upon increasing the residence time, there is a decrease in the fraction of ethyne when combining dataset 1a with 1b, while dataset 3 again indicates that the influence on the ethyne formation by other parameters than residence time/flow rate is much larger. For unsaturated hydrocarbons (ethene, ethyne), the best result is obtained with 1.25-1.4 mm beads in a 4.5 mm gap, while for saturated hydrocarbons (ethane), the best result is obtained with the larger beads (2.0-2.24 mm) in the same 4.5 mm gap.

To increase the fraction of unsaturated hydrocarbons, it is possible to add a packing material that functions as a hydrogen scavenger, or a dehydrogenation catalysts. On the other hand, hydrogen trapping will decrease the fraction of hydrogen available to form saturated hydrocarbons, unless the material that scavenges the hydrogen, will also catalyse the reaction of the trapped hydrogen towards saturated hydrocarbons.

The highest amount of oxygenated products is obtained for the smallest beads (in the larger gaps). The highest ratio of CH<sub>4</sub> conversion/CO<sub>2</sub> conversion is reached for the 2.0-

2.24 mm beads in the 3.5 mm reactor at 50 ml/min, while at constant residence time, it is reached for the 1.4-1.6 mm beads in the 2.5 mm gap.

Table 24: Product fractions in DRM, as a function of different bead size ranges and gap sizes.

Set	Flow (ml/min)	Gap (mm)	Bead size (mm)	Product fractions												CO/H <sub>2</sub>	CH <sub>4</sub> /CO <sub>2</sub>
				CO	H <sub>2</sub>	Ethane	Ethene	Ethyne	DME	Ethanol	Propane	Formaldehyde	Methanol				
1a	50	2	1.18-1.25	57.5%	8.7%	12.1%	2.2%	10.4%	0%	0.3%	2.6%	5.2%	1.0%	6.6	1.6		
	50	2.5	1.4-1.6	64.1%	8.8%	12.6%	1.6%	7.7%	0%	0.3%	2.6%	1.4%	0.8%	7.3	1.3		
	50	3.5	2.0-2.24	63.4%	8.9%	12.6%	1.6%	7.6%	0%	0.3%	2.8%	1.9%	0.9%	7.1	2.6		
2	50	4.5	2.0-2.24	61.4%	8.9%	13.7%	1.8%	9.0%	0.8%	0.3%	2.8%	0.6%	0.6%	6.9	2.0		
	50	4.5	1.6-1.8	59.0%	9.3%	12.4%	2.1%	11.4%	1.3%	0.4%	2.5%	1.0%	0.7%	6.3	1.9		
3	50	4.5	1.25-1.4	53.1%	8.9%	11.1%	2.5%	13.8%	1.6%	0.4%	2.4%	5.3%	0.9%	6.0	1.6		
	27	2	1.18-1.25	65.0%	9.2%	12.6%	1.3%	6.4%	0.0%	0.3%	2.9%	1.6%	0.7%	7.1	1.3		
1b	32	2.5	1.4-1.6	66.1%	9.4%	12.5%	1.1%	5.8%	0.0%	0.3%	2.9%	1.1%	0.7%	7.0	2.3		
	42	3.5	2.0-2.24	63.2%	8.9%	13.0%	1.4%	7.3%	0.0%	0.3%	2.9%	2.2%	0.8%	7.1	1.9		

As a final observation, it is important to realize that even when no catalytically active element is coated on the packing material, the packing material itself, more specifically the bead size, as well as the reactor gap size and the operating conditions (e.g. flow rate) have a clear influence on the product fractions. Hence, this must be accounted for when studying the effect of catalytic materials on the conversion and product fractions in plasma catalytic reactions.

### 5.3.3 Discussion

As can be seen from Table 21, a lot of parameters can influence both conversion and product fractions and no direct correlations can be made with any single parameter listed in Table 21 or electrical data recorded (see Table 22 and Table 23). This points to a complex role of intertwined parameters or including possibly unidentified or not yet measured parameters. However, it is not straightforward to change only one of the parameters in the reactor, which will be a challenge to elucidate the underlying mechanisms further in future research.

For set 1 (both a and b), the number of contact points and the cumulated void space between the beads remains constant, while the residence time increases as well as the bead size and thus also the length of the voids between them. In contrast, the total bead surface decreases. When comparing line 1a with line 1b, only the residence time alters. For data set 2, the number of contact points and the total surface area increase, while the length of the void between the beads remains constant. For data set 3, the number of contact points and the surface increase, while the length of the voids decreases.

Moreover, the residence time distribution can be altered by varying the packing of the beads in the reactor. Indeed, depending on the packing of the beads, the gas pathway can be altered and thus the contact time between the beads and the surface, which will alter the number of molecules adsorbing on this surface and thus the conversion and product fractions. How many beads are packed in the same gap size, will also alter the surface to volume ratio and thus how much product can interact with the packing material.

As can be seen, a lot of different parameters influence the CO<sub>2</sub> and CH<sub>4</sub> conversion, the difference between the conversion in DRM and for the pure component, and the ratio between CO<sub>2</sub> and CH<sub>4</sub> conversion.

Part of the explanation lies in a combination of SEI and energy transfer between the CO<sub>2</sub> and CH<sub>4</sub> molecules in a CO<sub>2</sub>/CH<sub>4</sub> plasma. For the individual components, the conversion was established by applying 100 Watt, yielding ± 60 Watt plasma power for 50 ml/min. For DRM, we again applied 100 Watt, yielding ± 60 Watt plasma power, for a total flow of 50 ml/min, which will be divided over both components. This equals a SEI of 17 eV/molecule in all experiments of data set 1a and 3 and for the pure component measurements shown in Figure 37. Plasma chemistry modelling [41] predicts an important charge transfer reaction from CO<sub>2</sub><sup>+</sup> ions to CH<sub>4</sub> molecules, (equation 10), which is very important during the streamers in the DBD plasma [47].



Furthermore, we know from streamer propagation modelling (for dry air) in a packed bed DBD that for packing materials with a high dielectric constant (≈ 4000 for BaTiO<sub>3</sub>) the discharge mode will exhibit local filamentary discharges [148], so the above reaction will be important in these filaments.

The above reaction indicates that some of the plasma power (or energy) that is used to activate (i.e. ionise) the CO<sub>2</sub> molecules, will thus be transferred to the CH<sub>4</sub> molecules. Hence, less CO<sub>2</sub><sup>+</sup> ions and more CH<sub>4</sub><sup>+</sup> ions are expected. These ions will undergo dissociative recombination with electrons, contributing to the dissociation of the molecules. Therefore, the CH<sub>4</sub> conversion will increase upon adding CO<sub>2</sub> to the mixture, while the CO<sub>2</sub> conversion will decrease upon adding CH<sub>4</sub> and differs substantially from the pure component conversion.

Another mechanisms that possibly lies at the basis of these observations, is that CO<sub>2</sub> dissociates more in the afterglow, and less in the streamers, while CH<sub>4</sub> mainly dissociates in the streamers and even recombines in the afterglow [9]. This means that the conversion of CH<sub>4</sub> is strongly dependant on the number of streamers and the residence time in these streamers, opposed to the CO<sub>2</sub> conversion. Moreover, in the presence of CH<sub>4</sub> and CO<sub>2</sub>, the formed hydrogen reacts with the oxygen atoms of CO<sub>2</sub>, limiting the back reaction of hydrogen to CH<sub>4</sub> in the afterglow, enhancing the CH<sub>4</sub>

conversion. Indeed, at high CH<sub>4</sub> conversions, it is possible that so much OH is formed, that CO reacts back to CO<sub>2</sub> and H.

The distribution of all formed intermediary species will strongly alter the forward and backward reactions, depending on the differences in streamers and afterglow. The different bead and gap sizes are expected to affect the discharge behaviour, number of streamers, dissipated charge, electric field strength, surface charge, electron density etc. and thus also the intermediate species distribution. Other not yet identified aspects can cause differences such as e.g. surface discharge behavior and/or charging, sorption effects, etc.

This complex system of mechanisms and ratios in intermediary species will affect both conversions and the product fractions (as can be seen in section 5.3.2).

In support of this hypothesis, we observed experimentally a link between the average charge per filament (higher for stronger pulses; can be found in Table 22) and the CH<sub>4</sub> conversion for sets 1a, 2 and 3, which indeed indicates that the CH<sub>4</sub> conversion takes place in streamers and their afterglow, and thus increases with stronger pulses. Furthermore, we observe that the non-packed reactor often leads to few strong pulses, while the packed reactor generates more strong pulses. Moreover, modelling of a packed bed DBD reactor showed that larger beads lead to a higher electron density [139] and a higher electron density is accompanied by more streamers [152].

A factor that has a definite influence is the residence time, which is obvious when comparing data sets 1a and 1b. When comparing at equal residence time (set 1b), we can observe that now, instead of going over a maximum, the CO<sub>2</sub> conversion now decreases. The CH<sub>4</sub> conversion on the other hand, instead of increasing, now goes over a maximum. The factors influencing the conversion are the SEI, the void spaces, and the surface area (and all parameters that depend on these 3 characteristics). Since for these 3 data points, the SEI and the void space between the beads are affected greatly, while the total surface area decreases slightly, the resulting conversions for CO<sub>2</sub> and CH<sub>4</sub> are probably affected by a combination of these parameters.

Since the effects of all these parameters on the conversion is very complex, it is even more challenging to investigate the influence on the product fractions as they are determined by, among others, the intermediate species distributions and thus the conversion of  $\text{CO}_2$  and  $\text{CH}_4$ . As mentioned before, it is important to realize that even when no catalytically active element is coated on the packing material, the bead size and gap size of the packing, have a clear influence on the product fractions. Hence, this must be accounted for when studying the effect of catalytic materials on the product fractions in plasma catalysis.

## 5.4 CONCLUSION

We studied the influence of the flow rate/residence time, the gap size and its ratio to the bead size, on the conversion and product fractions for DRM in a packed bed DBD reactor, and we compared with experiments for the individual components (pure  $\text{CO}_2$  and  $\text{CH}_4$  conversion), to gain insight in how  $\text{CO}_2$  and  $\text{CH}_4$  affect the combined conversion. It is clear that the effect of the packed bed DBD reactor seems to be different for pure  $\text{CO}_2$  and  $\text{CH}_4$  versus the DRM mixture. This can be explained by a charge transfer reaction between  $\text{CO}_2^+$  and  $\text{CH}_4$ , in combination with a difference in behaviour of  $\text{CH}_4$  and  $\text{CO}_2$  in the streamers and in the afterglow, affecting dissociation and recombination behaviour in combination with kinetic effect when both gases are present, also affecting product formation.

From the experiments it is clear that none of the implied changes in gap sizes, bead size, surface area, etc. nor measurement of the electrical characteristics on its own can explain the differences observed in conversion and product fractions.

It is clear however, that some do have an effect. For example, the flow rate affects the SEI and thus the conversion, and when keeping the residence time constant, indeed trends shift compared to when keeping the flow rate constant.

As a final remark, it should be realized that the packing material itself, more specifically the bead size, as well as the reactor gap size, and flow rate conditions, clearly affect the product fractions, even without catalytic activation of the packing.





## 6 GENERAL CONCLUSION

---

In this thesis, we studied the conversion of CO<sub>2</sub> and CH<sub>4</sub>, two greenhouse gases, to value-added chemicals. This conversion is important to reach our sustainability goals, but quite challenging. A high potential technology to tackle the current challenges is plasma catalysis.

The plasma can work at mild conditions, i.e. room temperature and ambient pressure, but is a very reactive mixture, which is highly unselective. Therefore, a catalytic/packing material is added to the plasma. This material can be a packing, support or catalytically activated material, and can enhance the conversion both chemically and/or physically. Five different spherical packing materials, as well as quartz wool and glass wool, were inserted in a DBD reactor, to study CO<sub>2</sub> splitting, and the conversion, energy efficiency and selectivity for dry reforming of methane (DRM). Moreover, a comparison was made to the conversion for CO<sub>2</sub> and CH<sub>4</sub> as individual components, to obtain detailed insights about the effect that both gases induce on each other and the plasma chemistry.

In Chapter 3, we first compared the results for different materials and packing sizes in a 4.5 mm gap for CO<sub>2</sub> splitting, to avoid complexity issues introduced by studying selectivity (which comes into play when also CH<sub>4</sub> is added). We observed that the highest conversion was roughly a factor two higher than in the non-packed reactor with the same flow rate, and a factor four higher than in the non-packed reactor with the same residence time. The highest energy efficiency was the same when compared with the non-packed reactor at the same residence time (thus higher flow rate), but again almost twice as high when compared at the same flow rate. A distinct impact of the type of packing material and its size has been observed.

It was clear that three effects can play a role: (1) the positive contribution of the packing, due to electric field enhancement at the contact points; (2) a negative contribution due to the lower residence time in the presence of a packing; and (3) the influence of the

voids between the beads, with a positive or negative effect depending on the material. Depending on the bead size and material, one or the other effect will dominate, explaining their different behaviour in conversion and energy efficiency. In addition, the changes in conversion can only partially be related to the dielectric constant of the packing material, indicating that also other material parameters must play a role, as was also seen in Chapter 4 and 5. Further improvement in conversion and energy efficiency can be expected when a large number of contact points can be generated, while maintaining large void space volumes and a large ratio of packing size/gap size. In Chapter 4, we increased the complexity of the studied matrix, by adding CH<sub>4</sub> to the feed flow. This way, we did not only study the conversion for DRM in a packed bed DBD reactor, but we investigated the influence of different packing materials on the product fractions as well. All results were also compared to the ones for CO<sub>2</sub> splitting obtained in Chapter 3. Again, five different packing materials in three different sizes were compared and it was seen that the type and size of packing materials cannot only influence the overall conversion, but also the CH<sub>4</sub>/CO<sub>2</sub> conversion ratio and the product fractions, even without being activated with catalytic elements.

Depending on the packing material applied, very high CO/H<sub>2</sub> ratios can be obtained, hinting to mechanisms where the H atoms (originating from CH<sub>4</sub>) are mainly involved in the formation of hydrocarbons or oxygenated products, rather than into H<sub>2</sub>.

By studying two types of Al<sub>2</sub>O<sub>3</sub> ( $\alpha$  and  $\gamma$ ), with the same dielectric constant, we can conclude that apart from differences in electrical characteristics and discharge behaviour, other materials' chemistry (e.g. crystal phases, acidity) or structural (e.g. porosity) related features have a vast impact on product formation, leading to a very different product distribution, in case of  $\alpha$ -Al<sub>2</sub>O<sub>3</sub> versus  $\gamma$ -Al<sub>2</sub>O<sub>3</sub>. It has to be noted that  $\gamma$ -Al<sub>2</sub>O<sub>3</sub> results in the highest product selectivity (higher than  $\alpha$ -Al<sub>2</sub>O<sub>3</sub>), with no detectable fractions of oxygenated products, except for a 10-fold higher ethanol formation (fraction of 3 %), in combination with a high CO content (~70 %), the latter being similar to  $\alpha$ -Al<sub>2</sub>O<sub>3</sub>.

Another interesting observation was the discrepancy between the high CO<sub>2</sub> conversion in case of BaTiO<sub>3</sub> for CO<sub>2</sub> splitting, in contrast to the low CO<sub>2</sub> conversion in case of DRM. This was investigated further in Chapter 5.

In Chapter 5, we studied the influence of the flow rate/residence time, the gap size and its ratio to the packing size, on the conversion and product fractions for DRM for the particular case of BaTiO<sub>3</sub> as packing material. We compared with experiments for the individual components (pure CO<sub>2</sub> and CH<sub>4</sub> conversion), to gain insight in how CO<sub>2</sub> and CH<sub>4</sub> affect the combined conversion and product fractions.

Firstly, as expected, a longer residence time enhances the conversion. Moreover, the product fractions of CO and H<sub>2</sub> increase, while the product fractions of ethyne and formaldehyde are reduced.

Secondly, the effect of the packed bed DBD reactor seems to be different for pure CO<sub>2</sub> and pure CH<sub>4</sub>. The CO<sub>2</sub> conversion decreases upon adding CH<sub>4</sub>, while the CH<sub>4</sub> conversion increases upon adding CO<sub>2</sub>. This could be explained by a charge transfer reaction between CO<sub>2</sub><sup>+</sup> and CH<sub>4</sub>, which is very important in streamers, that are abundant (i.e., more filamentary microdischarges) at a high dielectric constant (BaTiO<sub>3</sub>). The CH<sub>4</sub> conversion is also always higher than the CO<sub>2</sub> conversion in DRM, and the higher the conversion, the larger the difference between both. This can be explained by the fact that CH<sub>4</sub> is dissociated in the streamers and recombines in the afterglows between the pulses, while CO<sub>2</sub> is also dissociated in the streamers, but to a lower extent, and converts even further in the afterglows between the pulses. The protons generated by the CH<sub>4</sub> conversion will cause more CO<sub>2</sub> conversion and prevent the back reaction of CH<sub>4</sub>. Moreover, the number of streamers and the discharge type can alter which will affect the CO<sub>2</sub> and CH<sub>4</sub> conversion. Which of these processes will be dominant, depends on the specific conditions.

Thirdly, when altering the gap size/bead size ratio, three different effects come into play, depending on whether the bead size is constant at altering gap size or vice versa, or whether both are altered at a constant ratio. Overall, the determining factor seems to be the altered number of beads (which is accompanied by an altered total surface

area and changing number of contact points between the beads) and the differing void space between two beads, affecting the electric field.

Concluding all chapters, we can first of all say that, upon analysing all packing materials before and after plasma, most of the packing materials have a high resistance to coking, although SiO<sub>2</sub> showed clear D and G bands of carbon in Raman measurements.

Moreover, results obtained in different gap sizes and at different residence times, show that the kinetics play an important role and influence the different gas components in a different way. Future studies should thus involve experiments at multiple residence times and with different gas ratios.

Regarding the influence of the packing on the plasma and vice versa, we can conclude that, even without a catalytic activation, the packing material already has a vast effect on the conversions and product fractions. This indicates the importance of studying all materials aspects in case of plasma catalysis, including the non-activated packing materials and their size and shape. Furthermore, it shows that more research is needed, which has to combine extensive modelling with material research, to unravel the mechanisms at play. Finally, it exemplifies the tremendous future opportunities to create catalysts with true synergy in packing material and active element as well as packing geometry, that can significantly impact conversion, energy efficiency and selective production of chemicals, allowing to steer DRM to different types of products, ranging from oxygenates to higher hydrocarbons in a one-step process, and thus hopefully making plasma-catalytic DRM competitive with thermal DRM in the future. Indeed, although the energy efficiency reached in this work is lower than that currently obtained for thermal DRM, the DBD reactor has the advantage to operate with a packing material and/or catalyst able to make other products than syngas and to use renewable energy as an energy source. The modular nature of the reactor in combination with intermittent use are extra advantages of catalytic plasma-assisted DRM.

As a future outlook, it can be advised to study the differences between CO<sub>2</sub> and CH<sub>4</sub> more in depth, by varying the ratio between the CO<sub>2</sub> and CH<sub>4</sub> feed composition. This

will not only alter the conversions and their ratios, but also the species distributions and thus the different product fractions. We believe that increasing the fraction of  $\text{CO}_2$  will increase the product fractions of CO and all oxygenated components, whereas both saturated and unsaturated hydrocarbons will have increased product fractions when increasing the  $\text{CH}_4$  feed fraction.

Also, as residence time obviously plays a crucial role, it is important to study this further, always keeping the importance of the reactor configuration in mind.

A further study towards the packing material and more specifically its volume-to-surface ratio and morphology can be carried out as well. Indeed, rigid 3D structures with varying geometry can help studying the influence of the flow patterns, the contact between the gas and the surface, mass and heat transport, etc.

As for catalysis, multiple catalytic elements can be coated on the packing materials tested in this work. These elements can differ in nature, but also in coated weight percentage, distribution, metal support interaction etc. This will all contribute to a better understanding of DRM in a packed bed DBD reactor, and thus aid in converting  $\text{CO}_2$  and  $\text{CH}_4$ , two waste molecules, into value-added chemicals.



## 7 SUMMARY

---

This thesis investigated dry reforming of  $\text{CH}_4$  (DRM) in a packed bed DBD reactor. The objective of this research was to improve the current understanding of plasma-catalytic interactions for  $\text{CO}_2$  splitting and DRM.

**Chapter 1** not only explains why there is a need for the conversion of these greenhouse gases, but also describes the current state of the art in  $\text{CO}_2$  splitting and DRM. It indicates the need for an energy-efficient technology that selectively produces value-added chemicals, and illustrates how plasma-catalysis can be a suitable technique.

**Chapter 2** further specifies the reactor configuration, analytics and materials used in this work, for plasma catalysis. All experiments had a detailed analysis of the plasma characteristics and the catalytic materials, and the results of these are shown in the Appendix.

**Chapter 3** focusses on the splitting of  $\text{CO}_2$ , using four different spherical packing materials in three different sizes, as well as glass wool and quartz wool. The effect of packing material and size and gap size was studied, as well as the effect of glass wool, quartz wool and the interactions between the packing and the dielectric barrier material.

**Chapter 4** reveals the conversion of  $\text{CO}_2$  and  $\text{CH}_4$  for five different spherical packing materials in three different bead sizes. A detailed comparison is made with Chapter 3, and the influence of the applied packing materials on the product fractions is discussed.

**Chapter 5** investigates the peculiar case of  $\text{BaTiO}_3$ , performing best for pure  $\text{CO}_2$  splitting (Chapter 3) and worst in DRM (Chapter 4). This is achieved by comparing a  $\text{BaTiO}_3$  packing with different bead sizes, in different gap sizes, at multiple residence times. Moreover, a comparison is made between the conversion for  $\text{CO}_2$  and  $\text{CH}_4$  in DRM and as individual gas components.

Finally, **Chapter 6** gives a general conclusion.





## 8 SAMENVATTING

---

In deze thesis werd onderzoek gedaan naar *dry reforming* van  $\text{CH}_4$  in een gepakte bed DBD reactor. Het doel was om meer inzicht te krijgen in de interacties tussen plasma en pakking materialen en hun invloed op conversie, energie efficiëntie en product selectiviteit.

In **Hoofdstuk 1** wordt uitgelegd waarom het belangrijk is  $\text{CO}_2$  en  $\text{CH}_4$ , twee broeikasgassen, om te zetten naar chemische componenten met toegevoegd waarde. De huidige stand van de techniek wordt beschreven, waardoor duidelijk wordt dat er nood is aan een energie-efficiënte technologie die deze chemische componenten selectief kan converteren. Een techniek die hierin een hoog potentieel heeft is plasmakatalyse.

In **Hoofdstuk 2** wordt de methodologie van dit doctoraat beschreven. Zowel de karakteristieken van de DBD opstelling, als de specificaties van de gebruikte materialen komen hier aan bod. Ook de gebruikte karakterisatie-methoden voor de materialen worden toegelicht. De resultaten hiervan zijn terug te vinden in de Appendix.

**Hoofdstuk 3** toont de resultaten behaald voor  $\text{CO}_2$  splitsing. Hiervoor worden vier verschillende sferische pakkingmaterialen vergeleken, elk in drie verschillende groottes, net als de invloed van kwartswol en glaswol als pakkingmateriaal. De invloed van het materiaal zelf, de grootte van de sferen, en de interactie met de diëlektrische barrière wordt bestudeerd.

In **Hoofdstuk 4** worden vijf sferische pakkingmaterialen in drie verschillende groottes bestudeerd, ditmaal voor DRM, waarbij de  $\text{CO}_2$  conversie in aanwezigheid van methaan wordt vergeleken met die verkregen voor zuivere  $\text{CO}_2$  splitsing. Niet enkel de conversie, maar ook de fracties van de gevormde producten worden bestudeerd.

**Hoofdstuk 5** focust ten slotte op  $\text{BaTiO}_3$  als pakkingmateriaal, aangezien hiermee de hoogste conversies verkregen worden voor  $\text{CO}_2$  splitsing maar de laagste voor DRM. In

dit hoofdstuk wordt gekeken naar de invloed van de grootte van de sferen, de *gap* en de verblijftijd in de reactor voor de specifieke case van BaTiO<sub>3</sub>. Bovendien wordt de conversie voor DRM vergeleken met diegene voor de individuele componenten.

**Hoofdstuk 6** ten slotte, geeft een algemene conclusie van de bekomen resultaten.

## 9 APPENDIX

---

### 9.1 IR DATA

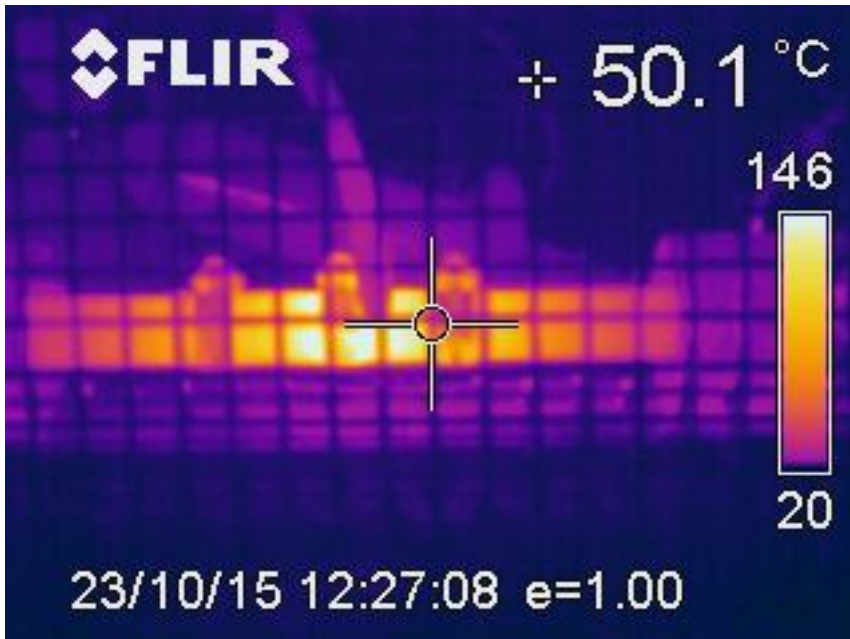


Figure 39: IR camera image of  $ZrO_2$  beads of 2.0-2.24 mm, in a 4.5 m gap, at 23.5 kHz,  $CO_2$ , 100 Watt input power, 50 ml/min.

As can be seen on the infrared data (Figure 39), obtained by measuring the temperature of the dielectric barrier and the outer electrode, the maximum temperature for this experiment is 146 °C.

### 9.2 PLASMA STABILISATION

Our experiments are normally performed as follows:

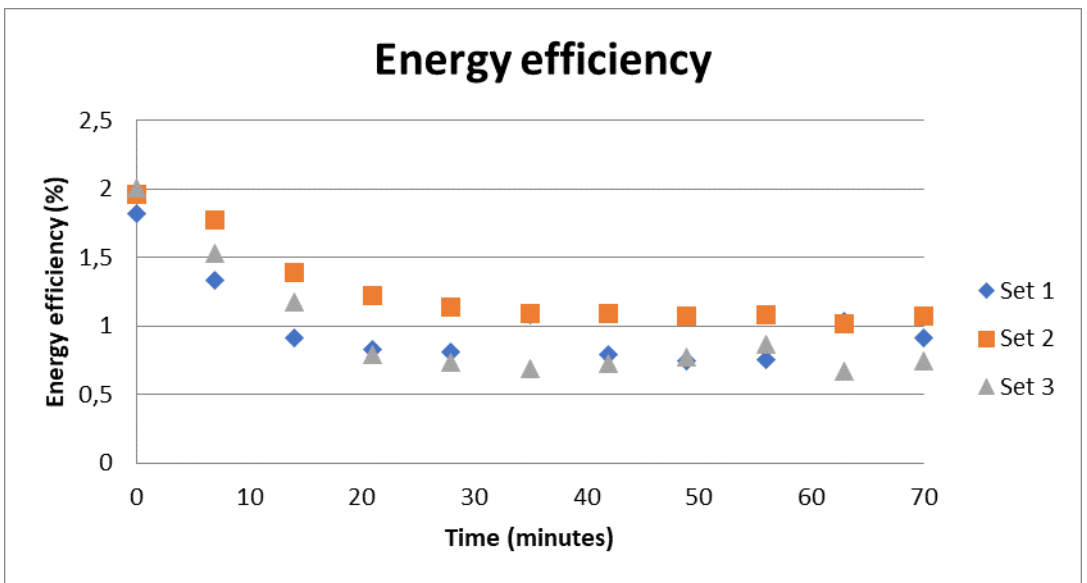
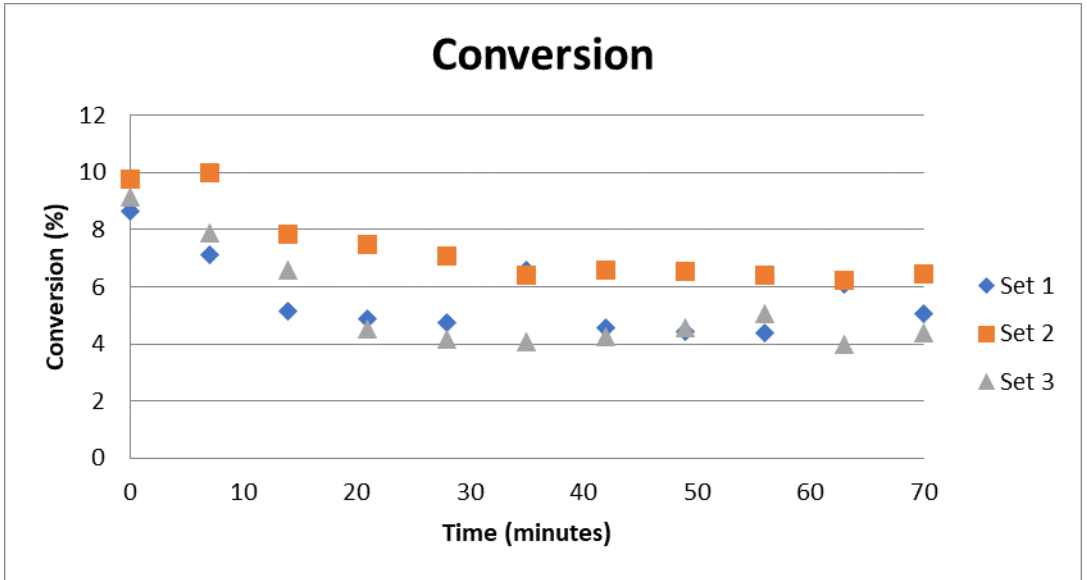
- Flushing the gases, to purge the equipment;
- Measuring the gas content as a 'blanc';
- Igniting the plasma;

- 40 minutes of plasma stabilisation (until there is no further change in peak-to-peak voltage);
- Measuring the gas content to measure the conversion.

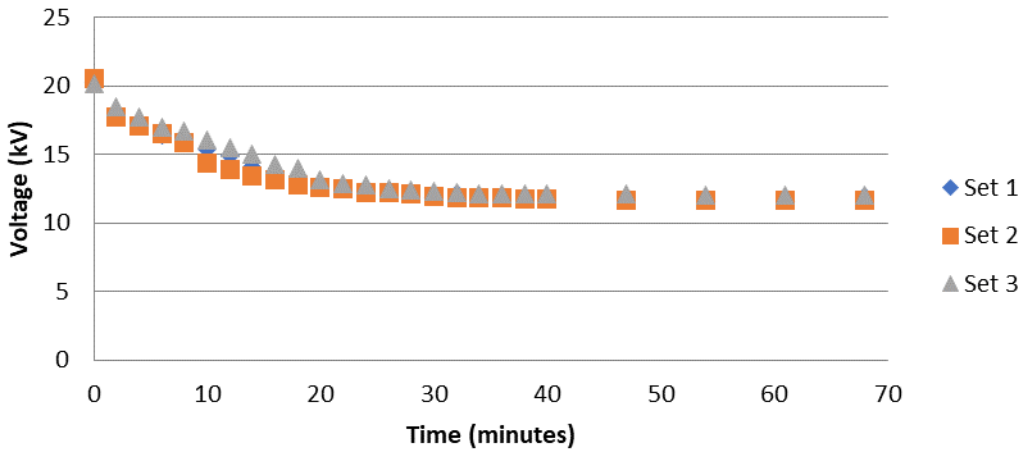
To elucidate the behaviour of the plasma during stabilisation, GC measurements are taken from the first moment the plasma is ignited. The experiment is conducted with  $\text{SiO}_2$  as dielectric packing, with beads ranging from 2.0 to 2.24 mm, at 50 ml/min gas flow rate and 100 Watt power. An alumina dielectric barrier is used. Experiments show here that the conversion and the energy efficiency (Figure 40) decrease with increasing stabilisation time. To understand this behaviour, further analysis of the Lissajous figures (see schematic representation in Figure 19) is performed.

Lines DA and CB in Figure 19 represent the phase when no plasma is formed; the slope of these lines indicates the total capacity of the reactor without plasma ( $C_{\text{cell}}$ ). The lines AB and DC in Figure 19 represent the phase when the plasma is formed inside the gap, so the slope of these lines indicates the effective capacity of the plasma reactor ( $C_{\text{eff}}$ ). From the Lissajous figures, the breakdown voltage (the minimum voltage to create the plasma) can be determined as well.

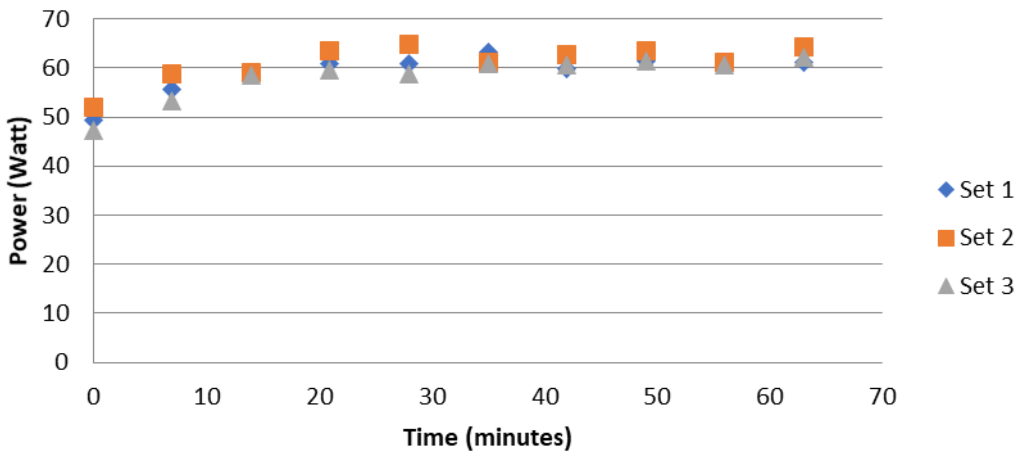
The results of the peak-to-peak voltage, the plasma power and the breakdown voltage are thus also plotted as a function of time (see Figure 40). The peak-to-peak voltage drops as a function of time, while the plasma power and breakdown voltage exhibit a rising trend.



## Peak-to-peak voltage



## Plasma power



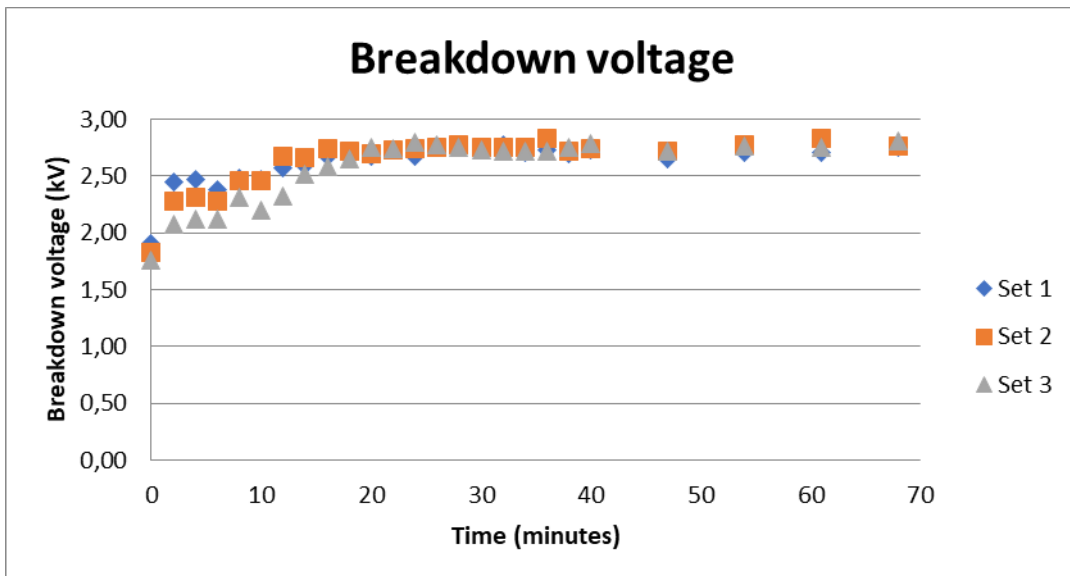


Figure 40: Conversion (a), energy efficiency (b), peak-to-peak voltage (c), plasma power (d) and breakdown voltage (e) as a function of stabilisation time, for an alumina dielectric barrier, at 50 ml/min, for 100 Watt power with 2.0-2.24 mm SiO<sub>2</sub> beads.

It is clear that the temporal behaviour in conversion and energy efficiency doesn't follow the same trend as the peak-to-peak voltage (Figure 40 (c)) or the plasma power (Figure 40 (d)). With an increasing power and a decreasing voltage, we expect an increasing current, which would result in an increasing conversion and energy efficiency. The explanation might be found in the increasing breakdown voltage (Figure 40 (e)). Since the breakdown voltage slightly increases when the experiment proceeds, less energy remains available for conversion, yielding in a lower conversion and energy efficiency. Based on these results, all our GC analysis data are sampled after a plasma stabilization time of 40 minutes. When monitoring the breakdown voltage and plasma power after 40 minutes for other materials, it was confirmed that they were all stable after 40 minutes and thus GC measurements could be taken.

### 9.3 MATERIAL CHARACTERISATION

The material characteristics of the different packing materials will influence the results obtained in this work, i.e. both conversion and product fractions/selectivities. Even

though we cannot yet identify which material properties are responsible for the differences in the plasma chemistry, we have measured those properties from which we expect a possible influence on the results. Therefore, all packing materials are studied with UV-DR (photon absorption, band gap), profilometry (surface roughness), nitrogen sorption (micro- and mesoporosity, surface area), Hg-porosimetry (meso- and macroporosity), SEM-EDX (chemical composition) and TGA (e.g. thermal stability and presence of surface adsorbed species). The specifics of the equipment are listed in Table 7.

### 9.3.1 UV-DR

By comparing the UV-DR spectrum (Figure 41) before and after plasma exposure, we can see that there is no significant change in the intersection of the tangent of the Tauc plot with the x-axis. The band-gap of the material thus remains unaltered after plasma exposure. The band gap of the tested SiO<sub>2</sub> beads was calculated as 3.4 eV, which is lower than the band gap for amorphous SiO<sub>2</sub> (9.2 eV). The SiO<sub>2</sub> beads are assumed to be glass, containing mostly Na, Ca and Mg. This is confirmed by the analysis with SEM-EDX (Table 25).



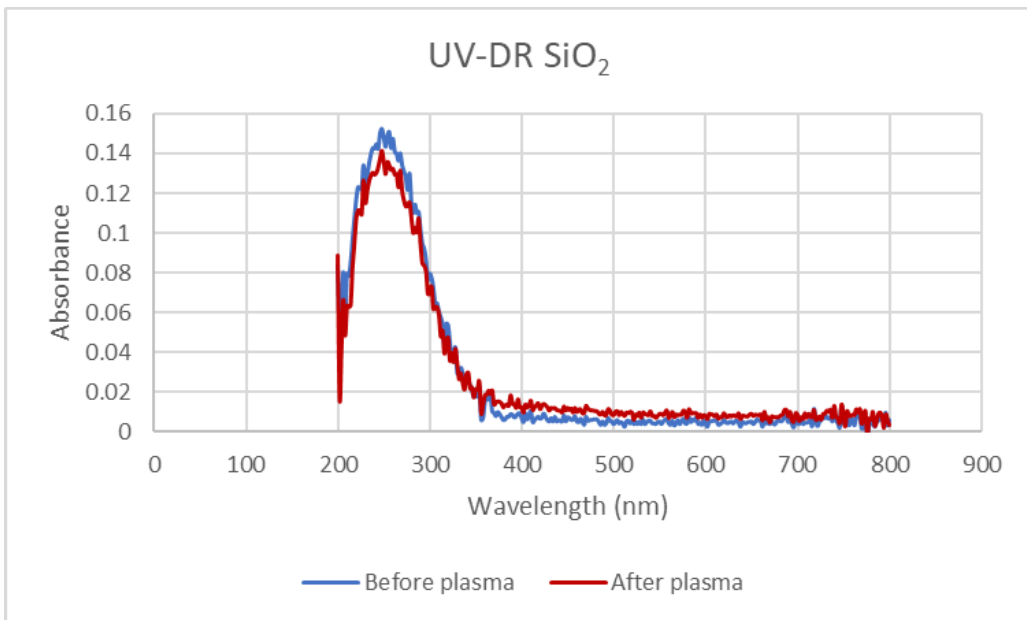


Figure 41: UV-DR spectra of SiO<sub>2</sub> before (blue graph) and after (red graph) plasma exposure (milled beads).

The UV-DR spectrum of ZrO<sub>2</sub> (Figure 42) shows a bandgap of 4.3 eV, which remains unaltered after plasma exposure.

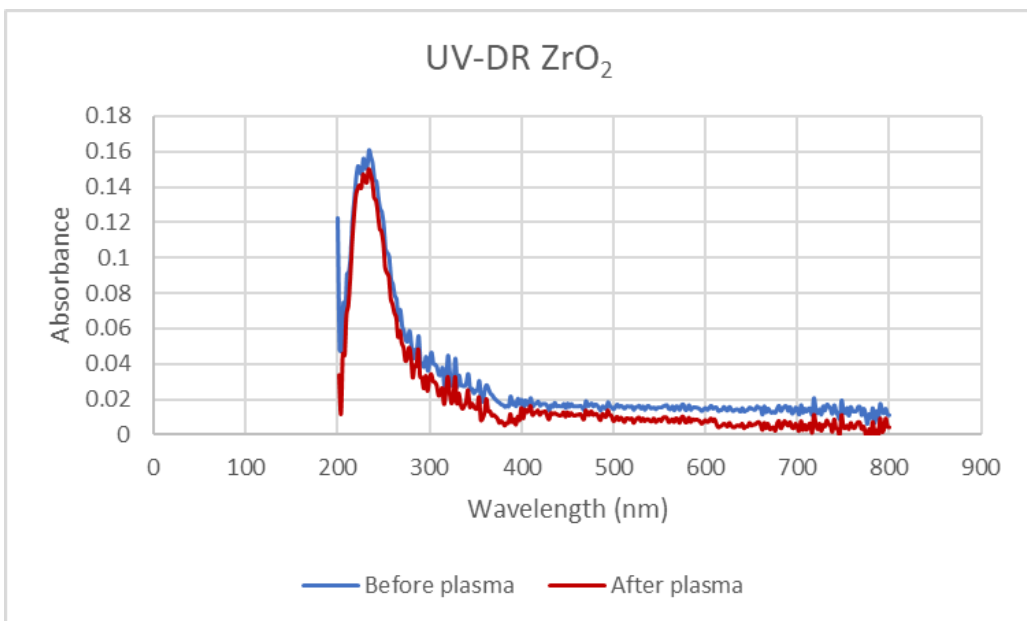


Figure 42: UV-DR spectra for ZrO<sub>2</sub> before (blue graph) and after (red graph) plasma exposure (milled beads).

$\alpha$ -Al<sub>2</sub>O<sub>3</sub> is not active in UV-DR.

The UV-DR spectra (Figure 43) for the BaTiO<sub>3</sub> beads before and after plasma lead to the same band gap: 2.98 eV; the band-gap of the material thus remains unaltered after plasma exposure. The literature gives a value of 3.2 eV for tetragonal BaTiO<sub>3</sub> [153]. At the moment we cannot explain this discrepancy in values, but it might be dependent on the crystal phase and/or structural composition [154,155].

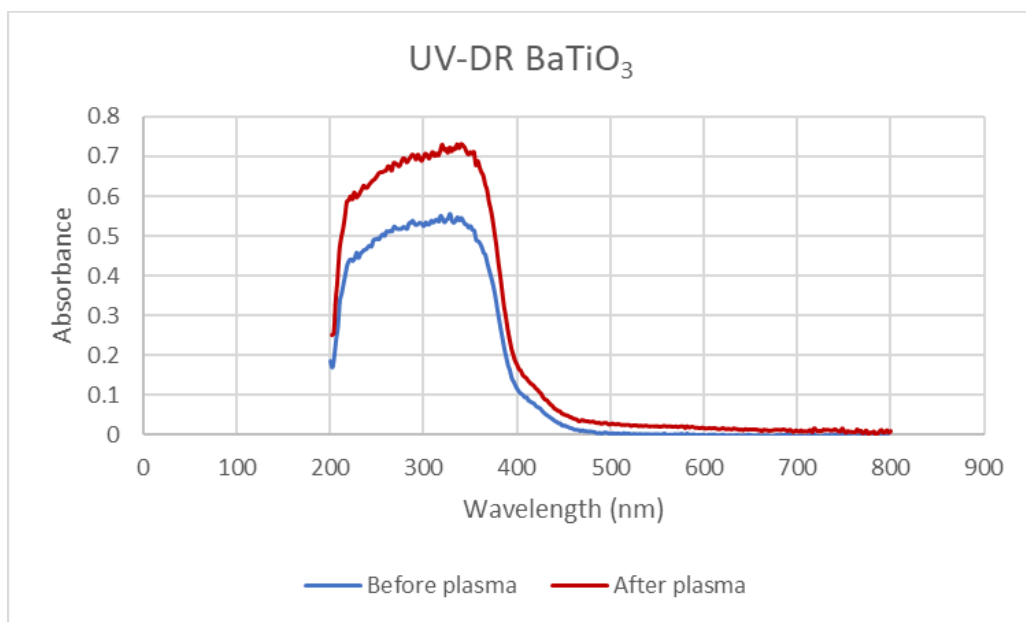


Figure 43: UV-DR spectra for BaTiO<sub>3</sub> before (blue graph) and after (red graph) plasma exposure (milled beads).

### 9.3.2 N<sub>2</sub>-sorption

The nitrogen-sorption isotherms, used to calculate the apparent surface area of the SiO<sub>2</sub>, ZrO<sub>2</sub>,  $\alpha$ -Al<sub>2</sub>O<sub>3</sub>,  $\gamma$ -Al<sub>2</sub>O<sub>3</sub> and BaTiO<sub>3</sub> beads, are shown in Figure 44, Figure 45, Figure 46, Figure 47 and Figure 48, respectively. Only the  $\gamma$ -Al<sub>2</sub>O<sub>3</sub> beads show a type IV isotherm, indicating mesoporosity. The other materials do not have measurable porosity below 50 nm (i.e. the pore sizes that can be evaluated by nitrogen sorption).

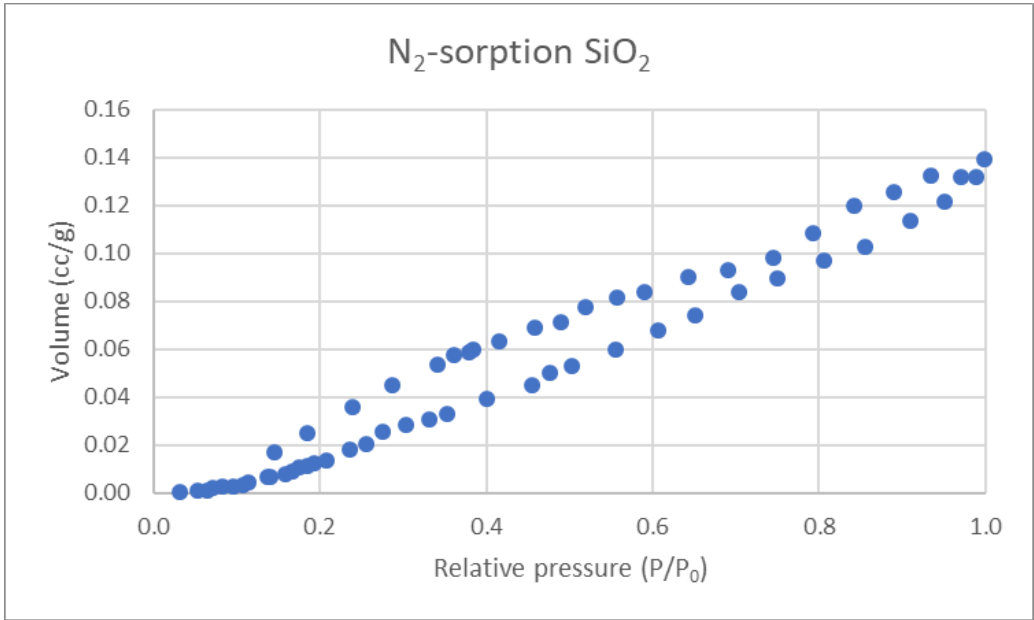


Figure 44: Nitrogen Sorption for SiO<sub>2</sub>.

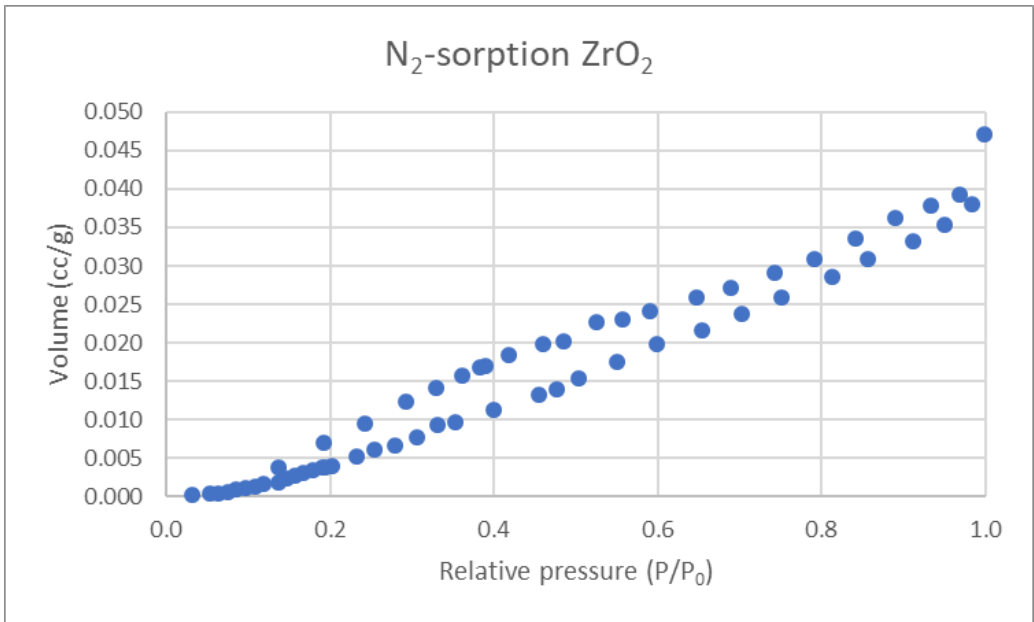


Figure 45: Nitrogen Sorption for ZrO<sub>2</sub>.

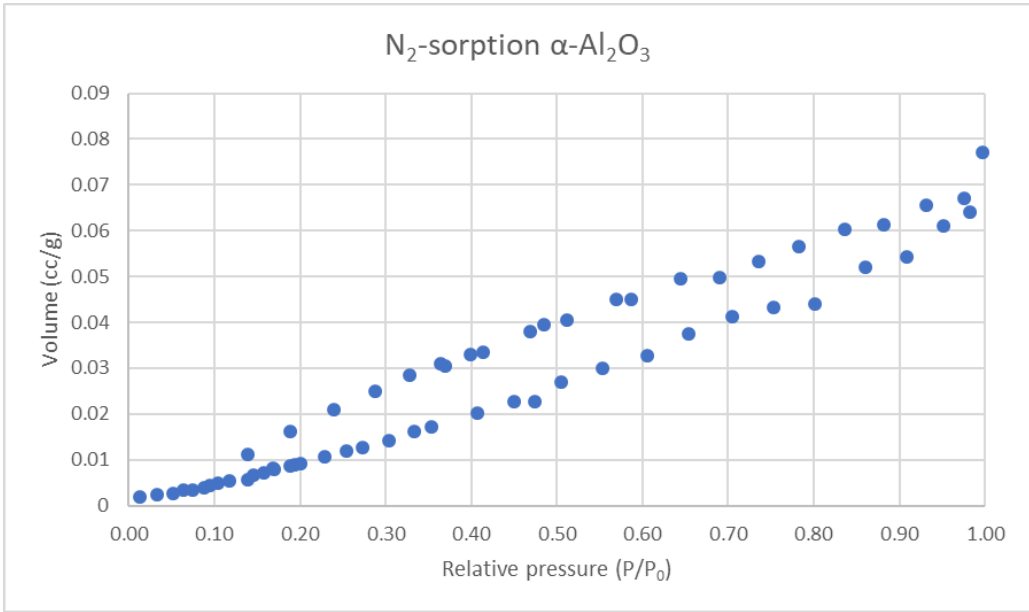


Figure 46: Nitrogen Sorption for α-Al<sub>2</sub>O<sub>3</sub>.

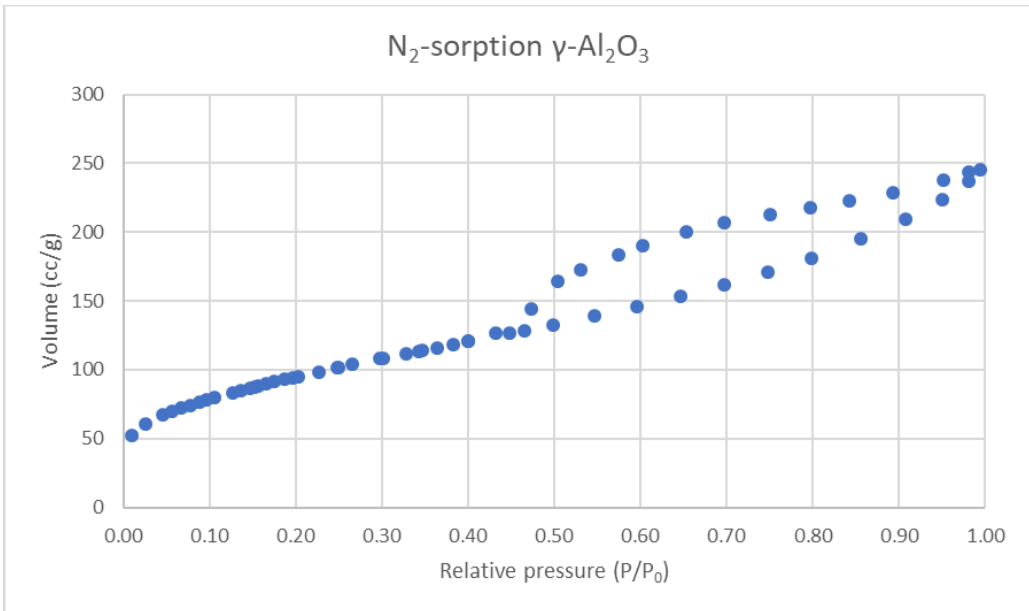


Figure 47: Nitrogen Sorption for γ-Al<sub>2</sub>O<sub>3</sub>.

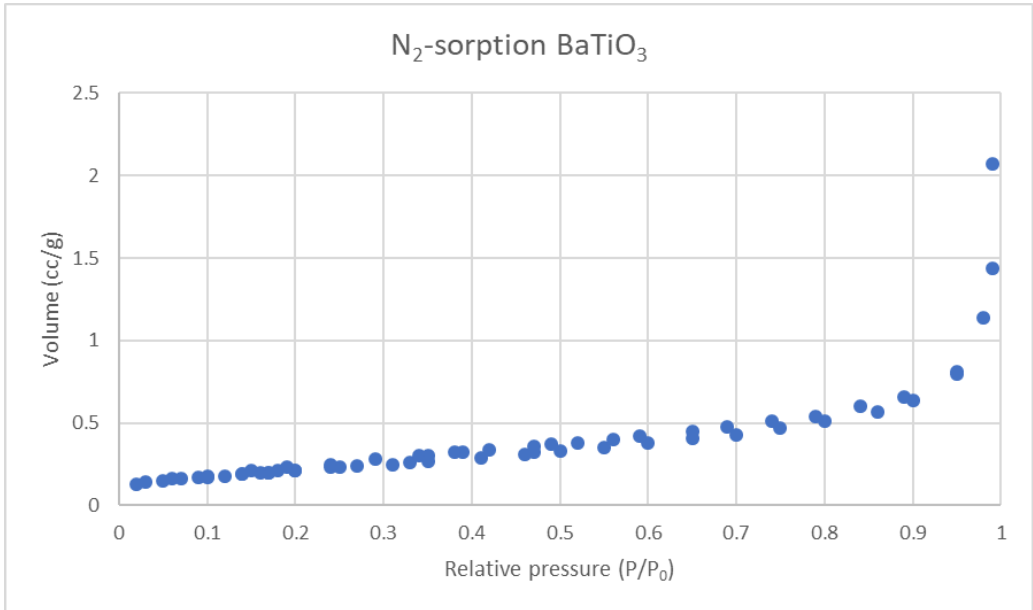


Figure 48: Nitrogen Sorption for BaTiO<sub>3</sub>.

### 9.3.3 Hg-porosimetry

Figure 49, Figure 50, Figure 51, Figure 52 and Figure 53 show the results for Hg-porosimetry, which is able to detect porosity above 8 nm up to micrometre sized micropores. The pore sizes and the total open pore volume of the SiO<sub>2</sub>, ZrO<sub>2</sub>, α-Al<sub>2</sub>O<sub>3</sub>, γ-Al<sub>2</sub>O<sub>3</sub> and BaTiO<sub>3</sub> beads are shown, respectively. The most important data for these figures (the total open pore volume and the pore size) are shown in Table 6. Moreover, it is clear that all samples have a (limited) macroporosity (>0.05 μm), but the amount of macropores and their size depend on the material.

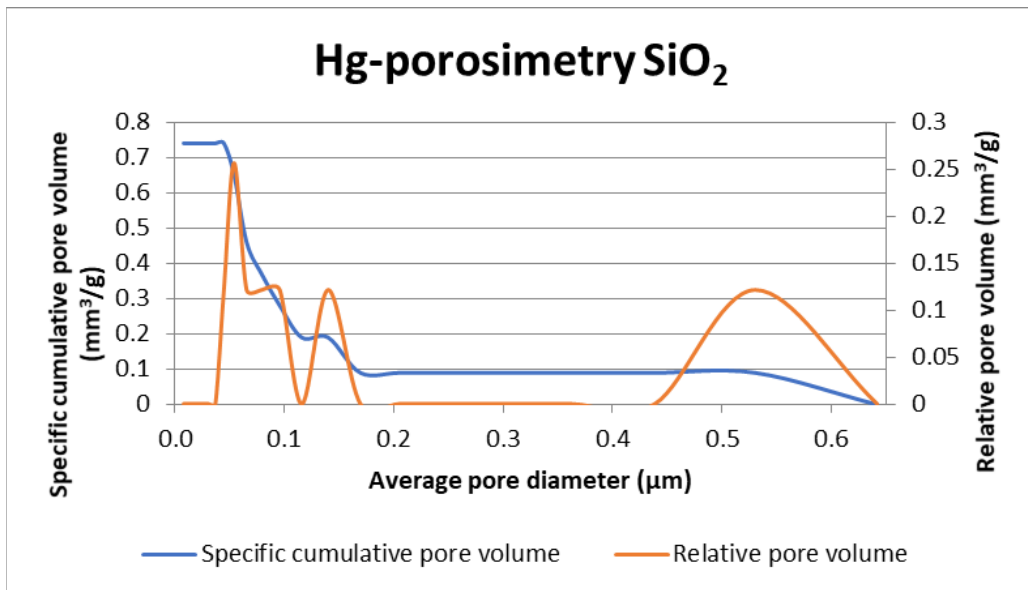


Figure 49: Hg-porosimetry for SiO<sub>2</sub>.

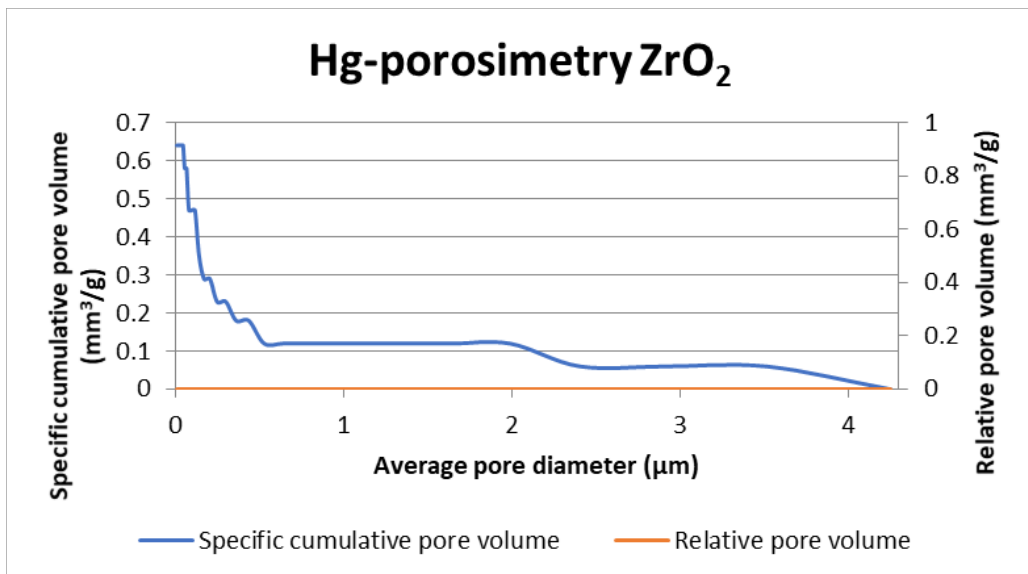


Figure 50: Hg-porosimetry for ZrO<sub>2</sub>.

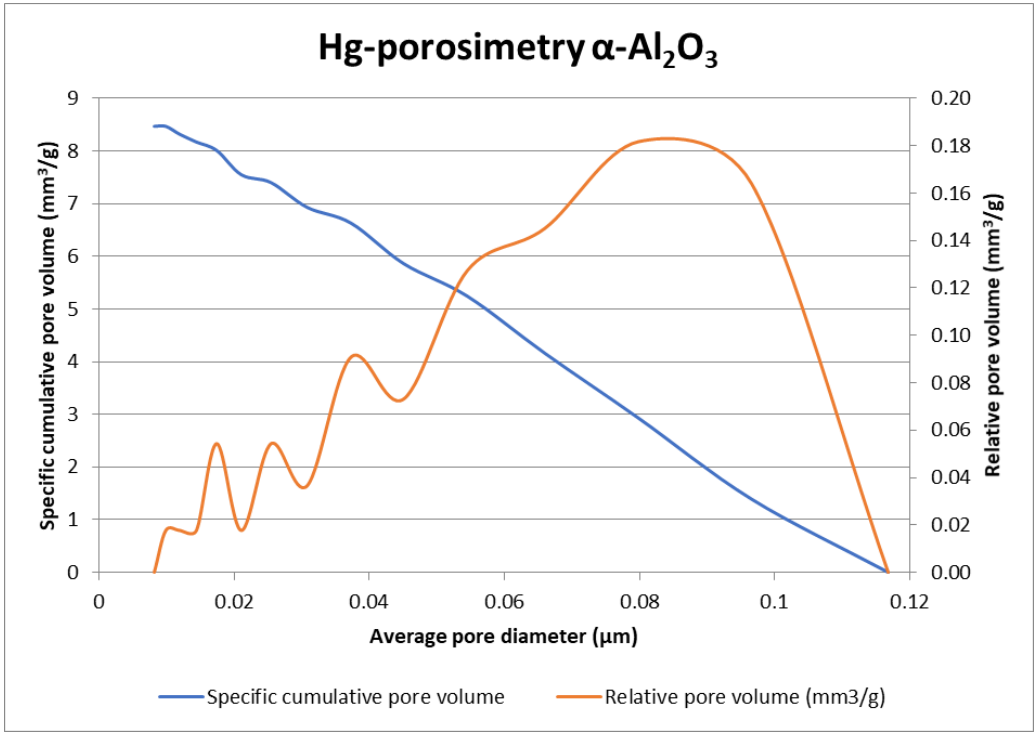


Figure 51: Hg-porosimetry  $\alpha$ -Al<sub>2</sub>O<sub>3</sub>.

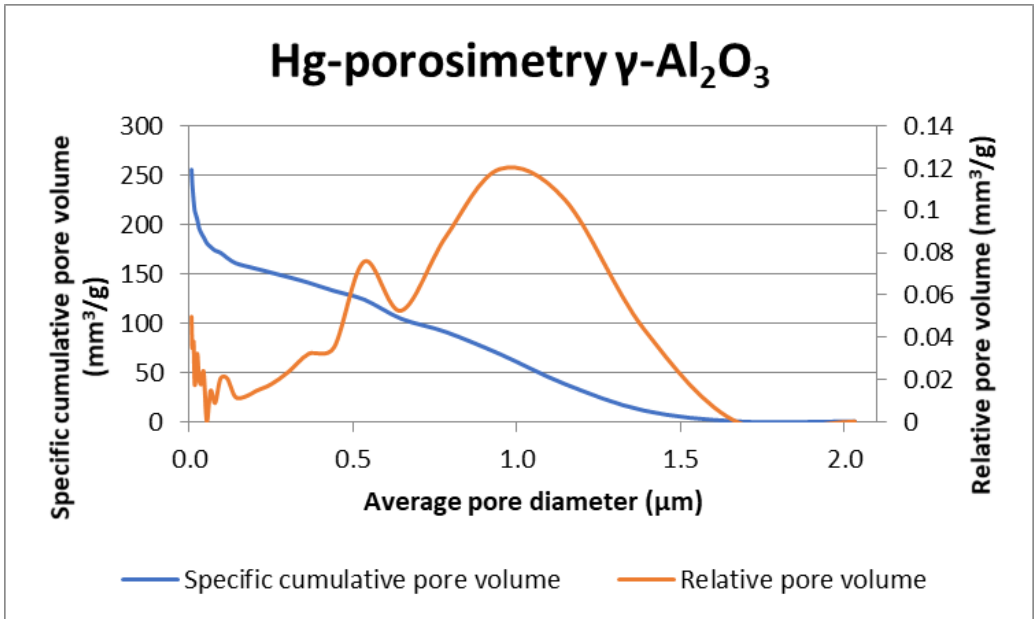


Figure 52: Hg-porosimetry  $\gamma$ -Al<sub>2</sub>O<sub>3</sub>.

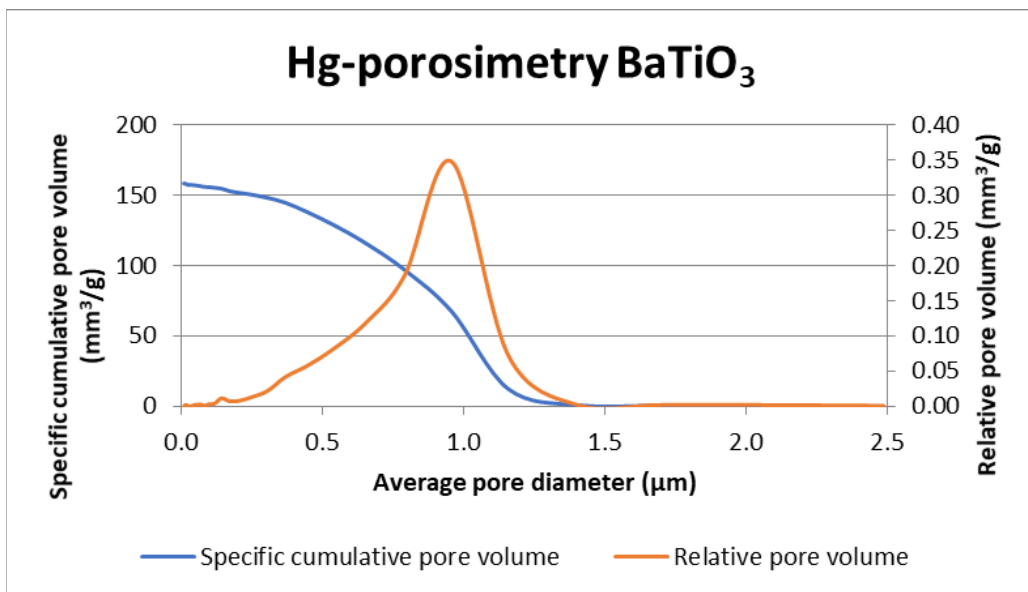


Figure 53: Hg-porosimetry BaTiO<sub>3</sub>.



### 9.3.4 SEM-EDX

Table 25: SEM-EDX measurements for all beads before and after plasma, measured at 3 points per bead.

	SiO <sub>2</sub>			ZrO <sub>2</sub>			α-Al <sub>2</sub> O <sub>3</sub>			γ-Al <sub>2</sub> O <sub>3</sub>			BaTiO <sub>3</sub>		
	Before	After	Weight%	Before	After	Weight%	Before	After	Weight%	Before	After	Weight%	Before	After	Weight%
	plasma	plasma		plasma	plasma		plasma	plasma		plasma	plasma		plasma	plasma	
<b>O</b>	45.8±0.9	45.8±0.8	26.0±0.1	26.0±0.1	26.0±0.1	49±4	47±0.1	47±0.1	20.8±0.2	20.8±0.2	20.7±0.1				
<b>Si</b>	33±2	32±1													
<b>Na</b>	11±2	14±3													
<b>Ca</b>	8±4	5±1	0.2±0	0.2±0	0±0	0±0	0.2±0.1	0.2±0.1							
<b>Mg</b>	2.2±0.5	2.6±0.3													
<b>Al</b>	0.5±0.2	0.5±0.2	0.5±0.3	0.5±0.3	0.3±0.1	52±2	52.5±0.4	52.8±0	0.2±0	0.2±0	0±0				
<b>K</b>	0.4±0	0.3±0.3													
<b>Zr</b>			71.5±0.2	72.5±0.2											
<b>Hf</b>			1.8±0.1	1.2±0.2											
<b>Ba</b>													58.4±0.6	58.7±0.1	
<b>Ti</b>													20.7±0.4	20.7±0.1	

The SEM-EDX data (Table 25) of  $\text{SiO}_2$ ,  $\alpha\text{-Al}_2\text{O}_3$ ,  $\gamma\text{-Al}_2\text{O}_3$  and  $\text{BaTiO}_3$  show no significant difference when analysing the beads before and after plasma. When comparing the results for  $\text{ZrO}_2$ , we can see that the content of Ca and Hf decreases after plasma exposure, but the deviation is minimal. Therefore, no conclusions can be drawn based on these measurements. The SEM-EDX images are shown in Figure 54-Figure 63.

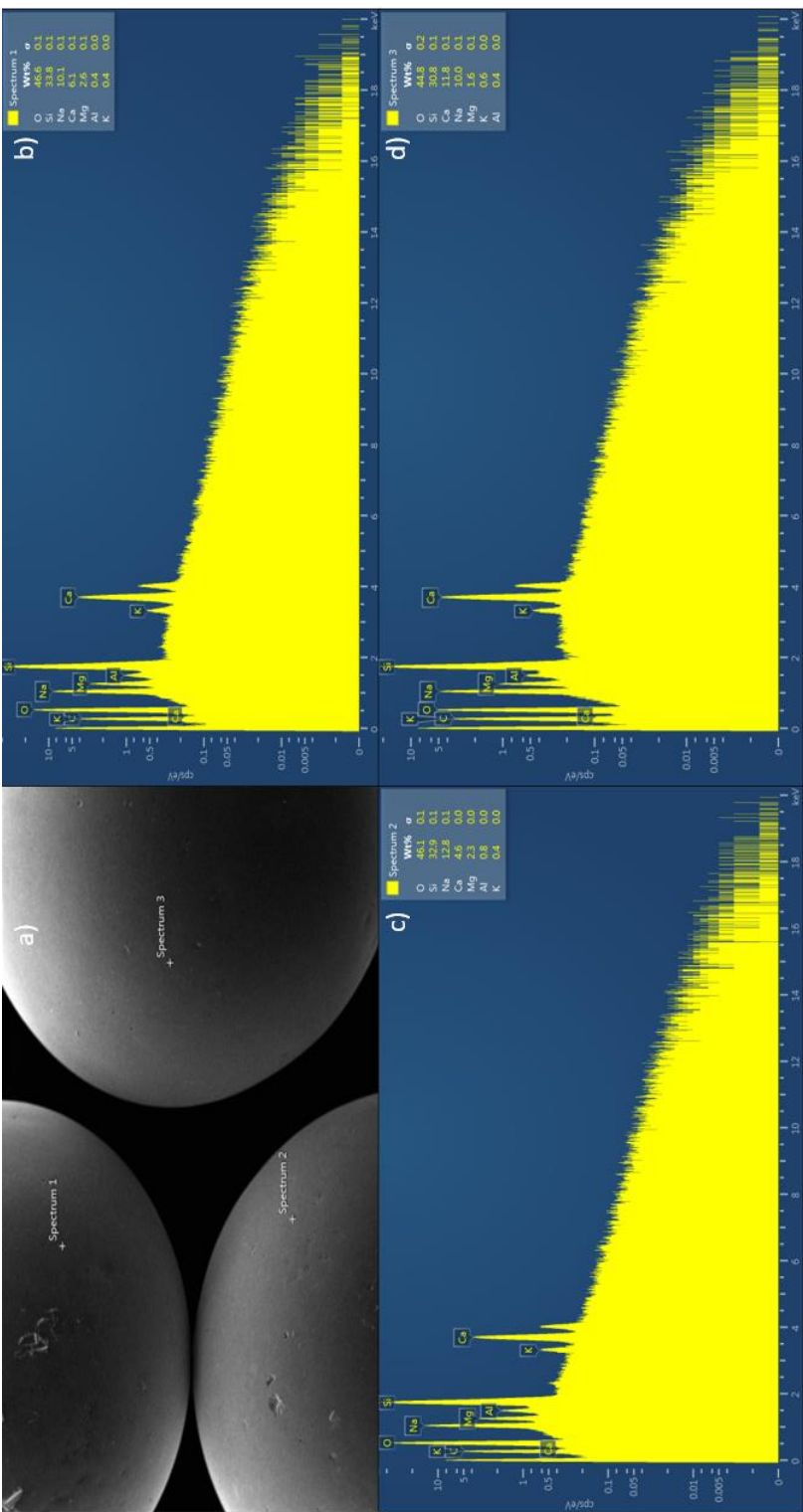


Figure 54: SEM-EDX SiO<sub>2</sub> beads (before plasma).

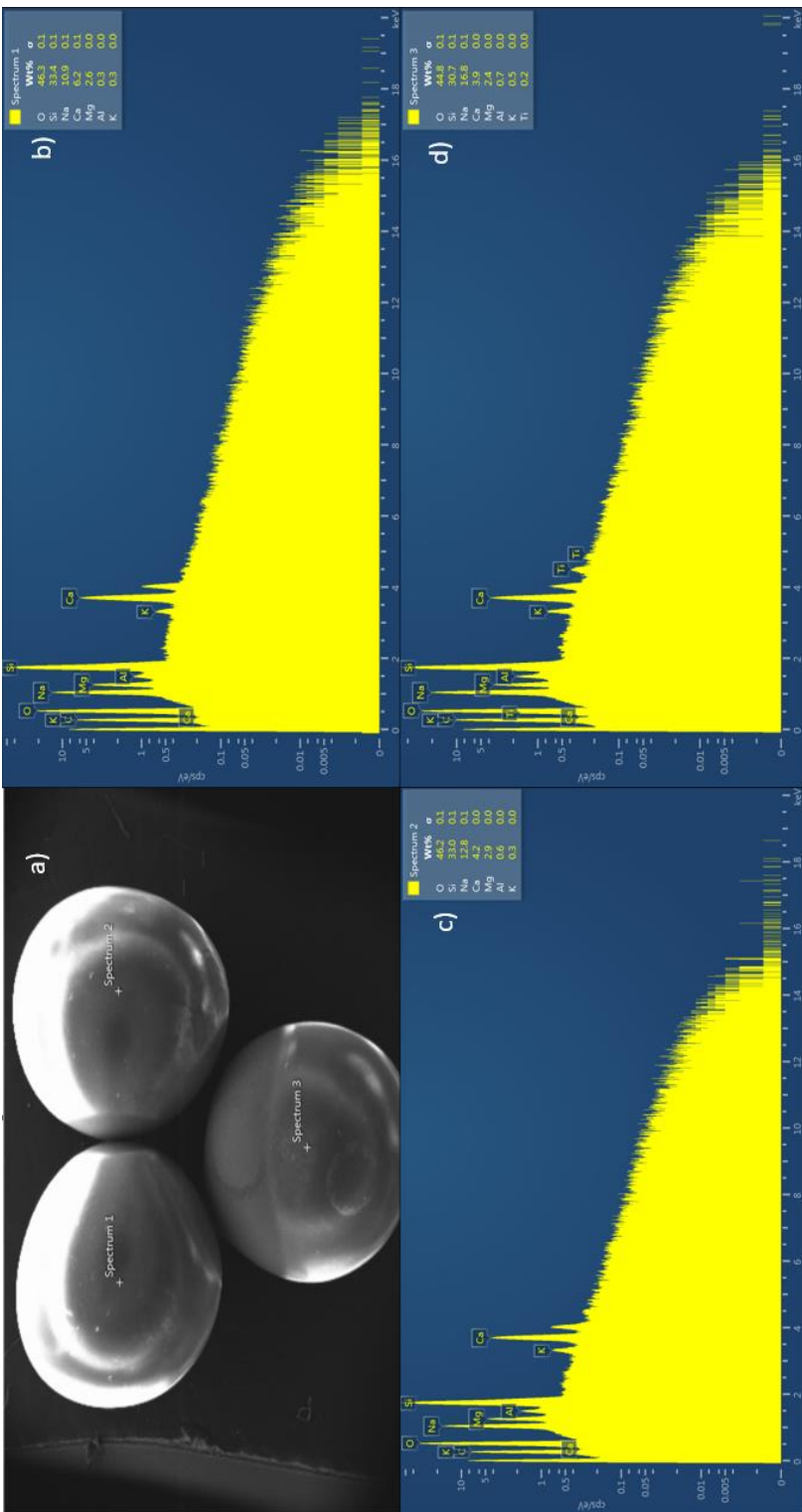


Figure 55: SEM-EDX SiO<sub>2</sub> beads (after plasma).

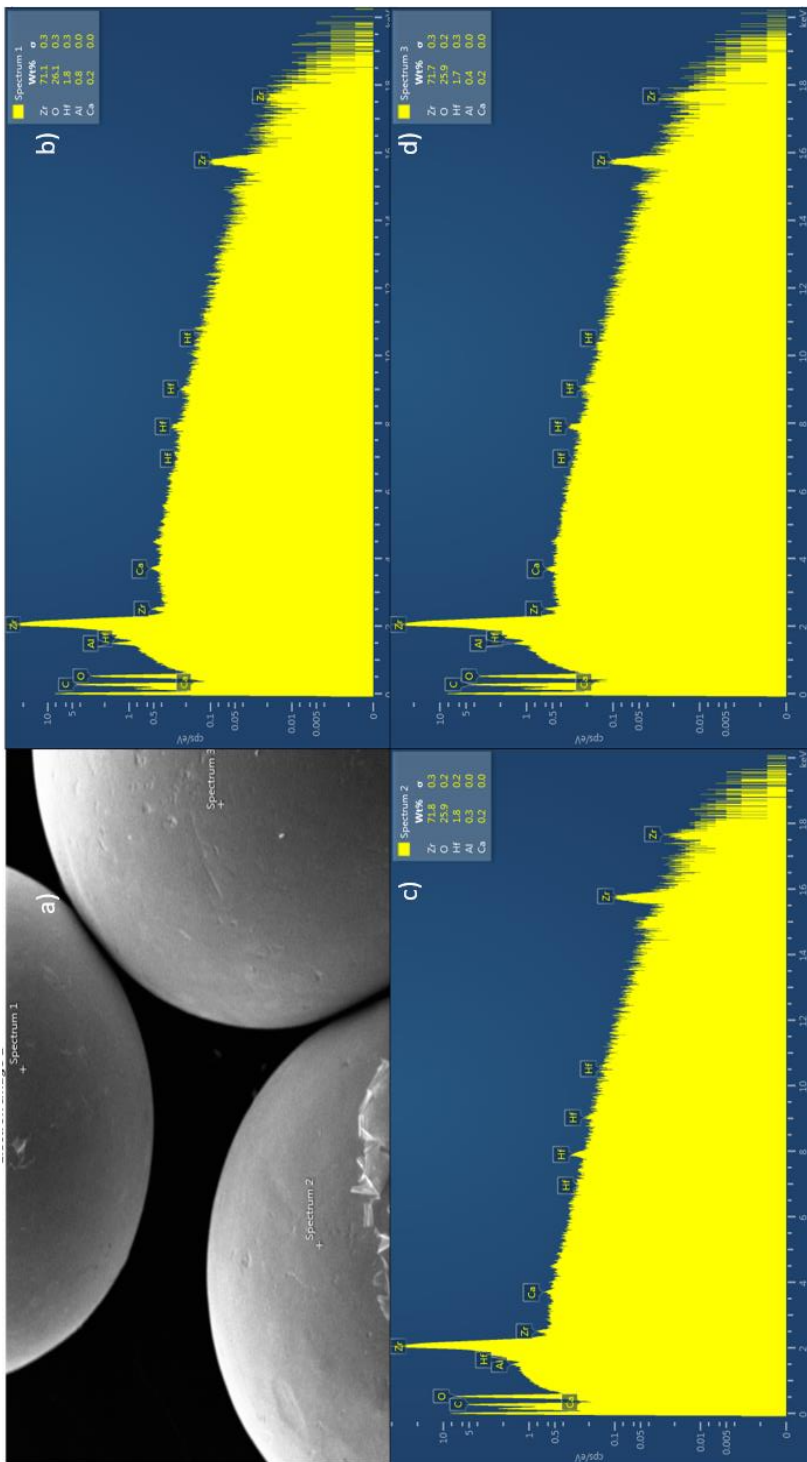


Figure 56: SEM-EDX ZrO<sub>2</sub> beads (before plasma).

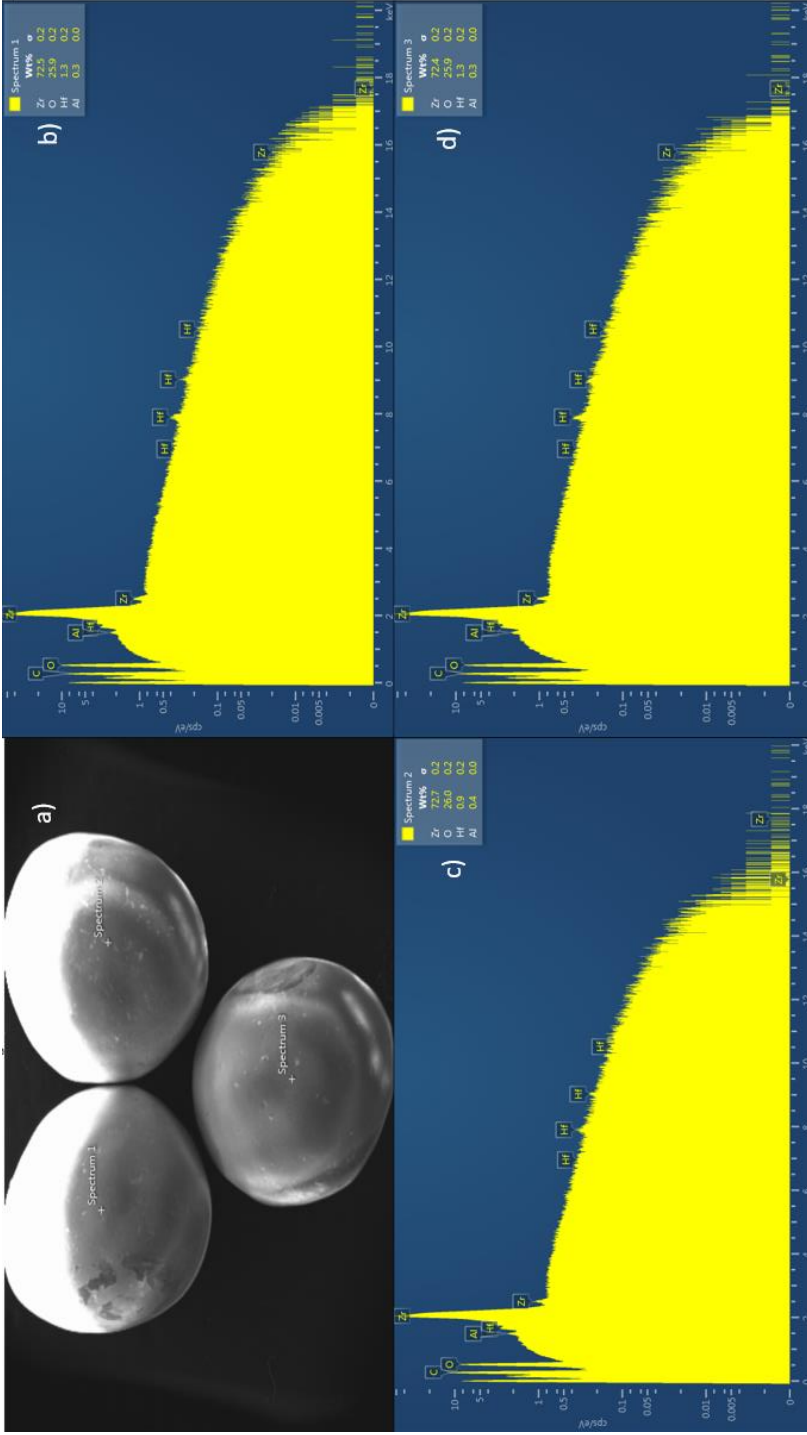


Figure 57: SEM-EDX ZrO<sub>2</sub> beads (after plasma).

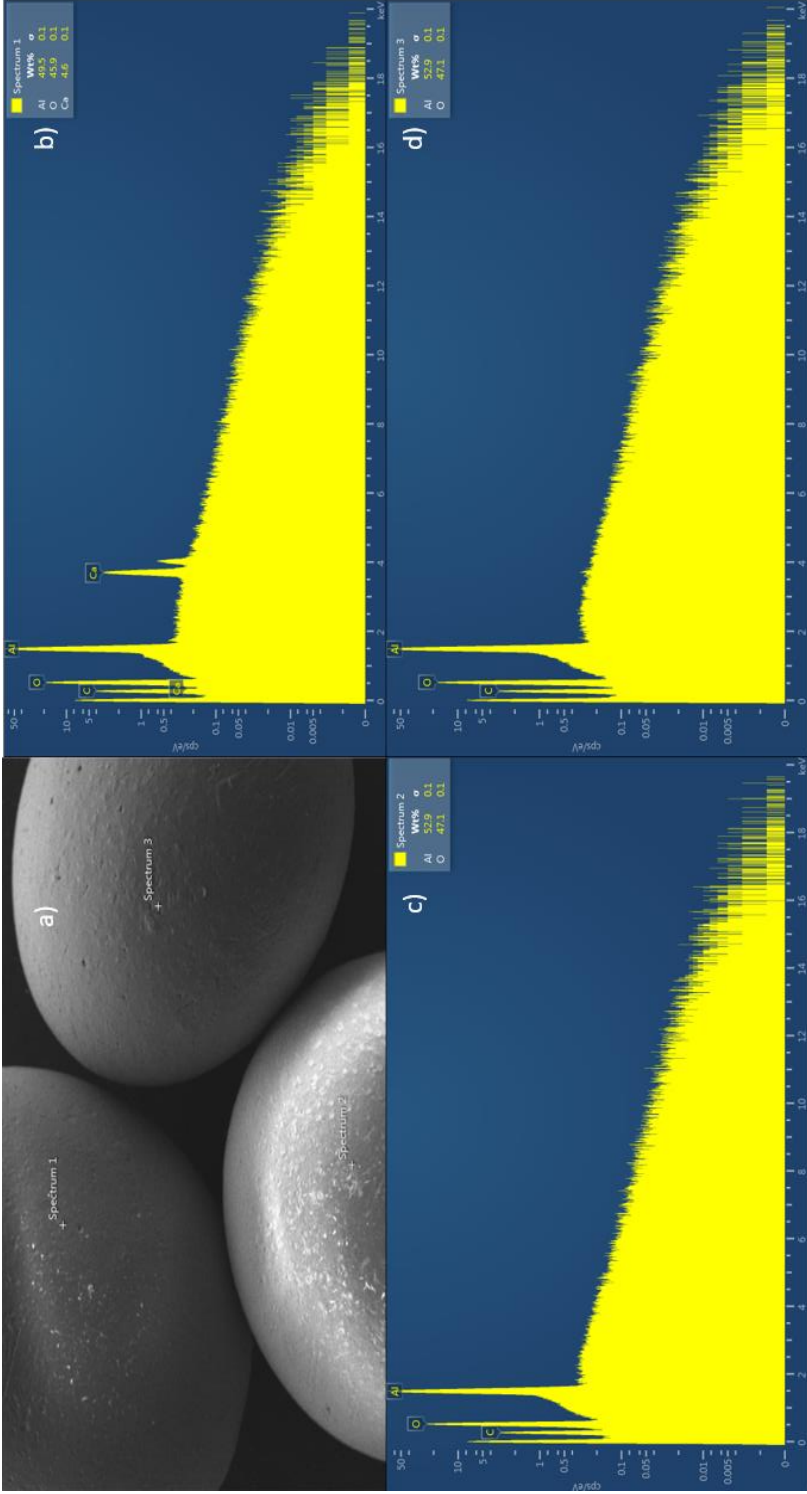


Figure 58: SEM-EDX  $\alpha$ - $\text{Al}_2\text{O}_3$  beads (before plasma).

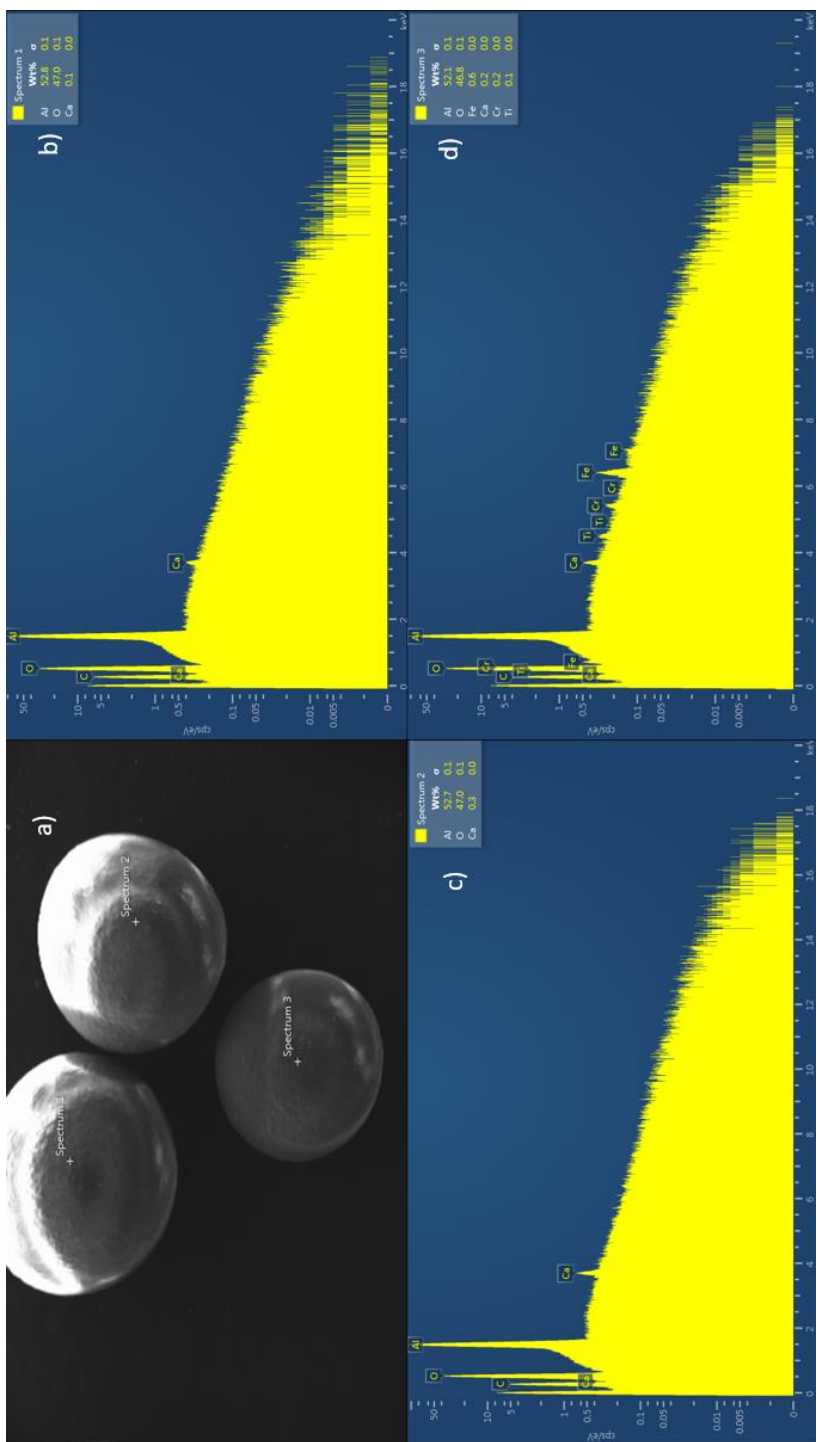


Figure 59: SEM-EDX  $\alpha$ - $\text{Al}_2\text{O}_3$  beads (after plasma).



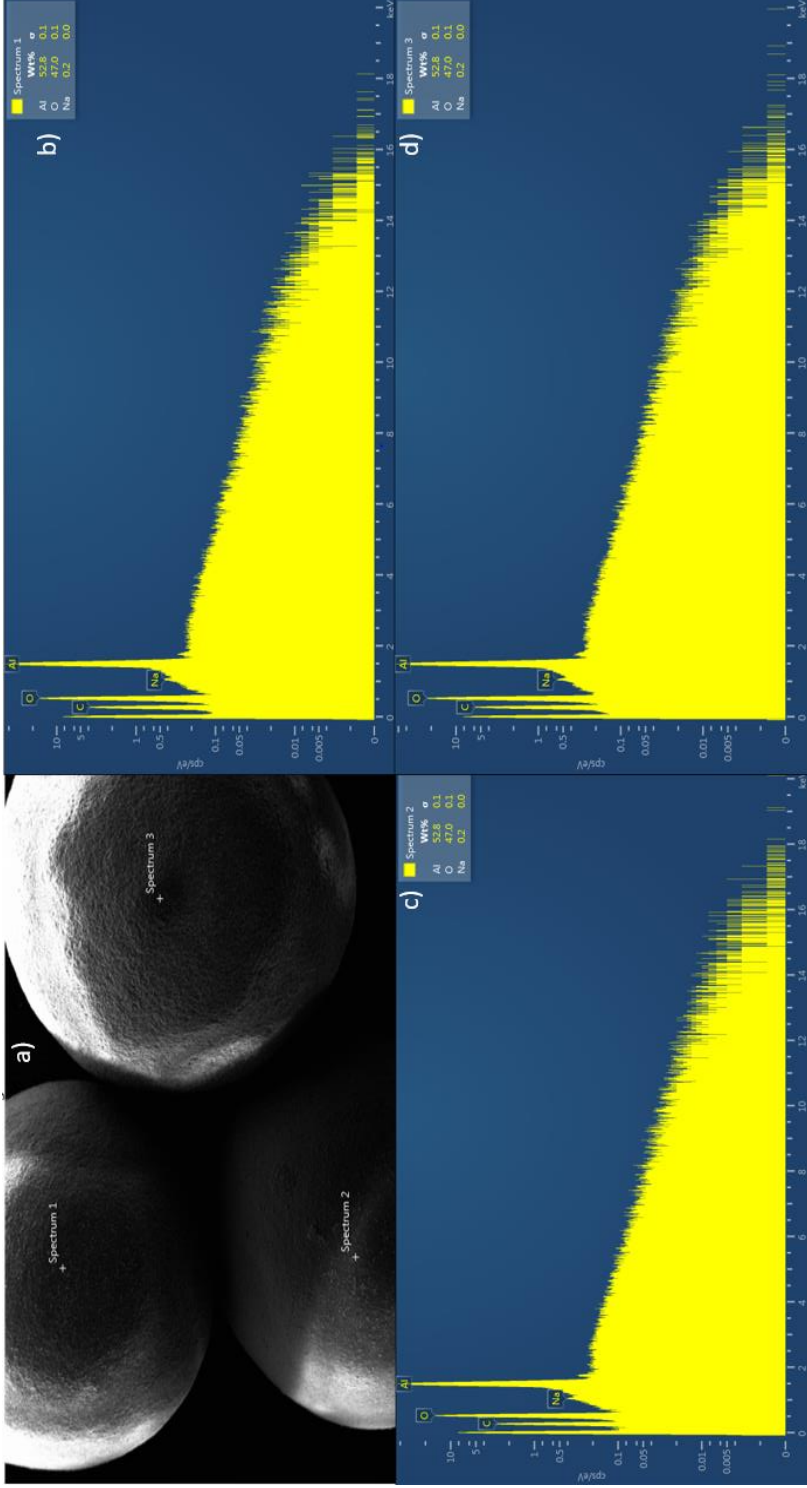


Figure 60. SEM-EDX  $\gamma$ - $\text{Al}_2\text{O}_3$  beads (before plasma).

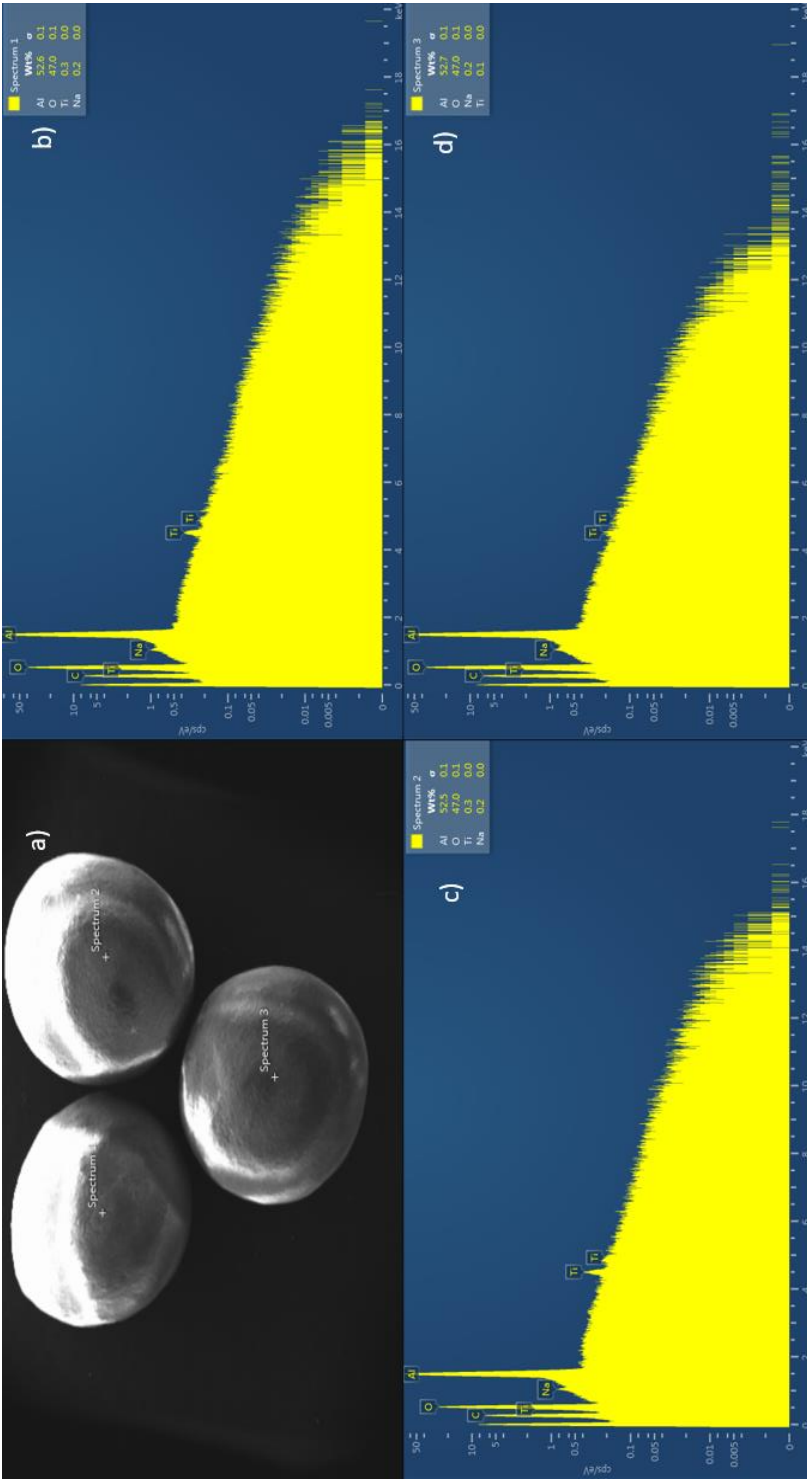


Figure 61: SEM-EDX  $\gamma$ - $\text{Al}_2\text{O}_3$  beads (after plasma).

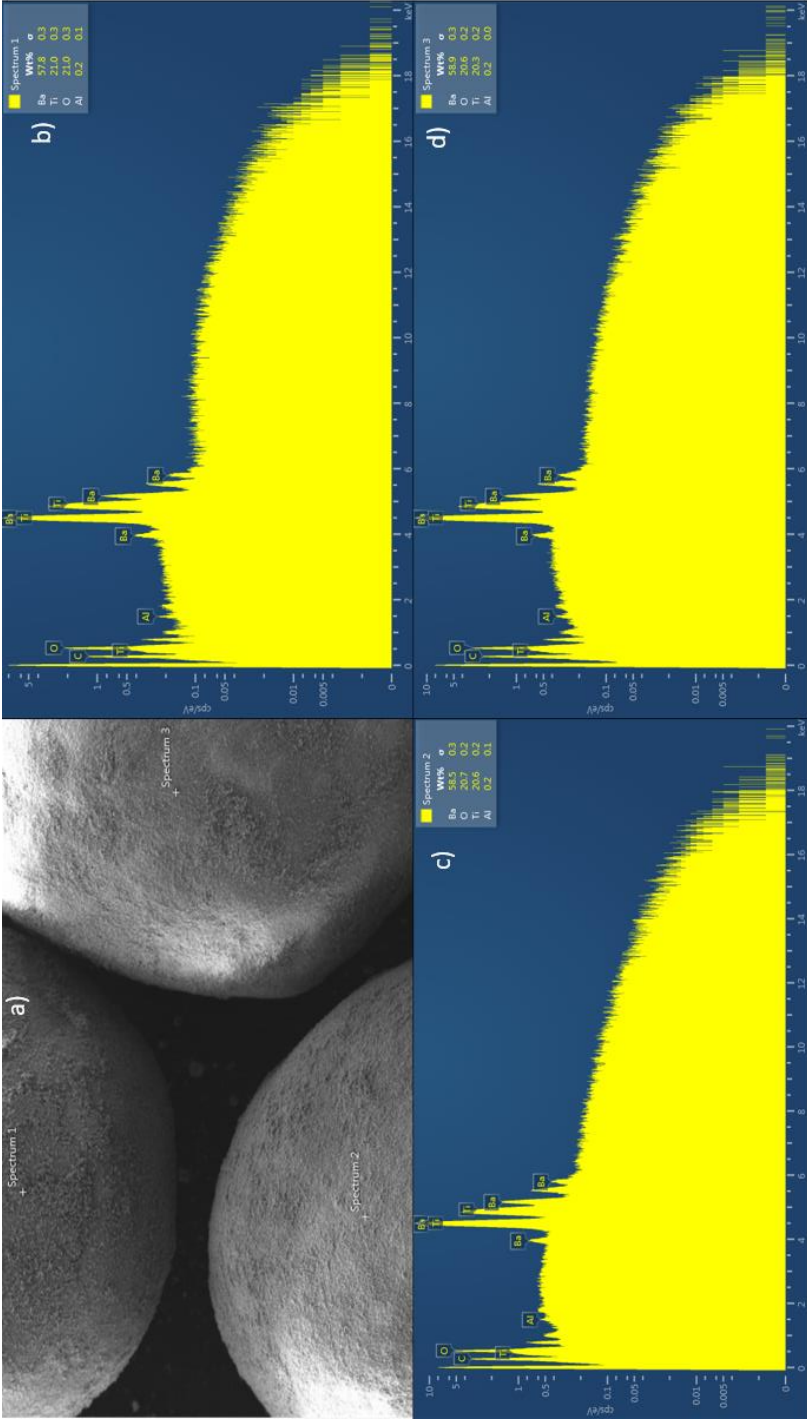


Figure 62: SEM-EDX  $\text{BaTiO}_3$  beads (before plasma).

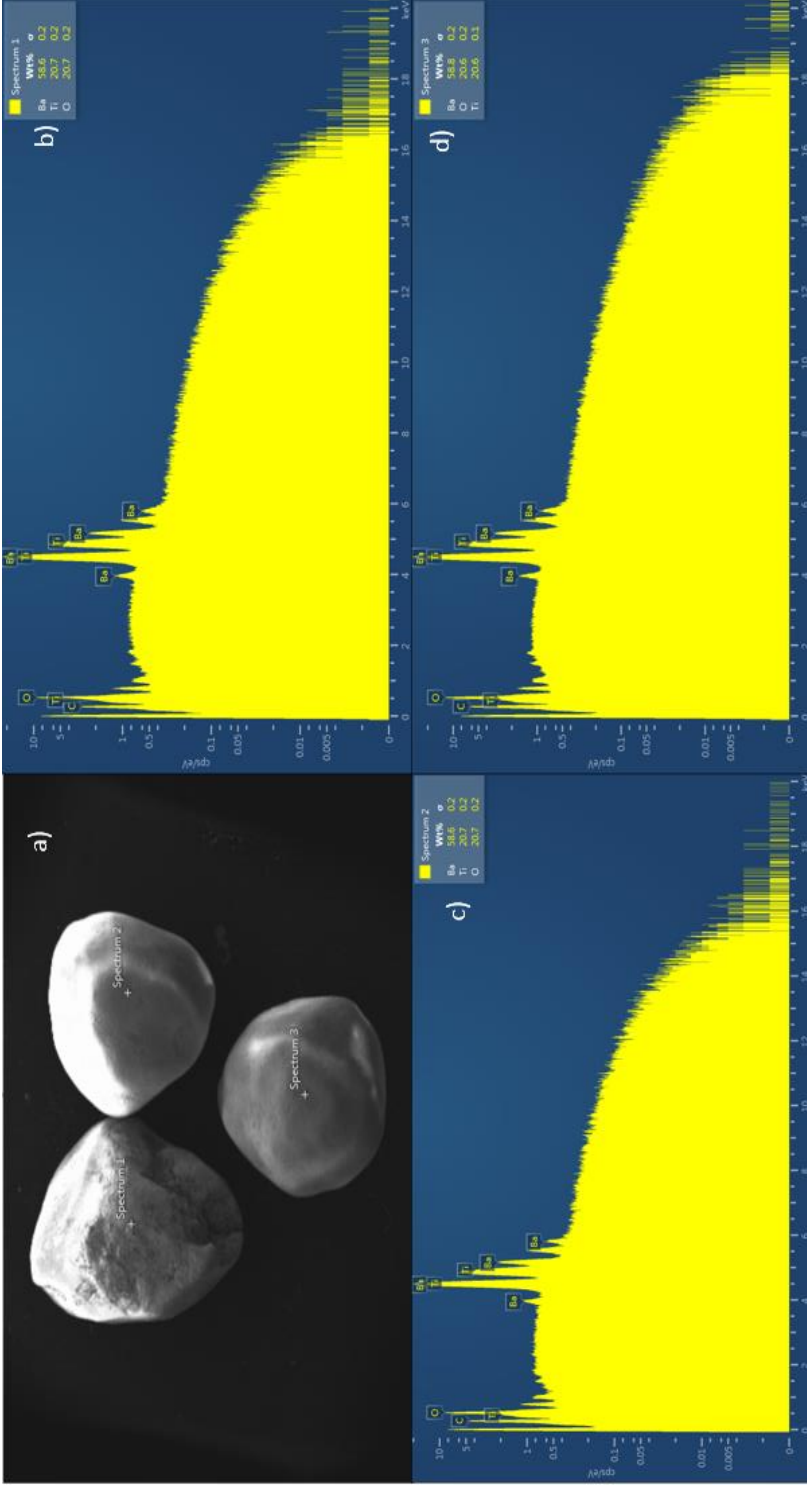


Figure 63: SEM-EDX  $\text{BaTiO}_3$  beads (after plasma).

### 9.3.5 Material stability against coking

None of the samples showed weight loss in TGA (performed up to 800 °C, so above the decoking temperature [156]). This indicates the limited amount of coke formation, which confirms the literature that the plasma process will induce less coking than thermal DRM [53]. Nevertheless, there are some coloured (black) spots when the packing is removed from the reactor, hence a more detailed analysis via Raman microscopy has been done to determine its origin. This shows that some coking is still present. The measurements were performed with a Horiba Xplora Plus micro-Raman, with a 50x magnification and a wavelength of 532 nm. Clear signals of the D and G bands of carbon can be observed for the SiO<sub>2</sub> packing (Figure 64) at 1330 cm<sup>-1</sup> and 1595 cm<sup>-1</sup>, including shoulders around 1472 cm<sup>-1</sup> and 1221 cm<sup>-1</sup>, as well as non-resolved overtone signals. When looking more closely to the α-Al<sub>2</sub>O<sub>3</sub> and ZrO<sub>2</sub> packing materials, unresolved broad signals can be observed in the region where also coke displays signals. However, as the signals are not resolved, it is difficult to confirm that this is due to some limited coke formation. Moreover, there was no detectable signal when measuring the bead and focussing on a black spot. For all beads, the Raman spectrum before and after plasma is shown, and for α-Al<sub>2</sub>O<sub>3</sub>, γ-Al<sub>2</sub>O<sub>3</sub> and BaTiO<sub>3</sub>, a second figure shows a zoomed-in frame to see the coking regions better.

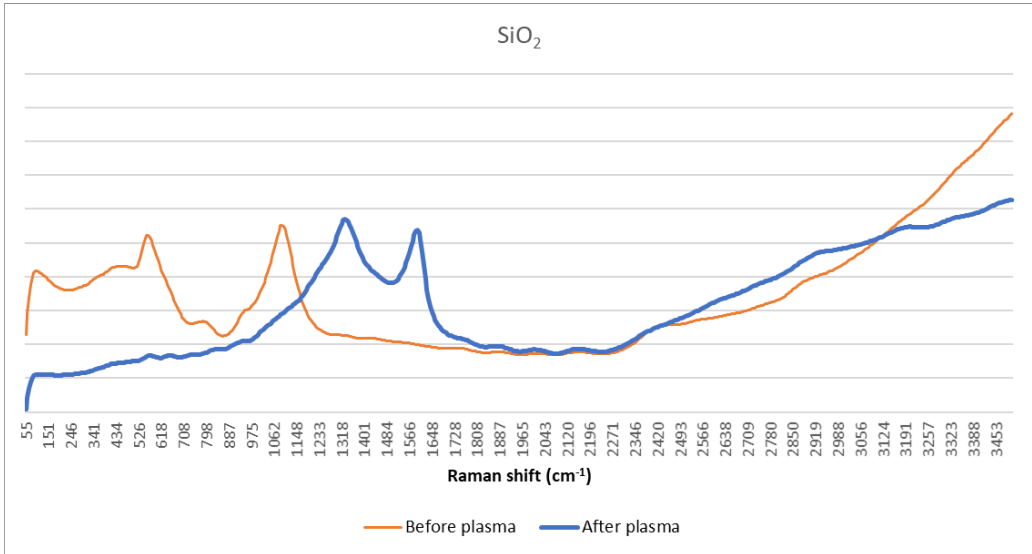


Figure 64: Raman spectrum for  $\text{SiO}_2$ , before and after plasma exposure.

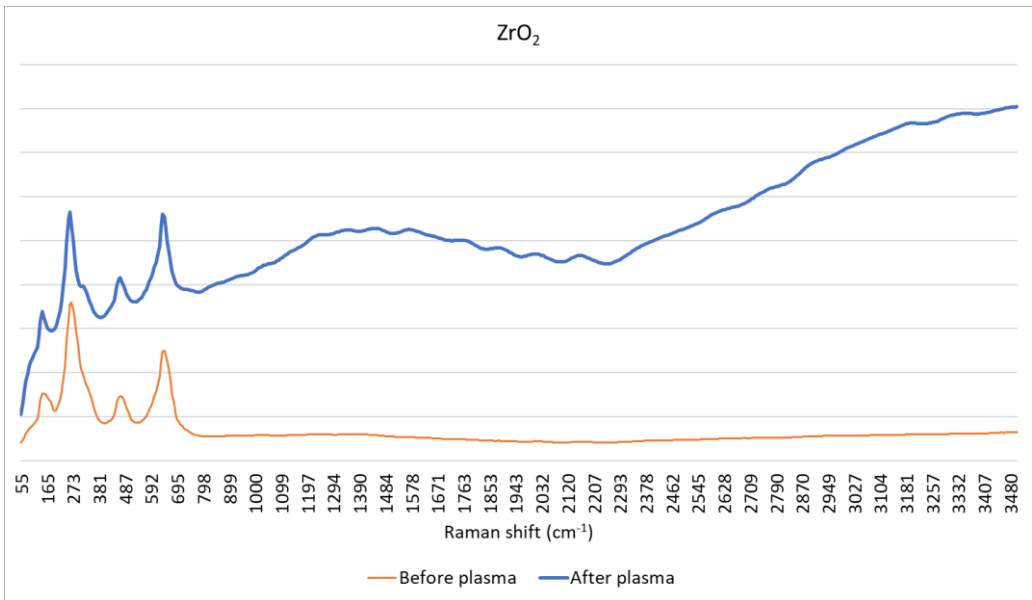


Figure 65: Raman spectrum for  $\text{ZrO}_2$ , before and after plasma exposure.

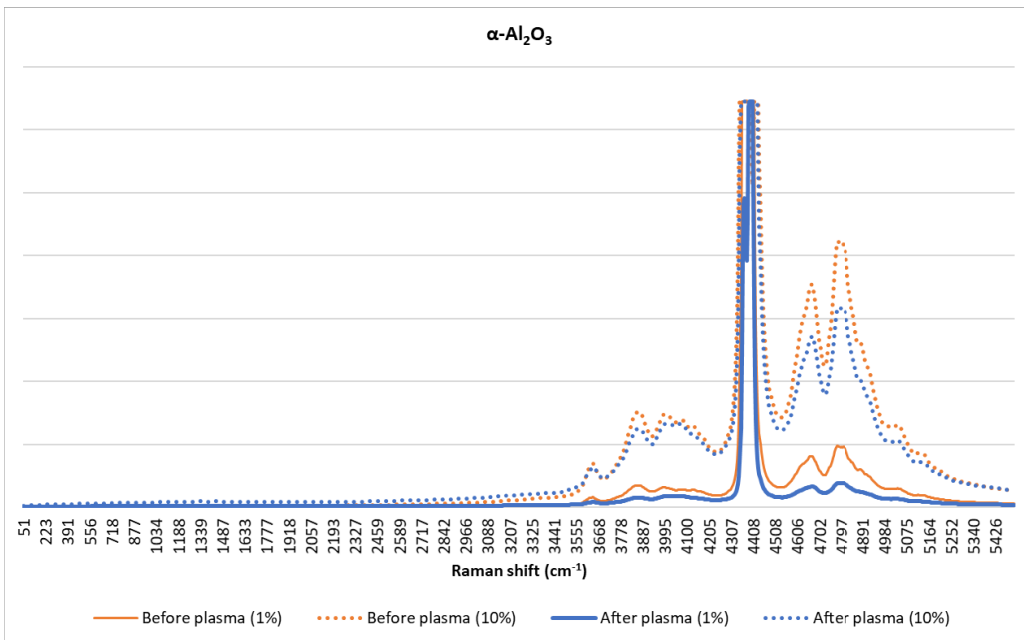


Figure 66: Raman spectrum for  $\alpha\text{-Al}_2\text{O}_3$ , before and after plasma exposure. For both beads (before and after plasma), two spectra are recorded: one with 90 % of the light filtered out, and one with 99 % of the light filtered out.

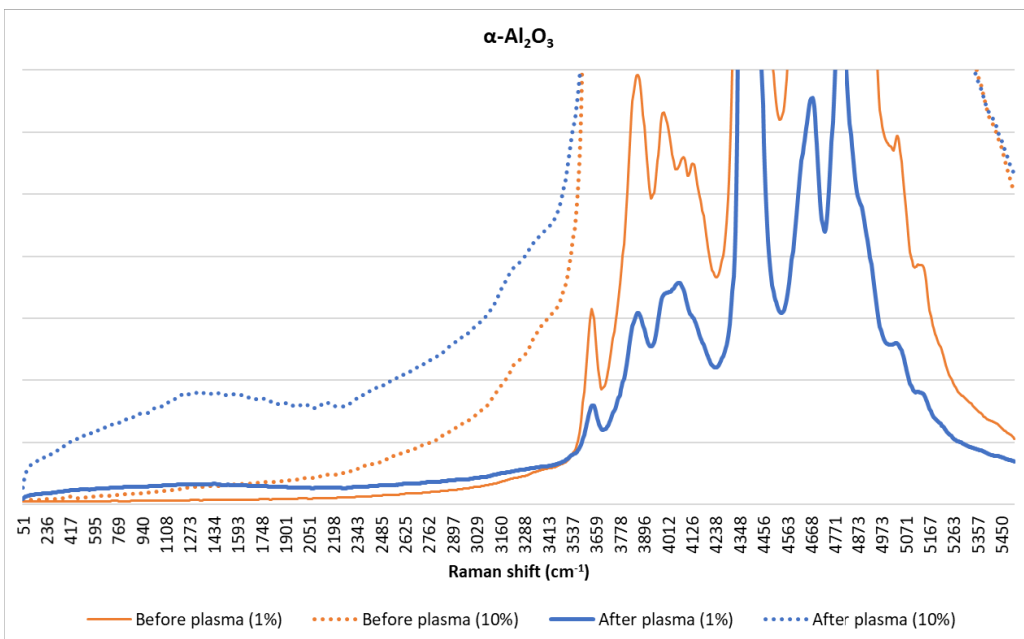


Figure 67: Zoomed-in (at coking regions) Raman spectrum for  $\alpha\text{-Al}_2\text{O}_3$ , before and after plasma exposure. For both beads (before and after plasma), two spectra are recorded: one with 90 % of the light filtered out, and one with 99 % of the light filtered out.

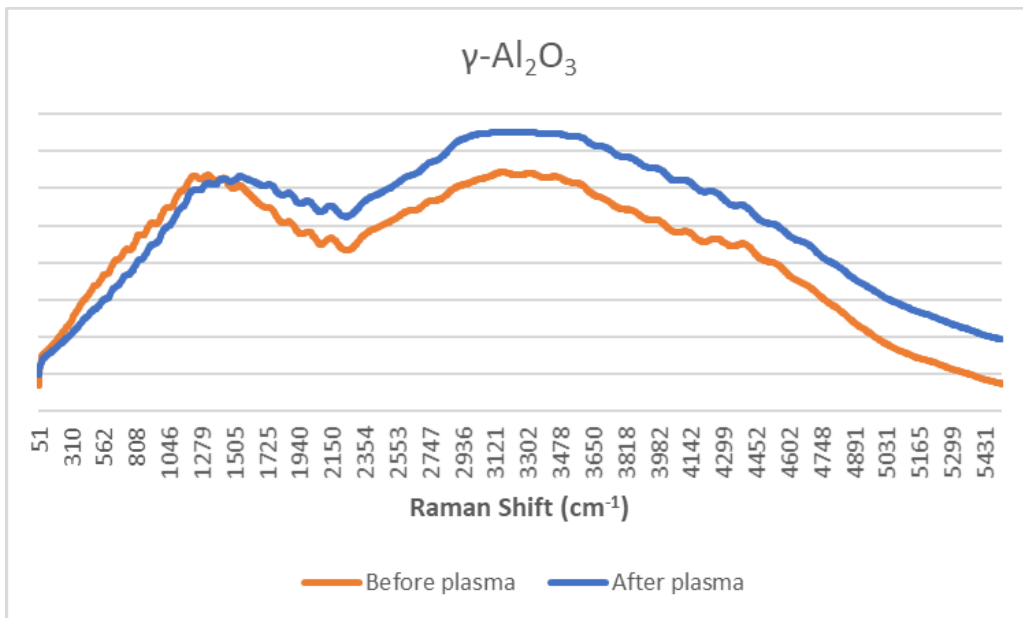


Figure 68: Raman spectrum for  $\gamma\text{-Al}_2\text{O}_3$ , before and after plasma exposure.

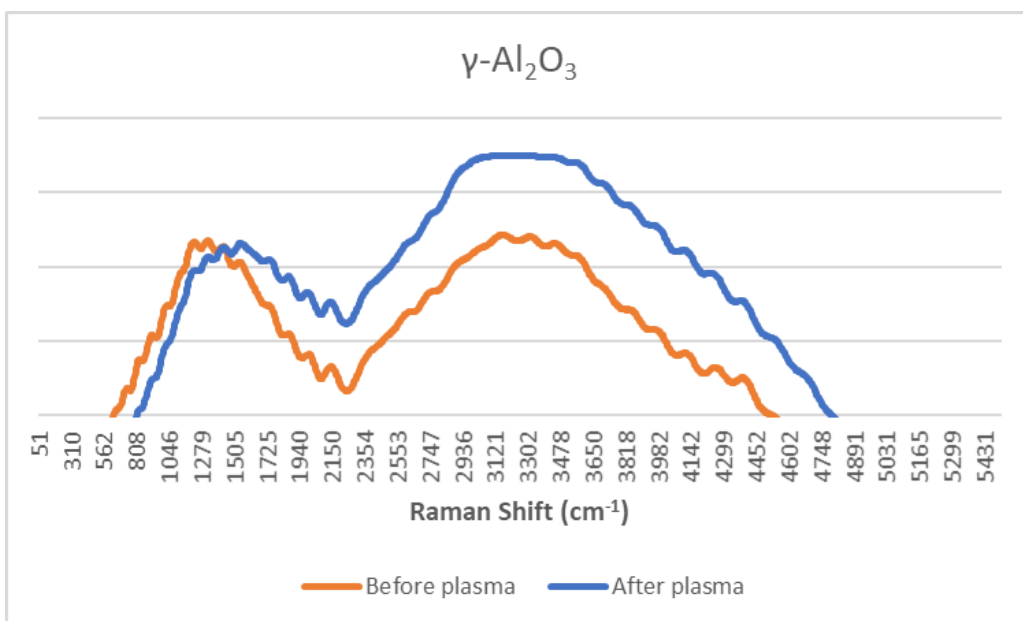


Figure 69: Zoomed-in (at coking regions) Raman spectrum for  $\gamma\text{-Al}_2\text{O}_3$ , before and after plasma exposure.



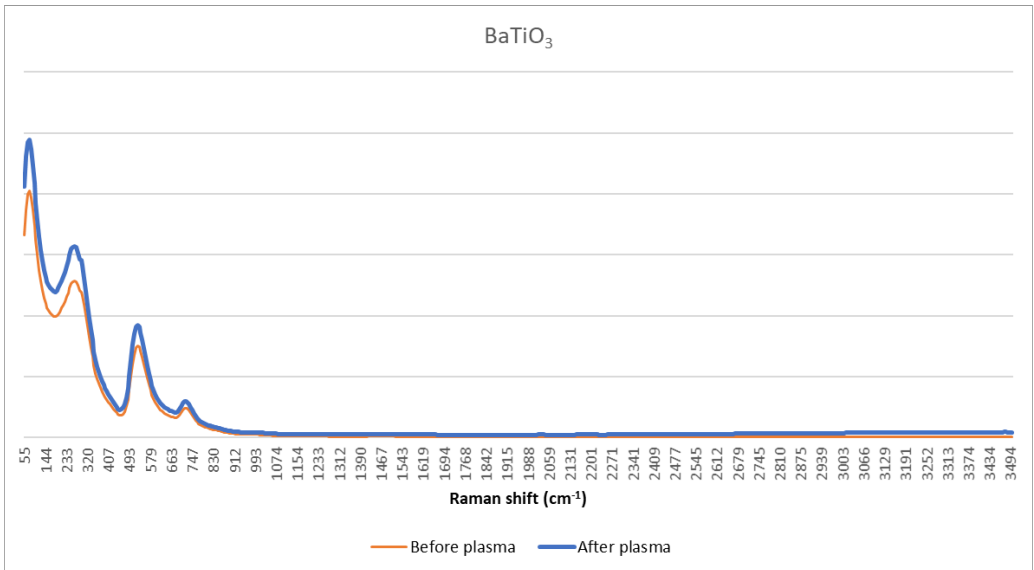


Figure 70: Raman spectrum for  $\text{BaTiO}_3$ , before and after plasma exposure.

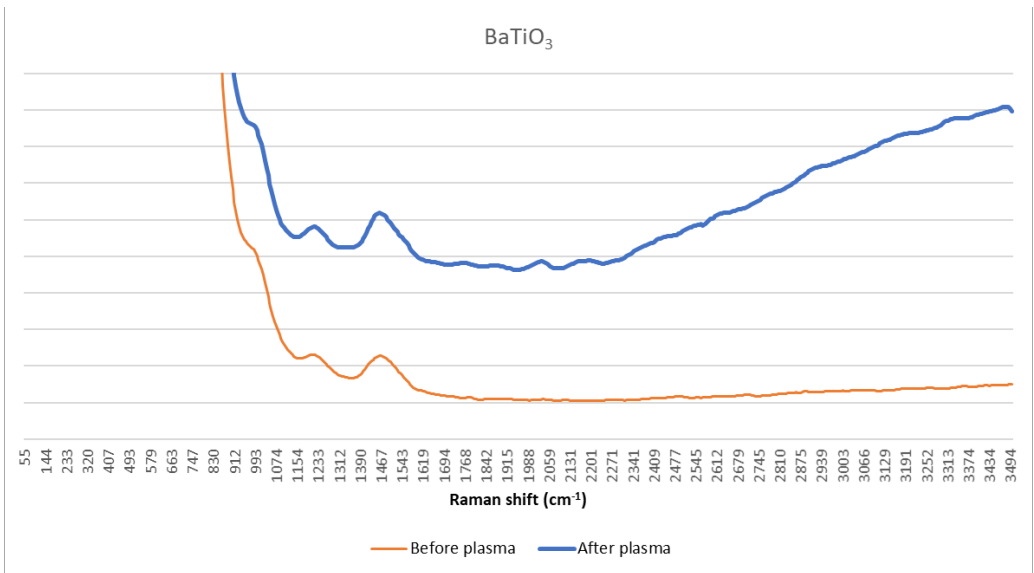
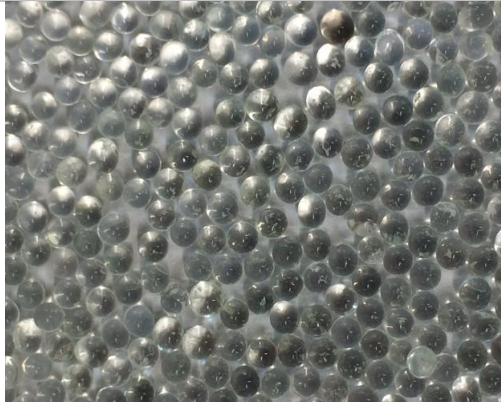







Figure 71: Zoomed-in (at coking regions) Raman spectrum for  $\text{BaTiO}_3$ , before and after plasma exposure.

Before plasma	After plasma
<b>SiO<sub>2</sub></b>	
	
<b>ZrO<sub>2</sub></b>	
	
<b>α-Al<sub>2</sub>O<sub>3</sub></b>	
	

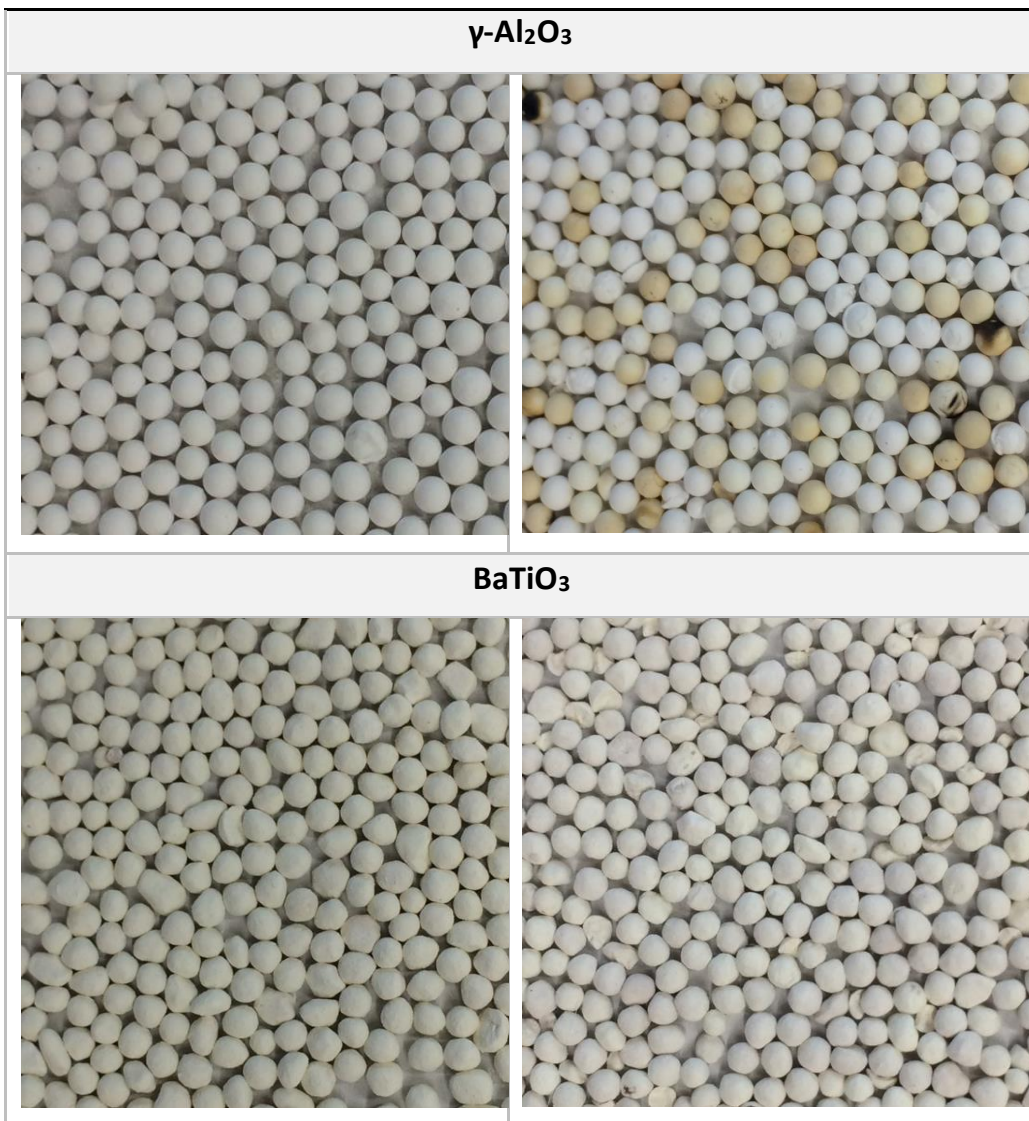


Figure 72: Visual image of the beads before and after plasma treatment.

### 9.3.6 Profilometry

The 3D profile and the surface profile (Figure 73) of the  $\text{SiO}_2$  beads indicate that the surface is rather smooth, with a surface roughness of  $82\pm 3$  nm. This can partly explain the lower conversions, since smooth surfaces have less contact points and edges that can increase the electric field.

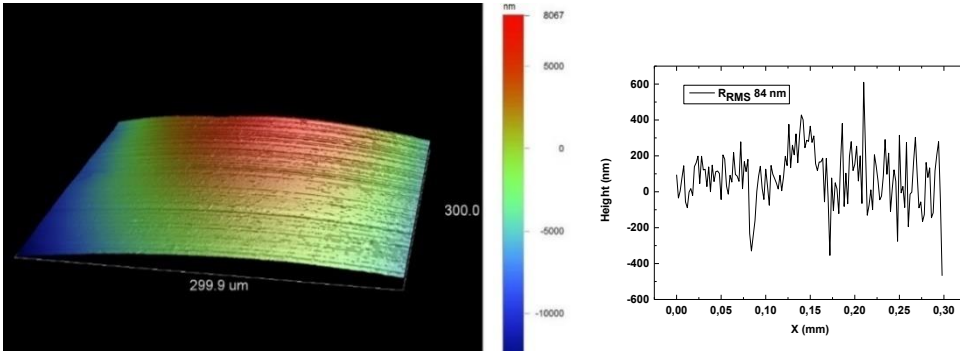


Figure 73: Profilometry profile for  $\text{SiO}_2$  beads of 2.0-2.24 mm.

The 3D profile and the surface profile (Figure 74) also indicate for  $\text{ZrO}_2$  that the surface is rather smooth, with a surface roughness of  $84 \pm 1$  nm.

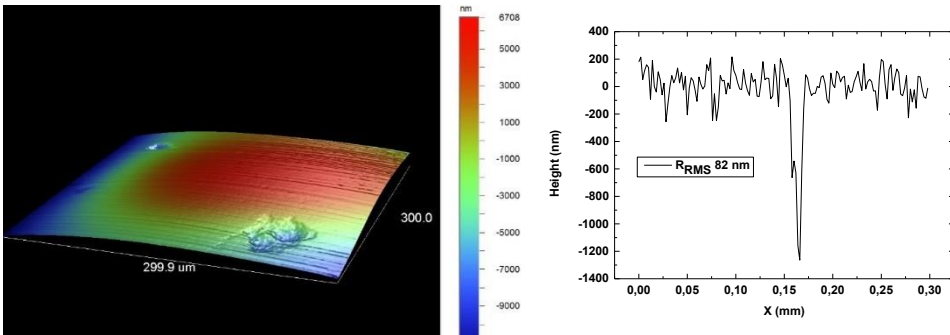


Figure 74: Profilometry profile for  $\text{ZrO}_2$  beads of 2.0-2.24 mm.

The profilometry of the  $\alpha\text{-Al}_2\text{O}_3$  (Figure 75) shows that the surface roughness is  $150 \pm 4$  nm.

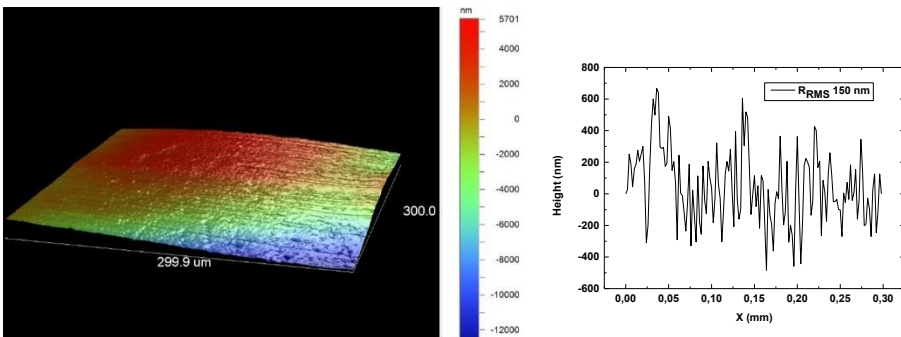


Figure 75: Profilometry profile for  $\alpha\text{-Al}_2\text{O}_3$  beads of 2.0-2.24 mm.



The profilometry for the BaTiO<sub>3</sub> beads (Figure 76) shows a surface roughness of 590±15 nm.

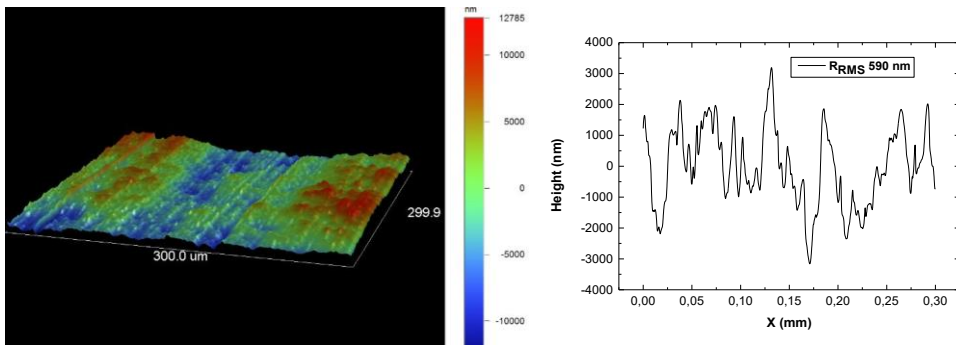


Figure 76: Profilometry profile for BaTiO<sub>3</sub> beads of 2.0-2.24 mm.

Finally, for the  $\gamma$ -Al<sub>2</sub>O<sub>3</sub> beads (Figure 77), a surface roughness of 3600 ± 460 nm is measured.

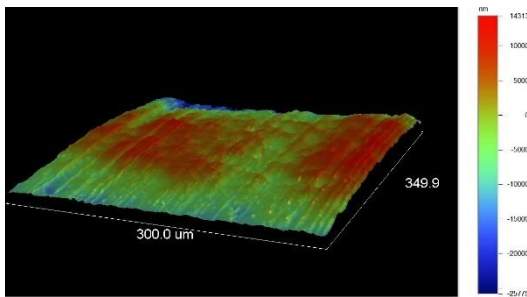


Figure 77: Profilometry profile for  $\gamma$ -Al<sub>2</sub>O<sub>3</sub> beads of 2.0-2.24 mm.

## 9.4 DETAILED CARBON, HYDROGEN AND OXYGEN BALANCES

First, for each element (carbon, hydrogen and oxygen) a complete balance is shown, with a detailed contribution of each component (figures: “total balance”). Then, to ensure better visibility, the same values were plotted, without the presence of the non-converted feed components (CO<sub>2</sub> and CH<sub>4</sub>) (figures: “detailed balance”). Finally, a figure is shown with the same values as in the latter figure, but normalised to 100 %.

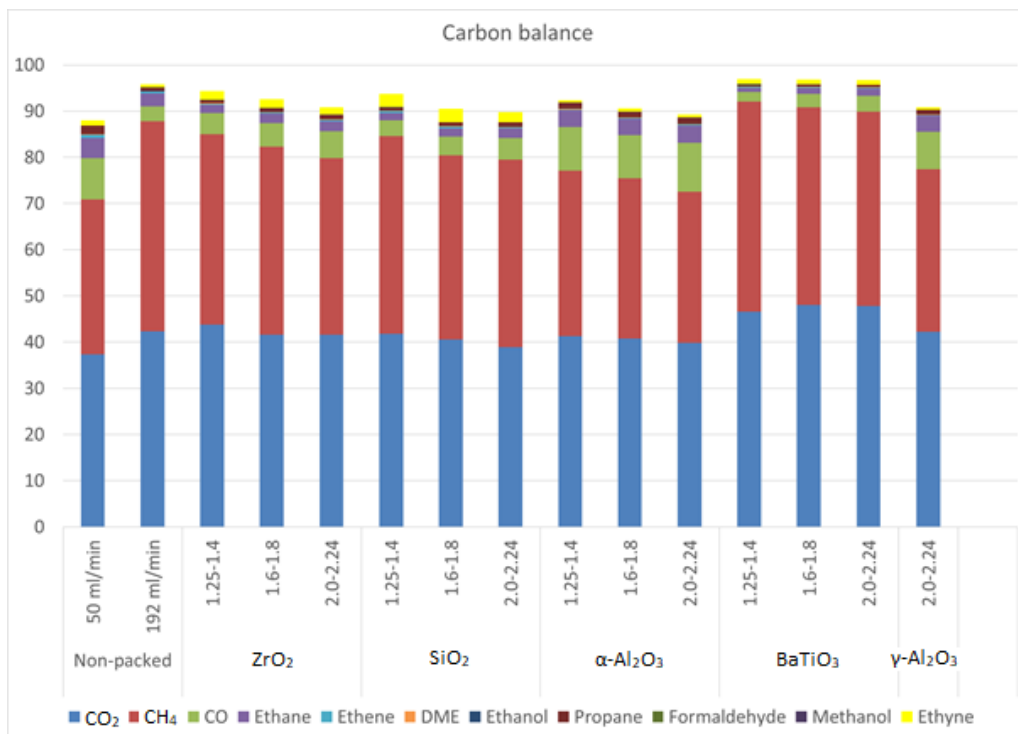


Figure 78: Total carbon balance for different bead sizes and materials.

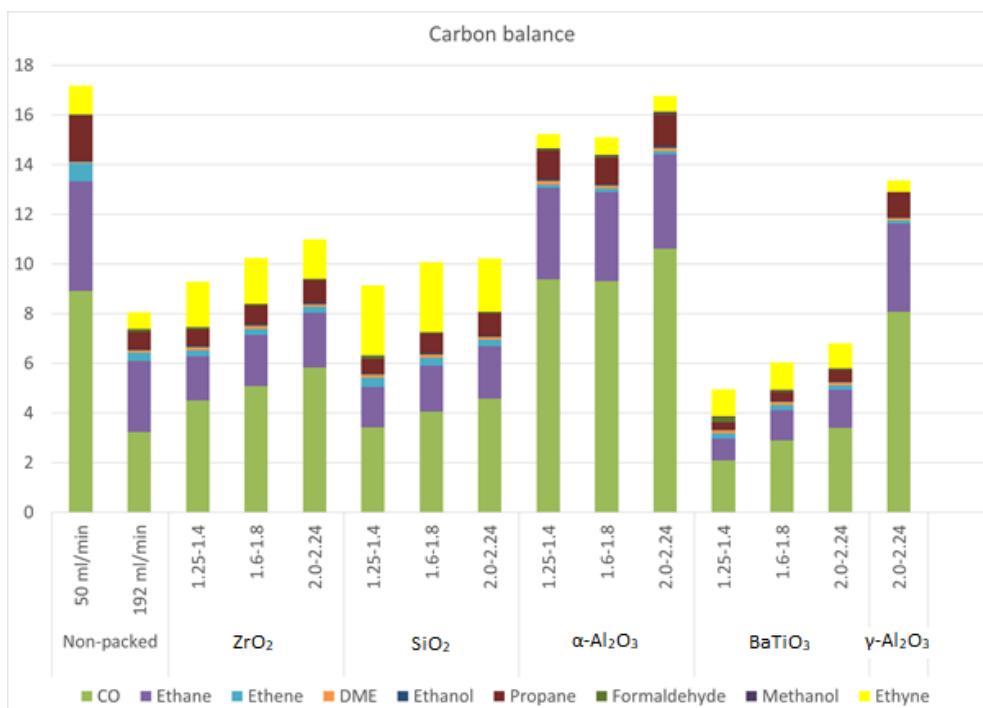


Figure 79: Detailed carbon balance for different bead sizes and materials, without CO<sub>2</sub> and CH<sub>4</sub> contribution.

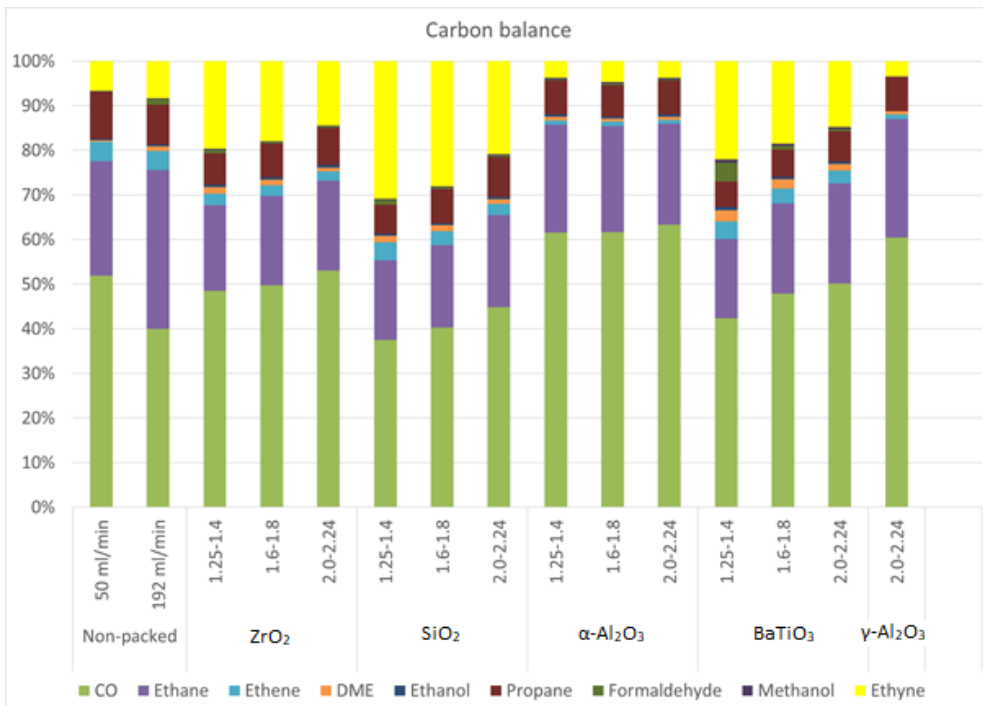


Figure 80: Normalized carbon balance for different bead sizes and materials, without CO<sub>2</sub> and CH<sub>4</sub> contribution.

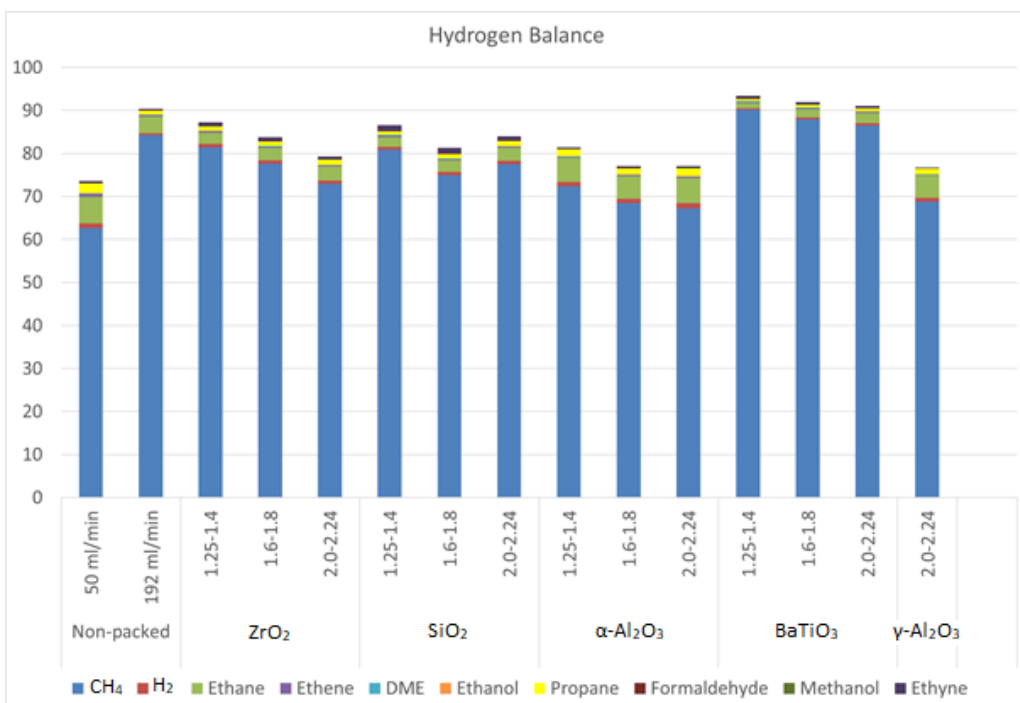


Figure 81: Total hydrogen balance for different bead sizes and materials.

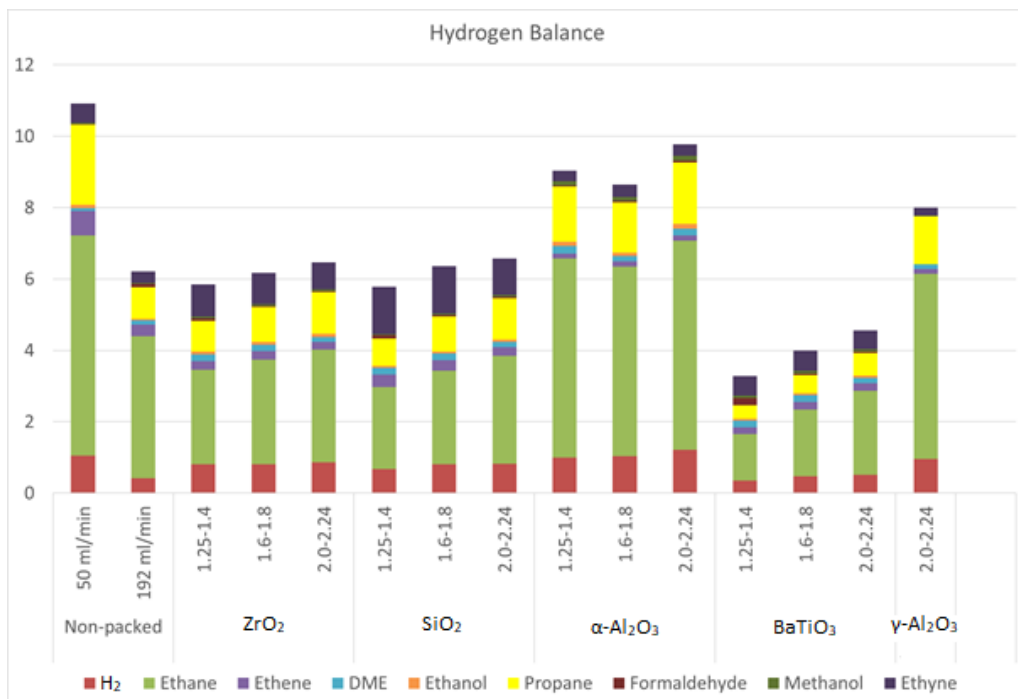


Figure 82: Detailed hydrogen balance for different bead sizes and materials, without CH<sub>4</sub> contribution.

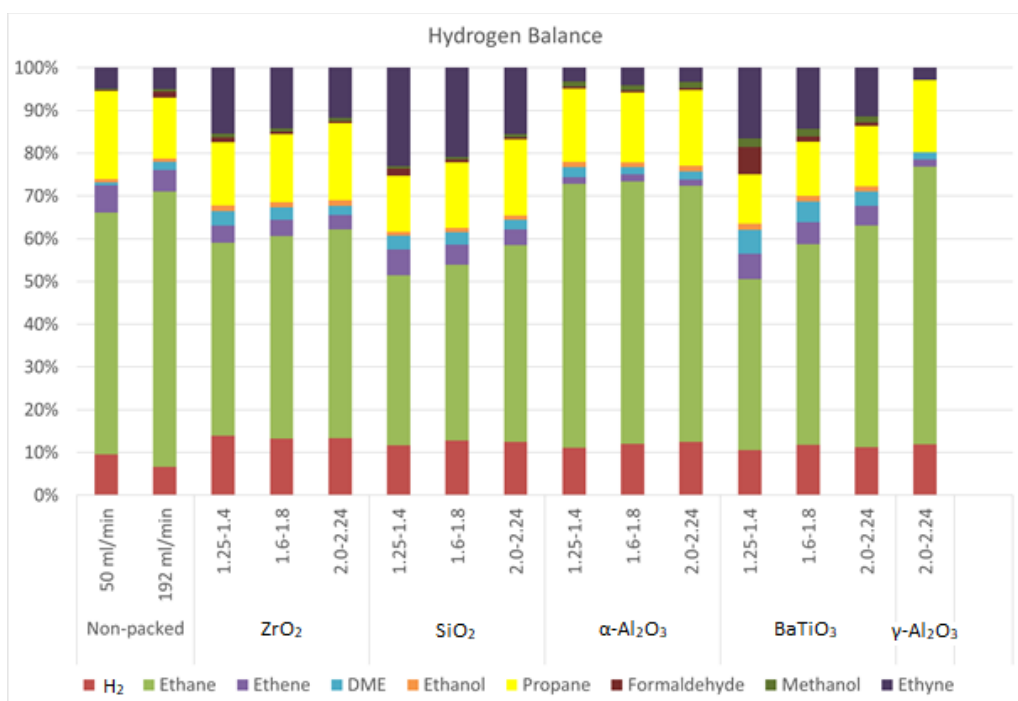


Figure 83: Normalized hydrogen balance for different bead sizes and materials, without CH<sub>4</sub> contribution.



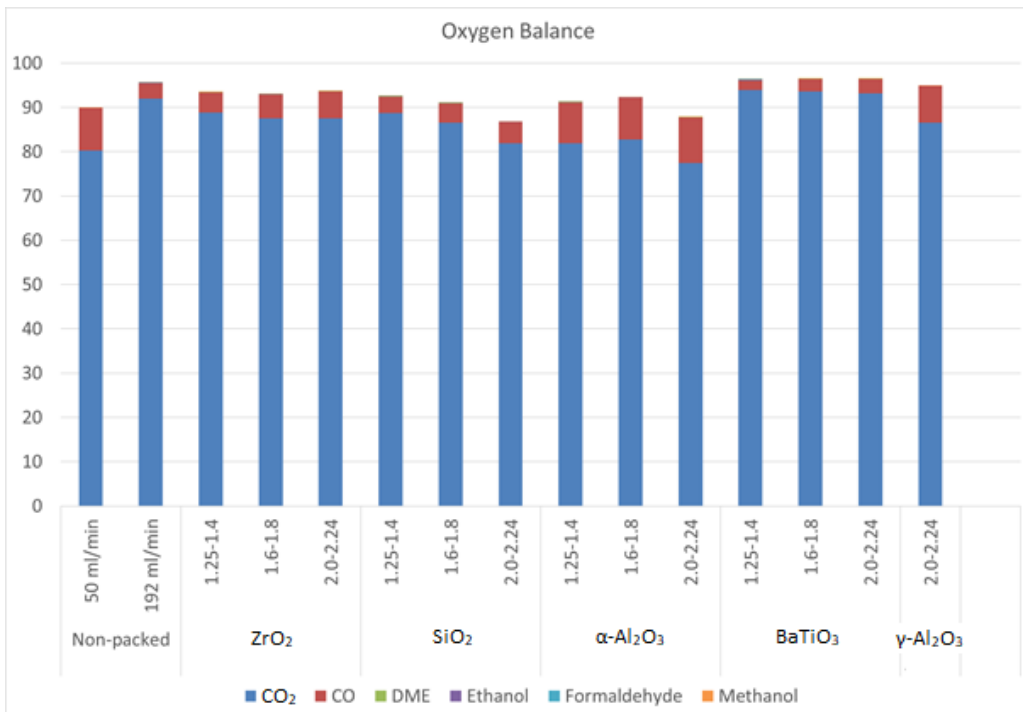


Figure 84: Total oxygen balance for different bead sizes and materials.

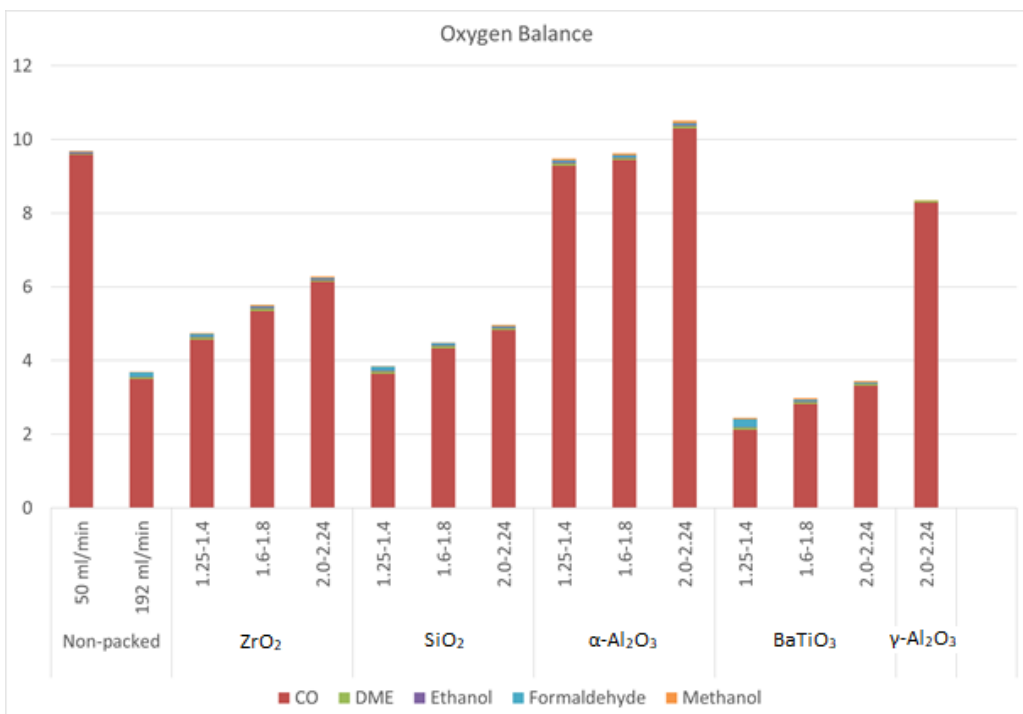


Figure 85: Detailed oxygen balance for different bead sizes and materials, without CO<sub>2</sub> contribution.

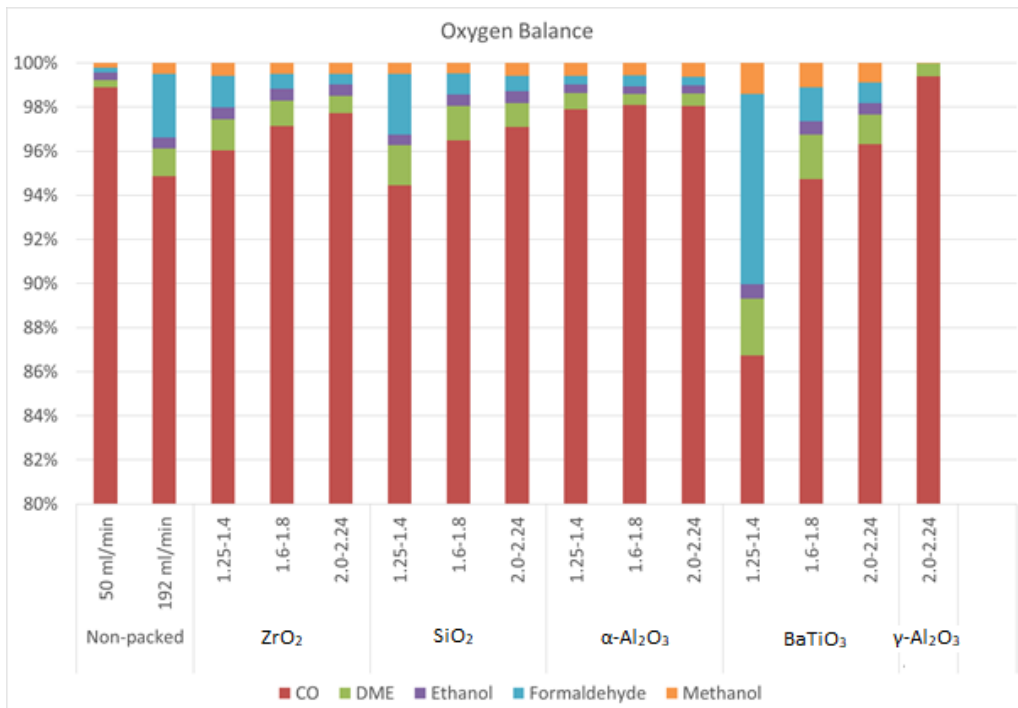


Figure 86: Normalized oxygen balance for different bead sizes and materials, without CO<sub>2</sub> contribution.

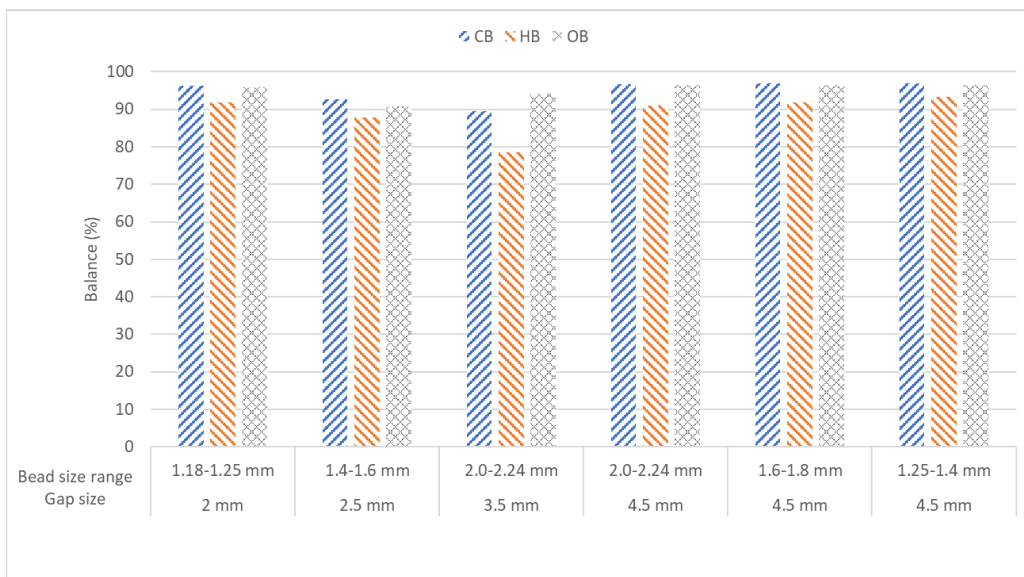


Figure 87: Carbon, hydrogen and oxygen balance for the experiments in Figure 37.

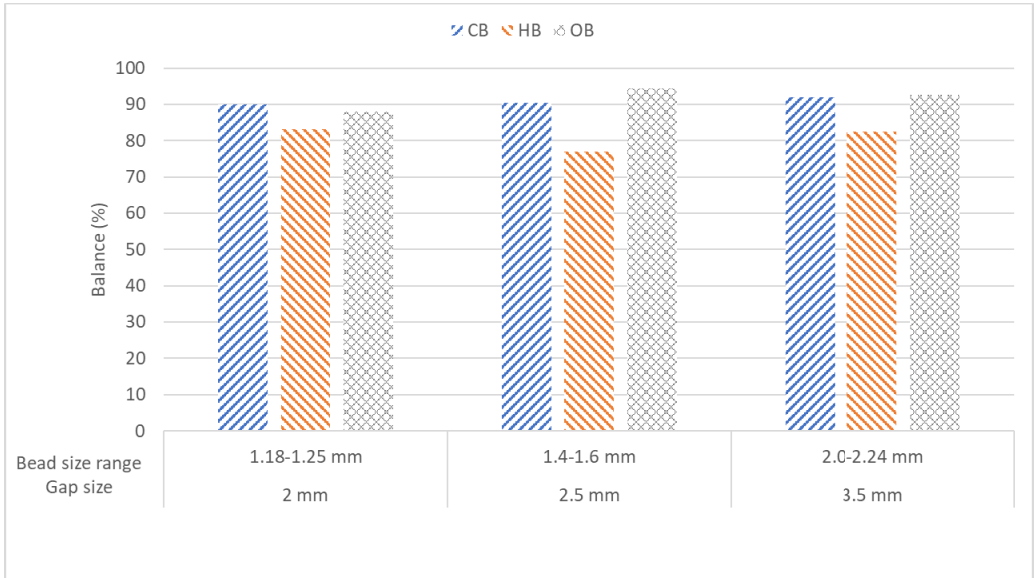


Figure 88: Carbon, hydrogen and oxygen balance for the experiments in Figure 38.

## 9.5 REACTION SCHEMES FROM LITERATURE

These figures are used to explain the results discussed in sections 4.2.6 and 5.3.3.

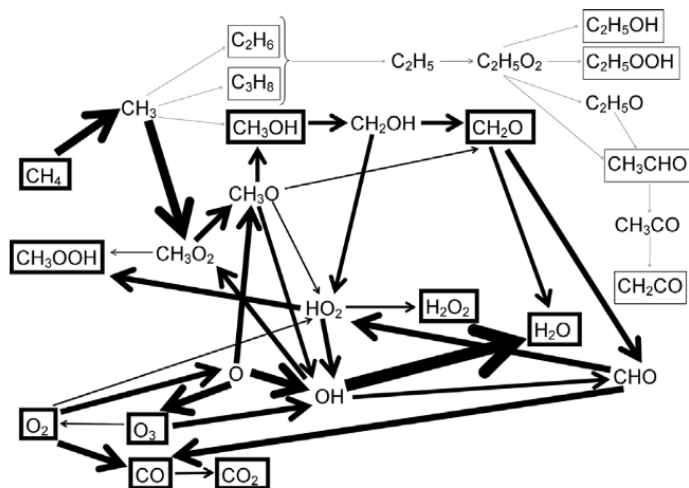


Figure 89: Reaction scheme to illustrate the main pathways for the conversions of CH<sub>4</sub> and O<sub>2</sub> and their interactions. Adopted with permission from ref. [157]. Copyright 2018 American Chemical Society.

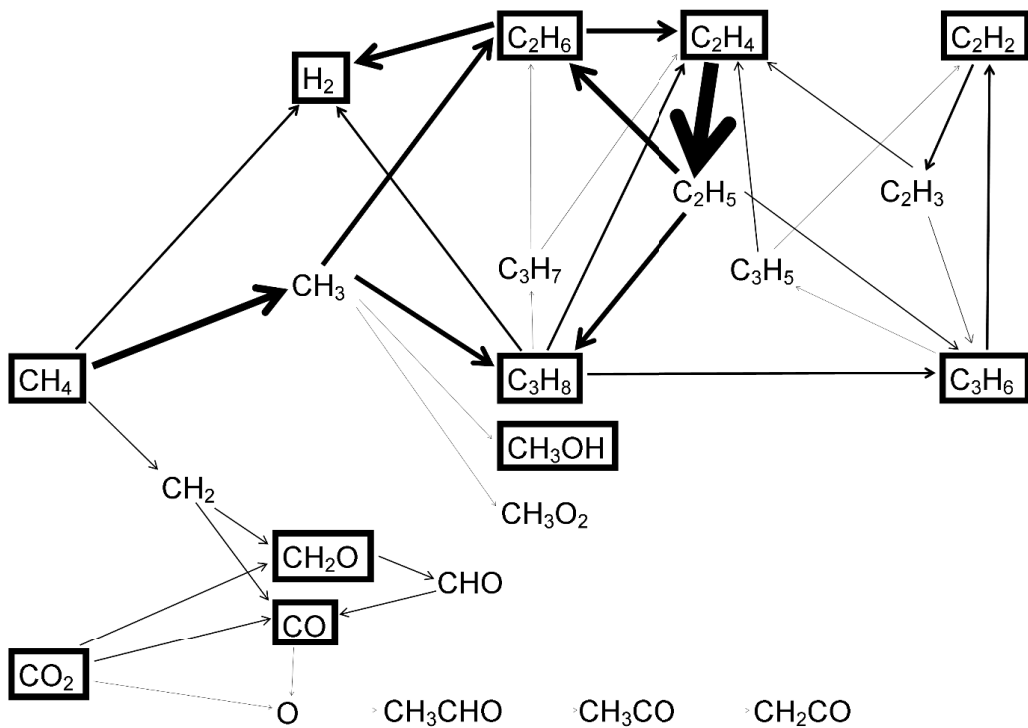


Figure 90: Reaction scheme to illustrate the main pathways for DRM. Adopted with permission from ref. [157]. Copyright 2018 American Chemical Society.

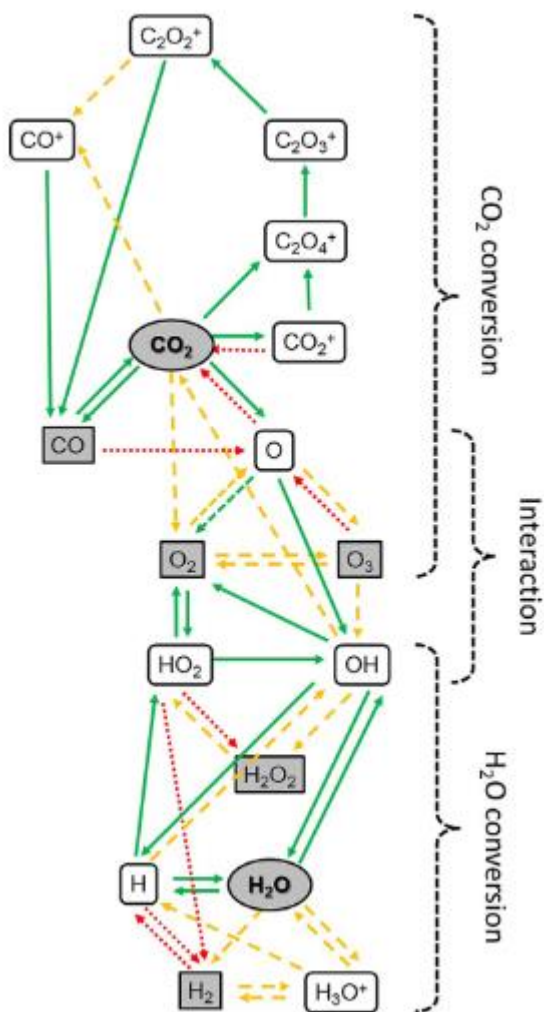


Figure 91: Reaction scheme to illustrate the main pathways for the conversions of  $\text{CO}_2$  and  $\text{H}_2\text{O}$  and their interactions. Adopted with permission from ref. [150]. Copyright 2018 Wiley-VCH.

## 9.6 YIELDS AND SELECTIVITIES FOR DRM

Table 26: Identified products, ranked in decreasing order of their yields, for the different packing materials and the non-packed reactor. The components highlighted are present for more than 1 %, the others for more than 100 ppm.

Non-packed	CO	C <sub>2</sub> H <sub>6</sub>	H <sub>2</sub>	C <sub>2</sub> H <sub>2</sub>	C <sub>3</sub> H <sub>8</sub>	C <sub>2</sub> H <sub>4</sub>	CH <sub>2</sub> O	C <sub>2</sub> H <sub>6</sub> O (DME)	C <sub>2</sub> H <sub>5</sub> OH (Ethanol)	CH <sub>3</sub> OH
ZrO <sub>2</sub>	CO	C <sub>2</sub> H <sub>6</sub>	C <sub>2</sub> H <sub>2</sub>	H <sub>2</sub>	C <sub>3</sub> H <sub>8</sub>	C <sub>2</sub> H <sub>4</sub>	C <sub>2</sub> H <sub>6</sub> O (DME)	CH <sub>2</sub> O	C <sub>2</sub> H <sub>5</sub> OH (Ethanol)	CH <sub>3</sub> OH
SiO <sub>2</sub>	CO	C <sub>2</sub> H <sub>2</sub>	C <sub>2</sub> H <sub>6</sub>	H <sub>2</sub>	C <sub>3</sub> H <sub>8</sub>	C <sub>2</sub> H <sub>4</sub>	C <sub>2</sub> H <sub>6</sub> O (DME)	CH <sub>2</sub> O	CH <sub>3</sub> OH	C <sub>2</sub> H <sub>5</sub> OH (Ethanol)
α-Al <sub>2</sub> O <sub>3</sub>	CO	C <sub>2</sub> H <sub>6</sub>	H <sub>2</sub>	C <sub>3</sub> H <sub>8</sub>	C <sub>2</sub> H <sub>2</sub>	C <sub>2</sub> H <sub>4</sub>	C <sub>2</sub> H <sub>6</sub> O (DME)	CH <sub>3</sub> OH	CH <sub>2</sub> O	C <sub>2</sub> H <sub>5</sub> OH (Ethanol)
γ-Al <sub>2</sub> O <sub>3</sub>	CO	C <sub>2</sub> H <sub>6</sub>	H <sub>2</sub>	C <sub>3</sub> H <sub>8</sub>	C <sub>2</sub> H <sub>2</sub>	C <sub>2</sub> H <sub>4</sub>	C <sub>2</sub> H <sub>6</sub> O (DME)	CH <sub>3</sub> OH	C <sub>2</sub> H <sub>5</sub> OH (Ethanol)	CH <sub>2</sub> O
BaTiO <sub>3</sub>	CO	C <sub>2</sub> H <sub>6</sub>	C <sub>2</sub> H <sub>2</sub>	H <sub>2</sub>	C <sub>3</sub> H <sub>8</sub>	C <sub>2</sub> H <sub>4</sub>	C <sub>2</sub> H <sub>6</sub> O (DME)	CH <sub>2</sub> O	CH <sub>3</sub> OH	C <sub>2</sub> H <sub>5</sub> OH (Ethanol)

In Chapter 4, we presented the product fractions, since the yields and selectivities both have some terms that are subject to the gas expansion, which cannot be accounted for, due to the uncertainty on this gas expansion. However, for the sake of completeness, we also present here both qualitative information on the order of the product yields (Table 26) and quantitative data on the selectivities (Table 27). The yields and selectivities are calculated with the following formulas, illustrated for H<sub>2</sub>:

The yields and selectivities are calculated with the following formulas, illustrated for H<sub>2</sub>:

$$Yield = [H_2]_{out} \quad (1)$$

$$Selectivity (\%) = \frac{2 * [H_2]_{out} * 100}{4 * ([CH_4]_{in} - [CH_4]_{out})} \quad (2)$$

Table 27: Product selectivities (%) for the different packing materials and sizes and for the non-packed reactor. The highest selectivities for each component are highlighted.

	CO	H <sub>2</sub>	C <sub>2</sub> H <sub>6</sub>	C <sub>2</sub> H <sub>4</sub>	C <sub>2</sub> H <sub>2</sub>	C <sub>3</sub> H <sub>8</sub>	C <sub>2</sub> H <sub>6</sub> O (DME)	C <sub>2</sub> H <sub>5</sub> OH (Ethanol)	CH <sub>2</sub> O	CH <sub>3</sub> OH
Non-packed	31	4	15	3	4	6.2	0.2	0.2	0.1	0.1
reactor	26	4	23	3	6	5.9	0.7	0.3	0.8	0.1



ZrO <sub>2</sub>	1.25-1.4	30	6	12	2	12	4.4	0.9	0.3	0.4	0.2
	1.6-1.8	29	5	12	1	10	4.4	0.7	0.3	0.2	0.1
	2.0-2.24	29	4	11	1	8	4.5	0.5	0.3	0.1	0.1
SiO <sub>2</sub>	1.25-1.4	22	5	11	2	18	3.9	0.9	0.2	0.6	0.1
	1.6-1.8	21	4	9	2	14	4.0	0.7	0.2	0.2	0.1
	2.0-2.24	22	4	10	1	10	4.5	0.5	0.2	0.2	0.1
α-Al <sub>2</sub> O <sub>3</sub>	1.25-1.4	41	4	16	1	3	5.0	0.6	0.3	0.2	0.2
	1.6-1.8	38	4	15	1	3	4.4	0.4	0.3	0.2	0.2
	2.0-2.24	39	4	14	1	2	4.6	0.4	0.3	0.2	0.2
BaTiO <sub>3</sub>	1.25-1.4	26	4	11	2	14	3.6	1.6	0.4	0.6	0.4
	1.6-1.8	32	5	13	2	12	4.0	1.3	0.4	0.5	0.4
	2.0-2.24	34	5	15	2	10	4.5	0.9	0.4	0.3	0.3
Y-Al <sub>2</sub> O <sub>3</sub>	2.0-2.24	36	4	16	1	2	4.6	0.4	0.0	0.0	0.0



## 10 BIBLIOGRAPHY

---

- [1] C. Song, Global challenges and strategies for control, conversion and utilization of CO<sub>2</sub> for sustainable development involving energy, catalysis, adsorption and chemical processing, *Catal. Today.* 115 (2006) 2–32. doi:10.1016/j.cattod.2006.02.029.
- [2] J.H. Christensen, K.K. Kanikicharla, Climate Phenomena and their Relevance for Future Regional Climate Change, IPCC. (2013). doi:10.1017/CBO9781107415324.028.
- [3] J.G. Canadella, C. Le Quere, M.R. Raupacha, C.B. Fielde, E.T. Buitenhuis, P. Ciais, T.J. Conway, N.P. Gillett, R.A. Houghton, G. Marland, Contributions to accelerating atmospheric CO<sub>2</sub> growth from economic activity, carbon intensity, and efficiency of natural sinks, *PNAS.* 104 (2007) 18866–18870. doi:10.1073/pnas.0702737104.
- [4] A. Zecchina, Energy sources and carbon dioxide waste, *Rend. Lincei.* 25 (2014) 113–117. doi:10.1007/s12210-013-0253-1.
- [5] H. Ritchie, M. Roser, CO<sub>2</sub> and other greenhouse gas emissions, Our World Data. (2017). <https://ourworldindata.org/co2-and-other-greenhouse-gas-emissions#>.
- [6] D.R. Tobergte, S. Curtis, Climate change: Causes, Effects and Solutions, 2013. doi:10.1017/CBO9781107415324.004.
- [7] U.S.E.P. Agency, Understanding Global Warming Potentials, (n.d.). <https://www.epa.gov/ghgemissions/understanding-global-warming-potentials>.
- [8] R.K. Pachauri, L. Meyer, Climate change 2014 Synthesis Report Summary for Policymakers, Scott B. Power N.H. Ravindranath. (2014).
- [9] R. Snoeckx, A. Bogaerts, Plasma technology – a novel solution for CO<sub>2</sub> conversion?, *Chem. Soc. Rev.* (2017). doi:10.1039/C6CS00066E.
- [10] M.M.F. Hasan, E.L. First, F. Boukouvala, C.A. Floudas, A multi-scale framework for CO<sub>2</sub> capture, utilization, and sequestration: CCUS and CCU, *Comput. Chem.*

- Eng. 81 (2015) 2–21. doi:10.1016/j.compchemeng.2015.04.034.
- [11] I. Omae, Recent developments in carbon dioxide utilization for the production of organic chemicals, *Coord. Chem. Rev.* 256 (2012) 1384–1405. doi:10.1016/j.ccr.2012.03.017.
- [12] R.M. Cuéllar-Franca, A. Azapagic, Carbon capture, storage and utilisation technologies: A critical analysis and comparison of their life cycle environmental impacts, *J. CO<sub>2</sub> Util.* 9 (2015) 82–102. doi:10.1016/j.jcou.2014.12.001.
- [13] D. Wille, *Verkennde studie naar de inzetbaarheid van biomassa en biomassa-reststromen in bioraffinageketens in Vlaanderen*, OVAM Publ. (2013) 192.
- [14] Aebiom, *A Biogas Road Map for Europe*, 2009.
- [15] U. Department of Agriculture, U. Environmental Protection Agency, U. Departement of Energy, *Biogas Opportunities Roadmap*, 2014.
- [16] M. Coffey, Energy and power generation: Maximising biogas yields from sludge, *Filtr. Sep.* 46 (2009) 12–15. doi:10.1016/S0015-1882(09)70085-0.
- [17] S. Rasi, *Biogas Composition and Upgrading to Biomethane*, 1979.
- [18] R. Snoeckx, S. Heijckers, K. Van Wesenbeeck, S. Lenaerts, A. Bogaerts, CO<sub>2</sub> conversion in a dielectric barrier discharge plasma: N<sub>2</sub> in the mix as a helping hand or problematic impurity?, *Energy Environ. Sci.* 9 (2016) 30–39. doi:10.1039/C5EE03304G.
- [19] B. Hu, C. Guild, S.L. Suib, Thermal, electrochemical, and photochemical conversion of CO<sub>2</sub> to fuels and value-added products, *J. CO<sub>2</sub> Util.* 1 (2013) 18–27. doi:10.1016/j.jcou.2013.03.004.
- [20] J. Tsao, N. Lewis, G. Crabtree, *Solar Frequently Asked Questions*, US Dep. Energy. (2006) 1–24. doi:10.1016/B978-0-12-415953-2.00005-4.
- [21] Arthouros Zervos, *Renewables 2018: global status report*, 2018. doi:978-3-9818911-3-3.
- [22] M. Fischer, M. Werber, P. V. Schwartz, Batteries: Higher energy density than gasoline?, *Energy Policy.* 37 (2009) 2639–2641.

- doi:10.1016/j.enpol.2009.02.030.
- [23] S.M. Jarvis, S. Samsatli, Technologies and infrastructures underpinning future CO<sub>2</sub> value chains: A comprehensive review and comparative analysis, *Renew. Sustain. Energy Rev.* 85 (2018) 46–68. doi:10.1016/j.rser.2018.01.007.
- [24] P. Lanzafame, S. Abate, C. Ampelli, C. Genovese, R. Passalacqua, G. Centi, S. Perathoner, Beyond Solar Fuels: Renewable Energy-Driven Chemistry, *ChemSusChem*. 10 (2017) 4409–4419. doi:10.1002/cssc.201701507.
- [25] C. Nigara, Yutaka, Bernard, Production of CO by direct thermal splitting of CO<sub>2</sub> at high temperature, *Chem. Soc. Japan*. 59 (1986) 1997–2002.
- [26] N. Itoh, M.A. Sanchez, W.C. Xu, K. Haraya, M. Hongo, Application of a membrane reactor system to thermal decomposition of CO<sub>2</sub>, *J. Memb. Sci.* 77 (1993) 245–253. doi:10.1016/0376-7388(93)85073-6.
- [27] Y. Fan, J. Ren, W. Onstot, J. Pasale, T.T. Tsotsis, F.N. Egolfopoulos, Reactor and Technical Feasibility Aspects of a CO<sub>2</sub> Decomposition-Based Power Generation Cycle, Utilizing a High-Temperature Membrane Reactor, *Ind. Eng. Chem. Res.* 42 (2003) 2618–2626. doi:10.1021/ie020980r.
- [28] Z. Jiang, T. Xiao, V.L. Kuznetsov, P.P. Edwards, Turning carbon dioxide into fuel., *Philos. Trans. A. Math. Phys. Eng. Sci.* 368 (2010) 3343–3364. doi:10.1098/rsta.2010.0119.
- [29] J. Spivey, K. Dooley, Y.-F. Han, *Catalysis*, Volume 22, Royal Society of Chemistry, 2015.
- [30] O. Muraza, A. Galadima, A review on coke management during dry reforming of methane, *Int. J. Energy Res.* 39 (2015) 1196–1216. doi:10.1002/er.3295.
- [31] S. Wang, G.Q.M. Lu, G.J. Millar, Carbon Dioxide Reforming of Methane To Produce Synthesis Gas over Metal-Supported Catalysts : State of the Art, *Energy & Fuels*. 0624 (1996) 896–904.
- [32] P. Ferreira-Aparicio, I. Rodr, I. Rodríguez-Ramos, J.A. Anderson, A. Guerrero-Ruiz, Mechanistic aspects of the dry reforming of methane over ruthenium catalysts, *Appl. Catal. A Gen.* 202 (2000) 183–196. doi:10.1016/S0926-860X(00)00525-1.

- [33] Y.H. Hu, Solid-solution catalysts for CO<sub>2</sub> reforming of methane, *Catal. Today*. 148 (2009) 206–211. doi:10.1016/j.cattod.2009.07.076.
- [34] S.C. Teuner, P. Neumann, F. Von Linde, The Calcor Standard and Calcor Economy Processes, *Oil Gas Eur. Mag.* 27 (2001) 44–46.
- [35] J. Rostrup-Nielsen, 40 Years in Catalysis, *Catal. Today*. 111 (2006) 4–11. doi:10.1016/j.cattod.2005.10.016.
- [36] DNV, Carbon dioxide utilization - Electrochemical conversion of CO<sub>2</sub> - Opportunities and challenges, 2011.
- [37] E.N. Coker, A. Ambrosini, M.A. Rodriguez, J.E. Miller, Ferrite-YSZ composites for solar thermochemical production of synthetic fuels: In operando characterization of CO<sub>2</sub> reduction, *J. Mater. Chem.* 21 (2011) 10767–10776. doi:10.1039/c1jm11053e.
- [38] S.C. Roy, O.K. Varghese, M. Paulose, C.A. Grimes, Toward Solar Fuels: Photocatalytic Conversion of Carbon Dioxide to Hydrocarbons, *ACS Nano*. 4 (2010) 1259–1278. doi:10.1021/nn9015423.
- [39] E. V. Kondratenko, G. Mul, J. Baltrusaitis, G.O. Larrazábal, J. Pérez-Ramírez, Status and perspectives of CO<sub>2</sub> conversion into fuels and chemicals by catalytic, photocatalytic and electrocatalytic processes, *Energy Environ. Sci.* 6 (2013) 3112. doi:10.1039/c3ee41272e.
- [40] S. Das, W.M. a. Wan Daud, A review on advances in photocatalysts towards CO<sub>2</sub> conversion, *RSC Adv.* 4 (2014) 20856. doi:10.1039/c4ra01769b.
- [41] B. Wang, Y. Li, N. Wu, C.Q. Lan, CO<sub>2</sub> bio-mitigation using microalgae., *Appl. Microbiol. Biotechnol.* 79 (2008) 707–18. doi:10.1007/s00253-008-1518-y.
- [42] A. Álvarez, M. Borges, J.J. Corral-Pérez, J.G. Olcina, L. Hu, D. Cornu, R. Huang, D. Stoian, A. Urakawa, CO<sub>2</sub> Activation over Catalytic Surfaces, *ChemPhysChem*. 18 (2017) 3135–3141. doi:10.1002/cphc.201700782.
- [43] A. Bogaerts, E. Neyts, R. Gijbels, J. van der Mullen, Gas discharge plasmas and their applications, *Spectrochim. Acta Part B At. Spectrosc.* 57 (2002) 609–658. doi:10.1016/S0584-8547(01)00406-2.

- [44] B. Eliasson, U. Kogelschatz, Nonequilibrium Volume Plasma Chemical Processing, *IEEE Trans. Plasma Sci.* 19 (1991) 1063–1077. doi:10.1109/27.125031.
- [45] L. Tonks, The Birth of “Plasma,” *Am. J. Phys.* 35 (1967) 857–858. doi:10.1119/1.1974266.
- [46] R. Snoeckx, Plasma technology. A novel solution for CO<sub>2</sub> conversion?, (2017). <https://www.uantwerpen.be/images/uantwerpen/container2642/files/PhD-theses/Snoeckx.pdf>.
- [47] R. Snoeckx, R. Aerts, X. Tu, A. Bogaerts, Plasma-Based Dry Reforming: A Computational Study Ranging From Nanoseconds to Seconds Timescale., *J. Phys. Chem.* 117 (2013) 4957–4970. doi:10.1021/jp311912b.
- [48] H. Conrads, M. Schmidt, Plasma generation and plasma sources, *Plasma Sources Sci. Technol.* 9 (2000) 441–454.
- [49] U. Kogelschatz, B. Eliasson, W. Egli, From ozone generators to flat television screens : history and future potential of dielectric-barrier discharges, *Pure Appl. Chem.* 71 (1999) 1819–1828.
- [50] A. Bogaerts, *Plasmatechnologie*, University of Antwerp, Antwerp, n.d.
- [51] K. Van Laer, A. Bogaerts, Fluid modelling of a packed bed dielectric barrier discharge plasma reactor, *Plasma Sources Sci. Technol.* 25 (2016) 15002. doi:10.1088/0963-0252/25/1/015002.
- [52] A. Fridman, *Plasma Chemistry*, First edit, Cambridge University Press, New York, 2008.
- [53] E.C. Neyts, A. Bogaerts, Understanding plasma catalysis through modelling and simulation—a review, *J. Phys. D. Appl. Phys.* 47 (2014) 224010. doi:10.1088/0022-3727/47/22/224010.
- [54] H.L. Chen, H.M. Lee, S.H. Chen, Y. Chao, M.B. Chang, Review of plasma catalysis on hydrocarbon reforming for hydrogen production—Interaction, integration, and prospects, *Appl. Catal. B Environ.* 85 (2008) 1–9. doi:10.1016/j.apcatb.2008.06.021.
- [55] P.K. Chu, X. Lu, *Low Temperature Plasma Technology*, CRC Press, 2013.

doi:10.1201/b15153.

- [56] J.C. Whitehead, Plasma–catalysis: the known knowns, the known unknowns and the unknown unknowns, *J. Phys. D. Appl. Phys.* 49 (2016) 243001. doi:10.1088/0022-3727/49/24/243001.
- [57] K. Van Laer, A. Bogaerts, Influence of Gap Size and Dielectric Constant of the Packing Material on the Plasma Behaviour in a Packed Bed DBD Reactor: A Fluid Modelling Study, *Plasma Process. Polym.* (2017) 14, e1600129. doi:10.1002/ppap.201600129.
- [58] P. Mehta, P. Barboun, F.A. Herrera, J. Kim, P. Rumbach, D.B. Go, J.C. Hicks, W.F. Schneider, Overcoming ammonia synthesis scaling relations with plasma-enabled catalysis, *Nat. Catal.* 1 (2018) 269–275. doi:10.1038/s41929-018-0045-1.
- [59] Q.Z. Zhang, A. Bogaerts, Propagation of a plasma streamer in catalyst pores, *Plasma Sources Sci. Technol.* 27 (2018). doi:10.1088/1361-6595/aab47a.
- [60] E.C. Neyts, K. Ostrikov, M.K. Sunkara, A. Bogaerts, Plasma Catalysis: Synergistic Effects at the Nanoscale, *Chem. Rev.* 115 (2015) 13408–13446. doi:10.1021/acs.chemrev.5b00362.
- [61] R. Aerts, W. Somers, A. Bogaerts, Carbon Dioxide Splitting in a Dielectric Barrier Discharge Plasma: A Combined Experimental and Computational Study, *ChemSusChem.* 8 (2015) 702–716. doi:10.1002/cssc.201402818.
- [62] S. Paulussen, B. Verheyde, X. Tu, C. De Bie, T. Martens, D. Petrovic, A. Bogaerts, B. Sels, Conversion of carbon dioxide to value-added chemicals in atmospheric pressure dielectric barrier discharges, *Plasma Sources Sci. Technol.* 19 (2010) 034015. doi:10.1088/0963-0252/19/3/034015.
- [63] A. Ozkan, A. Bogaerts, F. Reniers, LaNiO<sub>3</sub>@SiO<sub>2</sub> core–shell nano-particles for the dry reforming of CH<sub>4</sub> in the dielectric barrier discharge plasma, *J. Phys. D. Appl. Phys.* 50 (2017) 084004. doi:10.1088/1361-6463/aa562c.
- [64] A.-J. Zhang, A.-M. Zhu, J. Guo, Y. Xu, C. Shi, Conversion of greenhouse gases into syngas via combined effects of discharge activation and catalysis, *Chem. Eng. J.*



- 156 (2010) 601–606. doi:10.1016/j.cej.2009.04.069.
- [65] X. Zheng, S. Tan, L. Dong, S. Li, H. Chen, Plasma-assisted catalytic dry reforming of methane: Highly catalytic performance of nickel ferrite nanoparticles embedded in silica, *J. Power Sources*. 274 (2015) 286–294. doi:10.1016/j.jpowsour.2014.10.065.
- [66] X. Zheng, S. Tan, L. Dong, S. Li, H. Chen, LaNiO<sub>3</sub>@SiO<sub>2</sub> core–shell nano-particles for the dry reforming of CH<sub>4</sub> in the dielectric barrier discharge plasma, *Int. J. Hydrogen Energy*. 39 (2014) 11360–11367. doi:10.1016/j.ijhydene.2014.05.083.
- [67] J. Karupiah, P. Manoj Kumar Reddy, E. Linga Reddy, C. Subrahmanyam, Catalytic non-thermal plasma reactor for decomposition of dilute chlorobenzene, *Plasma Process. Polym.* 10 (2013) 1074–1080. doi:10.1002/ppap.201300060.
- [68] K. Krawczyk, M. Młotek, B. Ulejczyk, K. Schmidt-Szałowski, Methane conversion with carbon dioxide in plasma-catalytic system, *Fuel*. 117 (2014) 608–617. doi:10.1016/j.fuel.2013.08.068.
- [69] Q. Wang, Y. Cheng, Y. Jin, Dry reforming of methane in an atmospheric pressure plasma fluidized bed with Ni/γ-Al<sub>2</sub>O<sub>3</sub> catalyst, *Catal. Today*. 148 (2009) 275–282. doi:10.1016/j.cattod.2009.08.008.
- [70] Y. Zeng, X. Zhu, D. Mei, B. Ashford, X. Tu, Plasma-catalytic dry reforming of methane over γ-Al<sub>2</sub>O<sub>3</sub> supported metal catalysts, *Catal. Today*. 256 (2015) 80–87. doi:10.1016/j.cattod.2015.02.007.
- [71] K. Zhang, T. Mukhriza, X. Liu, P.P. Greco, E. Chiremba, A study on CO<sub>2</sub> and CH<sub>4</sub> conversion to synthesis gas and higher hydrocarbons by the combination of catalysts and dielectric-barrier discharges, *Appl. Catal. A Gen.* 502 (2015) 138–149. doi:10.1016/j.apcata.2015.06.002.
- [72] X. Tu, H.J. Gallon, M. V Twigg, P. a Gorry, J.C. Whitehead, Dry reforming of methane over a Ni/Al<sub>2</sub>O<sub>3</sub> catalyst in a coaxial dielectric barrier discharge reactor, *J. Phys. D: Appl. Phys.* 44 (2011) 274007. doi:10.1088/0022-3727/44/27/274007.
- [73] J. Sentek, K. Krawczyk, M. Młotek, M. Kalczewska, T. Kroker, T. Kolb, A. Schenk,

- K.-H. Gericke, K. Schmidt-Szałowski, Plasma-catalytic methane conversion with carbon dioxide in dielectric barrier discharges, *Appl. Catal. B Environ.* 94 (2010) 19–26. doi:10.1016/j.apcatb.2009.10.016.
- [74] L. Wang, Y. Yi, C. Wu, H. Guo, X. Tu, One-Step Reforming of CO<sub>2</sub> and CH<sub>4</sub> into High-Value Liquid Chemicals and Fuels at Room Temperature by Plasma-Driven Catalysis, *Angew. Chemie - Int. Ed.* 56 (2017) 13679–13683. doi:10.1002/anie.201707131.
- [75] M.H. Pham, V. Goujard, J.M. Tatibouët, C. Batiot-Dupeyrat, Activation of methane and carbon dioxide in a dielectric-barrier discharge-plasma reactor to produce hydrocarbons - Influence of La<sub>2</sub>O<sub>3</sub>/γ-Al<sub>2</sub>O<sub>3</sub> catalyst, *Catal. Today.* 171 (2011) 67–71. doi:10.1016/j.cattod.2011.03.015.
- [76] H.J. Gallon, X. Tu, J.C. Whitehead, Effects of Reactor Packing Materials on H<sub>2</sub> Production by CO<sub>2</sub> Reforming of CH<sub>4</sub> in a Dielectric Barrier Discharge, *Plasma Process. Polym.* 9 (2012) 90–97. doi:10.1002/ppap.201100130.
- [77] H.K. Song, J.-W. Choi, S.H. Yue, H. Lee, B.-K. Na, H.K. Songu, Synthesis gas production via dielectric barrier discharge over Ni/γ-Al<sub>2</sub>O<sub>3</sub> catalyst, *Catal. Today.* 89 (2004) 27–33. doi:10.1016/j.cattod.2003.11.009.
- [78] X. Tu, J.C. Whitehead, Plasma-catalytic dry reforming of methane in an atmospheric dielectric barrier discharge: Understanding the synergistic effect at low temperature, *Appl. Catal. B Environ.* 125 (2012) 439–448. doi:10.1016/j.apcatb.2012.06.006.
- [79] Q. Wang, B. Yan, Y. Jin, Y. Cheng, Dry Reforming of Methane in a Dielectric Barrier Discharge Reactor with Ni/Al<sub>2</sub>O<sub>3</sub> Catalyst: Interaction of Catalyst and Plasma, *Energy & Fuels.* 23 (2009) 4196–4201. doi:10.1021/ef900286j.
- [80] I. Michielsen, Y. Uytendhouwen, J. Pype, B. Michielsen, J. Mertens, F. Reniers, V. Meynen, A. Bogaerts, CO<sub>2</sub> dissociation in a packed bed DBD reactor: First steps towards a better understanding of plasma catalysis, *Chem. Eng. J.* 326 (2017) 477–488. doi:10.1016/j.cej.2017.05.177.
- [81] A.M. Vandenbroucke, R. Morent, N. De Geyter, C. Leys, Non-thermal plasmas

- for non-catalytic and catalytic VOC abatement, *J. Hazard. Mater.* 195 (2011) 30–54. doi:10.1016/j.jhazmat.2011.08.060.
- [82] S. Futamura, A. Zhang, H. Einaga, H. Kabashima, Involvement of catalyst materials in nonthermal plasma chemical processing of hazardous air pollutants, *Catal. Today*. 72 (2002) 259–265. doi:10.1016/S0920-5861(01)00503-X.
- [83] H.-H. Kim, Nonthermal Plasma Processing for Air-Pollution Control: A Historical Review, Current Issues, and Future Prospects, *Plasma Process. Polym.* 1 (2004) 91–110. doi:10.1002/ppap.200400028.
- [84] C. Subrahmanyam, M. Magureanu, A. Renken, L. Kiwi-Minsker, Catalytic abatement of volatile organic compounds assisted by non-thermal plasma, *Appl. Catal. B Environ.* 65 (2006) 150–156. doi:10.1016/j.apcatb.2006.01.006.
- [85] H.H. Kim, A. Ogata, Interaction of Nonthermal Plasma with Catalyst for the Air Pollution Control, in: 2011: pp. 43–48.
- [86] K.-P. Francke, H. Miessner, R. Rudolph, Plasmacatalytic processes for environmental problems, *Catal. Today*. 59 (2000) 411–416. doi:10.1016/S0920-5861(00)00306-0.
- [87] S. Pasquiers, Removal of pollutants by plasma catalytic processes, *Eur. Phys. J. Appl. Phys.* 28 (2004) 319–324. doi:10.1051/epjap.
- [88] O. Guaitella, F. Thevenet, E. Puzenat, C. Guillard, A. Rousseau, C<sub>2</sub>H<sub>2</sub> oxidation by plasma/TiO<sub>2</sub> combination: Influence of the porosity, and photocatalytic mechanisms under plasma exposure, *Appl. Catal. B Environ.* 80 (2008) 296–305. doi:10.1016/j.apcatb.2007.11.032.
- [89] J. Van Durme, J. Dewulf, C. Leys, H. Van Langenhove, Combining non-thermal plasma with heterogeneous catalysis in waste gas treatment: A review, *Appl. Catal. B Environ.* 78 (2008) 324–333. doi:10.1016/j.apcatb.2007.09.035.
- [90] R. Aerts, W. Somers, A. Bogaerts, A detailed description of the CO<sub>2</sub> splitting by dielectric barrier discharges, *ChemSusChem*. 8 (2015) 702–716.
- [91] Q. Yu, M. Kong, T. Liu, J. Fei, X. Zheng, Characteristics of the Decomposition of CO<sub>2</sub> in a Dielectric Packed-Bed Plasma Reactor, *Plasma Chem. Plasma Process.*

- 32 (2012) 153–163. doi:10.1007/s11090-011-9335-y.
- [92] D. Mei, X. Zhu, Y.-L.Y. He, J.D. Yan, X. Tu, Plasma-assisted conversion of CO<sub>2</sub> in a dielectric barrier discharge reactor: understanding the effect of packing materials, *Plasma Sources Sci. Technol.* 24 (2015) 15011. doi:10.1088/0963-0252/24/1/015011.
- [93] K. Van Laer, A. Bogaerts, Improving the Conversion and Energy Efficiency of Carbon Dioxide Splitting in a Zirconia-Packed Dielectric Barrier Discharge Reactor, *Energy Technol.* 3 (2015) 1038–1044. doi:10.1002/ente.201500127.
- [94] A. Berthelot, A. Bogaerts, Modeling of plasma-based CO<sub>2</sub> conversion: lumping of the vibrational levels, *Plasma Sources Sci. Technol.* 25 (2016) 045022. doi:10.1088/0963-0252/25/4/045022.
- [95] N. Pinhão, A. Moura, J.B. Branco, J. Neves, Influence of gas expansion on process parameters in non-thermal plasma plug-flow reactors: A study applied to dry reforming of methane, *Int. J. Hydrogen Energy.* 41 (2016) 9245–9255. doi:10.1016/j.ijhydene.2016.04.148.
- [96] S. Mahammadunnisa, P. Manoj Kumar Reddy, E. Linga Reddy, C. Subrahmanyam, Catalytic DBD plasma reactor for CO oxidation by in situ N<sub>2</sub>O decomposition, *Catal. Today.* 211 (2013) 53–57. doi:10.1016/j.cattod.2013.03.028.
- [97] A. Jahanmiri, M.R. Rahimpour, M. Mohamadzadeh Shirazi, N. Hooshmand, H. Taghvaei, Naphtha cracking through a pulsed DBD plasma reactor: Effect of applied voltage, pulse repetition frequency and electrode material, *Chem. Eng. J.* 191 (2012) 416–425. doi:10.1016/j.cej.2012.02.031.
- [98] M. Ramakers, I. Michielsen, R. Aerts, V. Meynen, A. Bogaerts, Effect of argon or helium on the CO<sub>2</sub> conversion in a dielectric barrier discharge, *Plasma Process. Polym.* 12 (2015) 755–763. doi:10.1002/ppap.201400213.
- [99] F. A.L. Dullien, *Porous Media*, Elsevier, San Diego, California, 1992. doi:10.1016/C2009-0-26184-8.
- [100] J. Niu, X. Yang, A. Zhu, L. Shi, Q. Sun, Y. Xu, C. Shi, Plasma-assisted selective catalytic reduction of NO<sub>x</sub> by C<sub>2</sub>H<sub>2</sub> over Co-HZSM-5 catalyst, *Catal. Commun.* 7

- (2006) 297–301. doi:10.1016/j.catcom.2005.10.016.
- [101] S. Kameshima, K. Tamura, Y. Ishibashi, T. Nozaki, Pulsed dry methane reforming in plasma-enhanced catalytic reaction, *Catal. Today*. 256 (2015) 67–75. doi:10.1016/j.cattod.2015.05.011.
- [102] M. Kraus, B. Eliasson, U. Kogelschatz, A. Wokaun, CO<sub>2</sub> reforming of methane by the combination of dielectric-barrier discharges and catalysis, *Phys. Chem. Chem. Phys.* 3 (2001) 294–300. doi:10.1039/b007015g.
- [103] T. Tojo, T. Atake, T. Mori, H. Yamamura, Heat capacity and thermodynamic functions of zirconia and yttria-stabilized zirconia, *J. Chem. Thermodyn.* 31 (1999) 831–845. doi:10.1006/jcht.1998.0481.
- [104] Y. Takahashi, H. Yokokawa, H. Kadokura, Y. Sekine, T. Mukaibo, Laser-flash calorimetry I. Calibration and test on alumina heat capacity, *J. Chem. Thermodyn.* 11 (1979) 379–394. doi:10.1016/0021-9614(79)90058-2.
- [105] M.W.J. Chase, NIST-JANAF Thermochemical Tables, *J. Phys. Chem. Ref. Data*, 4th editio, 1998.
- [106] Y. He, Heat capacity, thermal conductivity, and thermal expansion of barium titanate-based ceramics, *Thermochim. Acta.* 419 (2004) 135–141. doi:10.1016/j.tca.2004.02.008.
- [107] W. Martienssen, H. Warlimont, *Condensed matter and materials data*, 1st ed., Springer-Verlag Berlin Heidelberg, Berlin, 2005.
- [108] Zirconia - ZrO<sub>2</sub>, Zirconium Dioxide, (n.d.). <https://www.azom.com/properties.aspx?ArticleID=133>.
- [109] Alumina - Aluminium Oxide - Al<sub>2</sub>O<sub>3</sub> - A Refractory Ceramic Oxide, (n.d.). <https://www.azom.com/article.aspx?ArticleID=52>.
- [110] Silica - Silicon Dioxide (SiO<sub>2</sub>), (n.d.). <https://www.azom.com/properties.aspx?ArticleID=1114>.
- [111] T.D. Butterworth, *The Effects of Particle Size on CO<sub>2</sub> reduction in Packed Bed Dielectric Barrier Discharge Plasma Reactors*, 2015.
- [112] D.R. Lide, *CRC Handbook of Chemistry and Physics*, *J. Am. Chem. Soc.* 131 (2009)

12862–12862. doi:10.1021/ja906434c.

- [113] J. Pype, B. Michielsen, E.M. Seftel, S. Mullens, V. Meynen, Development of alumina microspheres with controlled size and shape by vibrational droplet coagulation, *J. Eur. Ceram. Soc.* 37 (2017) 189–198. doi:10.1016/j.jeurceramsoc.2016.07.020.
- [114] J. Rouquerol, G. Baron, R. Denoyel, H. Giesche, J. Groen, P. Klobes, P. Levitz, A. V. Neimark, S. Rigby, R. Skudas, K. Sing, M. Thommes, K. Unger, Liquid intrusion and alternative methods for the characterization of macroporous materials (IUPAC Technical Report), *Pure Appl. Chem.* 84 (2012) 107–136. doi:10.1351/pac-rep-10-11-19.
- [115] H.H. Kim, Y. Teramoto, N. Negishi, A. Ogata, A multidisciplinary approach to understand the interactions of nonthermal plasma and catalyst: A review, *Catal. Today.* 256 (2014) 13–22. doi:10.1016/j.cattod.2015.04.009.
- [116] I. Belov, S. Paulussen, A. Bogaerts, Appearance of a conductive carbonaceous coating in a CO<sub>2</sub> dielectric barrier discharge and its influence on the electrical properties and the conversion efficiency, *Plasma Sources Sci. Technol.* 25 (2016) 015023. doi:10.1088/0963-0252/25/1/015023.
- [117] H.L. Chen, H.M. Lee, S.H. Chen, M.B. Chang, S.J. Yu, S.N. Li, Removal of Volatile Organic Compounds by Single-Stage and Two-Stage Plasma Catalysis Systems: A Review of the Performance Enhancement Mechanisms, Current Status, and Suitable Applications, *Environ. Sci. Technol.* 43 (2009) 2216–27. doi:10.1021/es802679b.
- [118] J.C. Whitehead, Plasma catalysis: A solution for environmental problems, *Pure Appl. Chem.* 82 (2010) 1329–1336. doi:10.1351/PAC-CON-10-02-39.
- [119] A. Bogaerts, T. Kozák, K. van Laer, R. Snoeckx, Plasma-based conversion of CO<sub>2</sub> : current status and future challenges, *Faraday Discuss.* (2015) 217–232. doi:10.1039/C5FD00053J.
- [120] M. Kraus, W. Egli, K. Haffner, B. Eliasson, U. Kogelschatz, A. Wokaun, Investigation of mechanistic aspects of the catalytic CO<sub>2</sub> reforming of methane

- in a dielectric-barrier discharge using optical emission spectroscopy and kinetic modeling, *Phys. Chem. Chem. Phys.* 4 (2002) 668–675. doi:10.1039/b108040g.
- [121] L.F. Spencer, A.D. Gallimore, CO<sub>2</sub> dissociation in an atmospheric pressure plasma/catalyst system: a study of efficiency, *Plasma Sources Sci. Technol.* 22 (2013) 015019. doi:10.1088/0963-0252/22/1/015019.
- [122] H. Lee, H. Sekiguchi, Plasma–catalytic hybrid system using spouted bed with a gliding arc discharge: CH<sub>4</sub> reforming as a model reaction, *J. Phys. D. Appl. Phys.* 44 (2011) 274008. doi:10.1088/0022-3727/44/27/274008.
- [123] A. Ozkan, T. Dufour, A. Bogaerts, F. Reniers, How do the barrier thickness and dielectric material influence the filamentary mode and CO<sub>2</sub> conversion in a flowing DBD?, *Plasma Sources Sci. Technol.* 25 (2016) 18. doi:10.1088/0963-0252/25/4/045016.
- [124] R. Li, Q. Tang, S. Yin, T. Sato, Plasma catalysis for CO<sub>2</sub> decomposition by using different dielectric materials, *Fuel Process. Technol.* 87 (2006) 617–622. doi:10.1016/j.fuproc.2006.01.007.
- [125] R. Li, Influence of dielectric barrier materials to the behavior of dielectric barrier discharge plasma for CO<sub>2</sub> decomposition, *Solid State Ionics.* 172 (2004) 235–238. doi:10.1016/j.ssi.2004.02.036.
- [126] X. Duan, Z. Hu, Y. Li, B. Wang, Effect of Dielectric Packing Materials on the Decomposition of Carbon Dioxide Using DBD Microplasma Reactor, *AIChE.* 61 (2015) 898–903. doi:10.1002/aic.
- [127] C.-J. Liu, J. Zou, K. Yu, D. Cheng, Y. Han, J. Zhan, C. Ratanatawanate, B.W.-L. Jang, Plasma application for more environmentally friendly catalyst preparation, *Pure Appl. Chem.* 78 (2006) 1227–1238. doi:10.1351/pac200678061227.
- [128] H.H. Kim, A. Ogata, S. Futamura, Oxygen partial pressure-dependent behavior of various catalysts for the total oxidation of VOCs using cycled system of adsorption and oxygen plasma, *Appl. Catal. B Environ.* 79 (2008) 356–367. doi:10.1016/j.apcatb.2007.10.038.
- [129] T. Nozaki, N. Muto, S. Kado, K. Okazaki, Dissociation of vibrationally excited

- methane on Ni catalyst, *Catal. Today*. 89 (2004) 57–65. doi:10.1016/j.cattod.2003.11.040.
- [130] X. Tu, H.J. Gallon, J.C. Whitehead, Plasma-assisted reduction of a NiO/Al<sub>2</sub>O<sub>3</sub> catalyst in atmospheric pressure H<sub>2</sub>/Ar dielectric barrier discharge, *Catal. Today*. 211 (2013) 120–125. doi:10.1016/j.cattod.2013.03.024.
- [131] A.E. Wallis, J.C. Whitehead, K. Zhang, Plasma-assisted catalysis for the destruction of CFC-12 in atmospheric pressure gas streams using TiO<sub>2</sub>, *Catal. Letters*. 113 (2007) 29–33. doi:10.1007/s10562-006-9000-x.
- [132] S. Mahammadunnisa, E.L. Reddy, D. Ray, C. Subrahmanyam, J.C. Whitehead, CO<sub>2</sub> reduction to syngas and carbon nanofibres by plasma-assisted in situ decomposition of water, *Int. J. Greenh. Gas Control*. 16 (2013) 361–363. doi:10.1016/j.ijggc.2013.04.008.
- [133] J. Van Durme, J. Dewulf, W. Sysmans, C. Leys, H. Van Langenhove, Efficient toluene abatement in indoor air by a plasma catalytic hybrid system, *Appl. Catal. B Environ*. 74 (2007) 161–169. doi:10.1016/j.apcatb.2007.02.006.
- [134] H. Wang, J. Li, X. Quan, Y. Wu, Enhanced generation of oxidative species and phenol degradation in a discharge plasma system coupled with TiO<sub>2</sub> photocatalysis, *Appl. Catal. B Environ*. 83 (2008) 72–77. doi:10.1016/j.apcatb.2008.02.004.
- [135] T. Nozaki, K. Okazaki, Innovative Methane Conversion technology using atmospheric pressure non-thermal plasma, *J. Japan Pet. Institue*. 54 (2011) 146–158. doi:10.1627/jpi.54.146.
- [136] Y. Guo, X. Liao, D. Ye, Detection of hydroxyl radical in plasma reaction on toluene removal, *J. Environ. Sci*. 20 (2008) 1429–1432. doi:10.1016/S1001-0742(08)62544-9.
- [137] X. Bin Liao, Y.F. Guo, J.H. He, W.J. Ou, D.Q. Ye, Hydroxyl radicals formation in dielectric barrier discharge during decomposition of toluene, *Plasma Chem. Plasma Process*. 30 (2010) 841–853. doi:10.1007/s11090-010-9253-4.
- [138] H.J. Gallon, X. Tu, M. V. Twigg, J.C. Whitehead, Plasma-assisted methane



- reduction of a NiO catalyst—Low temperature activation of methane and formation of carbon nanofibres, *Appl. Catal. B Environ.* 106 (2011) 616–620. doi:10.1016/j.apcatb.2011.06.023.
- [139] K. Van Laer, A. Bogaerts, How bead size and dielectric constant affect the plasma behaviour in a packed bed plasma reactor: a modelling study, *Plasma Sources Sci. Technol.* 26 (2017) 085007. doi:10.1088/1361-6595/aa7c59.
- [140] Y.R. Zhang, K. Van Laer, E.C. Neyts, A. Bogaerts, Can plasma be formed in catalyst pores? A modeling investigation, *Appl. Catal. B Environ.* 185 (2016) 56–67. doi:10.1016/j.apcatb.2015.12.009.
- [141] Y. Zhang, H. -y. Wang, Y.-R. Zhang, A. Bogaerts, Formation of microdischarges inside a mesoporous catalyst in dielectric barrier discharge plasmas, *Plasma Sources Sci. Technol.* (n.d.).
- [142] Y. Uytendhouwen, S. Van Alphen, I. Michiels, V. Meynen, P. Cool, A. Bogaerts, A packed-bed DBD micro plasma reactor for CO<sub>2</sub> dissociation: Does size matter?, *Chem. Eng. J.* 348 (2018). doi:10.1016/j.cej.2018.04.210.
- [143] P. Atkins, L. Jones, *Chemical Principles: the quest for insight*, Fourth, Craig Bleyster, New York, 2008.
- [144] W. Wang, A. Berthelot, Q. Zhang, A. Bogaerts, Modelling of plasma-based dry reforming: How do uncertainties in the input data affect the calculation results?, *J. Phys. D. Appl. Phys.* 51 (2018). doi:10.1088/1361-6463/aab97a.
- [145] A. Berthelot, A. Bogaerts, Modeling of CO<sub>2</sub> plasma: Effect of uncertainties in the plasma chemistry, *Plasma Sources Sci. Technol.* 26 (2017). doi:10.1088/1361-6595/aa8ffb.
- [146] B. Saha, A. Khan, H. Ibrahim, R. Idem, Evaluating the performance of non-precious metal based catalysts for sulfur-tolerance during the dry reforming of biogas, *Fuel*. 120 (2014) 202–217. doi:10.1016/j.fuel.2013.12.016.
- [147] C. De Bie, J. Van Dijk, A. Bogaerts, The Dominant Pathways for the Conversion of Methane into Oxygenates and Syngas in an Atmospheric Pressure Dielectric Barrier Discharge, *J. Phys. Chem. C.* 119 (2015) 22331–22350.

doi:10.1021/acs.jpcc.5b06515.

- [148] W. Wang, H.H. Kim, K. Van Laer, A. Bogaerts, Streamer propagation in a packed bed plasma reactor for plasma catalysis applications, *Chem. Eng. J.* 334 (2018) 2467–2479. doi:10.1016/j.cej.2017.11.139.
- [149] R. Aerts, R. Snoeckx, A. Bogaerts, In-Situ Chemical Trapping of Oxygen in the Splitting of Carbon Dioxide by Plasma, *Plasma Process. Polym.* 11 (2014) 985–992. doi:10.1002/ppap.201400091.
- [150] R. Snoeckx, A. Ozkan, F. Reniers, A. Bogaerts, The Quest for Value-Added Products from Carbon Dioxide and Water in a Dielectric Barrier Discharge: A Chemical Kinetics Study, *ChemSusChem.* 10 (2017) 409–424. doi:10.1002/cssc.201601234.
- [151] I. Michielsen, Y. Uytendhouwen, A. Bogaerts, V. Meynen, Altering Conversion and Product Selectivity of Dry Reforming of Methane in a Dielectric Barrier Discharge by Changing the Dielectric Packing Material, 2019. doi:10.3390/catal9010051.
- [152] A. Ozkan, CO<sub>2</sub> splitting in a dielectric barrier discharge plasma : understanding of physical and chemical aspects, 2016.
- [153] S. Piskunov, E. Heifets, R.. Eglitis, G. Borstel, Bulk properties and electronic structure of SrTiO<sub>3</sub>, BaTiO<sub>3</sub>, PbTiO<sub>3</sub> perovskites: an ab initio HF/DFT study, *Comput. Mater. Sci.* 29 (2004) 165–178. doi:10.1016/j.commatsci.2003.08.036.
- [154] A.N. Chibisov, Effect of stoichiometry on the atomic and electronic structure of BaTiO<sub>3</sub> nanoparticles: A first-principles study, *Mol. Phys.* 113 (2015) 3291–3295. doi:10.1080/00268976.2015.1017544.
- [155] S. Ramakanth, K.C. James Raju, Band gap narrowing in BaTiO<sub>3</sub> nanoparticles facilitated by multiple mechanisms, *J. Appl. Phys.* 115 (2014) 173507. doi:10.1063/1.4871776.
- [156] R. Ahmed, C.M. Sinnathambi, D. Subbarao, Kinetics of de-coking of spent reforming catalyst, *J. Appl. Sci.* 11 (2011) 1225–1230.
- [157] A. Bogaerts, C. De Bie, R. Snoeckx, T. Kozák, Plasma based CO<sub>2</sub> and CH<sub>4</sub>

conversion: A modeling perspective, *Plasma Process. Polym.* 14 (2017).  
doi:10.1002/ppap.201600070.



# 11 CURRICULUM VITAE

---

## 11.1 LIST OF PUBLICATIONS

- I. M. Ramakers, I. Michiels, R. Aerts, V. Meynen, A. Bogaerts, Effect of argon or helium on the CO<sub>2</sub> conversion in a dielectric barrier discharge, *Plasma Process. Polym.* 12 (2015) 755–763. Doi:10.1002/ppap.201400213.
- II. I. Michiels, Y. Uytendhouwen, J. Pype, B. Michiels, J. Mertens, F. Reniers, V. Meynen, A. Bogaerts, CO<sub>2</sub> dissociation in a packed bed DBD reactor: First steps towards a better understanding of plasma catalysis, *Chem. Eng. J.* 326 (2017) 477–488. Doi:10.1016/j.cej.2017.05.177
- III. Y. Uytendhouwen, S. Van Alphen, I. Michiels, V. Meynen, P. Cool, A. Bogaerts, A packed-bed DBD micro plasma reactor for CO<sub>2</sub> dissociation: Does size matter?, *Chem. Eng. J.* 348 (2018) 557-568. Doi:10.1016/j.cej.2018.04.210
- IV. I. Michiels, Y. Uytendhouwen, A. Bogaerts, V. Meynen, Altering Conversion and Product Selectivity of Dry Reforming of Methane in a Dielectric Barrier Discharge by Changing the Dielectric Packing Material, *Catalysts* 9, 51 (2019). Doi:10.3390/catal9010051
- V. Y. Uytendhouwen, K.M. Bal, I. Michiels, E.C. Neyts, V. Meynen, P. Cool, A. Bogaerts, How process parameters and packing materials tune chemical equilibrium and kinetics in plasma-based CO<sub>2</sub> conversion, *Chem. Eng. J.* 372 (2019) 1253-1264. Doi: 10.1016/j.cej.2019.05.008

## 11.2 LIST OF CONFERENCE CONTRIBUTIONS

### 11.2.1 Oral presentations

- I. "Packing effect of SiO<sub>2</sub>, ZrO<sub>2</sub>, BaTiO<sub>3</sub> and Al<sub>2</sub>O<sub>3</sub> beads on CO<sub>2</sub> conversion in a packed-bed DBD reactor", I. Michielsen, K. Van Laer, Y. Uytendhouwen, V. Meynen and A. Bogaerts, 22<sup>nd</sup> International Symposium on plasma chemistry, Belgium, Antwerp, 05-10/07/2015
- II. "Influence of packing material on CO<sub>2</sub> conversion in a packed-bed DBD reactor", I. Michielsen, Y. Uytendhouwen, V. Meynen and A. Bogaerts, Zing conference on Carbon Dioxide Catalysis, Portugal, Albufeira Portugal, 19-22/04/16
- III. "CO<sub>2</sub> splitting in a packed bed DBD reactor – interaction between packing and dielectric barrier", I. Michielsen, Y. Uytendhouwen, V. Meynen and A. Bogaerts, International Workshop on Plasmas for Energy and Environmental Applications, UK, Liverpool, 21-24/08/16
- IV. "Altering the packing in a packed-bed DBD plasma reactor for CO<sub>2</sub> splitting: effect of porosity", I. Michielsen, Y. Uytendhouwen, V. Meynen and A. Bogaerts, International Conference on Carbon Dioxide Utilization, UK, Sheffield, 11-15/09/16
- V. "Effect of dielectric material and packing parameters in a packed bed DBD reactor", I. Michielsen, Y. Uytendhouwen, V. Meynen and A. Bogaerts, Combining non-thermal plasma and heterogeneous catalysis for sustainable development, France, Lille, 13/10/16
- VI. "Plasma Catalysis", I. Michielsen, V. Meynen and A. Bogaerts, European Nanoporous Materials Institute of Excellence: Young Researcher Forum
  - a. Germany, Stuttgart, 22/01/2016
  - b. Belgium, Antwerp, 3-4/10/2016
  - c. Spain, Alicante, 27-28/09/2017
  - d. Spain, Valencia, 28/09/08

### 11.2.2 Poster presentations

- I. “Plasma catalysis for better CO<sub>2</sub> conversion”, I. Michielsen, K. Van Laer, Y. Uytendhouwen, V. Meynen and A. Bogaerts, 2015 Brussels Sustainable Development Summit, Belgium, Brussels, 19-20/10/2015.
- II. “Altering the packing in a packed-bed DBD plasma reactor for CO<sub>2</sub> splitting: effect of porosity”, I. Michielsen, Y. Uytendhouwen, V. Meynen and A. Bogaerts, International Conference on Carbon Dioxide Utilization, UK, Sheffield, 11-15/09/16

### 11.3 AWARDS

- I. IWT-grant, 01/01/2015-31/12/2018, grant-number 141093.
- II. Winning First Prize at the SCOT Project Flash Presentation Prize for “Altering the packing in a packed-bed DBD plasma reactor for CO<sub>2</sub> splitting: effect of porosity”, I. Michielsen, Y. Uytendhouwen, V. Meynen and A. Bogaerts, International Conference on Carbon Dioxide Utilization, UK, Sheffield, 11-15/09/16

### 11.4 EXTRA-CURRICULAR ACTIVITIES

- I. Godmother for first year students
- II. Ombudsperson for the Master in Chemistry
- III. President of the ENMIX Young Researchers Division (2016-2018)

